THE UNIVERSITY OF ST. ANDREWS

X-ray and Optical Variability in X-ray Binaries

Kieran O'Brien

Submitted for the degree of Ph.D.

22nd May 2000

THE UNIVERSITY OF ST. ANDREWS

X-ray and Optical Variability in X-ray Binaries

Submitted for the degree of Ph.D.

22nd May 2000

Kieran O'Brien

ABSTRACT

Observations of Low-mass X-ray Binaries (LMXBs) have shown that a large fraction of the optical emission arises from the reprocessing of X-rays in regions such as the accretion disk and the donor star. In this thesis, I have used several datasets, including coordinated observations from Keck II and *RXTE* and archival data, to study the simultaneous X-ray and optical variability in X-ray Binaries. They allow us to study the distribution of reprocessing regions in X-ray binaries by determining the range of time delays between the directly observed X-ray lightcurves and the reprocessed optical lightcurves, that are delayed in time of arrival relative to the X-ray lightcurves, due to time of flight differences. I have used such models to determine that in the case of Scorpius X-1, a persistent LMXB, the range of time delays observed mean that there is considerable companion star and accretion disk reprocessing, whereas in the case of GRO J1655-40, a LMXB in outburst, the outer accretion disk has swelled up enough to cast a shadow over much of the donor star.

In the case of Cygnus X-2, another persistent LMXB, I have have found that, while the correlated variability is more complicated than suspected previously, we can use simultaneous observations to study changes in the accretion flow associated with changes in the X-ray spectral state of the object. I have used simultaneous optical spectroscopic observations from Keck II, along with X-ray observations with *RXTE*, to construct a model for the X-ray emission from the central compact object that fits the observations well. Using similar observations, I have characterized the first observation of a low frequency QPO in the X-ray pulsar Hercules X-1. I show that this is not simply a reprocessed X-ray pulsation, but is likely caused by the interaction of the accretion flow with material in the inner regions of a warped accretion disk.

DECLARATION

I, Kieran O'Brien, hereby certify that this thesis, which is approximately 36000 words in length has been written by me, that it is the record of work carried out by me and that it has not been submitted in any previous application for a higher degree

I was admitted as a research student in October 1996 and as a candidate for the degree of Ph.D. in Astronomy in October, 1996; the higher study for which this is a record was carried out in the University of St. Andrews between 1996 and 2000.

In submitting this thesis to the University of St. Andrews I understand that I am giving permission for it to be made available for use in accordance with the regulations of the University Library for the time being in force, subject to any copyright vested in the work not being affected thereby. I also understand that the title and abstract will be published, and that a copy of the work may be made and supplied to any bona fide library or research worker.

date 15 Sept 2000 signature of candidate

I hereby certify that the candidate has fulfilled the conditions of the Resolution and Regulations appropriate for the degree of Ph.D. in the University of St. Andrews and that the candidate is qualified to submit this thesis in application for that degree.

date 15 Sep 2000 signature of supervisor

ACKNOWLEDGMENTS

I would like to begin by thanking Prof. Keith Horne, my PhD supervisor, for all the help and support he has given me during my time in St Andrews. His knowledge and guidance have been invaluable and his enthusiasm very infectious. I just hope that this thesis falls into the 'new and exciting' category. I have learnt so much and look forward to many more long coffee-time conversations.

A big thank-you goes to Richard Gomer and Bev Oke who gave me the opportunity to go to Hawaii to get some great data (...and a great tan!). I hope we can do it again some time. Many thanks also go to Rob Hynes and Carole Haswell for letting me share their data. I would also like to thank the various people I have met during my PhD for their help and interesting conversations.

I would like to thank my parents who, despite probably not understanding what I have been studying for the last few years, or even why I have been doing it, have given me their never-ending love and support. Without your help and that of the rest of the family, I definitely wouldn't be where I am today. I'll remember the day you all turned up to visit me in a mini-bus for the rest of my life!

To the members of the BCCTC, both original and honorary, thanks for the frequent and, more often than not, painful visits. They sure hit the spot!

Last, but by no means least, I would like to thank all the friends I have made while I've been in St Andrews. I would especially like to thank Danny and Marti for helping to keep me sane (most of the time!). Also Gaitee, Jim, Lewis, Dave, Sharky, Warren, Kevin... the list is endless, for all the laughs and all the help.

I never did learn how to play golf properly!

CONTENTS

LIST OF FIGURES

LIST OF TABLES

CHAPTER 1

A brief guide to X-ray binaries

Accretion is one of the most widely studied areas of astrophysics. It plays a key role in many varied astrophysical systems, from the formation of proto-stars and planetary discs, to the power source for objects from interacting binaries to active galactic nuclei and quasars. In order to understand the physical mechanisms of accretion on all scales, astronomers have used interacting binaries as their laboratories. They have chosen to study interacting binaries for a number of reasons. They have a relatively simple geometry, which can be described using classical equations, they are easily observed due to their proximity, but perhaps most importantly because they emit on short timescales over a broad range of the electro-magnetic spectrum, making it possible to investigate a range of phenomena.

In recent years, with the advances in X-ray astronomy, most noticeably from EXOSAT and *RXTE*, it has become possible to explore the high energy characteristics of binaries. This has renewed the interest in interacting binaries and led to the discovery of new, distinct classes of objects. In this chapter I summarize some of the characteristics of interacting binaries and explain why I have chosen them to study in this thesis.

1.1 Interacting binaries

Binary systems contain two stars that are gravitationally bound, orbiting around their common centre of gravity. The gravitational potential for the system can be adequately described using classical equations. The force acting on a mass m, in the corotating frame of the binary, is

$$\mathbf{F}_m = \mathbf{F}_{M_1} + \mathbf{F}_{M_2} + \mathbf{F}_{centrifugal} + \mathbf{F}_{Coriolis}, \tag{1.1}$$

where $\mathbf{F}_{M_1}$ and $\mathbf{F}_{M_2}$ are the gravitational force vectors due to the presence of the two stars, with masses M_1 and M_2. $\mathbf{F}_{centrifugal}$ is the Centrifugal force due to the motion of the binary around the centre of mass of the stars and $\mathbf{F}_{Coriolis}$ is the observed Coriolis force due to the rotating reference frame. The net force in the co-rotating frame of the binary is given by

$$\mathbf{F}_m = -\frac{GM_1m}{|\mathbf{r}_1 - \mathbf{r}|^3}(\mathbf{r} - \mathbf{r}_1) - \frac{GM_2m}{|\mathbf{r}_2 - \mathbf{r}|^3}(\mathbf{r} - \mathbf{r}_2) - m\boldsymbol{\Omega} \times (\boldsymbol{\Omega} \times \mathbf{r}) - 2m(\boldsymbol{\Omega} \times \mathbf{v}), \tag{1.2}$$

where $\mathbf{r}$, $\mathbf{r}_1$ and $\mathbf{r}_2$ are the positions of the test mass, and the two stars respectively, relative to the centre of mass of the system. $\boldsymbol{\Omega}$ is the angular velocity of the binary and $\mathbf{v}$ is the velocity of the test mass in the rotating frame.

Interacting binaries are binary systems where at some stage the components are physically close enough to transfer material from one binary component to the other. In order for this to happen material must pass from the Roche lobe of the donor star into the Roche lobe of the accreting object. This can take the form of a wind from the stellar photosphere or, as in the case of the LMXBs, via Roche lobe overflow. In Roche lobe overflow the material in transfered through the inner Lagrangian point into the Roche lobe of the compact object. This Roche lobe overflow can be driven by evolutionary effects, or through the shrinking of the binary orbit, caused by loss of angular momentum for example by the emission of gravitational radiation or by magnetic braking. If the donor star is an evolved star then the star can expand to overflow its Roche lobe, which is thought to be the case for objects such as Scorpius X-1 and Cygnus X-2. An artists impression of an X-ray binary, showing the different emission regions is shown in Figure 1.2.

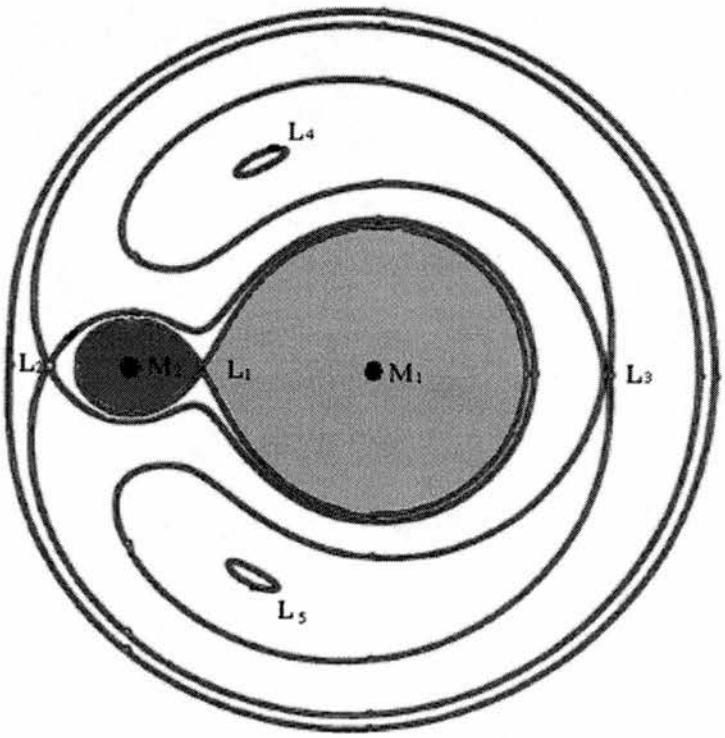

Figure 1.1: Schematic diagram of the cut through the equipotential surfaces in the orbital plane of the binary. Also highlighted are the Roche Lobes of the stellar objects, assumed to have different masses. This Figure was obtained from Z. Ioannou (http://www.astro.keele.ac.uk/~zac/)

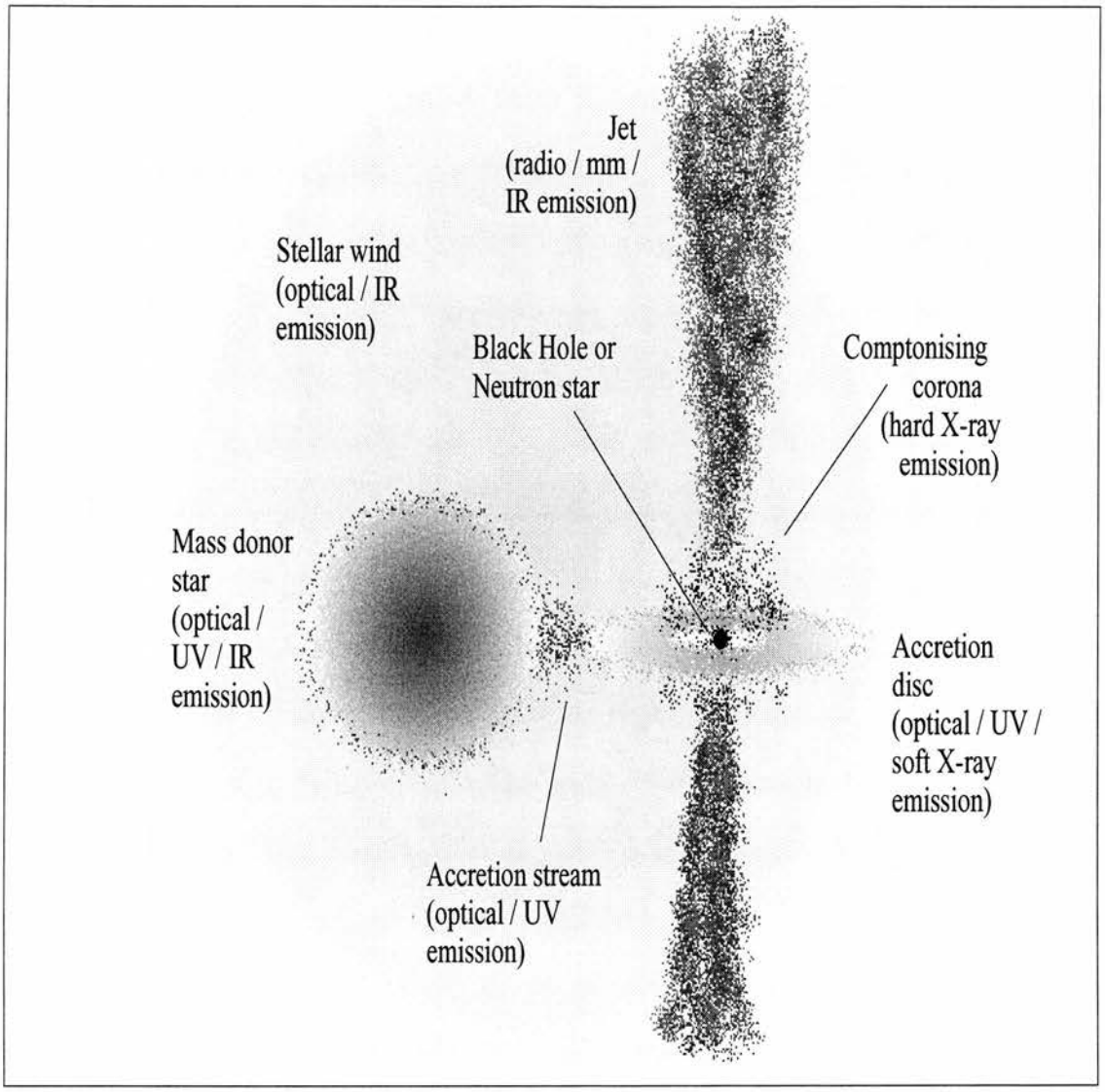

Figure 1.2: Artists impression of a low mass X-ray binary, or a black hole binary, showing the different emission sites within the binary. The existence of the jet in the source depends on the exact nature of the binary. This Figure was obtained from Fender (1999)

1.1.1 Sub-classes of interacting binaries

While the underlying phenomenon of accretion is common to all types of interacting binaries, the mechanism responsible and the processes involved vary dramatically between the different classes of objects. The principal difference between the classes of interacting binaries is the nature of the compact object and its effect on the accretion flow. While there are many similarities between the different objects, there are also major differences. In cataclysmic variables (CVs) the compact object is a white dwarf, supported by the electron degeneracy pressure. In such systems the optical emission from the disk is dominated by the viscous dissipation of energy as the material spirals through the disk to the white dwarf. In X-ray binaries (XRBs), the compact object is a neutron star or black hole and the optical spectrum is dominated by the emission from the X-ray heating of the accretion disk.

1.2 Subclasses of XRBs

1.2.1 Low Mass X-ray Binaries

The low mass X-ray binaries (LMXBs) contain a donor star of less than approximately $2M_{\odot}$. In LMXBs an accretion disk will form. The accreting material spirals in through the accretion disk losing angular momentum until it is accreted onto the compact object at the centre of the disk. In this thesis I shall be concentrating on LMXBs and I shall give a review of the features of X-ray binaries in Sections 1.3 - 1.7.

1.2.2 High Mass X-ray Binaries

The High Mass X-ray Binaries (HMXBs) contain a donor star of greater than approximately $10M_{\odot}$, in a binary orbit with a neutron star or black hole. The HMXBs generally fall into two sub-groups, the supergiants, with a normal O or B star, and the Be/X-ray binaries that contain an O or B emission line star (see White, Nagase & Parmar (1995) for a summary of the characteristics of HMXBs). In the case of the supergiants the matter is accreting via a wind from the $> 10M_{\odot}$ donor star. In the case of the Be/X-ray binaries,

with their eccentric orbits, the matter can be transferred via quasi-Roche lobe overflow, as the compact object approaches periastron. In both cases, the optical spectrum is dominated by the spectrum of the donor star, which has a higher luminosity than the X-ray source and thus irradiation has a small effect in such systems. This fact makes HMXBs unsuitable for studies of short-timescale correlated X-ray and Optical variability and I will not discuss these further.

In this thesis I will concentrate on the LMXBs, in the next section I will describe some of the optical and X-ray characteristic of LMXBs and how I have used the variability in these sources to study the geometry and accretion flow in LMXBs.

1.3 X-ray emission from LMXBs

In all types of LMXBs the X-ray emission occurs due to the release of gravitational energy of material which is falling in the deep potential well of the compact object. This compact object is either a neutron star or black hole. The black hole X-ray binaries show many similarities to their neutron star counterparts. They have many similar features in their X-ray power spectra and exhibit similar hard/soft spectral transitions. The X-ray emissions mechanism is similar, although lacking features, such as X-ray bursts, associated with a hard stellar surface. These similarities allow me, for this thesis, to treat BHBs in the same manner as the neutron star sources, as I will not be considering the inner regions of the accretion disk, where relativistic effects become important.

This leads to two separate components, one from the accretion disk and the other from effects close to or on the surface of the neutron star. The emission from the disk has the spectrum of a multi-colour blackbody, with a temperature of several keV and is seen to be highly variable. There is also evidence for Compton scattering of the blackbody emission in a corona around the central compact object.

During the final stages of accretion the exact emission mechanism is dependent on the mass accretion rate and the magnetic field strength. If the mass accretion rate is high, the radiation pressure decelerates the infalling material and the increased optical depth causes the radiation to have a blackbody spectrum, as in the case of the high luminosity

($L_X \sim 10^{38-39}$ erg s^{-1}) LMXBs.

If no radiation shock occurs, as is the case in the LMXBs with low mass accretion rate, the material travels unhindered all the way to the surface of the neutron star. In this case, if the magnetic field strength is low, then the emission is in the form of thermal Bremsstrahlung, as in the case of the low luminosity ($L_X < 10^{37}$ erg s^{-1}) LMXBs. In the case of high magnetic field strength systems, cyclotron radiation becomes important, as is the case of binary X-ray pulsars.

1.4 Optical emission from LMXBs

In X-ray binaries the optical emission arises from two main sources. The first is the optical emission from the mass losing donor star and the second is from the reprocessing of X-rays into lower energy optical and UV photons. I will discuss the mechanism of reprocessing of X-rays into optical photons in Chapter 2.

The optical lightcurves of LMXBs are very similar to those of all interacting binaries. In eclipsing systems, the orbital motion of the two stellar components around their common centre of mass can clearly be seen as one stellar component passes in front of the other, producing a reduction in the observed flux. The optical lightcurves of LMXBs often show an additional modulation of the persistent optical flux, caused by the irradiation of the binary by X-rays from accretion onto the compact object. This X-ray heating causes the inner face of the donor star to be hotter (and brighter) than the backside of the star. This causes a modulation in the optical lightcurve as the fraction of the heated inner face changes with orbital phase. This orbital modulation is most obvious in eclipsing systems, but can help to constrain the inclination in non-eclipsing systems.

In this thesis I concentrate on the objects that show large changes in X-ray flux on short timescales, as these are most likely to show the correlated X-ray and optical variability. These sources fall into three categories. The first group are the bright persistent sources, such as LMXBs, which show large changes in X-ray flux due to a cycle of changes in the inner accretion flows. The second group are the transient sources, where large, infrequent outbursts occur due to sudden changes in the properties of the accretion flow.

The third group are pulsating sources, where the change in X-ray irradiating flux occurs every spin period of the neutron star.

1.5 Persistent sources

The persistent LMXBs are further sub-divided into two types, 'Z-sources' and 'Atoll sources', depending on their properties in an X-ray colour-colour diagram, see Figure 1.3 for an example of a colour-colour diagram of a 'Z-source' (Top panel) and an 'Atoll source' (bottom panel). They are thought to physically be very similar systems. The Z-sources show higher X-ray luminosities and hence inferred mass accretion rates. The magnetic field strength is thought to be higher in Z-sources than in Atoll sources, although this is hard to observe.

In this thesis I am not concerned with Atoll sources, due to their lower X-ray luminosities and the fact they do not show the large amplitude changes in X-rays as seen in Z-sources. It is these large amplitude variations that I use to search for correlated X-ray and optical variability. I will however give a brief review of some of their salient features in Section 1.5.2.

1.5.1 Z-sources

Z-sources are so-called because of the pattern they trace in an X-ray colour-colour diagram. The three 'strokes' of the 'Z' are identified with three branches, the upper stroke is known as the Horizontal Branch (HB), the middle stroke as the Normal Branch (NB) and the lower stroke as the Flaring Branch (FB).

The features of the Z-curve in the X-ray colour-colour diagram can best be described using a rank number, S_z. This number describes the position of the source on the Z-curve at any given time. In this system, S_z=1 is defined as the HB/NB intersection, also known as the "hard vertex" and S_z=2 as the NB/FB intersection, also called the "soft vertex". Hence the HB has $S_z < 1$, the NB has S_z from 1-2 and the FB has $S_z > 2$. This treatment allows us to study the observed features as a function of the rank number.

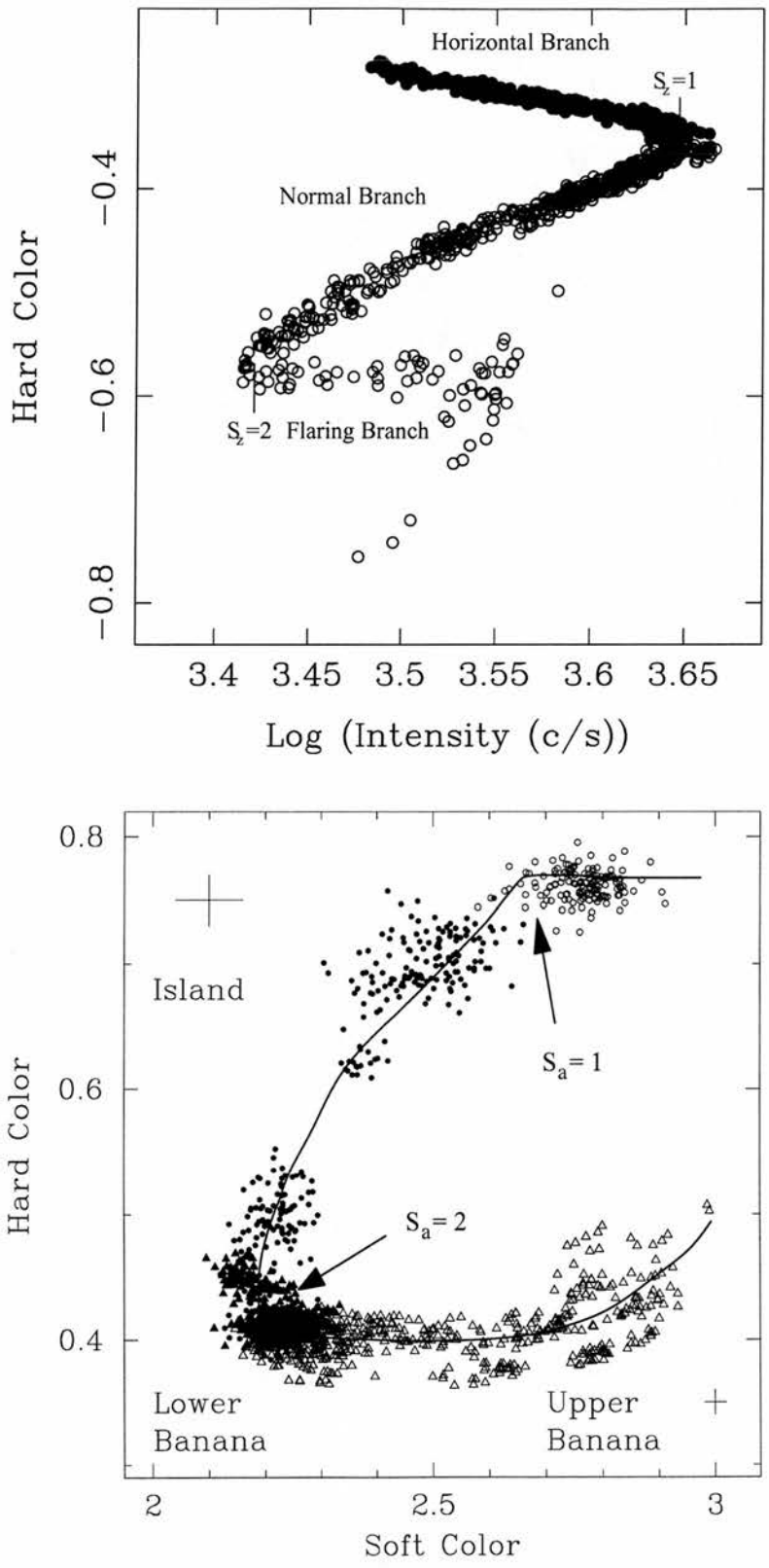

Figure 1.3: Example of an X-ray hardness intensity diagram of a Z-source (top panel) and of a colour-colour diagram of an Atoll source (bottom panel). The Z-source is GX 340+0 (from Jonker et al. (1998)). The atoll source is 4U 1608-52 (from Méndez et al. (1999)).

A fundamental property of Z-sources is that movement along the Z-curve is thought to be correlated with the mass transfer rate, $\dot{M}$, ie $S_z = f(\dot{M})$. Its position in the diagram changes in the sense that the lowest accretion rate occurs at the lowest S_z and increases, possibly to super-Eddington accretion rates as it moves to the end of the Flaring Branch at the highest S_z. The position of the 'Z' can move within the diagram, which is possibly evidence for a precessing accretion disc affecting the viewing geometry (Kuulkers, van der Klis & Vaughan 1996), one example of how disk structure is very important in the mass transfer rate of the system.

Since the launch of *RXTE* in 1995, it has been possible to explore the timing properties of X-ray binaries over several decades in frequency. This has lead to the characterisation of the phenomena of Quasi-Periodic Oscillations, QPOs, seen previously with EXOSAT. The observed QPOs are caused by material in the final stages of accretion interacting with the spinning magnetized neutron star. Z-sources show four principal QPOs, along with other noise features in their power spectra. In the next sections I shall describe the form and possible production mechanisms for the different features seen in the power spectra.

The six observed Z-sources are Scorpius X-1, Cygnus X-2, GX 17+2, GX 5-1, GX 340+0 and GX 349+2. One characteristic in common to all the sources are the observations of the so-called 'kilohertz QPOs', which were first discovered in Scorpius X-1 (van der Klis et al. 1996). The observed kilohertz QPO frequencies are summarized in Table 1.1. If these frequencies are interpreted as a beat frequency between material in the inner regions of the accretion disk and the spin of the neutron star, then one can determine that the spin frequencies of the neutron stars in Z-sources, given by the separation of the kHz QPO peaks, is around 300 Hz.

Horizontal Branch

On the HB, the X-ray intensity appears to be directly correlated with $\dot{M}$, which can be seen in the Hardness Intensity diagrams of Z-sources. Other features of the HB are strong very low frequency noise (VLFN) and horizontal branch oscillations (HBOs). The HBOs are strong and their frequency depends on both S_z and $\dot{S}_z$. These QPOs have also been

Source	HBO	NBO	FBO	lower kHz	upper kHz	reference
Cygnus X-2	36 - 54	5 - 7	NO	530 - 660	730 - 1010	1
Scorpius X-1	41 - 48	5 - 7	20	550 - 860	870 - 1080	2,3
GX 17+2	25 - 61	5 - 16	20	480 - 780	640 - 1090	4,5
GX 5-1	17 - 56	4 - 8	NO	210 - 700	500 - 890	6
GX 340+0	20 - 50	5 - 7	NO	250 - 625	570 - 820	7,8,9
GX 349+2	NO	6[a]	6[a]	710	980	10,11,12

Table 1.1: The QPO characteristics of the six known Z-sources, all frequencies are in Hz. NO means that the QPO, if it exists, has not been observed. In the case of GX 349+2 the kHz QPOs have only been observed once. The FBO frequency refers to the highest frequency observed.

a. The coherence of the oscillation oberved is too low to be strictly referred to as a QPO, it is more accurately referred to as 'peaked noise' (Kuulkers & van der Klis 1998)

1. Wijnands et al. (1998a)
2. van der Klis et al. (1996)
3. van der Klis (1997)
4. Wijnands et al. (1997)
5. Kuulkers et al. (1997)
6. Wijnands et al. (1998b)
7. Jonker et al. (1998)
8. Penninx et al. (1991)
9. Kuulkers & van der Klis (1996)
10. ponman, cooke & Stella (1988)
11. Kuulkers & van der Klis (1998)
12. Zhang, Strohmayer & Swank (1998)

called 'decahertz QPOs', in an analogy to the kilohertz QPOs, as they appear in the range 20-60 Hz (for a summary of their frequencies see Table 1.1)

The most likely explanation for these oscillations is a magnetospheric beat-frequency model (MBFM), where the oscillation is caused by a beating between material on a Kepler orbit at the magnetospheric radius and the spin of the neutron star.

$$\Omega_{HBO} = \Omega_{spin} - \Omega_{kepler} \tag{1.3}$$

The increase in HBO frequency with increasing $\dot{M}$, is understood as an increase in the Kepler frequency of the material as the pressure of the infalling material increases, causing the magnetosphere to shrink.

Normal Branch

The Normal Branch appears to represent a transition region from Horizontal Branch characteristics to those exhibited on the Flaring Branch, with features from both being present at different points. A notable change is that X-ray intensity is *inversely* proportional to $\dot{M}$. The NB is characterized by weak VLFN and HBOs, but also strong normal branch oscillations (NBOs). These NBOs are observed simultaneously with HBOs indicating a separate production mechanism. The NBO frequency is $\sim$ 5 - 10 Hz (see Table 1.1 and increases smoothly with S_z. The amplitude and central frequency of the HBOs on the NB remain constant or decreases with S_z.

Flaring Branch

The Flaring Branch represents the highest accretion rates and it takes its name from the flaring activity seen in Scorpius X-1. The main characteristics are strong VLFN, high frequency noise (HFN) with a frequency of up to 200 Hz and, in the cases of Scorpius X-1 and GX 17+2, flaring branch oscillations (FBOs). FBOs are thought to be physically connected with NBOs as the frequency varies smoothly through the NB/FB intersection, $S_z \sim 2$.

The characteristic variability of Z-sources changes smoothly along the various branches. Much work has gone into determining the source of the variability in Z-sources and in this thesis I shall show that the interactions of the highly variable X-rays with material, producing optical photons, can be used as a tool for investigating this variability.

1.5.2 Atoll sources

Like Z-sources, Atoll sources are named due to the shape of the track they produce in the X-ray colour-colour diagram, see Figure 1.3. They trace a 'U' or a 'C' in the diagram, similar to a the shape of an Atoll on a map. Atoll sources also show three distinct states, the upper and lower 'banana' states, separated by the 'island' state. In a similar manner to the Z-sources, they are given a rank number to describe their spectral state, as determined by their position in the X-ray colour-colour diagram. One feature of the Atoll sources is that they show X-ray bursts, thought to be nuclear burning of material on the surface of the neutron star, which would make the good candidates for searching for X-ray and optical correlated variability. However, due to the unpredictability of the bursts, observing campaigns are very difficult to organize, leading us to concentrate on the *slightly* more predictable, persistent sources.

1.6 Transient sources

Soft X-ray Transients (SXTs) are interacting binaries with accretion onto a neutron star or black hole that exhibit transient features, known as outbursts. During outbursts, the optical and X-ray flux of the object can increase by several orders of magnitude. Outbursts are thought to reflect a period of very high mass accretion rate compared to that in their quiescent state. There are two models that have been put forward to explain this feature: the disk instability model, where the mass transfer through the disk is affected by a thermal instability, causing the mass transfer to become highly non-linear, and the mass transfer instability model, where the X-ray irradiation of the donor star affects the mass transfer rate through the inner Lagrangian point. In both cases the structure of the disk is thought to be highly dependent on the X-ray illumination, making them good candidates

for echo-mapping.

1.7 Pulsating sources

In XRBs that contain an X-ray pulsar, such as Hercules X-1, the axis of the neutron star's dipole magnetic field is mis-aligned to its spin axis. The high magnetic field strength (B $> 10^{12}$ Gauss) channels accreting material onto the polar caps. This material emits X-rays via thermal Bremsstrahlung, which are swept out with a searchlight effect. One example of this is Hercules X-1, where the pulsar has a spin period of 1.24 seconds. These X-rays irradiate the X-ray binary, leading to enhanced optical/UV emission that is modulated on the spin period of the neutron star.

CHAPTER 2

Reprocessing of X-rays in X-ray Binaries

In the standard model of reprocessing, X-rays are emitted by material in the deep potential well of the compact object, as described in Chapter 1. The X-rays photoionize and heat the surrounding regions of gas, which later recombine and cool, producing lower energy photons. Hard X-rays that penetrate below the photosphere emerge as continuum photons, with an energy distribution characteristic of the temperature of the photosphere. Soft X-rays that are absorbed above the photosphere emerge as emission line photons, e.g. from a temperature inversion layer near the surface.

Much work has been done to calculate the effects of irradiation in LMXBs (eg. de Jong, van Paradijs & Augusteijn (1996)). This had lead to investigations of the effects of the irradiation on the structure and emission from the accretion disk (Ko & Kallman 1991) and donor star (Hameury & Ritter 1997), as well as during transient events, such as outbursts in SXTs (Tuchman, Mineshige & Wheeler 1990). In this chapter I will not try to reproduce these results, but I shall use some simplifying assumptions to estimate how the different stages of reprocessing affect the model we have used.

The density at the stellar photosphere can be estimated using the equation for hydrostatic equilibrium, with the equation for the optical depth, assuming a constant sound speed,

$$\frac{dP}{dz} = -\rho g(z), \tag{2.1}$$

$$\frac{d\tau}{dz} = -\rho\kappa, \tag{2.2}$$

$$\frac{dP}{d\rho} = C_s^2, \tag{2.3}$$

where P is the pressure, z is the radial distance, ρ is the density, C_s is the sound speed, τ is the optical depth of the material and κ is the opacity. Combining these we find

$$\frac{d\rho}{d\tau} = \frac{g(z)}{C_s^2 \kappa}. \tag{2.4}$$

The gravity for a stellar object is given by,

$$g(z) = \frac{GM}{R^2} \tag{2.5}$$

where G is the universal gravitational constant and M and R are the mass and radius of the star. The speed of sound in the material is given by

$$C_s^2 = \frac{\gamma k T}{\mu m_H}, \tag{2.6}$$

where γ is the adiabatic index ($= C_p/C_v = 5/3$ for a monatomic gas) and μ is the mean molecular weight (~ 0.67 for Population I abundances), k, is Boltzmann's constant, m_H is the mass of a hydrogen atom. The opacity is calculated using Kramers opacity, with Population I abundances ($X = 0.61$, $Y = 0.37$, $Z = 0.02$),

$$\kappa = \kappa_0 \rho T^{-3.5}, \tag{2.7}$$

where κ_0 is a constant. The value of κ_0 depends on the relative contributions from the bound-free and free-free opacities. These are, respectively,

$$\begin{aligned} \kappa_{\rm bf} &= 4.34 \times 10^{24} \, (1+X) \, (Z) \\ \kappa_{\rm ff} &= 3.68 \times 10^{22} \, (1+X) \, (1-Z). \end{aligned} \tag{2.8}$$

The relative contributions are found by determining the ionized fraction,

$$\mathcal{F} = \exp\left(\frac{-\Phi}{kT}\right), \tag{2.9}$$

where Φ is the ionisation potential (Hydrogen $\equiv$ 13.6 eV). Hence the opacity coefficient is given by,

$$\kappa_0 = (1 - \mathcal{F}) \, \kappa_{\rm bf} + \mathcal{F} \kappa_{\rm ff}. \tag{2.10}$$

Combining these equations we find that the density at the photosphere, ρ_p, where the optical depth is unity, is

$$\rho_p^2 = \frac{4 m_H}{5 k \kappa_0} T^{2.5} g. \tag{2.11}$$

T_4 $(10^4 K)$	$\log g$ (ms^{-2})	$H = \frac{C_s^2}{g}$ (m)	$\frac{\rho_p}{m_H}$ (m^{-3})	$\frac{\Sigma}{m_H}$ (m^{-2})
0.5	2	1.24×10^6	1.1×10^{19}	1.4×10^{25}
1.0	2	2.48×10^6	2.7×10^{19}	6.6×10^{25}
1.5	2	3.71×10^6	4.4×10^{19}	1.6×10^{26}
2.0	2	4.95×10^6	6.4×10^{19}	3.2×10^{26}
0.5	3	1.24×10^5	3.6×10^{19}	4.4×10^{24}
1.0	3	2.48×10^5	8.5×10^{19}	2.1×10^{25}
1.5	3	3.71×10^5	1.4×10^{20}	5.2×10^{25}
2.0	3	4.95×10^5	2.0×10^{20}	1.0×10^{26}
0.5	4	1.24×10^4	1.1×10^{20}	1.4×10^{24}
1.0	4	2.48×10^4	2.7×10^{20}	6.6×10^{24}
1.5	4	3.71×10^4	4.4×10^{20}	1.6×10^{25}
2.0	4	4.95×10^4	6.4×10^{20}	3.2×10^{25}

Table 2.1: The scale height, optical photospheric density and column density for models with different temperatures and gravity coefficients. (NB. SI units are used in all calculations)

We can use this to determine what fraction of the X-ray flux for a given X-ray energy is absorbed above and below the photosphere. The X-ray optical depth is given by,

$$\tau_{\rm x}(E) = \Sigma \kappa_{\rm x}(E), \tag{2.12}$$

where the surface density above the photosphere is

$$\Sigma = \frac{\rho_p C_s^2}{g} = \left(\frac{m_H T^{2.5}}{k\kappa_0}\right)^{1/2} \frac{C_2^2}{g^{1/2}}. \tag{2.13}$$

Table 2.1 shows the results of calculations of the scaleheight, photospheric density and column density for different temperatures and gravities. We find that for the range of temperatures covered, the bound-free opacity dominates over the free-free opacity, due to the low ionized fraction.

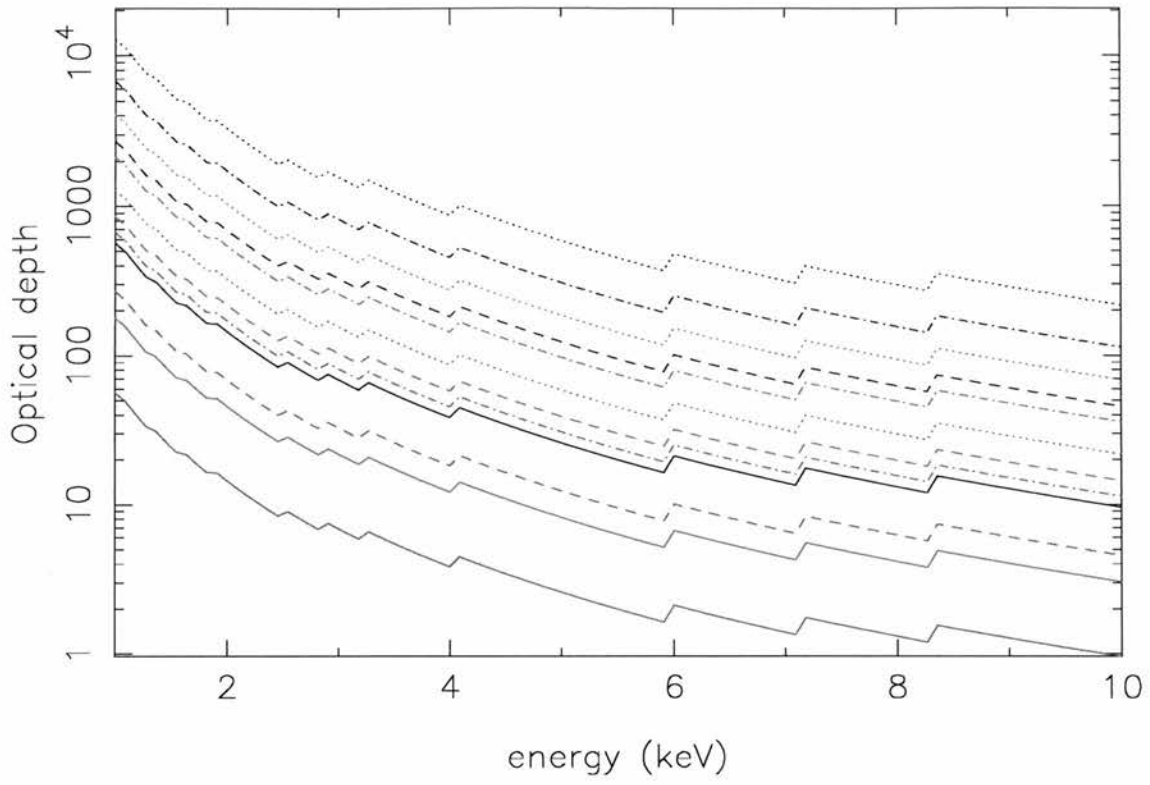

Figure 2.1: The optical depth for an X-ray photon at the optical photosphere. The black, red and green colours represent the cases where log(g) = 2, 3 and 4 respectively. The solid, dashed, dot-dashed and dotted lines represent the cases where T= 5000K, 10000K, 15000K and 20000K respectively.

The results from calculations of Equation 2.12, shown in Figure 2.1, give the X-ray optical depth as a function of the input X-ray photon energy for the cases shown in Table 2.1. The X-ray opacities are those used by XSPEC, taken from Balucinska-Church & McCammon (1992) in the energy range 0.01 - 10 KeV, using the abundances from Anders & Grevesse (1989). We can see from this that the low energy X-ray photons, below 10 keV, are absorbed in a region above the photosphere that is optically thin to optical photons. The optical optical depth (as opposed to the X ray optical depth) at the X ray photosphere can be calculated in a similar manner. The results of the are shown in Figure 2.2, which shows that the optical depth is much less than 1, for most of the temperatures and gravities considered. Hence the optical emission from reprocessing should appear as optically thin emission.

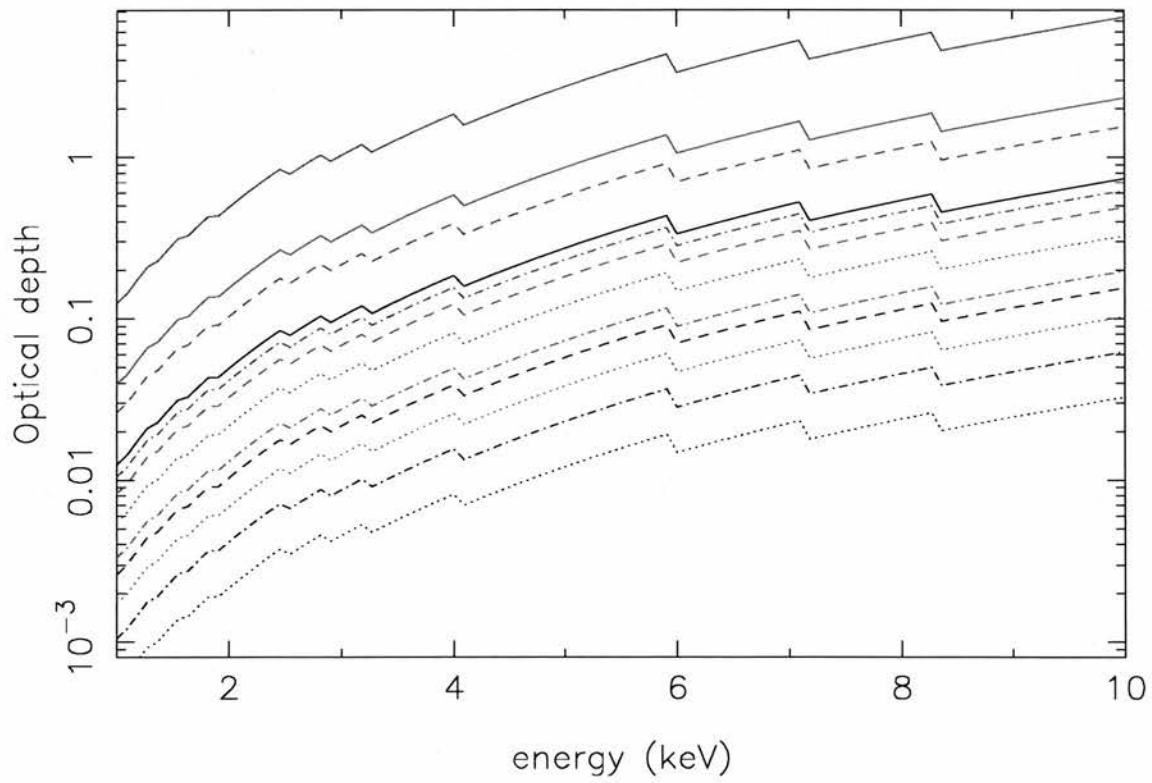

Figure 2.2: The optical depth for an optical photon at the X-ray photosphere. The black, red and green colours represent the cases where log(g) = 2, 3 and 4 respectively. The solid, dashed, dot-dashed and dotted lines represent the cases where T= 5000K, 10000K, 15000K and 20000K respectively.

2.1 Time delays

The optical emission seen by a distant observer is delayed in time of arrival relative to the X-rays by two mechanisms. The first is a finite reprocessing time for the X-ray photons to be converted into optical photons and the second is the light travel times between the X-ray source and the reprocessing sites within the binary system. In the next sections I shall derive expressions for these two quantities and show that the light travel time is the dominant effect in the study of X-ray binaries.

2.1.1 Reprocessing times

Line photons

The average reprocessing time for line photons is given by the average recombination time, (Hummer & Seaton 1963)

$$\frac{t_{\rm rec}}{\rm s} = \left(1.627 \times 10^{-19} N_e \, T_4^{-1/2} \left[1 - 1.657 \log(T_4) + 0.584 \, T_4^{1/3}\right]\right)^{-1}, \tag{2.14}$$

where $T_4 = 10^{-4} T$ and N_e is the electron number density in m^{-3}.

Continuum photons

The continuum photons which scatter from deeper within the accretion disk undergo a 'random walk' before escaping through the photosphere, leading to a longer reprocessing time. The exact determination of this continuum reprocessing time is complicated, requiring detailed model atmosphere calculations. However by making some simple assumptions, we can estimate the reprocessing timescale for continuum photons. The reprocessing of an X-ray photon into an optical photon takes place in two stages. The X-ray photon is absorbed by the reprocessing material which, in turn, is ionised, recombines and produces an optical photon, with the recombination timescale, $t_{\rm rec}$. Finally the photon diffuses back up through the atmosphere, with the diffusion timescale, $t_{\rm diff}$.

$$t_{\rm rep} = t_{\rm rec} + t_{\rm diff} \tag{2.15}$$

The mean free path of the photon through the material, $\mathcal{L}$, is given by,

$$\mathcal{L} = \frac{1}{N_e \sigma}, \tag{2.16}$$

where N_e is the electron number density and σ is the absorption cross section.

The recombination timescale is shown in Equation 2.14. The diffusion timescale through the atmosphere is calculated using a random walk, where the timescale is the product of the number of scatters, N, and the time between scatters,

$$t_{\rm diff} = \frac{N \mathcal{L}_{\rm opt}}{c}. \tag{2.17}$$

The number of scatters is calculated using a random walk,

$$N \approx \frac{R^2}{\mathcal{L}_{\rm opt}^2}, \tag{2.18}$$

where $\mathcal{L}_{\rm opt}$ is the optical mean free path and R is the total distance traveled. Hence the diffusion timescale is

$$t_{\rm diff} \approx \frac{1}{N_e c \sigma_{\rm x}^2} \sigma_{\rm opt} \cos^2 \theta_{\rm x}, \tag{2.19}$$

where $\sigma_{\rm opt}$ is the optical cross section, which is equal to the Thomson cross section and $\theta_{\rm x}$ is the incidence angle of the initial X-ray photon. Hence the reprocessing timescale is

$$t_{\rm rep} \approx \frac{1}{\alpha N_e} + \frac{1}{N_e c \sigma_{\rm x}} \left(\frac{\sigma_{\rm opt}}{\sigma_{\rm x}} \cos^2 \theta_{\rm x} \right). \tag{2.20}$$

We can estimate the reprocessing time for photons at the stellar photosphere using the number density derived from the photospheric density in Equation 2.11 and the Thomson cross section. The results from these calculations based on the results shown in Figure 2.1 are shown in Figure 2.3. From these calculations, we find that the recombination time is the dominant timescale involved. The energy dependence of the reprocessing timescale arises from the observation that soft photons are absorbed high in the atmosphere, where the density is low, leading to a longer recombination time. The large range of time-delays imply that our model of instantaneous reprocessing may not be realistic in low gravity atmospheres.

The short time delays between X-ray and optical bursts (Pedersen et al. 1982) and the observations of 1.24 second optical pulsations from Hercules X-1 (Chester 1979),

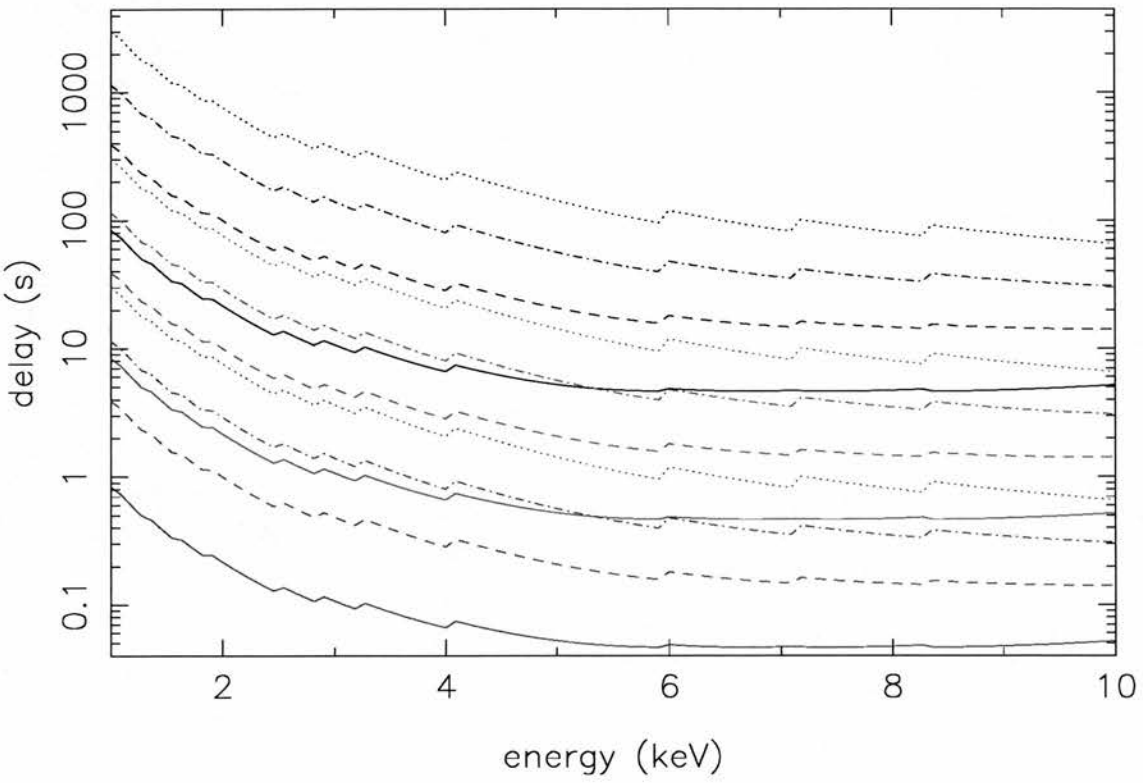

Figure 2.3: The reprocessing time for an X-ray photon absorbed near the photosphere. The black, red and green colours represent the cases where log(g) = 2, 3 and 4 respectively. The solid, dashed, dot-dashed and dotted lines represent the cases where T= 5000K, 10000K, 15000K and 20000K respectively.

support the result that a significant fraction of the reprocessed optical photons emerge from the reprocessing site within $\sim$ 0.4 seconds of the absorption of the incident X-ray photons. This delay is smaller than the measured uncertainty in the mean delay for the systems and so we treat the continuum reprocessing as instantaneous.

We have also treated the reprocessing of X-rays as "passive" reprocessing, where the absorbed X-rays do not affect the structure of the material in the binary.

2.1.2 Light travel times

The light travel times arise from the time of flight differences for photons that are observed directly and those that are reprocessed and re-emitted before traveling to the observer. These delays can be up to twice the binary separation, obtained from Kepler's third law,

$$\frac{a}{c} = 9.76\text{s} \left(\frac{M_{\rm x} + M_c}{M_\odot}\right)^{\frac{1}{3}} \left(\frac{P}{\text{days}}\right)^{\frac{2}{3}} \tag{2.21}$$

where a is the binary separation, $M_{\rm x}$ and M_c are the masses of the compact object and donor star, P is the orbital period. In LMXBs the binary separation ranges from $\sim$ 3-30 light seconds.

The time delay τ at binary phase ϕ for a reprocessing site with cylindrical coordinates (R, θ, Z) is

$$\tau(\mathbf{x}, \phi) = \frac{\sqrt{R^2 + Z^2}}{c}(1 + \sin i \cos(\phi - \theta)) - \frac{Z}{c}\cos i \tag{2.22}$$

where i is the inclination of the system and c is the speed of light. This can also be expressed using the position vector, $\mathbf{x}$ and the unit vector, $\mathbf{e}(\phi)$, pointing toward the earth,

$$\tau(\mathbf{x}, \phi) = \frac{|\mathbf{x}| - \mathbf{e}(\phi).\mathbf{x}}{c} \tag{2.23}$$

An illustration showing the time delays expected from different regions of of the binary can be in Figure 3.5.

Transfer functions

The X-ray driving lightcurve, $f_{\mathrm{rm\ x}}(t)$, is described as the sum of a constant and a variable component,

$$f_{\mathrm{X}}(t) = \overline{f_{\mathrm{X}}} + \Delta f_{\mathrm{X}}(t). \tag{2.24}$$

The reprocessed lightcurve, $f_{\nu}(t)$, is similarly divided into two components. In the simple linear reprocessing model adapted here, the relationship between the two is given by

$$f_{\nu}(\lambda, t) = \overline{f_{\nu}}(\lambda) + \int \Psi_{\nu}(\lambda, \tau, \phi) \left(f_{\mathrm{X}}(t - \tau) - \overline{f_{\mathrm{X}}} \right) d\tau \tag{2.25}$$

where $\Psi_{\nu}(\lambda, \tau, \phi)$ is the time delay transfer function. This transfer function is the strength of the reprocessed variability delayed by τ relative to the X-ray variability.

The dynamic response function is found by considering how a change in X-ray flux drives a change in the reprocessed flux. We can define the dynamic time delay transfer function to be,

$$\Psi_{\nu}(\lambda, \tau, \phi) = \int \left[\frac{\delta I_{\nu}(\lambda, \mathbf{x}, \Delta f_{\mathrm{X}}(t - \tau))}{\delta f_{\mathrm{X}}(t - \tau)} \right] d(\tau - \tau(\mathbf{x}, \phi)) \tag{2.26}$$

where $\tau(\mathbf{x}, \phi)$ is the geometric time delay of a reprocessing site at position $\mathbf{x}$, see Equation 2.22. In the next Chapter I describe the model X-ray binary code we have developed and how we have used this to find the reprocessed flux.

CHAPTER 3

Methods of Echo-mapping

In this chapter I shall describe the different methods used to characterize the form of the transfer functions described in Chapter 2. I will start by describing two simple methods. The first of these is Cross Correlation analysis, where we use the driving and reprocessed lightcurves to determine a mean time delay from the centroid of the cross correlation function for the two lightcurves. The second method compares the goodness of fit between a synthetic lightcurve, created by convolving a Gaussian transfer functions with the driving lightcurve, and the observed reprocessed lightcurve. The Gaussian representation of the transfer function measures the strength of the reprocessing, the mean time delay between the two lightcurves and also the range of time delays. In this method, no assumptions of the geometry of the system are made, but the form of the transfer function is fixed to be that of an acausal Gaussian (ie. one that allows response at negative time delays). The final method I will describe uses transfer functions we have created from our model X-ray binary code convolved with the driving lightcurve, in the same way as with the Gaussian method. The results are used to constrain the geometric parameters of the system, using our knowledge of the binary parameters. These three methods will be used to characterize any correlated variability found in the X-ray binaries discussed in later chapters.

3.1 Cross correlation analysis

The technique of cross correlation analysis has been used very successfully in studies of Active Galactic Nuclei (AGN), where time delays between emission line and continuum lightcurves are used to estimate the size of the Broad Line Region. There are two principal methods of creating correlation functions. These are the Discrete Correlation Function (DCF), where the discretely sampled driving and reprocessed lightcurves are compared and the correlation coefficient is placed into discrete bins (Edelson & Krolik 1988) and the Interpolated Correlation Function (ICF), where the the discretely sampled driving lightcurve is interpolated to form a continuous function, which is compared to the reprocessed lightcurve (Gaskell & Peterson 1987).

I have used the discrete (DCF) method in my analysis, since interpolation of the X-ray driving lightcurve is difficult and a potential source of error in X-ray binaries, due to the rapid variability of the X-ray source. Another advantage of using the DCF method is that it allows meaningful errors to be placed on the individual points of the correlation function. However, White & Peterson (1994) show that, for well sampled data sets, the results of the two methods converge well, when given suitable weightings. In contrast to the analysis of AGN lightcurves, I shall not ignore the so-called 'zero-lag pairs' (Edelson & Krolik 1988). These concern data points taken from the same spectrum, eg. continuum versus line variability and may contain spurious correlations from eg. calibration errors.

Following the method described by Edelson & Krolik (1988), the Un-binned Discrete Correlation Function (UDCF), is defined for the data pair (D_i, R_j), taken from the driving lightcurve, $D(t)$ and the reprocessed lightcurve $R(t)$, as,

$$UDCF_{ij} = \frac{\left(D_i - \overline{D}\right)\left(R_j - \overline{R}\right)}{\sigma(D)\sigma(R)}, \tag{3.1}$$

where the mean and variance of a data set A_i, $\overline{A}$ and $\sigma^2(A)$ respectively, containing N data points are

$$\begin{aligned} \overline{A} &= \frac{1}{N}\sum_{i=1}^{N} A_i \\ \sigma^2(A) &= \frac{1}{N-1}\sum_{i=1}^{N}\left(A_i - \overline{A}\right)^2. \end{aligned} \tag{3.2}$$

Each data pair is separated by a time difference, τ_{ij},

$$\tau_{ij} = t_j - t_i. \tag{3.3}$$

The discrete correlation function can now be determined with a resolution of $\delta\tau$ by finding the average value of the UDCF, in the range $\tau - \delta\tau/2 \leq \tau_{ij} < \tau + \delta\tau/2$,

$$DCF(\tau) = \frac{1}{M} \sum_{ij=1}^{M} UDCF_{ij}, \tag{3.4}$$

where M is the number of data pairs with a delay that falls into the above range. The variance of this mean value is given by

$$\sigma^2_{DCF}(\tau) = \frac{\Sigma\left[UDCF_{ij} - DCF(\tau)\right]^2}{M(M-1)}. \tag{3.5}$$

Due to the existence of non-correlated, long timescale variability in X-ray binaries (see for example Figure 8.6), the time series are no longer *stationary*. (A stationary time series is one whose mean and variance are not functions of time.) In order to create nearly stationary data sets I have detrended the driving and reprocessed lightcurves to remove slow variations. I have also chopped the reprocessed lightcurve into smaller segments in order to reduce the importance of any spurious correlations introduced by variability that is not caused by irradiation. This is equivalent to having a mean, or background, level that varies slowly with time. The size of these chopped data sets are chosen to be large enough to create a reasonable mean, that only removes long timescale variability. The individual DCFs are simply averaged, creating an Average Discrete Correlation Function (ADCF).

In order to test this method I have calculated the DCF including and excluding zero-lag pairs and the ADCF for the SXT GRO J1655-40 data shown in Figure 3.1. This data is stationary and will act as a test to check that the methods are consistent. The resulting CCFs are shown in Figures 3.2 (top panel), 3.2 (bottom panel) and 3.3 respectively. (The ICF for this data was shown in Hynes et al. (1998b), which is reproduced in Panel 3 of Figure 3.4.)

The results show that, while all three methods recover the DCF well, the ADCF is narrower than the others. This is important when considering non-stationary datasets,

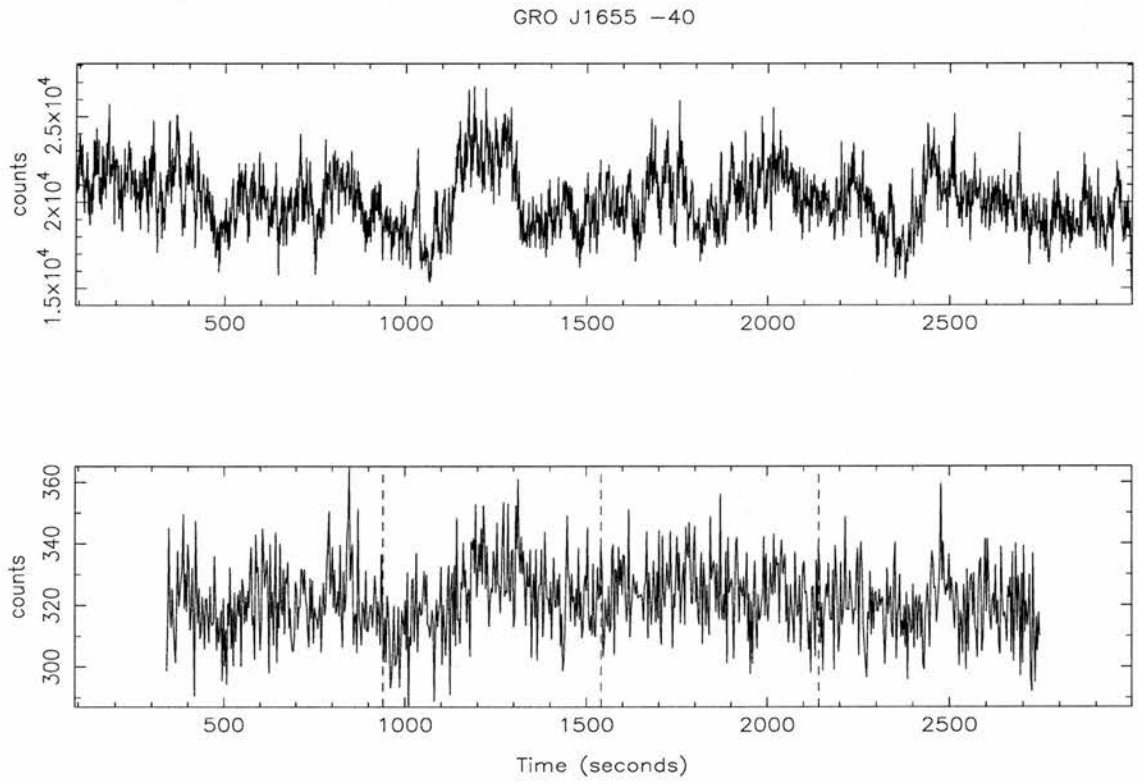

Figure 3.1: The simultaneous RXTE (top panel) and HST (bottom panel) lightcurves of the variability in GRO J1655-40. The dotted lines show where the 4 subsets begin and end that are used to calculate the ADCF.

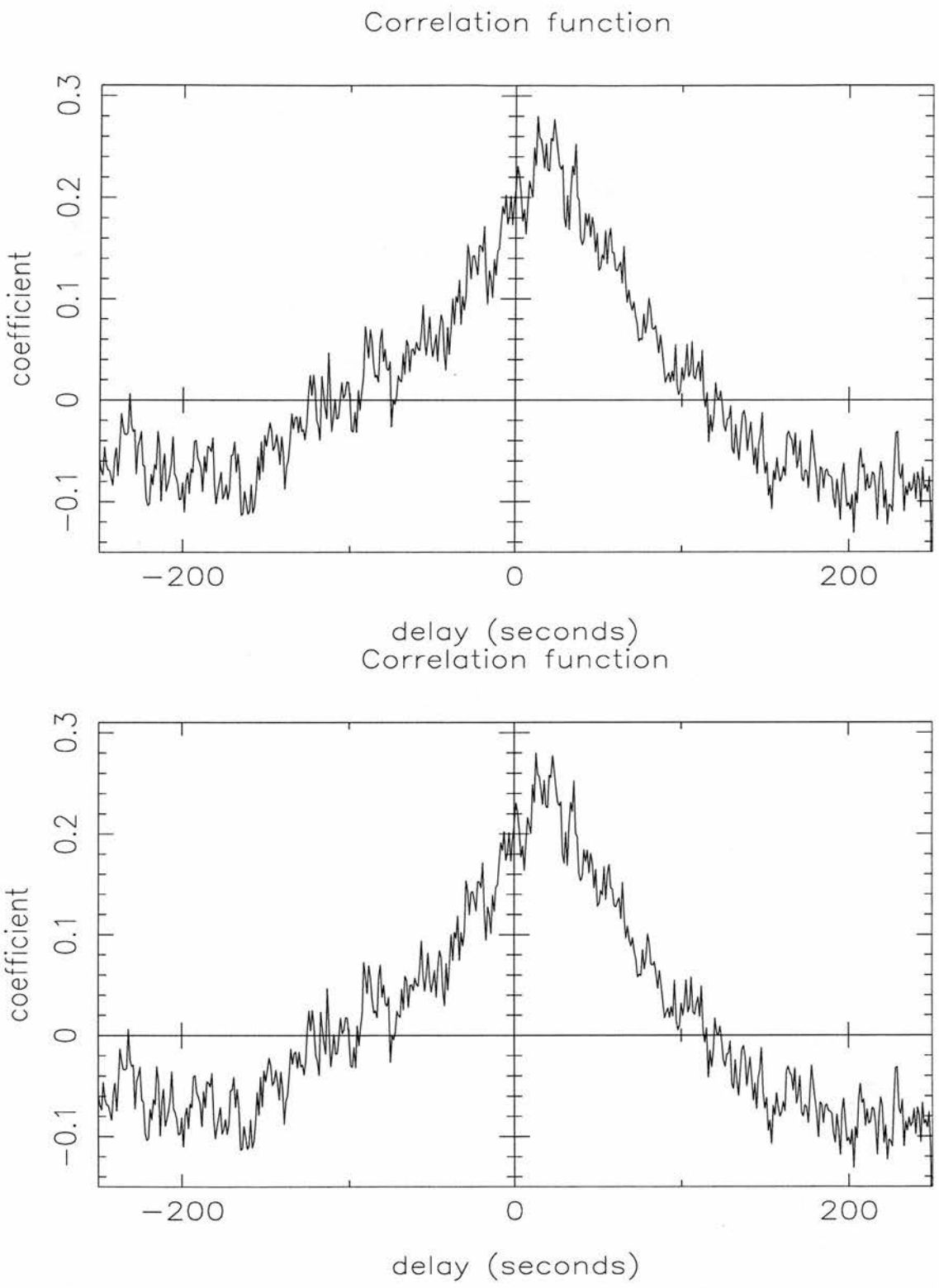

Figure 3.2: The classical DCF for the lightcurves shown in Figure 3.1. The correlation coefficient is calculated for the whole dataset. The top panel ignores zero-lag pairs, whilst the bottom panel includes all data pairs.

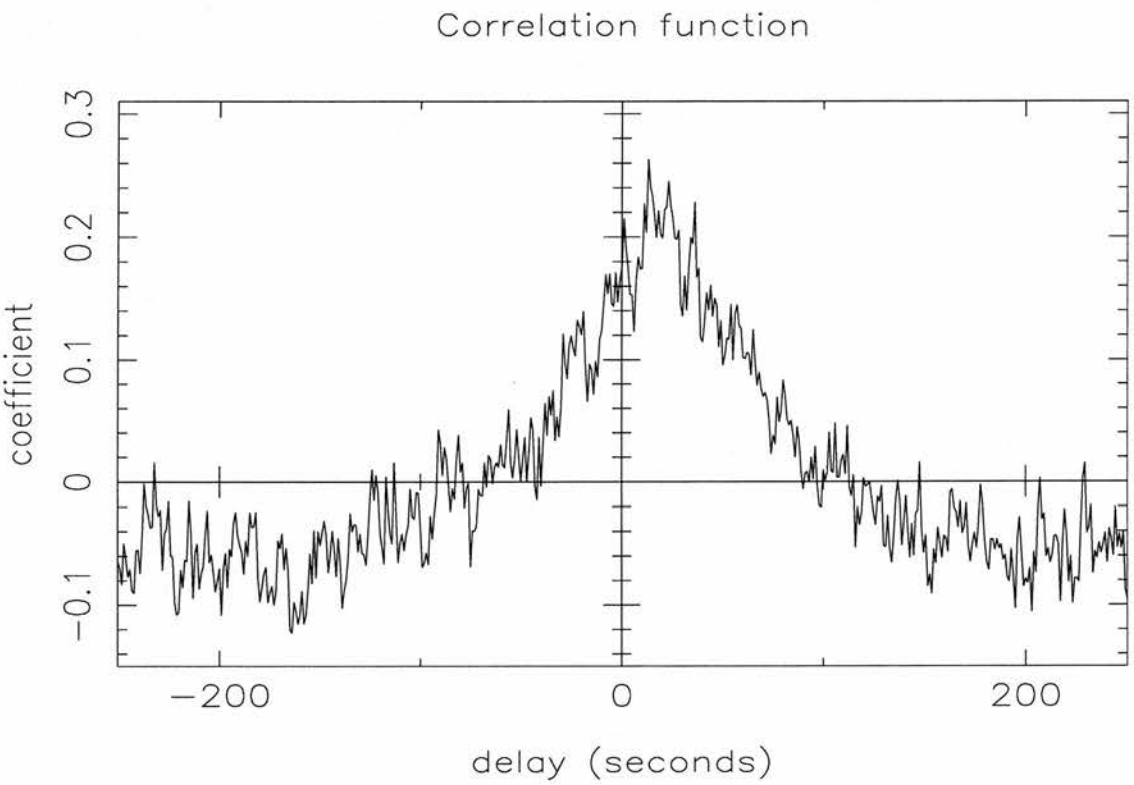

Figure 3.3: The average DCF for the 4 subsets shown in Figure 3.1. The correlation coefficient is calculated by averaging the contributions from the 4 individual DCFs

as non-correlated features that broaden the DCF, will have less effect on the ADCF. The variance of the ADCF can also be calculated using the individual variances of the DCFs.

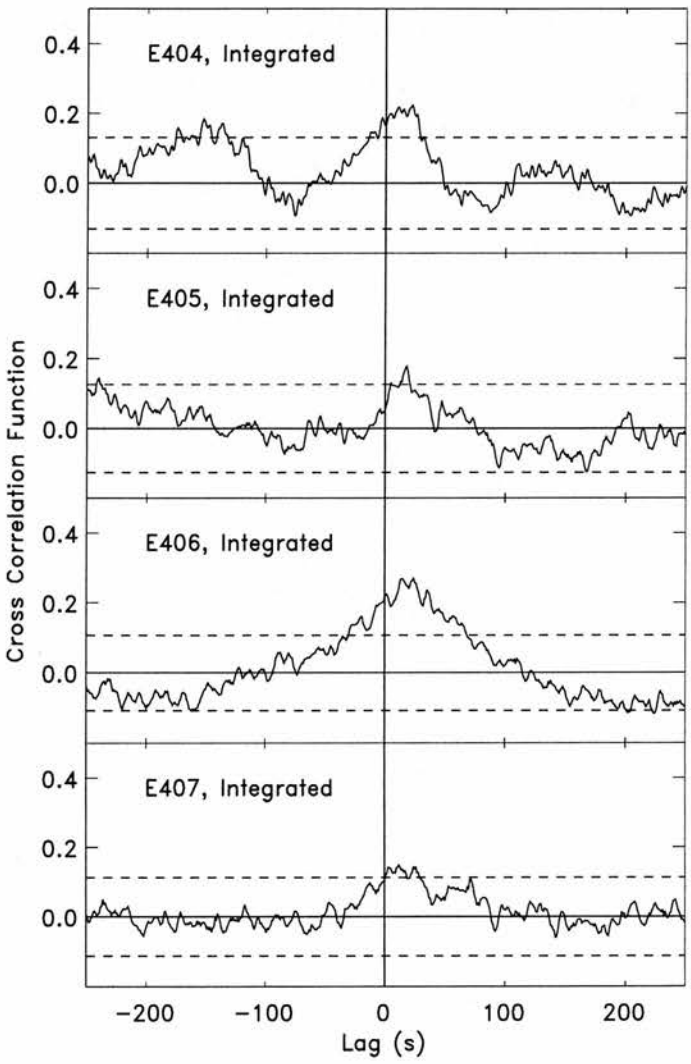

Figure 3.4: The ICFs for 4 simultaneous HST and RXTE observations of the SXT GRO J1655-40. Panel 3 (labelled E406) shows the ICF for the lightcurves shown in Figure 3.1. The dashed line shows the 3σ confidence level. This plot is reproduced from Figure 2 in Hynes et al. (1998b).

3.2 Gaussian transfer functions

In section 3.1 I described how we used cross correlation analysis to find the mean time delay between two datasets. In this section I shall describe how the transfer function can be constrained using our prior knowledge of the possible time delays from the binary system. We can determine that the transfer function should be real and positive, if the reprocessing is effectively instantaneous (ie. the geometric time delay is much greater than the time delay caused by reprocessing, see section 2). The existence of short timescale correlations show that at least some of the X-ray photons are instantaneously reprocessed. Detrending of the data on long timescales removes any effects of binary rotation from the lightcurves, which may show correlations. In this method we are only interested in correlations that are due to reprocessing.

We use a Gaussian function to represent the first and second moments of the true transfer function. This is a simple parameterized form of transfer function as it assumes nothing about the geometry of the system. Gaussian transfer functions have the form,

$$\psi(\tau) = \frac{\Psi}{\sqrt{2\pi}\Delta\tau} \exp\left(-\frac{1}{2}\left(\frac{\tau-\tau_0}{\Delta\tau}\right)^2\right), \tag{3.6}$$

with three parameters, the mean time delay τ_0, its RMS $\Delta\tau$ and the strength of the response Ψ. Whilst any physically realistic transfer function is defined to be causal, since only any positive lags are physically allowed, the Gaussian functions can be acausal, since they are only represent the moments of the true transfer function.

The best-fit Gaussian transfer function is found by convolving the X-ray driving lightcurve with trial transfer functions to find a set of synthetic reprocessed lightcurves. The badness of fit between the synthetic and observed lightcurves is calculated using a χ^2 analysis and the best-fit parameter values determined. The one-parameter one-sigma confidence regions are also found by searching the parameter space of the trial solutions found.

Since the true transfer functions are causal, the X-ray lightcurve must precede the optical lightcurve by at least the maximum delay present in the transfer function, in order to be able to calculate the predicted optical data for the earliest data point. Thus we reject any points from our fitting routine, where less than 99 % of the transfer function is

used to create the synthetic reprocessed data point. In order to retain a constant number of degrees of freedom whilst doing the grid search for the confidence regions, we use the transfer function with the largest range of delays, where the mean and variance is highest, to determine which points to reject from our fit.

3.3 Model X-ray binary code

We have developed a code to model time delay transfer functions based on determining the contributions from different regions in the binary. In this section I shall describe the models used to construct the individual regions of the binary; the donor star, the accretion stream and the accretion disk. The code uses distances scaled to the binary separation in a right-handed Cartesian coordinate system corotating with the binary. The X-direction lies along the line of centres for the binary, the Y-direction lies perpendicular to this in the orbital plane of the binary, pointing in the direction of rotation, so that the X-ray source is at (0,0,0) and the centre of mass of the donor star is at (1,0,0). The surface elements are triangular, individually characterized by an area dA, orientation $\mathbf{n}$, position $\mathbf{x}$ and temperature T.

The total monochromatic flux is calculated by summing up contributions from all visible elements. The area dA and the normal vector $\mathbf{n}$ for the triangular panel are calculated and then the projected area of the panel is calculated using the projected earth vector $\mathbf{e}(\phi, i)$. The effects of occultations by regions in the binary are also considered. Hence, the observability, $O(\mathbf{x}, \phi)$, is given by,

$$O(\mathbf{x}, \phi) = d\mathbf{A}(\mathbf{x}).\mathbf{e}(\phi). \tag{3.7}$$

This is the foreshortened area of pixel $\mathbf{x}$, observable at phase ϕ. It is related to the solid angle of the observed pixel, $d\Omega$ by the relation

$$d\Omega(\mathbf{x}, \phi) = \frac{O(\mathbf{x}, \phi)}{D^2}, \tag{3.8}$$

where D is the distance to the source. If $d\Omega(\mathbf{x}, \phi) < 0$, or the panel is behind another one, then the panel is not visible to the observer and does not contribute to the flux. The monochromatic intensity is calculated using the Planck function,

$$B_\nu(\lambda, T) = \frac{2hc}{\lambda^3 \left[\exp\left(\frac{hc}{k\lambda T}\right) - 1\right]}. \tag{3.9}$$

This is scaled using the projected area of the panel $|O(\mathbf{x}, \phi)|$, as seen by the observer. The standard linear limb-darkening law is assumed,

$$L(u, \alpha) = \frac{1 - u + u\cos(\alpha)}{1 + u/3} \tag{3.10}$$

where u is the linear limb-darkening coefficient, assumed to be 0.6, and α is the angle between the normal vector $\mathbf{n}$ and the earth vector $\mathbf{e}(\phi, i)$,

$$\cos\alpha = \mathbf{n}.\mathbf{e}. \tag{3.11}$$

The response curve for a given detector, $P(\lambda)$, is combined with the limb-darkened Planck function to create the synthetic reprocessed flux from each visible triangular element. The total flux over a given passband, $P(\lambda)$, detected from a single panel is $F_\nu(T)$. This is given by,

$$F_\nu(T) = \int\int B_\nu(\lambda, T)\, P(\lambda)\, L(u, \alpha)\, d\Omega(\mathbf{x}, \phi)\, d\lambda, \tag{3.12}$$

where $L(u, \alpha)$ and $d\Omega(\mathbf{x}, \phi)$ are the expressions for the limb-darkening and the solid angle of the exposed panel, see equations 3.10 and 3.8 respectively. The next stage is to consider the effect of irradiation on the panels.

3.3.1 Irradiation model

In our model, the effect of X-ray irradiation is to elevate the temperature for any panel exposed to X-rays. The effective temperature of a region at a distance R from the X-ray source, assumed in our model to be a point source located at the centre of the accretion disk, is found from the accretion luminosity for a typical LMXB,

$$T_{\rm x}^4 = \frac{L_{\rm x}(1-A)}{4\pi\sigma R^2} \tag{3.13}$$

and

$$L_{\rm x} = \eta\frac{GM_{\rm x}\dot{M}}{R_{\rm ns}} \tag{3.14}$$

where $T_{\rm x}$ is the temperature, A is the albedo, η is the efficiency, $M_{\rm x}$, the mass of the compact object, $\dot{M}$ the accretion rate onto the compact object, $R_{\rm ns}$ is the size of the compact object and R is the distance between the compact object and the irradiated element. This is normalized using the binary separation, a, the distance between the centres of mass of the stars, as is the coordinate system for the binary. In the case of Scorpius X-1, this gives $T_{\rm x} \sim 10^5 K$ for a 1.4 $M_\odot$ neutron star ($R_{\rm NS} \sim 10km$) accreting $10^{-9} M_\odot yr^{-1}$, with an efficiency $\eta = 0.1$, an albedo of 0.5 and a binary separation of 3.4 x 10^{11} cm ($\equiv$ 11.3 light-seconds).

Our treatment of the irradiation of the binary takes place in three stages. The first stage is to calculate the temperature structure of the binary in the absence of any irradiation. This is done with characteristic temperatures for the donor star (from its spectral type) and the accretion stream and disk. The temperature structure of the disk is assumed to be that for an unirradiated disk as given in equation 3.20.

The surface elements of the binary exposed to X-rays are determined by projecting the binary surfaces onto a spherical polar representation of the sky, as it appears from the X-ray source. Each triangular element is mapped to the sky starting with the one furthest from the source and ending with the triangle closest. Those elements remaining visible and unocculted on the sky map are irradiated. The change in effective temperature of an element is scaled by the projected area with respect to the X-ray source at a distance R from the source. Hence the temperature after irradiation is given by,

$$T^4 = T_{\rm x}^4 \cos\theta_{\rm x} \left(\frac{a}{R}\right)^2 + T_{\rm eff}^4 \tag{3.15}$$

where T is the temperature of the panel, $\theta_{\rm x}$ the angle between the line of sight from the central source and the normal to the surface of the element and $T_{\rm eff}$ is the unirradiated effective temperature of the panel.

Since we are interested in finding the correlation between the variable component of the X-ray and reprocessed fluxes, we split the X-ray flux into constant and time-dependent components. These components of the flux are converted into components of temperature,

$$T_{\rm x}(t) = \overline{T_{\rm x}} + \Delta T_{\rm x}(t) \tag{3.16}$$

where

$$\frac{\Delta f_\nu(t)}{\overline{f_\nu}} \simeq \frac{4\Delta T_{\rm x}(t)}{\overline{T_{\rm x}}}. \tag{3.17}$$

The second stage is to irradiate the binary with the constant component of the X-ray flux. This component of the X-ray flux is equated to the mean effective temperature of the X-ray source, as given in equation 3.15, where $T_{\rm x} \equiv \overline{T_{\rm x}}$. The third and final stage is to repeat stage two with $T_{\rm x} \equiv \Delta T_{\rm x}(t)$, which represents irradiating the binary with a time varying component, so that the temperature of the region depends on the time difference

between the irradiation source and the irradiated region. The difference between stages two and three represents the temperature change of the elements due to the time varying component of the X-ray flux alone.

Thus the response of a panel to the variable component of the irradiating X-ray flux is given by,

$$I_\nu\left(\lambda, \mathbf{x}, \Delta f_{\mathrm{x}}(t)\right) = \int \left[B_\nu\left(\lambda, T_{\mathrm{x}}(t)\right) - B_\nu\left(\lambda, \overline{T_{\mathrm{x}}}\right)\right] P(\lambda)\, I(u, \alpha)\, d\Omega(\mathbf{x}, \phi)\, d\lambda. \quad (3.18)$$

This response is substituted into the expression for the dynamic response given in equation 2.26. In the next section we describe the geometric model used to calculate the time delay for a given panel, which is then mapped onto our delay grid to find the dynamic response function.

3.3.2 Donor star

The donor star is modeled assuming it fills its critical Roche potential, so that mass transfer occurs via Roche lobe overflow through the inner Lagrangian point. Optically thick panels are placed over the surface of the Roche potential. The panels are again triangular so that the curved surfaces of the binary are mapped more accurately than is possible using 4-sided shapes (Rutten & Dhillon 1994). These panels are equally spaced in longitude and latitude across the surface of the star. The panels, when unirradiated, are assigned an effective temperature T_{star}, derived from the spectral type of the donor star.

3.3.3 Accretion stream

The accretion stream is modeled by following the ballistic trajectories of 4 test particles. The thickness, w, of the stream defines the initial positions of the test particles. These test particles determine the 'width' of the stream (Its deviation from the line of centres of the binary, in the plane of the binary, or y-direction) and the 'height' of the stream (its extent in the direction normal to the plane of the binary, the z-direction), assuming the stream is symmetric about the x-y plane.

The particles start at the L1 point with a small velocity in the direction of the compact object (-v,0,0), from positions (R(L1),0,0), (R(L1),w,0), (R(L1),-w,0) and (R(L1),0,w). The trajectory is cut into discrete steps, with the step size as a parameter of the code. The velocity and position of each particle are determined from the Roche potential after each step. The stream is curtailed when one of two criteria are reached; (1) the stream has collapsed vertically, or (2) the core trajectory is moving outwards, ie. the stream has passed the compact object without collapsing vertically.

The unirradiated accretion stream is assumed to have a constant temperature T_s along its length and the effects of irradiation are considered in the same way as those for the donor star in section 3.3.1.

3.3.4 Accretion disk

The disk thickness is assumed to increase with radius from 0 at R = R_{in} to H_{out} at R = R_{out}, with the form,

$$H = R_{out} \left(\frac{H}{R}\right)_{out} \left(\frac{R - R_{in}}{R_{out} - R_{in}}\right)^{\beta}, \tag{3.19}$$

where the parameters are the inner and outer disk radii, R_{in} and R_{out} in units of $R(L1)$, the half thickness of the outer disk $(H/R)_{out}$ and the exponent β which describes the overall shape of the disk. The temperature structure of the un-irradiated disk is assumed to be that of a steady state disk, in the absence of irradiation,

$$T_{disk}(R) = T_{out} \left(\frac{R}{R_{out}}\right)^{-\frac{3}{4}}, \tag{3.20}$$

where T_{out} is the temperature at the outer disk and T_{in} is the temperature of the inner disk.

The disk is divided radially and azimuthally, into N_R and N_θ sections. The monochromatic intensity is again calculated using the Planck function, corrected for limb-darkening using a linear limb-darkening law, with a constant coefficient. The intensity is again scaled using the projected area of the panel, for the given values of binary phase ϕ and inclination i.

3.3.5 Transfer functions

In order to transform the reprocessed flux into a time delay transfer function, we define iso-delay surfaces. These surfaces are nested paraboloids around the line of sight to the X-ray source, defined by the earth vector, $\mathbf{e}(\phi,i)$. The parabolic surfaces have a mean time delay τ and a width $\delta\tau$. The mean time delay τ between the directly observed X-ray flux from the central source and the reprocessed signal from a point with cylindrical coordinates (R, θ, Z) is

$$\tau(\mathbf{x}, \phi) = \frac{\sqrt{R^2 + Z^2}}{c}(1 + \sin i \cos(\phi - \theta)) - \frac{Z}{c}\cos i \tag{3.21}$$

where i is the inclination of the system, ϕ is the binary phase and θ is the angle between the line of centres of the binary and $\mathbf{x}$, in the direction of the binary rotation. Examples of these transfer functions and the associated schematic diagram of the X-ray binary can be seen in Figure 3.5. The left panels show the X-ray binary and the right panels the associated transfer functions.

The phase dependence of τ allows us to create time-delay transfer functions as a function of binary phase, allowing us to produce phase-delay diagrams for the system, see figure 3.6.

3.4 The effects of binary parameters

We consider models where reprocessing takes place in the accretion disk, accretion stream and companion star. Each of these regions makes a contribution to the transfer function for the system. X-rays reprocessed at the companion star have a time delay that varies sinusoidally in phase with semi-amplitude $(a/c)\sin i$ around a mean value a/c. The accretion stream shows up as a non-symmetric contribution that varies roughly sinusoidally with the orbital motion of the companion star and can be seen in the diagram as the contribution near superior conjunction between the outer rim of the disk and the inner-face of the companion star.

The relative intensities of the contributions, represented by the area under the transfer function, constrain the geometric parameters of the system, especially the contribution

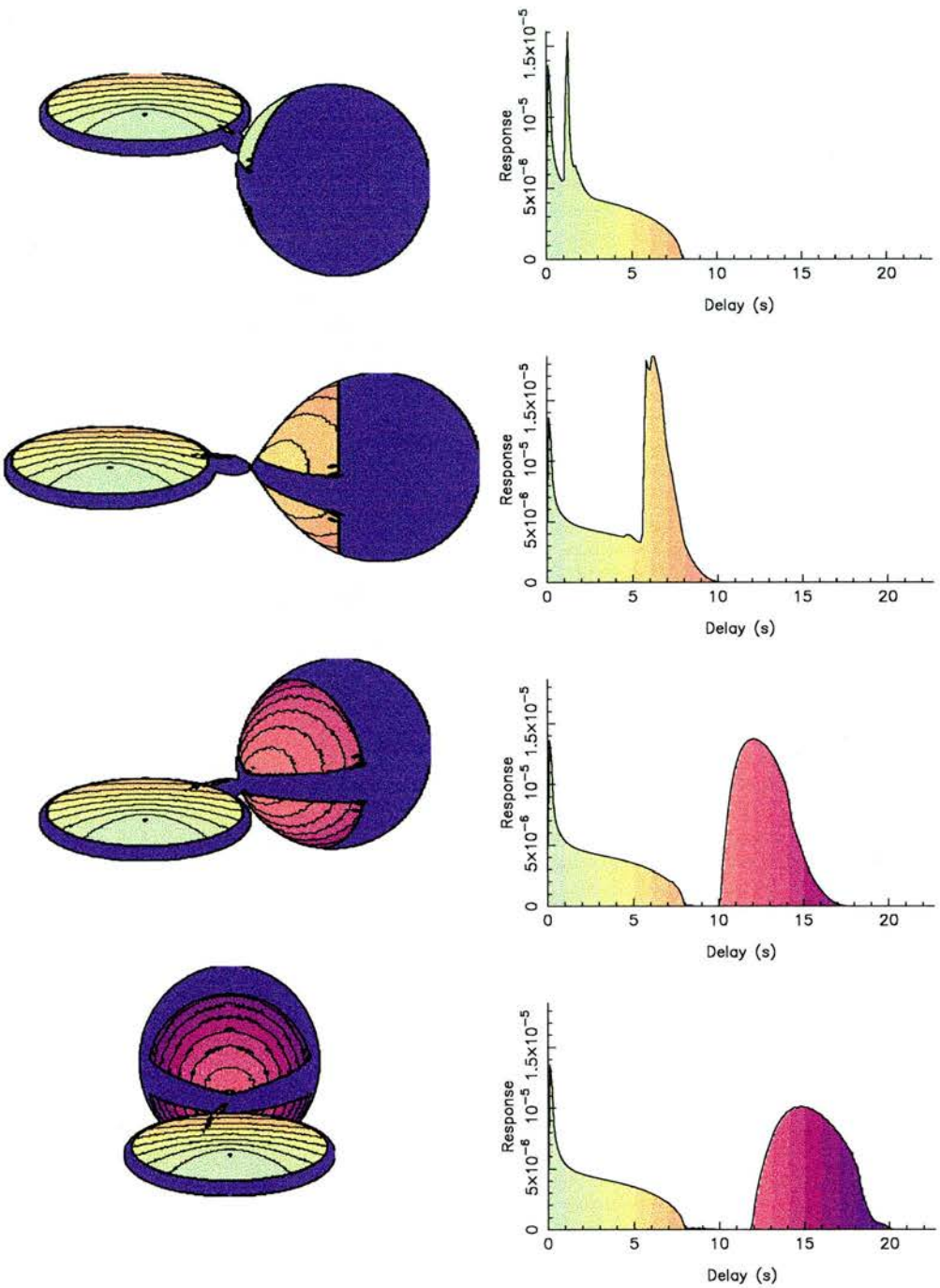

Figure 3.5: Left, schematic diagrams of an X-ray binary, based on the binary parameters of Scorpius X-1, shown in Table 4.2. Right, the associated time delay transfer function. The accretion disk has constant time delays in the region 0-8 seconds, whereas the time delays from the companion star are seen to vary sinusoidally with binary phase between 0 and 20 seconds. The inclination of the system has been set to 60°, to highlight the range of time delays. The iso-delay surfaces are plotted and the colour scale represents the time delay of the regions.

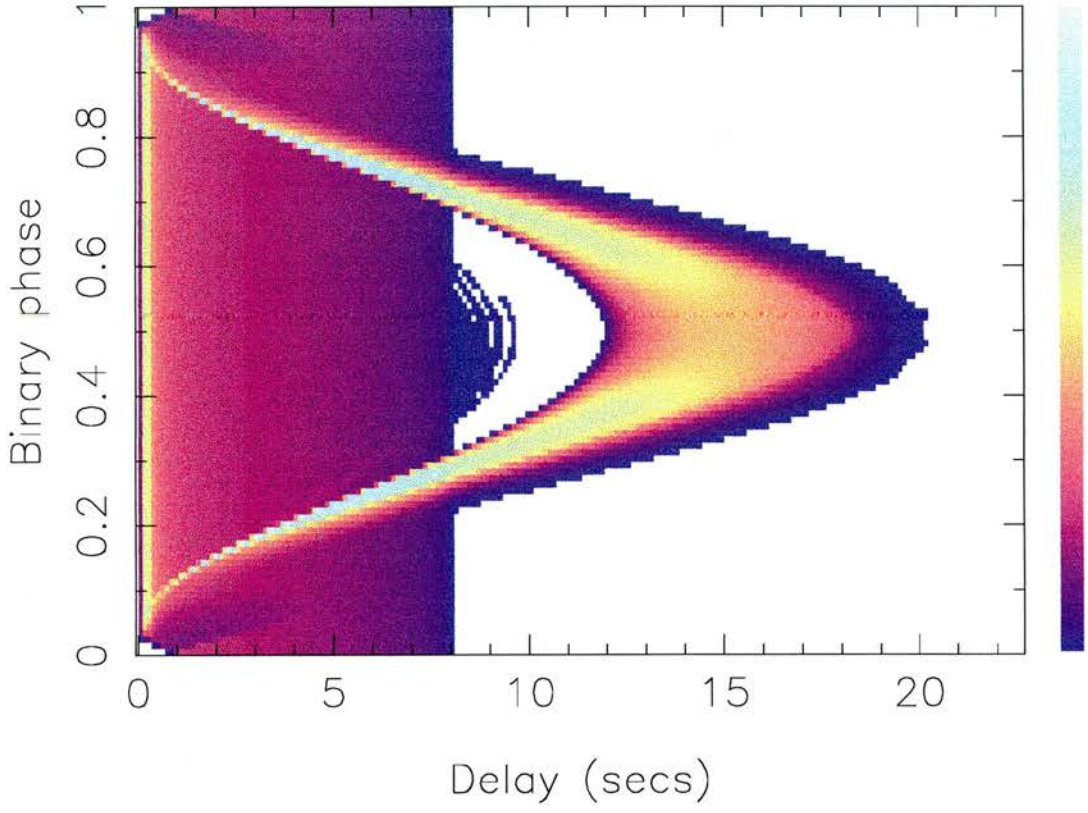

Figure 3.6: A plot of time-delay transfer functions as a function of binary phase, based on the binary parameters of Scorpius X-1, shown in Table 4.2. The accretion disk has constant time delays in the region 0-8 seconds, whereas the time delays from the companion star are seen to vary sinusoidally with binary phase between 0 and 20 seconds. The inclination of the system has been set to 60°, to highlight the range of time delays. The colour scale represents the relative intensity of the response.

from the accretion disk, which is probably the most important region for reprocessing of X-rays in interacting binaries.

3.4.1 Inclination

The shape of the iso-delay surfaces when projected onto the plane of the binary depends on the inclination of the system. For a face-on disk ($i = 0°$) the projected iso-delay surfaces are simple circles on the disk, as shown in panel a, in figure 3.7. As the inclination of the system increases these surfaces become elongated along the line of sight to the X-ray source, until finally they form parabolae when viewed edge-on ($i = 90°$). This inclination dependence is shown in figure 3.7, together with the resulting transfer functions.

The peak in these transfer functions is also a function of inclination, with the peak occurring with the time delay of the outermost iso-delay surface that is contained entirely within the disk. This is given by

$$\tau_{\text{peak}} = \frac{R}{c}(1 - \sin(i - \delta)) \tag{3.22}$$

where δ is height above the mid-plane of the disk at the edge of the disk (ie. $\delta = \tan^{-1}(H/R)$).

3.4.2 Disk thickness

The outer disk thickness, H/R, determines the relative contributions of the disk and companion star reprocessing. A thick outer disk will intercept a large amount of the X-ray flux and shield the companion star from irradiation. This can be seen in figure 3.9, where disks of increasing thickness move the peak of the transfer function from the companion star to the outer disk. In the extreme case the outer disk shields the companion star completely, although this case is physically unlikely as the X-ray irradiation of the companion star is thought to drive the accretion in X-ray binaries.

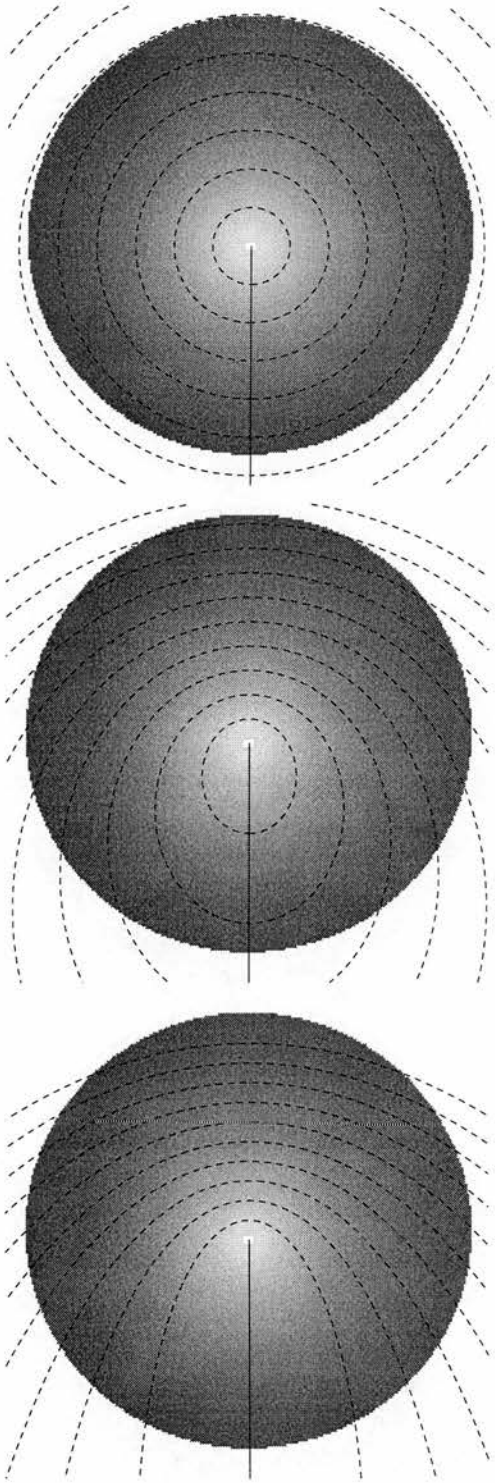

Figure 3.7: Model disks, based on the Scorpius X-1 binary parameters, showing iso-delay surfaces with inclinations of 0°, 35°, 70° from top to bottom respectively.

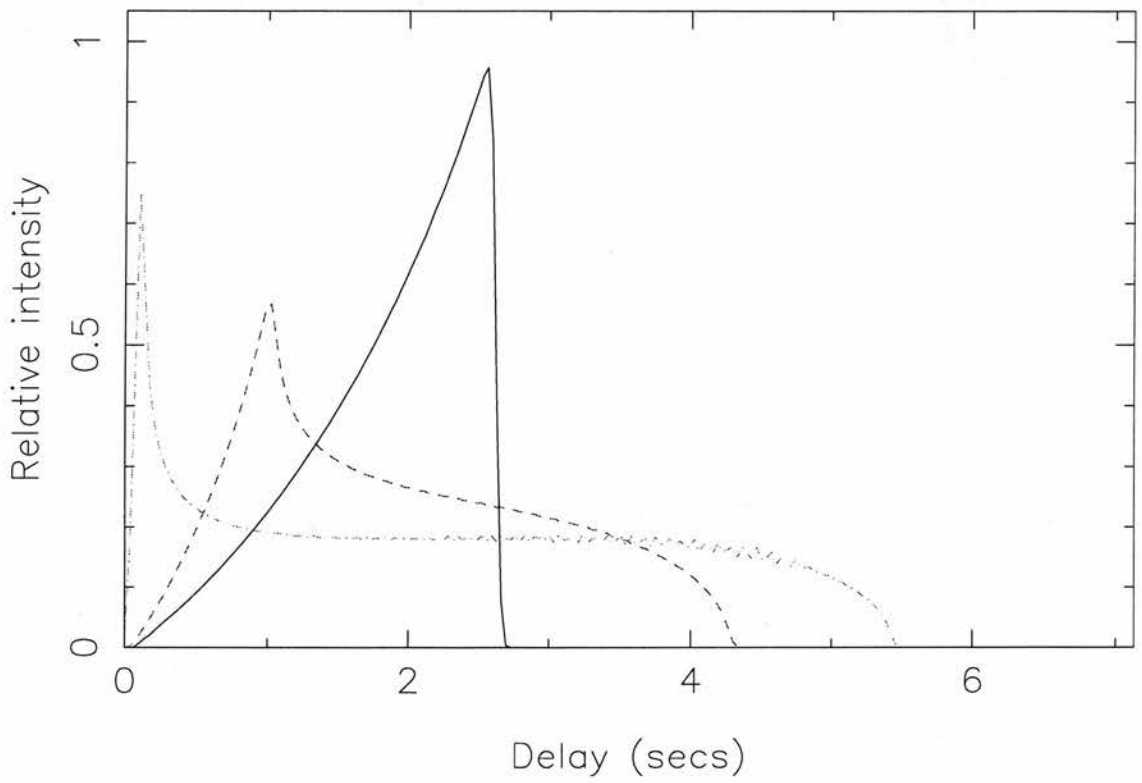

Figure 3.8: Transfer functions created using model disks with different inclinations. The solid line is for a disk inclination of 0°, the dashed for 35° and the dot-dash line for 70°. The peak value of the transfer functions is normalised to unity.

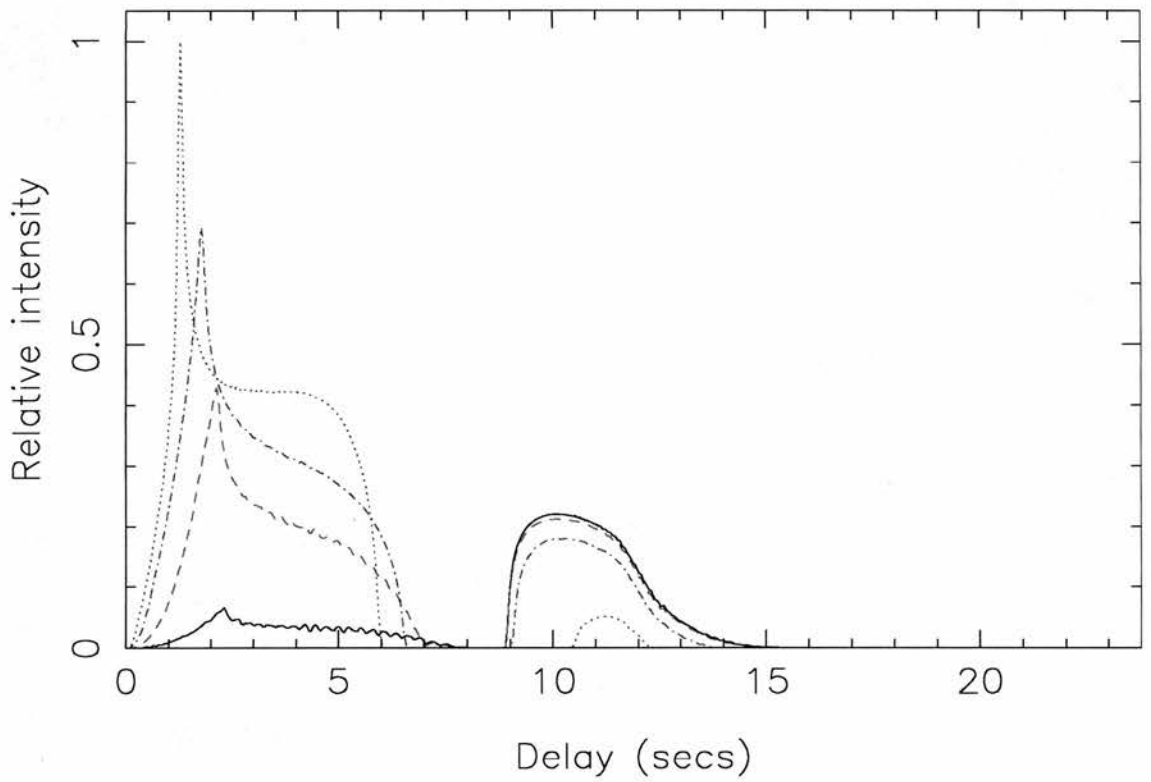

Figure 3.9: Transfer functions created using model disks with different outer disk thicknesses (H/R_{out} = 0.01 (solid black), 0.05 (dashed red), 0.15 (dot-dashed green), 0.35 (dotted blue)). These are based on the binary parameters for Scorpius X-1, shown in Table 4.2. The binary phase is fixed at 0.5. The peak value of the transfer functions is normalised to unity.

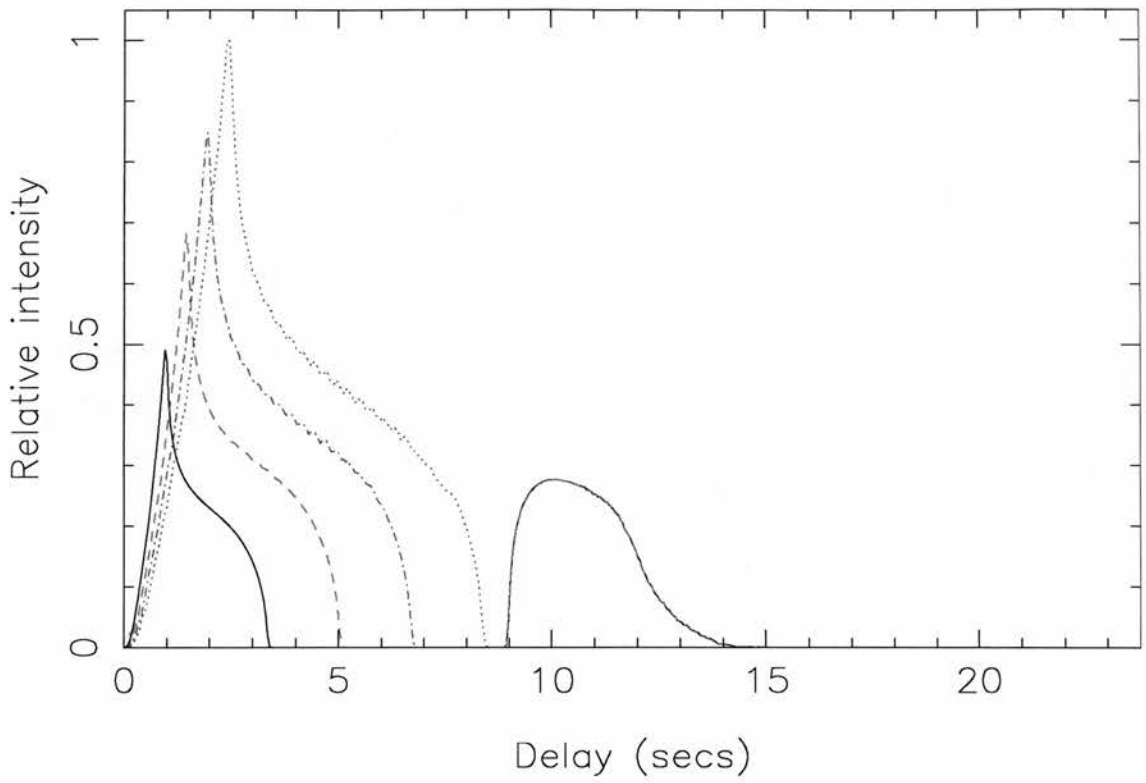

Figure 3.10: Transfer functions created using model disks with different outer disk radii (R_{out} = 0.4 (solid black), 0.6 (dashed red), 0.8 (dot-dashed green), 1.0 (dotted blue)). These are based on the binary parameters for Scorpius X-1, shown in Table 4.2. The binary phase is fixed at 0.5. The peak value of the transfer functions is normalised to unity.

3.4.3 Disk size

The disk size is set by the parameter R_{out}, in units of the distance to the inner Lagrangian point. This parameter determines the overall disk size and hence where the outer disk contribution appears in the transfer function. The mean of the transfer function will move to larger delays as R_{out} increases. This is shown in figure 3.10.

3.4.4 Disk shape

The disk shape, characterized by the exponent β, also affects the position and shape of the peak in the transfer function. Since the contribution is scaled with the projected area of the surface element, increasing β should move the peak to lower time delay, as the

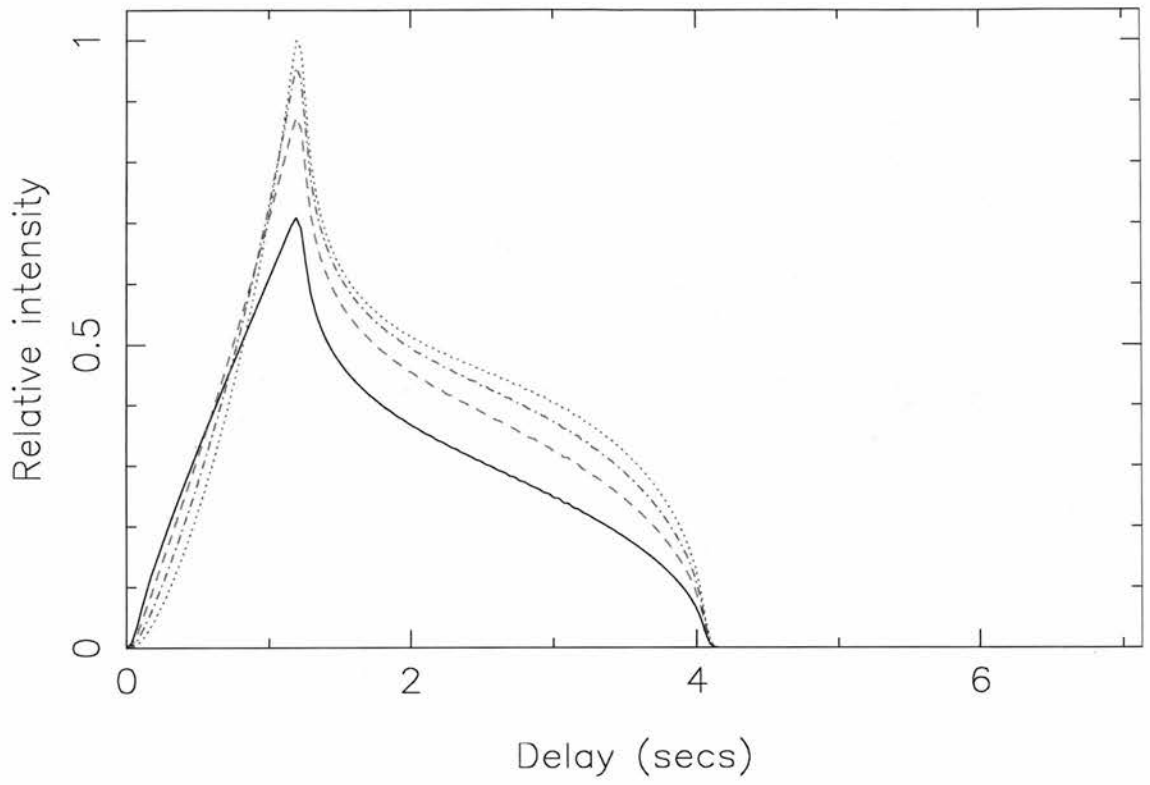

Figure 3.11: Model time-delay transfer functions as a function of β, the disk exponent for β= 1.5(solid line), 2(dashed line), 2.5(dot-dash line) and 3(dotted line). The peak value of the transfer functions is normalised to unity.

edge of the disk becomes steeper and the projected area decreases. This can be seen in figure 3.11, where time-delay transfer functions are plotted as a function of β with values between 1.01 and 3. (nb: When β=1, the surface of the disk is flat, and the thickness goes to zero at the position of the compact object. In this case, the projected area of the disk as seen from the compact object is zero, except at the inner edge. For this reason, the case of β just greater than 1 was selected to indicate the limit as β tends towards an un-flared disk.)

X-rays reprocessed by a circular disk appear at a constant time delay in the echo-phase diagram, between the inner and outer radii of the disk. Any deviation from this is evidence for a non-circular disk. For example, for an elliptical disk, the outer rim varies sinusoidally with a mean value equal to the sum of the semi-major and semi-minor axis lengths, an amplitude equal to the difference between the two semi-axes lengths and a period equal to half the orbital period.

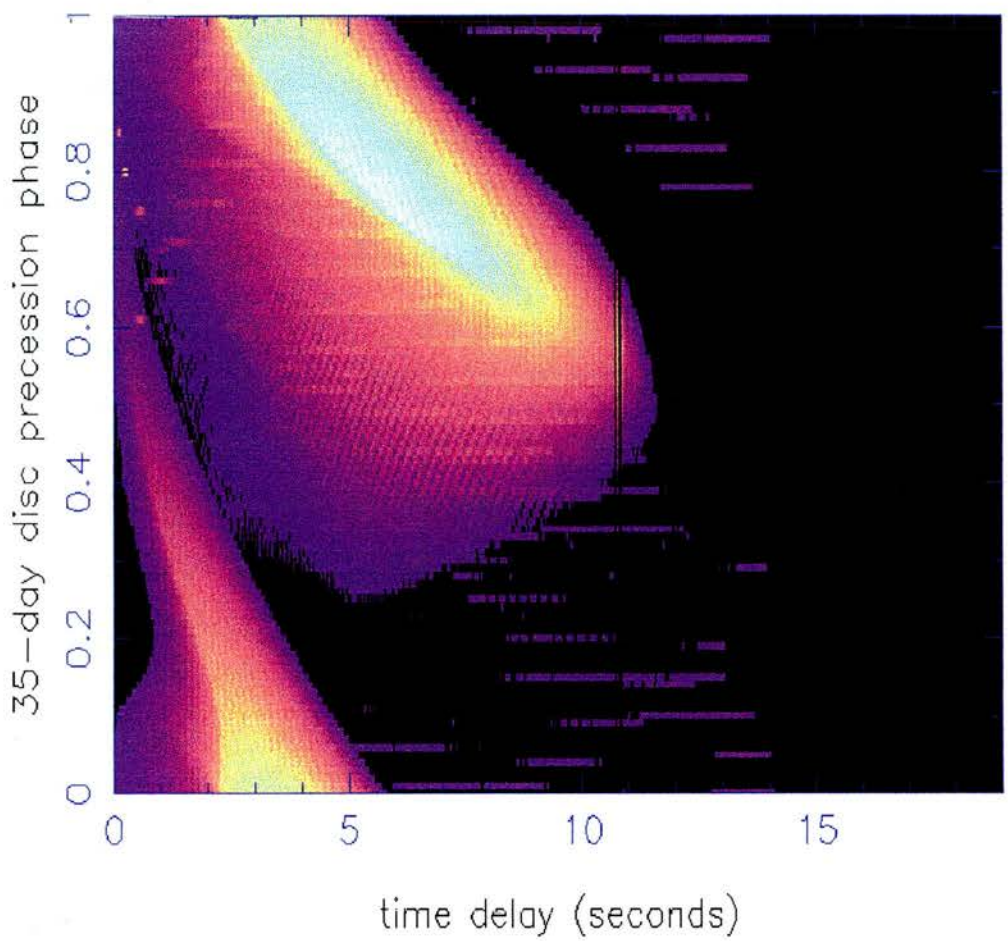

Figure 3.12: A plot of time-delay transfer functions as a function of binary phase, based on the model of Schandl (1996). The colour scale has been conserved so that black background shows no expected time delay and the bright (white) regions show the maximum response. The warp of the disk is clearly seen going from a ~10 second delay at disk phase 0.6 to ~2 seconds at disk phase 0.4.

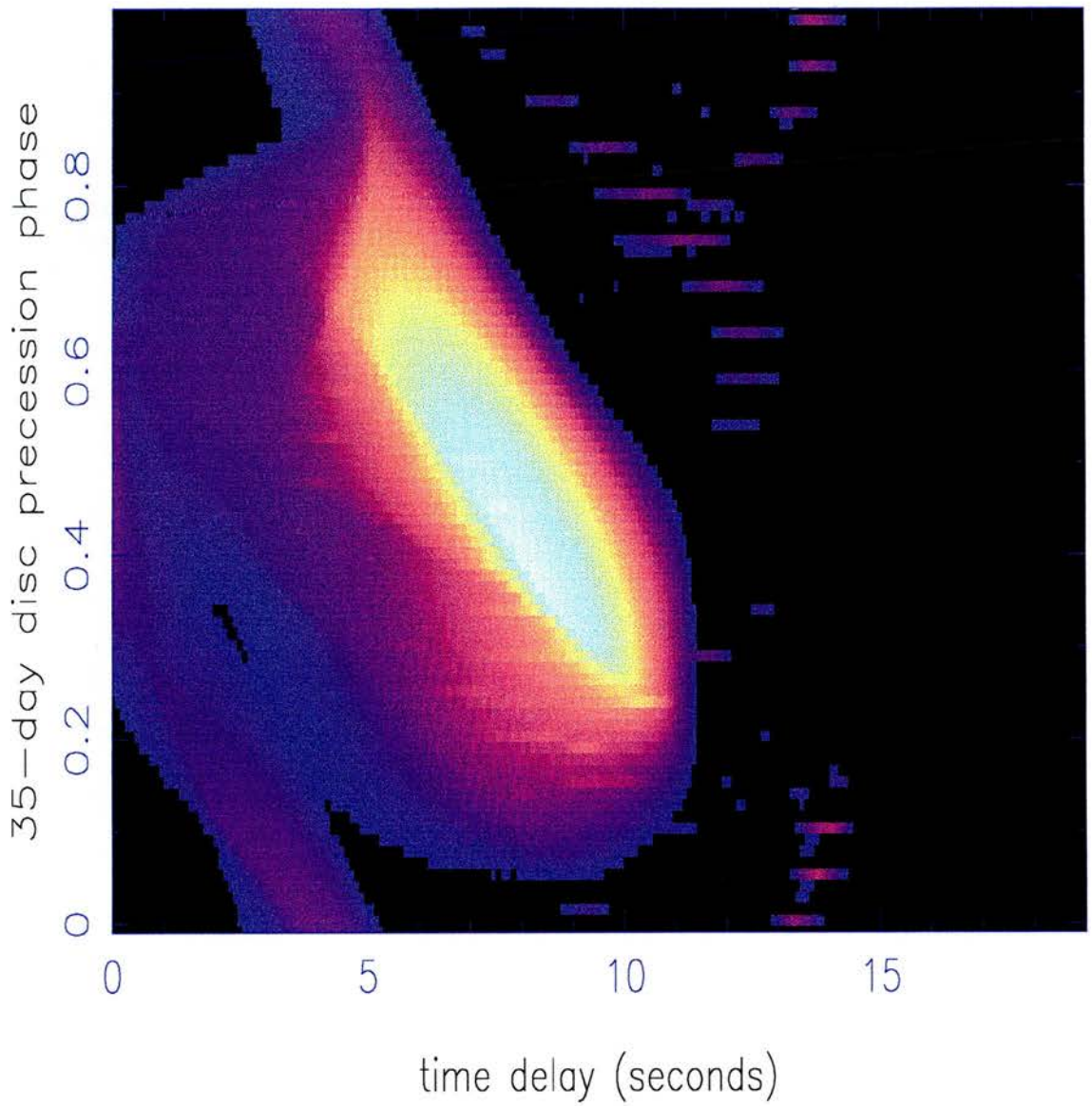

Figure 3.13: A plot of time-delay transfer functions as a function of binary phase, based on the model of Wijers (private communication). The colour scale has been conserved so that black background shows no expected time delay and the bright (white) regions show the maximum response. The warp of the disk is clearly seen going from a ~10 second delay at disk phase 0.25 to ~5 seconds at disk phase 0.7.

3.4.5 Disk warps

The existence of disk warps has been proposed to explain the existence of super-orbital periodicities in some persistent X-ray binaries. In Hercules X-1 the 35-day modulation of the X-ray source is clearly seen and is thought to be due to the precession of a warped accretion disk that blocks our line of sight to the X-ray source, during the so-called main-off and short-off states. This is shown in Figure 9.1, where the X-ray modulation is clearly seen. A similar argument has been put forward to explain the 78-day third periodicity in Cygnus X-2. Such warps are clearly shown in our transfer functions as additional contributions to the accretion disk component of the transfer functions.

If we create an echo-phase diagram for these systems, the variation as a function of the third periodicity is clear. This is shown in Figure 3.12, where the disk parameters are those determined by Schandl for Hercules X-1. (Note: The companion star contribution has been removed for clarity.) Figure 3.13 shows the same plot for the disk parameters from Wijers. One goal of echo-mapping in X-ray Binaries is to distinguish observationally between these models by mapping the warp of the disk as a function of the 35-day periodicity in Hercules X-1. In order to do this we will need phase resolved delays of the transfer function in Hercules X-1.

CHAPTER 4

Scorpius X-1

Scorpius X-1 comprises a 1.4 $M_{\odot}$ neutron star in 19.8 hour binary orbit with a $1.2M_{\odot}$ companion, V818 Sco. Since its discovery by Giacconi et al. (1962) and due to the fact that it is the brightest extra-solar X-ray source in the sky, Scorpius X-1 has been studied extensively at all wavelengths. It belongs to the sub-class of LMXBs known as Z-sources (Hasinger & van der Klis 1989). These sources trace a 'Z' shape in an X-ray colour-colour diagram. According to the standard interpretation, motion along the Z from the top left to bottom right corresponds to increasing mass transfer rate, see for example Hasinger et al. (1990). Z-sources exhibit different power spectrum features depending upon their position on the 'Z' diagram. See van der Klis (1997) and Chapter 1, for a review of the characteristics of Z-sources.

Scorpius X-1 exhibits strong optical and X-ray flares, with timescales of seconds to minutes, whilst on the flaring branch of the Z-curve. The origin of these flares is thought to be inhomogeneities in the accretion flow interacting with the magnetosphere of the neutron star. Local density enhanced regions cause sudden increases in the accretion rate, which in turn produce enhanced X-ray emission. This enhanced X-ray emission in turn irradiates the binary giving rise to sudden changes in the reprocessed optical light.

4.1 Observations

The data we have used were first presented as evidence for reprocessing in a hot plasma, possibly in the accretion disk (Petro et al. 1981). The X-ray data were taken with the

SAS-3 X-ray observatory, with 0.83 secs time resolution. The optical data were obtained using the 2.5m Hooker telescope on Mount Wilson. The absolute timing accuracy of these measurements is 1 sec between the X-ray and optical measurements. For a more in-depth discussion of the observations refer to (Petro et al. 1981). Figure 4.1 shows the two lightcurves from Petro et al. (1981), used in our analysis. The binary phase of the observations is 0.5, where the irradiated, inner face of the donor star is most visible. This binary phase is the best phase to observe to detect a reprocessing time delay.

The data show evidence for two types of flares, those with a rapid rise time (< 3 seconds) which lasted from 3-100 secs and those with a slower rise time (30-60 seconds) which occurred quasi-periodically and lasted from 30-60 seconds. The rapid flares were interpreted as a convolution of lots of short duration flares. These are difficult to resolve in the optical lightcurves because of the smearing of the individual flares. This width is due to the finite width of the time-delay transfer function, caused by reprocessing in different parts of the binary. The isolated 30 second flares were well correlated with the X-ray flares. From a comparison of the rise times of these flares Petro *et al.* concluded that "Qualitatively the optical flares may be described as filtered versions of the X-ray flares where the filter time constant is approximately 20 seconds." The difference in rise times for the flares showed that the X-ray and optical emission could not be from the same region and concluded that a geometrical time delay was the most likely reason for the observed delay.

Our aim here is to model the observations in more detail, using the methods described in Chapter 3, to test this hypothesis quantitively and clarify whether the reprocessing is taking place in the donor star, the accretion disk, or both.

4.2 Results of modeling

4.2.1 Gaussian transfer functions

The input driving lightcurve and its reprocessed optical lightcurve for the two pairs of observations are shown in Figure 4.2. Superimposed over the optical lightcurves are the

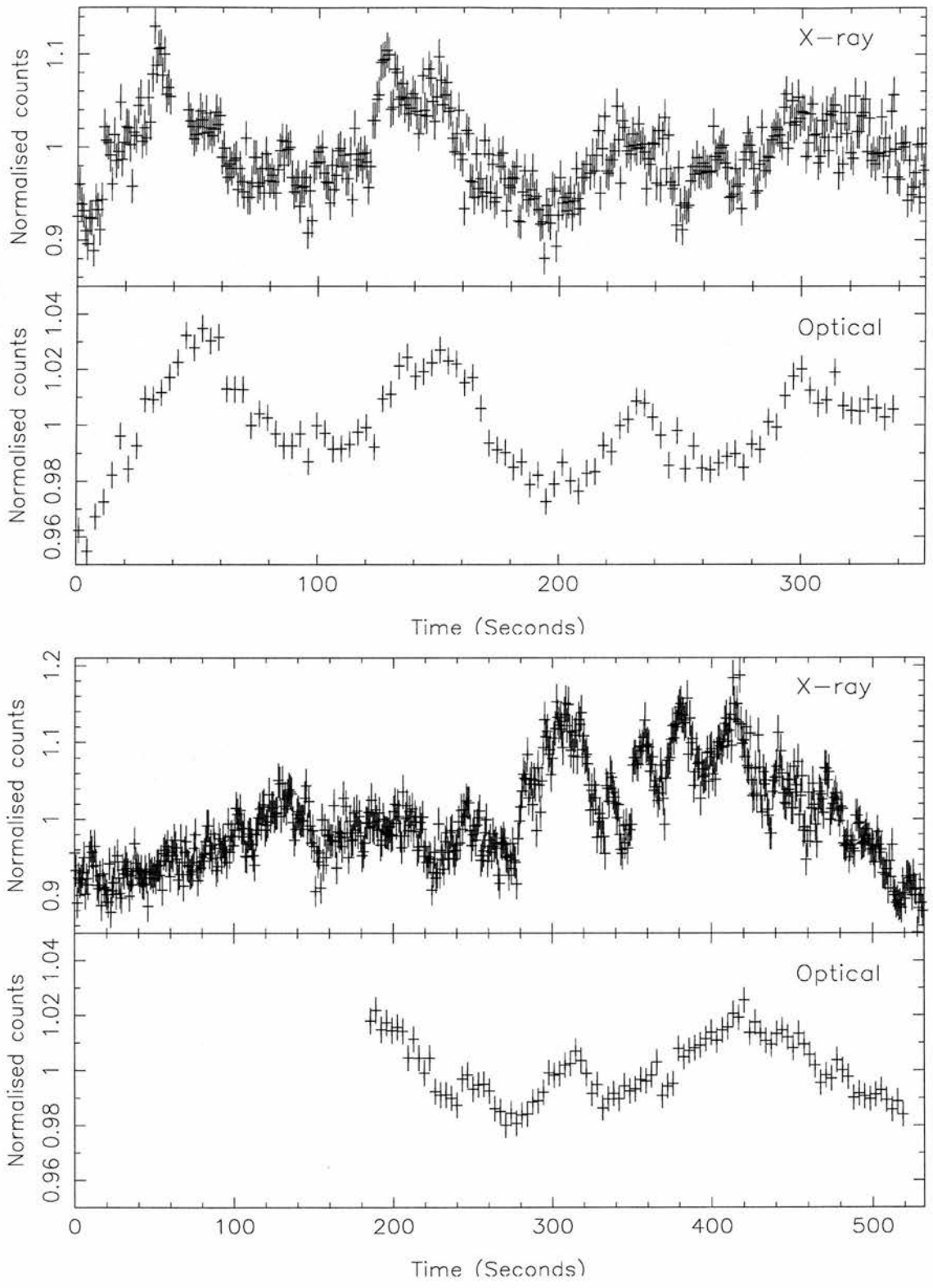

Figure 4.1: X-ray (top) and optical (bottom) lightcurves of Scorpius X-1 showing correlated flaring activity from Petro *et al.* 1981. Lightcurves from visit A are shown in the upper two panels, whilst the lightcurves from visit B are in the bottom two panels.

Dataset	A	B
ϕ	0.5	0.5
N	95	100
$\chi^2/(N\text{-}3)$	1.57	4.03
τ_0	9.3 ± 0.6	6.9 ± 1.2
$\Delta\tau$	8.7 ± 1.1	4.6 ± 1.1
Ψ	0.152 ± 0.006	0.054 ± 0.006

Table 4.1: Best fit values for the acausal Gaussian time delay transfer function fitting to the X-ray and optical lightcurves for Scorpius X-1. The results for lightcurves A and B are shown, with ϕ the binary phase of the observations and N the number of data points included in the fit.

synthesized optical lightcurves (the X-ray lightcurve convolved with the acausal Gaussian time-delay transfer function). The residuals of the fit are shown in the bottom panel. We find a mean time delay of 9.3 seconds for lightcurve A and 6.9 seconds for B, with RMS delay ranges of 8.7 and 4.6 seconds, for A and B respectively. The χ^2 surfaces for these fits are shown in Figure 4.3. The results of these fits are summarized along with their 1-parameter 1-sigma confidence regions in Table 4.1.

The reduced χ^2 for the two fits are relatively high, suggesting a poor fit. This is due to a longer term variability that can be seen in the lightcurves, see Figure 4.2. The fit in the case of lightcurve A is better than in B. It is clear from the fits in Figure 4.2 that there is both correlated and uncorrelated variability in the second set of lightcurves, whereas in the first set all of the major features present in the X-ray lightcurve are reproduced in the optical lightcurve. In Table 4.1 the formal error bars, based on $\Delta\chi^2 = 1$ are scaled by factors $\sqrt{\chi^2_{min}/(N-P)}$, where $N-P$ is the number of degrees of freedom in the fit, to allow for the poor fit (large χ^2_{min}).

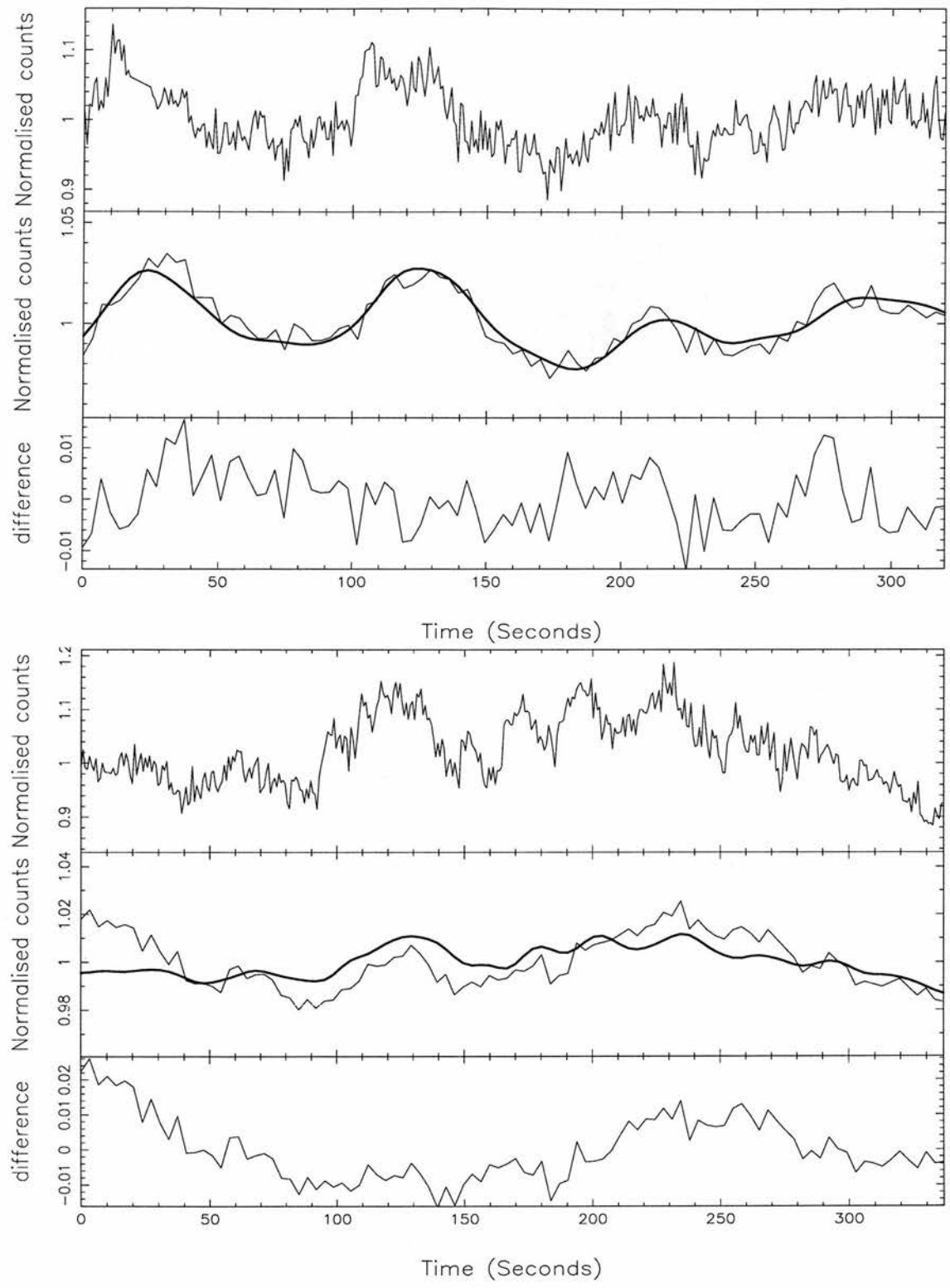

Figure 4.2: The best-fit results for Scorpius X-1 using acausal Gaussian transfer functions. Top panel, normalized X-ray driving lightcurve. Middle panel, real optical lightcurve with synthetic optical lightcurve superimposed (thick line). Bottom panel, residuals of the fit to the real optical lightcurve.

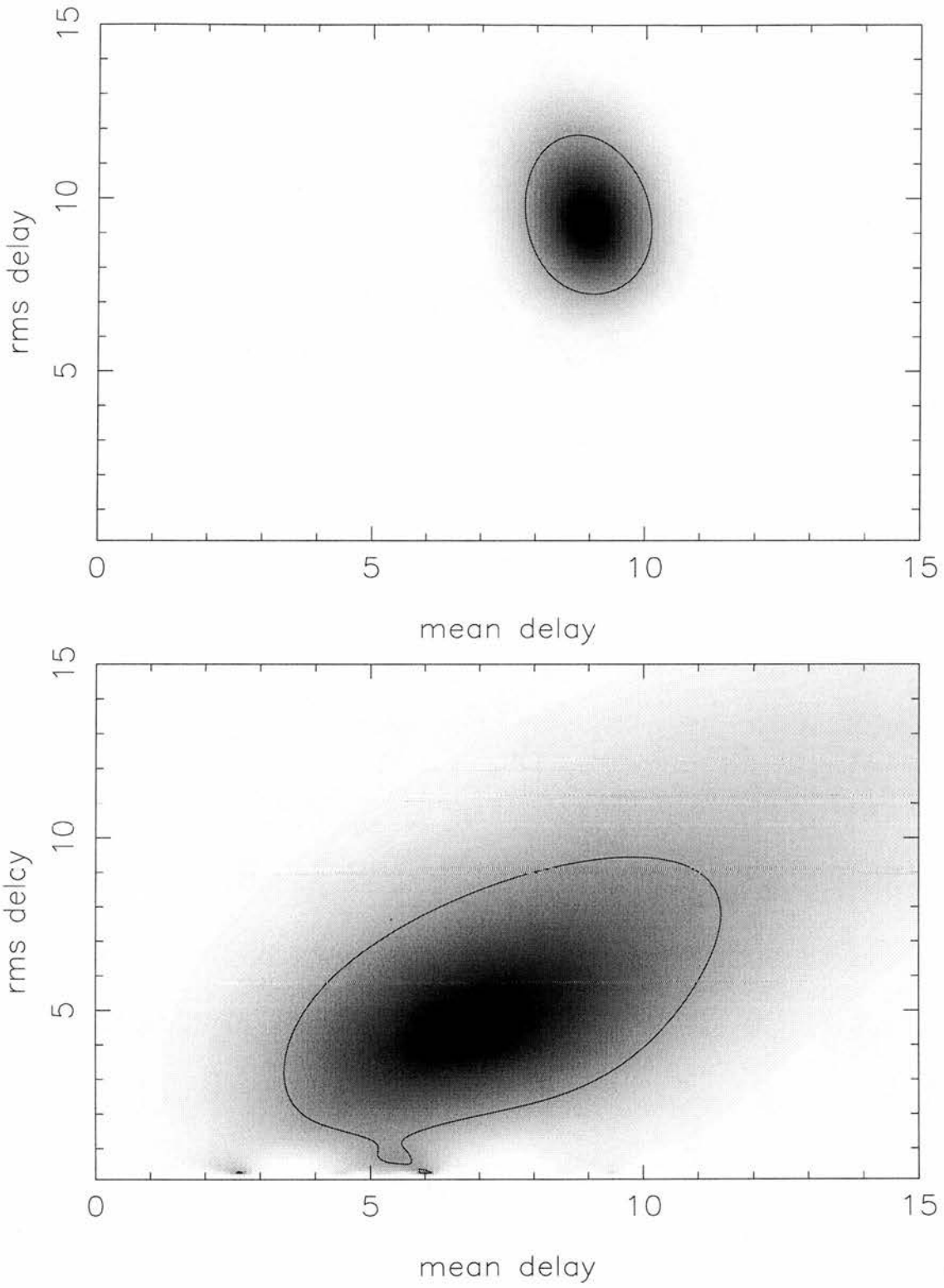

Figure 4.3: χ^2 surfaces for acausal Gaussian fitting to Scorpius X-1 X-ray and optical lightcurves A(top) and B(bottom). The best fit values from this fitting are a mean delay of 9.3 seconds, with an RMS delay of 8.7 seconds, for lightcurves A and a mean delay of 6.9 seconds, with an RMS delay of 4.6 seconds for lightcurves B.

4.2.2 Synthetic binary transfer functions

The transfer functions created by our synthetic X-ray binary code, using the binary parameters from Vrtilek et al. (1991) and Kallman, Raymond & Vrtilek (1991), were convolved with the X-ray driving lightcurves to create synthetic optical lightcurves. The free parameters in the fit, $R_{out}, H/R$ and β, were optimized by calculating the χ^2 between the synthetic and observed optical lightcurves and moving through parameter space, using a grid search method, until the global minimum was found. In order to create the synthetic optical lightcurve, the X-ray lightcurve must precede the reprocessed lightcurve by at least the maximum time delay in the transfer function. For this reason some optical points, near the beginning of the observations, were rejected from the fit, explaining why there are fewer points in the fit, than in the case of the Gaussian fits.

The results from our synthetic X-ray binary model transfer functions for the two observations of Scorpius X-1 are summarized in Table 4.3 along with their 1-parameter 1-sigma confidence confidence regions. The results show that the disk extends to approximately 70 percent of the distance to the inner Lagrangian point, that the disk is relatively thin, with an opening angle of 5 degrees. The value of beta, the exponent of the disk that describes the amount of flaring present is poorly constrained, which is to be expected in the case of a thin disk.

A comparison of the best fit transfer functions from the Gaussian and synthetic binary methods can be seen in Figure 4.4.

4.3 Discussion

In this chapter I have shown that the simultaneous X-ray and optical lightcurves originally shown in Petro et al. (1981) allows us to constrain the positions of the reprocessing regions in the binary. I have used two methods to do this, comparing the results of fitting Gaussian and model binary transfer functions, as described in Chapter 3. The best fit transfer functions to both datasets, labelled A and B, are the Gaussian shaped transfer functions, despite having fewer it parameters.

Parameter	symbol	unit	Sco X-1
Period	P	days	0.787
Inclination	i	deg.	30
Mass ratio	q		0.8
Primary mass	M_x	$M_\odot$	1.4
Binary sep.	a	lt-sec	11.3
Star Temp	T_*	K	5000
Stream Temp	T_s	K	5000
Outer Disk	T_{out}	K	10000
Inner Disk	T_{in}	K	50000
Irrad Temp	T_x	K	10^4
Inner radius	R_{in}	R(L_1)	0.01
Outer radius	R_{out}	R(L_1)	free
Disk thickness	H/R		free
disk exponent	β		free

Table 4.2: Parameters used in our model of Scorpius X-1, taken from Vrtilek *et al.* (1991) and Kallman *et al.* (1991)

Dataset	A	B
ϕ	0.5	0.5
N	92	100
χ^2/(N-4)	1.87	4.39
R_{out}	$0.69^{+0.10}_{-0.05}$	$0.78^{+0.20}_{-0.12}$
H/R	$0.02^{+0.03}_{-0.01}$	$0.07^{+0.18}_{-0.05}$
β	$3.0^{+\infty}_{-2.0}$	3.7 ± 2.4

Table 4.3: Best fit values for the model time delay transfer function fitting to the X-ray and optical lightcurves for Scorpius X-1

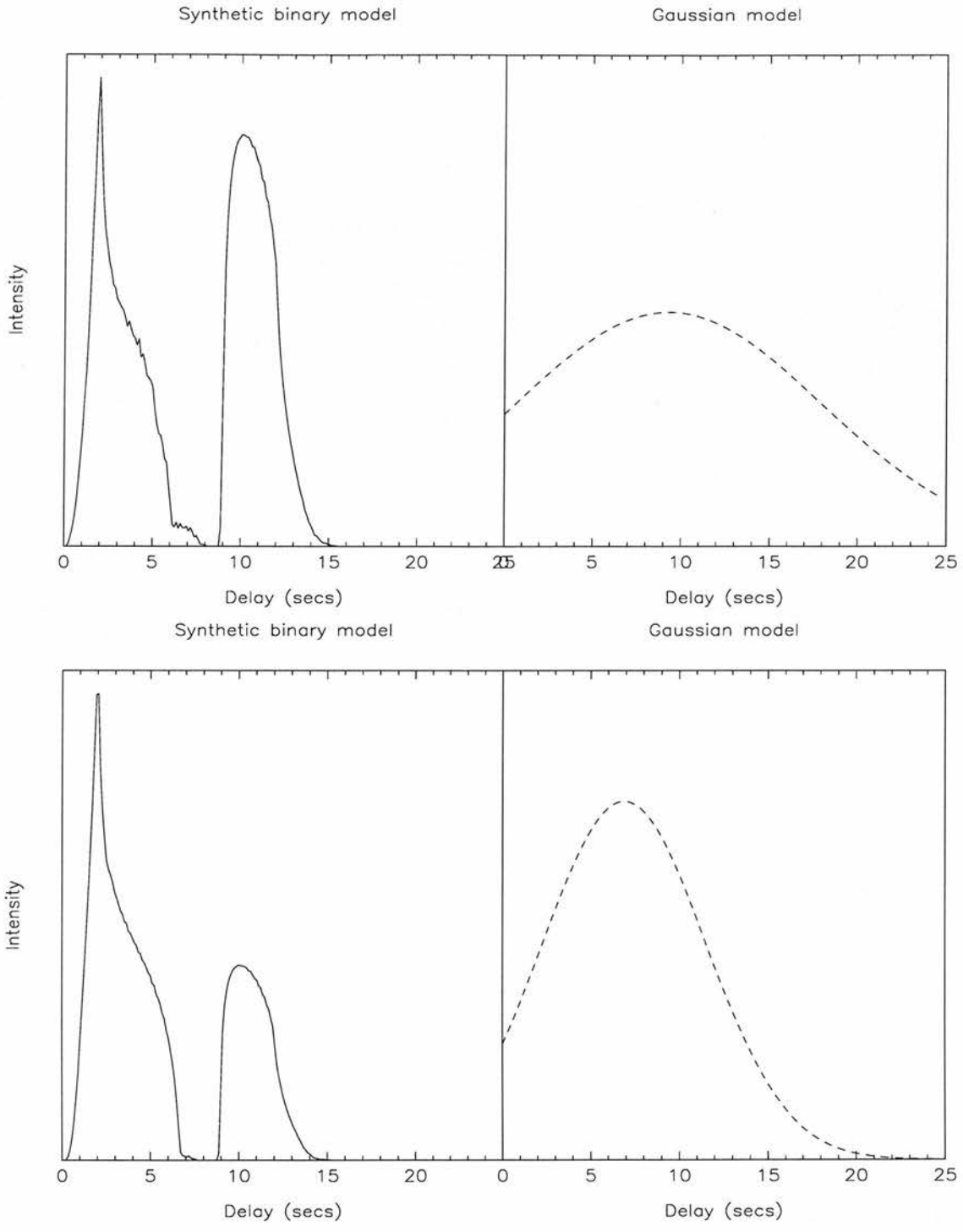

Figure 4.4: A comparison of the best fit transfer functions for both pairs of lightcurves for Scorpius X-1 from our two modeling methods. The best-fit solutions for lightcurve A are shown in the top panel and those for lightcurves B are shown in the bottom panel. On the left is the synthetic X-ray binary model transfer function and on the right is the acausal Gaussian transfer function. The best-fit parameters used for the synthetic binary model transfer function and the Gaussian transfer function are shown in Table 4.3 and Table 4.1 respectively.

The first dataset, labelled A, shows the clearest correlations and produces the better of the two fits. The best-fit Gaussian has a mean delay of 9.3-sec and an RMS delay of 8.7-sec. This suggests there is reprocessing both in the disk and on the innerface of the companion star. This is also shown in the best-fit synthetic binary transfer function, which has a thin disk that extends to 70% of the way to the inner Lagrangian point.

The second dataset, labelled B, also shows significant correlated variability in its lightcurve, shown in Figure 4.1 (bottom panels), although there appears to be non-correlated behaviour at the beginning of the visit. The best-fit Gaussian transfer function once again shows evidence for disk and companion star reprocessing, with a mean delay of 6.9-sec and an RMS delay of 4.6 sec. Once again the best-fit synthetic binary transfer function is a relatively large, thin disk, roughly consistent with the results from dataset A.

These are the results expected from a persistent X-ray binary, of which Scorpius X-1 is probably the archetypal object. The results show that reprocessing in such a source makes a large contribution to the optical flux and that we can use correlated variability to study this effect and constrain the geometric shape of the binary.

CHAPTER 5

Echoes from a thick accretion disk in GRO J1655-40

GRO J1655-40 belongs to the subclass of interacting binaries known as Soft X-ray Transients (SXTs). These systems exhibit dramatic outbursts lasting a few months separated by long periods of quiescence, often lasting decades. The trigger for the outbursts is thought to be a disk instability, similar to those observed in Dwarf Novae, where the mass transfer rate through the disk increases during outburst, effectively emptying the disk, causing a dramatic change in the X-ray flux. GRO J1655-40 was discovered in July 1994 when the Burst and Transient Source Experiment (BATSE) on *GRO* observed it in outburst at a level of 1.1 Crab in the 20–200 keV energy band (Harmon et al. 1995). The system remained in outburst until late 1995, this was followed by a further outburst between April 1996 and August 1997.

We carried out a series of simultaneous *HST* and *RXTE* observations during May-July 1996. One of the primary goals of this project was to search for rapid correlated variability in the two wavelength bands. Despite the anti-correlation between the X-ray and UV lightcurves on long timescales (Hynes et al. 1998a), we do observe short timescale correlated variability, suitable for echo-mapping purposes.

In a paper by Hynes et al. (1998b), we have analyzed these correlations using both acausal and causal Gaussian transfer functions. We were able to put constraints on the possible regions responsible for X-ray reprocessing. In this Chapter, I summarize this previous analysis and develop it further, using our synthetic binary model to create more physical transfer functions.

5.1 Data

The *HST* and *RXTE* observations used in this Chapter was first presented, along with similar exposures in Hynes et al. (1998b). The authors fitted causal and acausal Gaussian transfer functions to 4 similar exposures in a similar analysis as used in Chapter 4. I would like to thank the authors of Hynes et al. (1998b) for allowing me to use this data in my thesis and for providing a description of the *HST* data.

5.1.1 *HST*

The *HST* observations are shown in Figure 1(b) of Hynes et al. (1998b), along with a detailed description of the data reduction techniques used. In this chapter I have used one of the observations, referred to as exposure 6 in the paper. The lightcurves are reproduced in this chapter as Figure 5.1. This observation took place during the June 8 1996 visits, using The Faint Object Spectrograph in RAPID mode with the PRISM and blue detectors (PRISM/BL), covering the spectral range $\sim 2000 - 9000$ Å. The resulting lightcurve has a time resolution of ~ 3 seconds, the absolute time accuracy of this data is limited to 0.255 seconds.

5.1.2 *RXTE*

The X-ray data were taken with the PCA onboard *RXTE* on June 8 1996, simultaneous with the *HST* data. The lightcurve was created from the standard-1 EDS mode data, using the saextrct task in the FTOOLS software package. This mode has a maximum time-resolution of 0.125 seconds, but with no spectral resolution. It is desirable for echo-mapping for the driving X-ray lightcurve to have a higher time resolution than the reprocessed one, so that the time delay transfer function can have a time resolution greater than the time resolution of the reprocessed lightcurve. A lightcurve with a time resolution of 1 second and an absolute timing accuracy of about 8 μs was extracted.

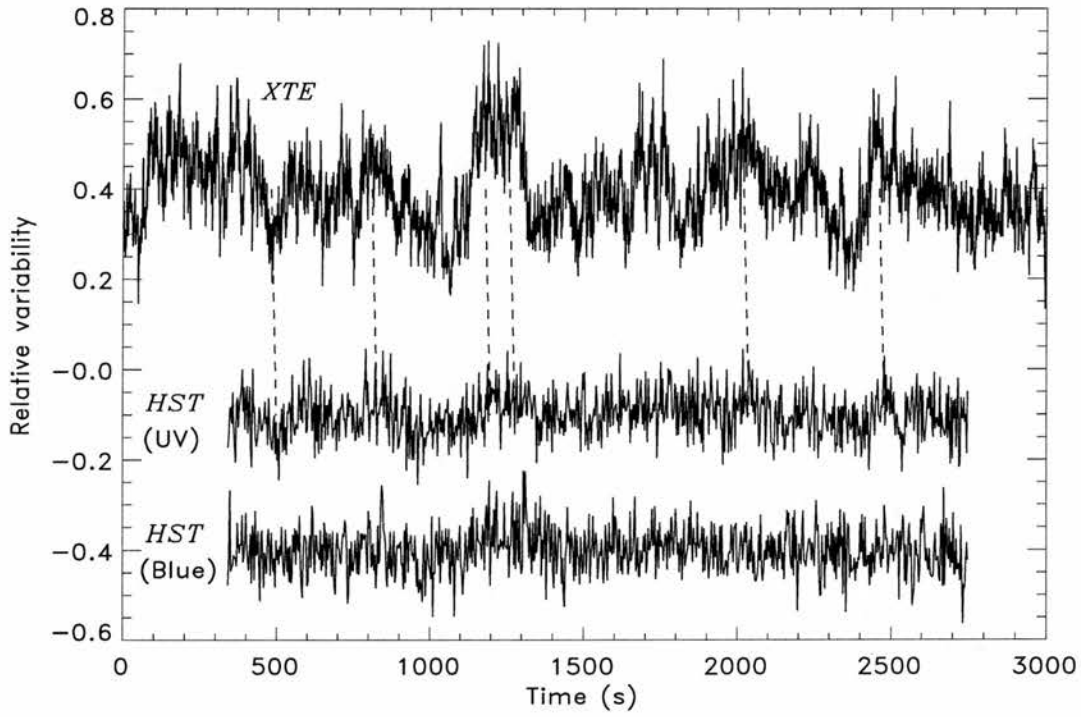

Figure 5.1: *RXTE* and *HST* lightcurves of GRO J1655-40 showing correlated flaring activity. The *HST* lightcurve has been separated into two colours to show the colour dependence of the correlations. This Figure is reproduced from Figure 1(b) in Hynes et al. (1998).

Dataset	Exp. 6
ϕ	0.42
N	782
χ^2/(N-3)	1.230
τ_0	19.3 ± 2.2
$\Delta\tau$	$10.8^{+3.7}_{-3.3}$
$\Psi/10^{-3}$	55^{+11}_{-7}

Table 5.1: Best fit values for the acausal Gaussian time delay transfer function fitting to the X-ray and optical lightcurves for GRO J1655-40. The label exp. 6 refers to exposure 6 in Hynes et al. (1998b).

5.2 Results of modeling

5.2.1 Gaussian transfer functions

The results for the fits to the acausal Gaussian transfer functions are summarized in Table 5.1, together with their 1-parameter 1-sigma confidence regions, in order to compare them to the results from our modeling of the X-ray binary. The mean and rms values for the delay in the Gaussian transfer function represent the first and second moments expected for the model transfer functions. The best fit Gaussian transfer function has a mean delay τ_0 of 19.3 seconds with an rms delay 10.8 seconds. Hynes et al. (1998b) interpreted this result as evidence for reprocessing in the outer regions of a thick accretion disk that could be thick enough to shield the companion star from significant irradiation. If this were not the case and we had considerable disk and companion star reprocessing we would expect the width of the transfer function to be much greater.

5.2.2 Synthetic binary transfer functions

The transfer functions created by our X-ray binary model, using the binary parameters determined by Orosz & Bailyn (1997) and summarized in Table 5.3 were used to create synthetic *HST* lightcurves by convolving them with the *RXTE* lightcurves. The badness

Dataset	Exp. 6
ϕ	0.42
N	782
χ^2/(N-4)	1.230
R_{out}	$0.67^{+0.03}_{-0.08}$
H/R	$0.25^{+0.54}_{-0.03}$
β	$3.8^{+\infty}_{-1.1}$

Table 5.2: Best fit values for the synthetic X-ray Binary model time delay transfer function fitting to the *RXTE* and *HST* lightcurves for GRO J1655-40.

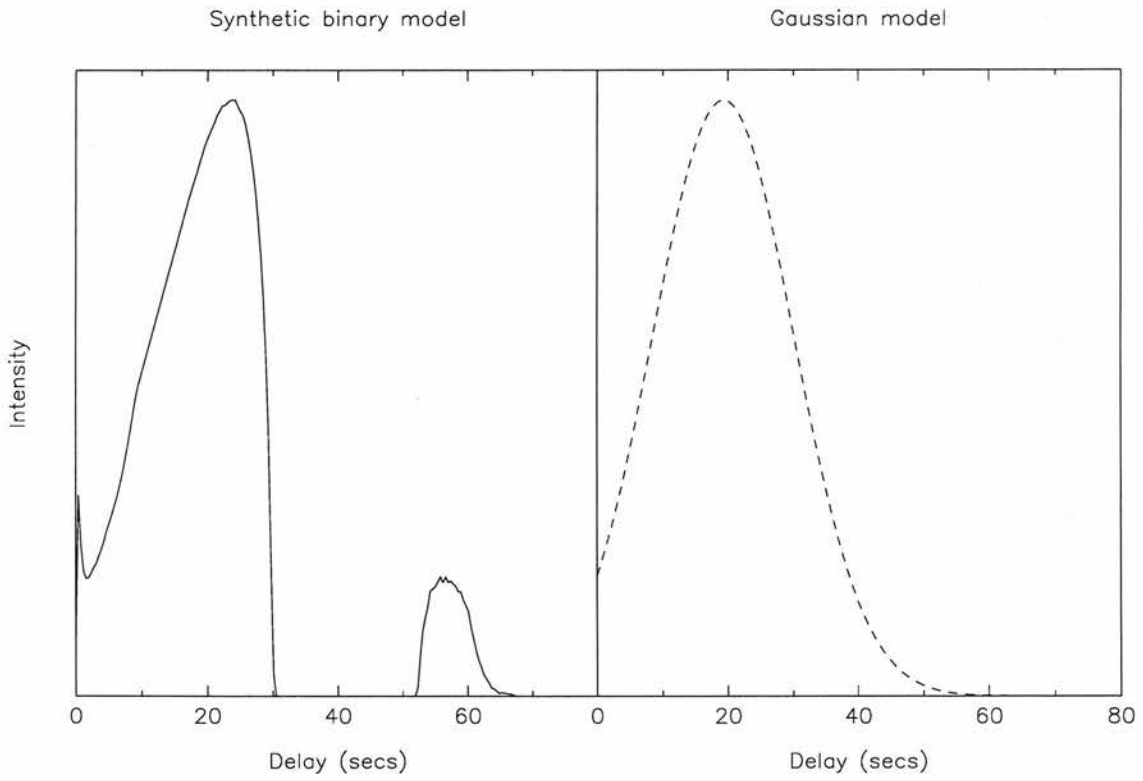

Figure 5.2: A comparison of the best fit transfer functions for GRO J1655-40 from our two modeling methods. On the left is the synthetic X-ray binary model transfer function and on the right is the acausal Gaussian transfer function.

Parameter	symbol	unit	GRO J1655-40
Period	P	days	2.6
Inclination	i	deg.	69.5
Mass ratio	q		0.3344
Primary mass	M_x	$M_\odot$	7.02
Binary sep.	a	lt-sec	40
Star Temp	T_*	K	6500
Stream Temp	T_s	K	5000
Outer Disk	T_{out}	K	10000
Inner Disk	T_{in}	K	100000
Irrad Temp	T_x	K	10^5
Inner radius	R_{in}	R(L_1)	.0001
Outer radius	R_{out}	R(L_1)	free
Disk thickness	H/R		free
disk exponent	β		free

Table 5.3: Parameters used in our model of X-ray Binary for GRO J1655-40, the values are taken from Orosz & Bailyn (1997).

of fit between this synthetic reprocessed lightcurve and the real reprocessed lightcurve, from *HST* was calculated. The fitting contained 4 parameters, including the nuisance parameter of the scale factor Φ, which were optimized as before. The best-fit parameters, together with their 1-parameter 1-sigma confidence regions are given in Table 5.2. We find that the disk extends to 67 percent of the distance to the inner Lagrangian point (in good agreement with that found for Scorpius X-1 in section 4.2.2), with an opening angle of 15 degrees and an exponent of 3.8. This result is not surprising when compared to our acausal Gaussian time-delay transfer functions, which centre the reprocessing in the outer disk.

This best-fit solution from our modeling is shown along with the best-fit solution from the acausal Gaussian fitting in Figure 5.2. The best-fit solution for this modeling shows a similar χ^2 to the Gaussian fitting, which shows that our modeling of the binary system and simple Gaussian fits are both good fits to the data. The first and second moments from the model transfer function are, as expected, similar to the best fit parameters from the Gaussian fitting.

5.3 Discussion

In this chapter I have shown that during our observations of GRO J1655-40 there is evidence for considerable disk reprocessing. The geometric parameters determined from our fit give an opening angle of 14 degrees and a very flared geometric shape, implying that most of the reprocessing is taking place in the outer regions of the disc. This means that the companion star is almost entirely shielded from X-rays, which in turn could reduce the mass accretion rate, if driven by irradiation. The observations of GRO J1655-40 took place during outburst, which could explain the flared shape of the outer disk. Another possible interpretation is that there is a localized region of enhanced reprocessing in the outer disk that is non-axisymmetric that is adding a large component from the outer disc region to the transfer function but is difficult to distinguish from reprocessing from a thick disk. This would explain the high value of β observed, as the model attempts to move all the reprocessing to the outer disk. The most likely site for this reprocessing would

be at the disk-stream interaction point, where the rim of the disk swells greatly. This inhomogeneity is observed in GRO J1655-40 as X-ray dips around binary phase 0.8. This is the site proposed for the reprocessing of the X-ray bursts seen in 4U/MXB 1636-53 (Matsuoka et al. 1984).

The effect of reprocessing timescales in different regions of the binary also needs to be studied in more detail, with detailed radiative transfer models. The incidence angle of the X-rays to the atmosphere may cause large variations in the timescale. Normally incident X-ray photons may be reprocessed deeper within the companion star and hence take longer to diffuse to the surface, than those with a grazing incidence angle. This would also affect the ratio of disk to companion star reprocessing, as the incidence angles for the disk will be predominantly grazing.

In order to distinguish between these scenarios and to determine the importance of reprocessing timescales it is necessary to have data with better phase coverage to observe a change in the time delay of this enhanced region as a function of binary phase and any reprocessing timescale effects. It is clear from our analysis that the companion star is responsible for a small fraction of the instantaneously reprocessed flux, see Figure 5.2.

CHAPTER 6

High Time Resolution Keck II data

Recently, with the advent of 4+ metre optical telescopes and fast CCDs it has become possible to perform high time resolution optical spectroscopy. Continuous read-out modes are becoming available on these telescopes allowing 1-2k pixel spectra to be read out every second or so. This allows us to use spectroscopy to explore the rapid optical variability of X-ray binaries, with sufficient signal to noise, where previously only broad-band photometry had been possible. One such system was developed by Richard Gomer for use with the Low-Resolution Imaging Spectrograph (LRIS; Oke et al. (1995)) at the Cassegrain focus of the 10 metre Keck II telescope, situated near the summit of Mauna Kea, Hawaii, see Figure 6.1. (The data system has since been nicknamed the "Gomerizer" due to the unusual data format used. I would like to thank Richard Gomer for supplying the description of the data system used in this thesis.)

Keck II is at an elevation of 4146 metres and consists of 36 hexagonal mirror elements, each 1.8 metres in diameter, weighing 400 kg each. The position and shape of each element is adjusted twice per second to create an hyperboloid mirror with an effective collecting area of 76 square metres. The light-path showing the general layout of the telescope, including the mirror array, is shown in Figure 6.2.

The data were obtained during 5 clear nights 01-06 July 1998. During the observations over 1.2 million spectra were obtained. The principal objects were Cygnus X-2, Hercules X-1 and Scorpius X-1, for which the observations were simultaneous with *RXTE* to search for correlated X-ray and optical variability. Table 6 is a summary of the observations, including the approximate number of optical spectra taken on each target.

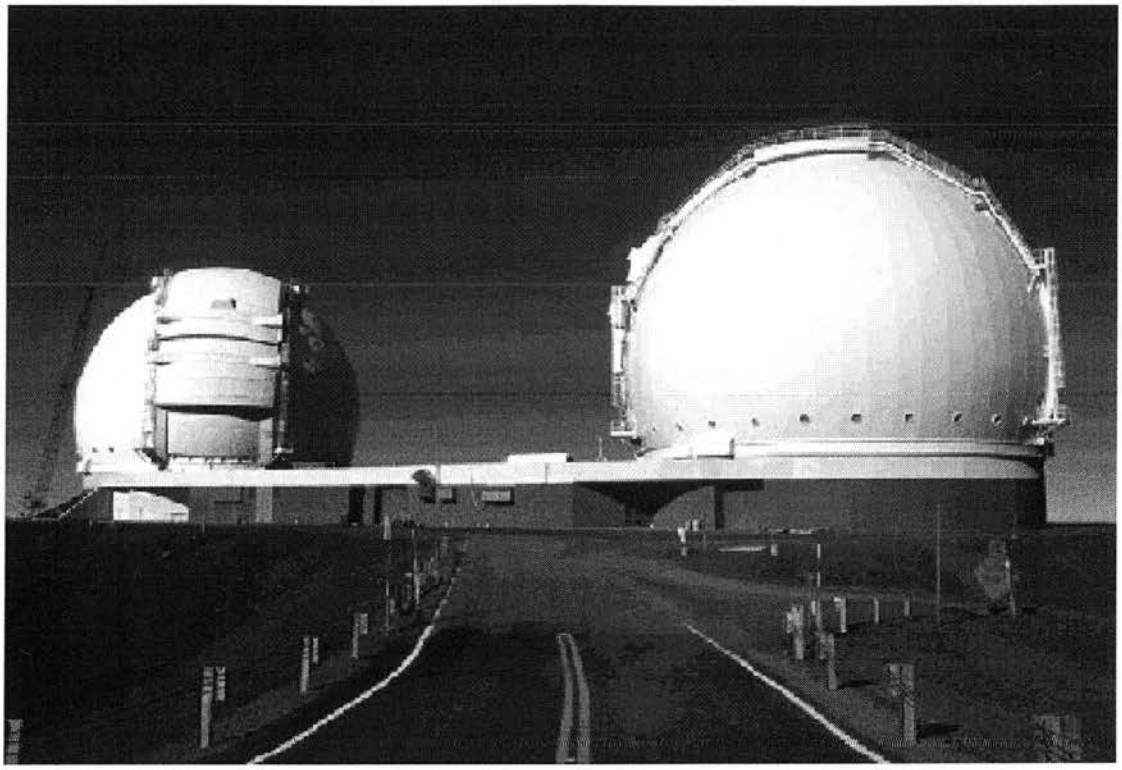

Figure 6.1: A photograph showing the twin domes of the Keck observatory on the summit of Mauna Kea.

Object name	Night observed	Number of optical spectra	*RXTE* coverage?	Object type
Cygnus X-2	1,2,4,5	504,000	Y	LMXB, Z-source
Hercules X-1	2,5	105,000	Y	Binary X-ray Pulsar
Scorpius X-1	1,2,3,4	355,000	Y	LMXB, Z-source
AE Aqr	2,4,5	87,000	N	Magnetic Cataclysmic Variable
V2051 Oph	3,4	89,000	N	Dwarf Nova
SS Cyg	2,5	50,000	N	Dwarf Nova
AM Her	2	25,000	N	Polar
V404 Cyg	5	14,000	N	Black Hole Binary

Table 6.1: Summary of the target list of our high speed spectroscopy observations, using the Gomerizer on Keck II.

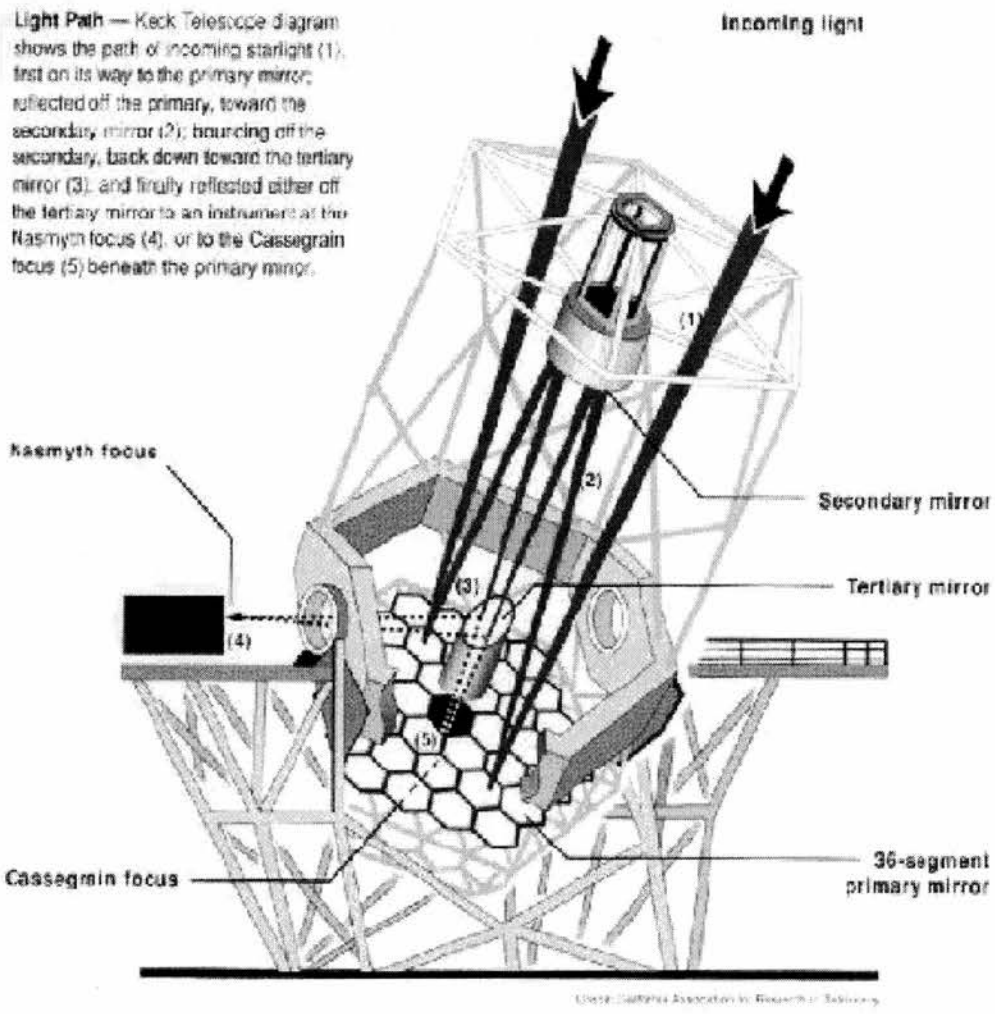

Figure 6.2: A schematic of the light-path for the Keck II telescope.

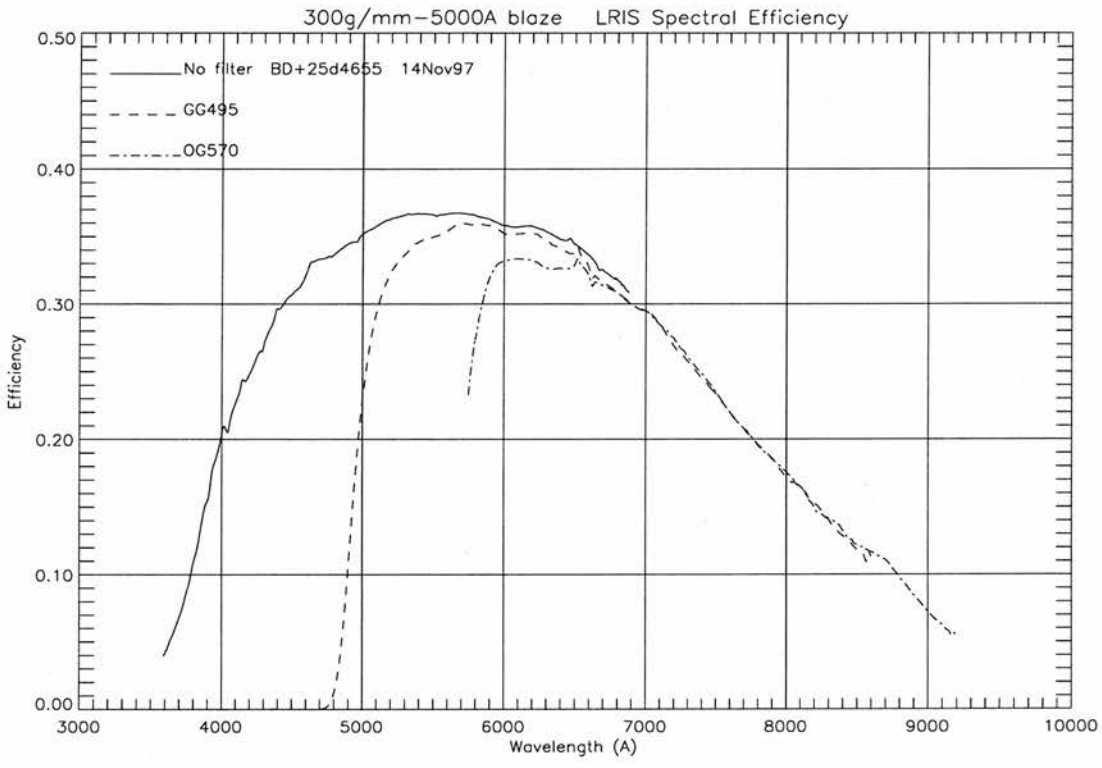

Figure 6.3: The response function for the 300/5000 grating used on the LRIS on Keck II.

The 300/5000 grating, with 300 grooves per mm and a blaze wavelength of 5000Å, gave a mean dispersion of 2.55 Å/pixel in the range 3800Å- 9200Å. The response function for the grating is shown in Figure 6.3.

The data system works by creating an invisible tap on the fibre optic cable between the VME and timing boards, to intercept and record the data from the CCD in the form of a continuous byte stream. With the data system switched on, the CCD is set into continuous read-out mode, where the rows of the CCD are shifted down the CCD and readout every ~ 0.072 seconds, fixing the time resolution of the data system. The data can be thought of as coming from a virtual CCD with 2148 columns (including 25 pixels of under-scan and 75 pixels of over-scan) and $(A + T/0.072)$ rows, where T is the duration of the run in seconds and A is the row number where the image of the slit falls on the CCD. The spatial dispersion is 4.6 pixels/arcsecond, so with on-chip binning of 8, each row covers 1.74 arcseconds. A 5.2 arcsecond slit was used to ensure that all the incident starlight was collected. The slit was partially covered using aluminized mylar tape to create a 5.2x5.2 arcsecond square aperture. Thus the image of the aperture covers three rows of pixels on the CCD, one row containing the object and two rows containing sky. Since we have no information as to the exact location of the image on the CCD our uncertainty in A is ± 1, leading to an intrinsic uncertainty in the absolute timing of ± 0.072 seconds. It also leads to a correlation between adjacent spectra, since three pixels are being exposed simultaneously, however this is low since the seeing was ~ 0.8 arcseconds during the observations.

6.1 "Degomerizing" the data

The spectra appear as a continuous byte stream. Each 2048 pixel spectrum also contains a 25 pixel under-scan region and a 75 pixel over-scan region. Occasionally a pixel would be missing from the raw spectra, usually during telescope movement. When this occurred, the entire affected spectrum was removed from any further analysis, creating a gap in the time series. The median bias level for a spectrum was determined from the over-scan and under-scan regions and subtracted. The bias strips were then removed from the spectra.

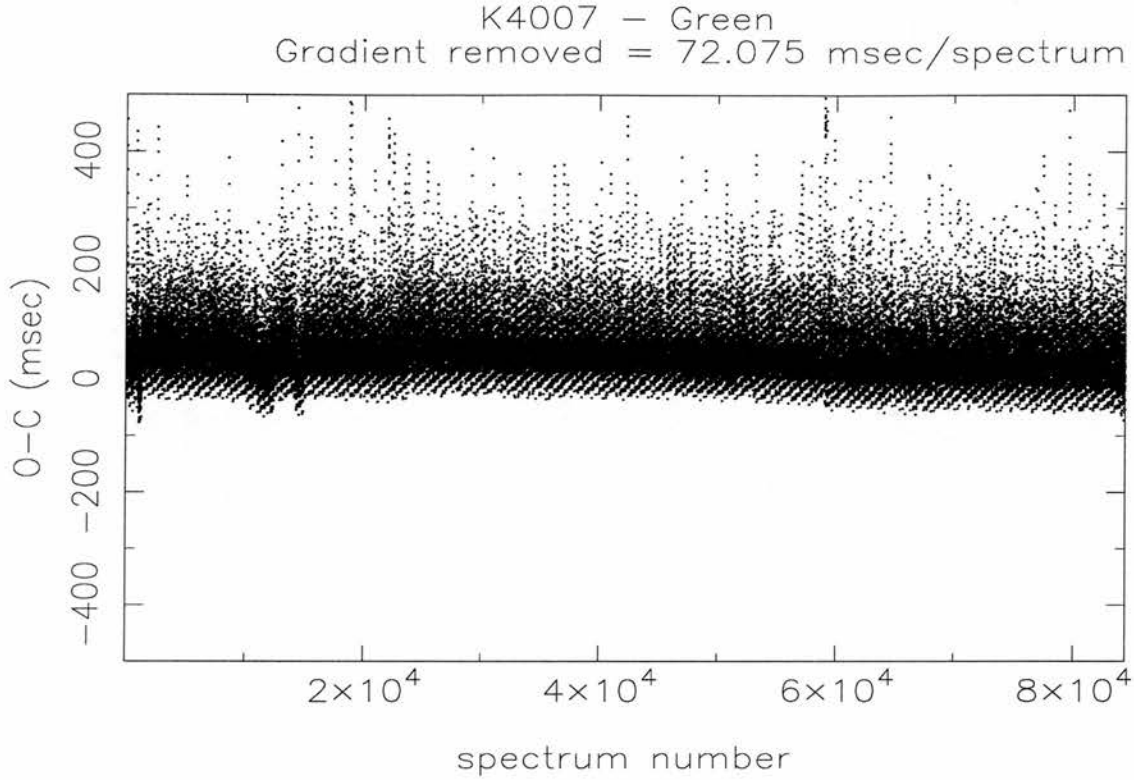

Figure 6.4: The difference in milliseconds between the Observed and Calculated times, with a mean exposure time of 72.075 milliseconds.

The noise for a given pixel was calculated using a readout noise of 6.3 e and a gain of 4.7 e/ADU. Cosmic rays were rejected from the de-biased frames, by taking the median of 3 spectra either side of the spectrum in time and rejecting the pixel if it was above a threshold of 7-sigma from the expected value. A master flatfield image was created by finding the median of 700 individual flatfield spectra. This image showed no deviations above 0.3 % in all but 3 pixels. It was decided that it was therefore not necessary to flatfield individual spectra.

6.2 Time calibration

Two time reference systems were used. First, an internal clock which updated roughly every 55 ms was used to mark the time on each 2148-pixel spectrum. This clock was used to display the time on the monitor, and the displayed time was compared to the audible WWVH time signal received by a short wave radio. The offset could be determined to

roughly 0.1 seconds, and this was recorded roughly every 30 minutes.

Due to the nature of the continuous byte stream of data, it was impossible to obtain accurate times for each individual spectrum. In order to find the times accurately timestamps were placed at several points throughout the observations. These timestamps were created using an incandescent lamp that illuminated the CCD at a known time, from which we found an ephemeris and exposure time. Individual time marks, accurate to approximately 200ms, were placed after every other spectrum using the computer clock. These were used as a check for our calculated ephemeris and exposure time. The results of this fit is shown in Figure 6.4.

In this fit four timestamps at the beginning of the run were used to find the ephemeris and the slope of the 'O-C' diagram was used to calculate the mean exposure time. The fit was checked using four timestamps at the end of the exposure, using the observed times and those predicted by our model. The two sets of time marks were separated by 71000 spectra and the difference between the observed and calculated times was less than 200 milliseconds.

6.3 Background subtraction

Sky spectra were taken at the beginning and end of each run, by moving the telescope, so that long timescale variations could be detected. The mean and variable components of the sky spectrum were found by creating a lightcurve for each pixel and extracting the mean (coefficient 1) and gradient (coefficient 2) of this lightcurve. An example of this fit is shown in Figure 6.5. This is typical of the spectra found for fits to the other observations in the dataset. The average gradient was found to be $< 5 \times 10^{-7}$ counts/spectrum. Each run consisted of $\sim 40,000 - 80,000$ spectra, so that the expected change in the sky level during the run is $\sim$ 0.1%. The gradient was therefore set to zero during our analysis so that no spurious pixel to pixel variations were introduced. The mean value was calculated for each run and filtered in wavelength, with a running median filter of width 11 pixels.

This mean sky spectrum also shows several electronic features, the most noticeable of these are at pixel 977 and around pixel 1100. The origin of these features is unknown,

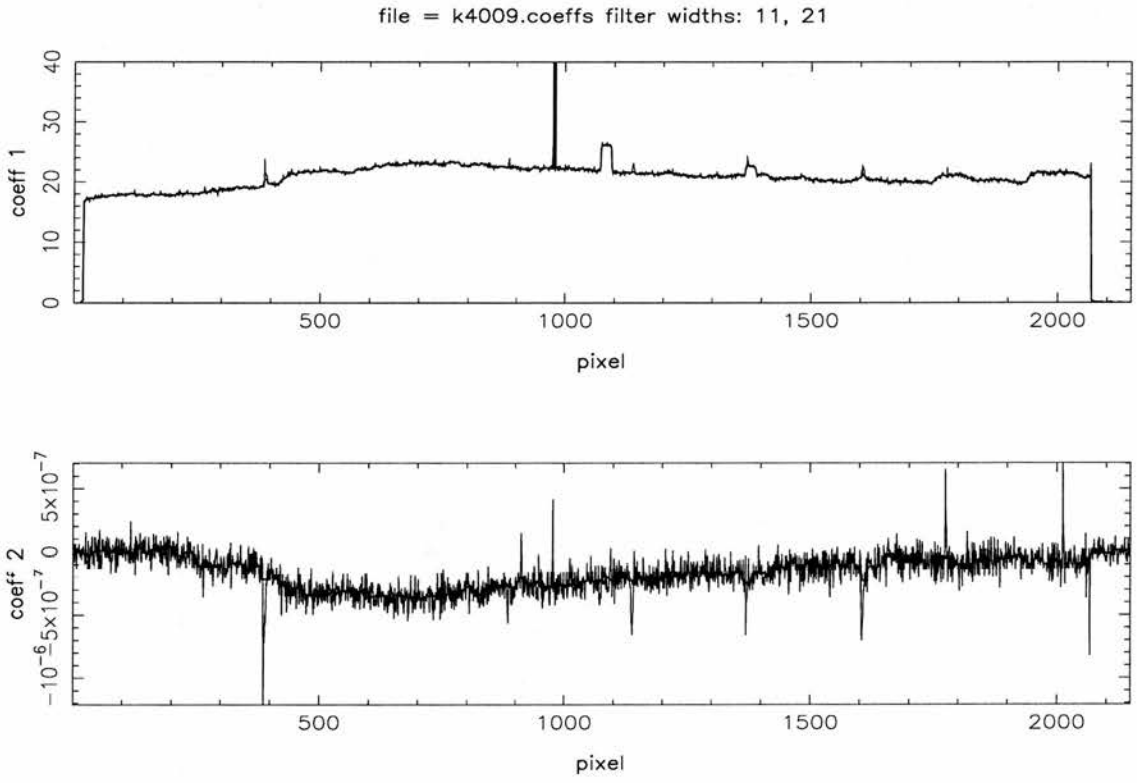

Figure 6.5: An example of an average sky background spectrum and its time derivative. The plot is in counts and pixels and is taken from the file named K4009. The average spectrum and the lightcurve are passed through a running median filter, with filter widths of 11 and 21 pixels respectively.

but they appear to be removed very well from the object spectra if modeled as sky features. During the sky subtraction, the variance of these points was increased so that their weighting in subsequent analysis was reduced.

6.4 Wavelength calibration

The arc calibration was done by fitting a second order polynomial to 7 identified lines in a median spectrum of 1400 individual exposures of Hg and Ar lamps. The individual arc lines are broad due to the large slit width used in our observations (5.2 arcseconds, or 60 $\AA$), however the Gaussian fits to the lines find the centroid well (This can be seen by comparing the calculated wavelengths of spectral lines to their known wavelengths). Arc spectra from the beginning and end of the exposures were used to take into account any drifts in the wavelength scale. The wavelength calibration was applied using the MOLLY spectral analysis package.

6.5 Flux calibration

The individual spectra on a given night were flux calibrated using exposures taken of the standard star, Feige 67 (Oke 1990), see Figure 6.6. A low order polynomial fit was found to the median of 2000 individual spectra and this calibration was applied using the subroutine FCAL in the analysis package MOLLY. Unfortunately, due to the sudden drop off in the response of the grating used, it was not possible to fit to the standard star below $\sim$ 3600Å, thus reducing our effective wavelength coverage.

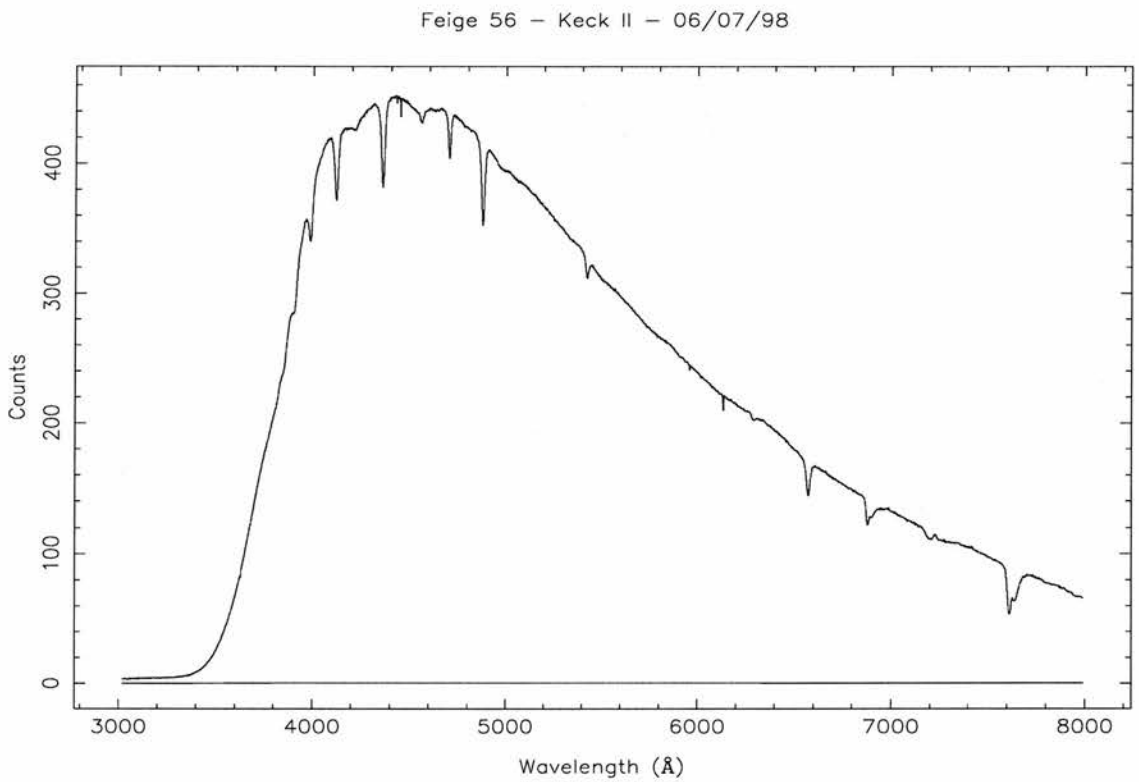

Figure 6.6: A plot of the average spectrum of Feige 67, used to flux calibrate individual spectra.

CHAPTER 7

Methods of analyzing variability

In this chapter I shall describe two methods I have used to characterize the variability in the lightcurves of XRBs. The first of these is the variability spectrum, which is used to describe the spectral shape of the variability, whilst the second is the power spectrum, which I have used to characterize the temporal variability of the systems. When used in conjunction the two methods complement each other. In this way we can constrain the geometry of the varying source. In section 7.1, I will describe the method I have used to create variability spectra which decompose the lightcurves into orthogonally varying components. In section 7.2, I will describe the method I have used to create dynamic power spectra by combining the power spectra of short segments of the data and then recombining them to increase the sensitivity to quasi-periodic signals. This method is described in more detail in the excellent review on Fourier techniques in X-ray timing by van der Klis (1989).

7.1 Variability spectra

The data set can be described as a spectral time-series, $D(\lambda, t)$, with its associated variances, $\sigma^2(\lambda, t)$. In order to recover the spectra of the variability in the time series I have decomposed the spectral time series into suitable components, depending on the type of variability present in the data set. In section 7.1.1 I use a simple linear model, where the variability is assumed to have the spectral shape of the average spectrum. In section 7.1.2 I use a model with an average spectrum and one variable component and finally in section 7.1.3 I use two orthogonal components to isolate two different types of variability present. I have created a fake spectral time series to illustrate the results from the different methods. This fake dataset is created using four Gaussian-shaped line profiles centred at different wavelengths that have different temporal characteristics. The first line profile is constant in time, the second and third vary sinusoidally in time with different periods and the fourth is a mixture of all the previous three components. These synthetic data are then given Poisson noise and Poisson error bars to ensure we obtain realistic values of χ^2 when calculating the badness of fit for the different models.

7.1.1 Average spectrum and lightcurve

The simplest way to decompose the spectral time series is to average over time and wavelength, creating an average spectrum, $\hat{S}$ and an average lightcurve, $\hat{L}$, respectively. In order to achieve optimal weighting of the two components we can use the individual inverse variances to weight the contributions, giving us the optimally weighted average spectrum and average lightcurve,

$$\begin{aligned} S_0(\lambda) &= \frac{\sum_{j=1}^{K} \frac{D(\lambda,t_j)}{\sigma^2(\lambda,t_j)}}{\sum_{j=1}^{K} \frac{1}{\sigma^2(\lambda,t_j)}}, \\ L_0(t) &= \frac{\sum_{i=1}^{N} \frac{D(\lambda_i,t)}{\sigma^2(\lambda_i,t)}}{\sum_{i=1}^{N} \frac{1}{\sigma^2(\lambda_i,t)}}, \end{aligned} \tag{7.1}$$

where N is the number of pixels per spectrum and K is the number of spectra. The model for the spectral time-series, $M(\lambda, t)$, can be represented as a product of these two components,

$$M(\lambda, t) = S(\lambda) L(t) \tag{7.2}$$

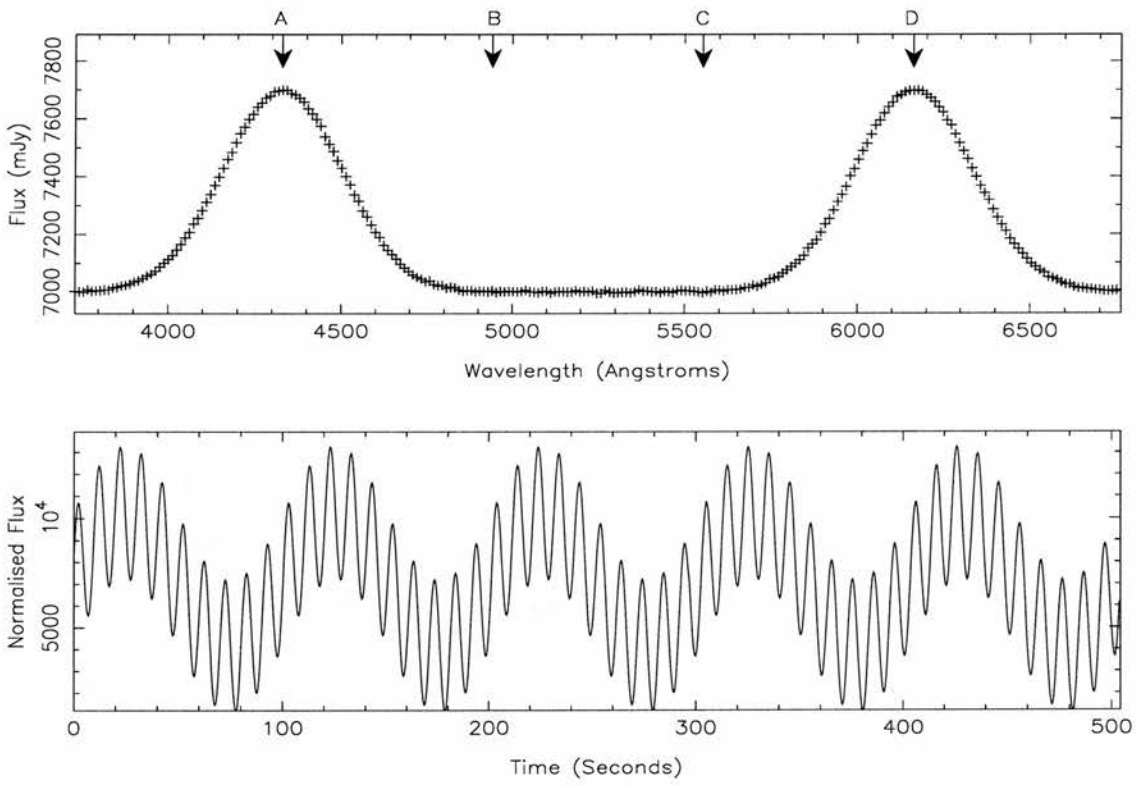

Figure 7.1: The average spectrum and lightcurve for our synthetic data set, showing the line profiles of the first and fourth lines and the total variability.

where S_0 and L_0 are estimates of $S(\lambda)$ and $L(t)$, found using $L(t) = 1$ and $S(\lambda) = 1$ respectively

The results of applying this method to the synthetic data set are shown in Figure 7.1, where two line profiles, labelled A and D, are seen in the spectrum and both variable components are clearly seen in the lightcurve. It is however impossible to determine which part of the spectrum is responsible for the variability and one would be naturally drawn (incorrectly) to say that the source is varying with a spectrum equal to the average spectrum.

The badness of fit between this model and the input data can be calculated using the χ^2 statistic for $(N * K - K - N)$ degrees of freedom,

$$\chi^2 = \frac{\sum_{i=1}^{N} \sum_{j=1}^{K} \frac{(D(\lambda_i,t_j) - M(\lambda_i,t_j))^2}{\sigma^2(\lambda_i,t_j)}}{\sum_{i=1}^{N} \sum_{j=1}^{K} \frac{1}{\sigma^2(\lambda_i,t_j)}} \tag{7.3}$$

7.1.2 The spectrum of the variability

In order to determine the spectrum of the variability and its associated lightcurve I have decomposed the spectral time-series using a number of different models, containing different components. In the first method I have decomposed the spectral time-series into a constant (or 'average') spectrum and a spectrum that represents the total variability, so the model for the spectral time series is

$$M(\lambda, t) = S_0(\lambda) + S_1(\lambda)\,\overline{L_1(t)}. \tag{7.4}$$

The data are once again given optimal weights to reduce the influence of spurious data points affecting the individual components. Using this model the individual components are given by,

$$\begin{aligned}
S_0(\lambda) &= \frac{\sum_{j=1}^{K} \frac{D(\lambda,t_j) - S_1(\lambda)L_1(t_j)}{\sigma^2(\lambda,t_j)}}{\sum_{j=1}^{K} \frac{1}{\sigma^2(\lambda,t_j)}} \\
S_1(\lambda) &= \frac{\sum_{j=1}^{K} \frac{(D(\lambda,t_j) - S_0(\lambda))L_1(t_j)}{\sigma^2(\lambda,t_j)}}{\sum_{j=1}^{K} \frac{L_1(t_j)L_1(t_j)}{\sigma^2(\lambda,t_j)}} \\
L_1(t) &= \frac{\sum_{i=1}^{N} \frac{(D(\lambda_i,t) - S_0(\lambda_i))S_1(\lambda_i)}{\sigma^2(\lambda_i,t)}}{\sum_{i=1}^{N} \frac{S_1(\lambda_i)S_1(\lambda_i)}{\sigma^2(\lambda_i,t)}}.
\end{aligned} \tag{7.5}$$

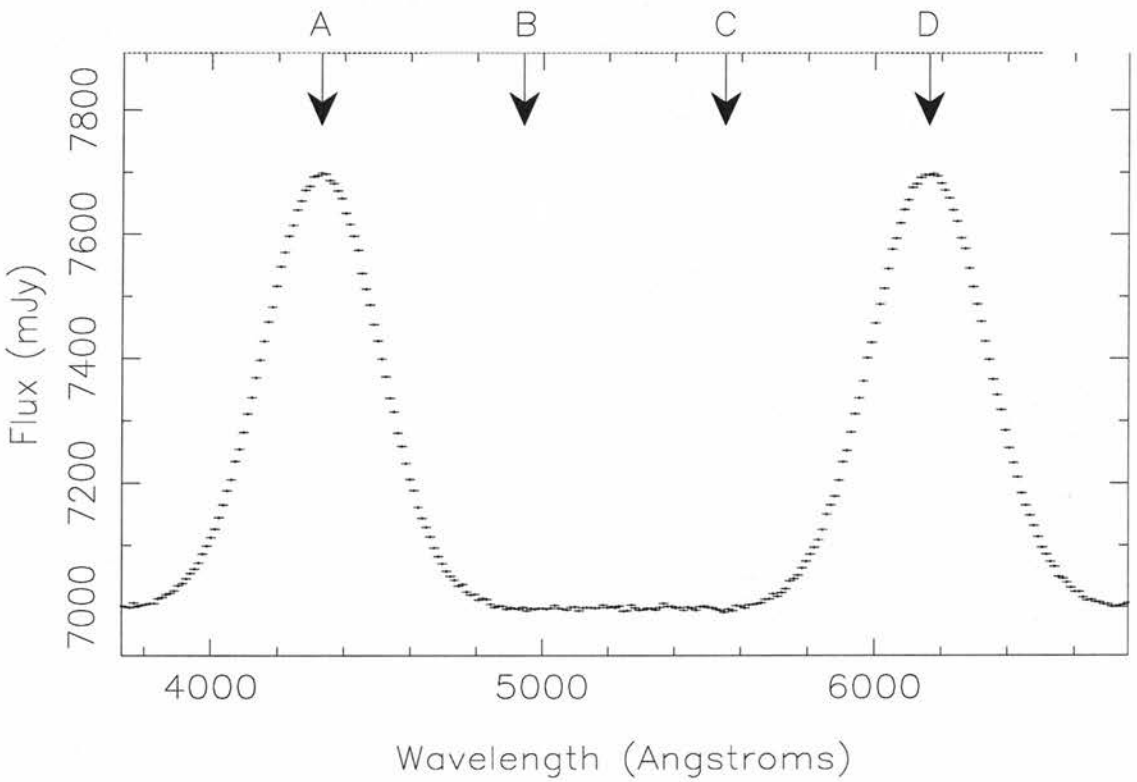

Figure 7.2: The constant spectrum for our synthetic spectral time series, based on a fit with one variability component.

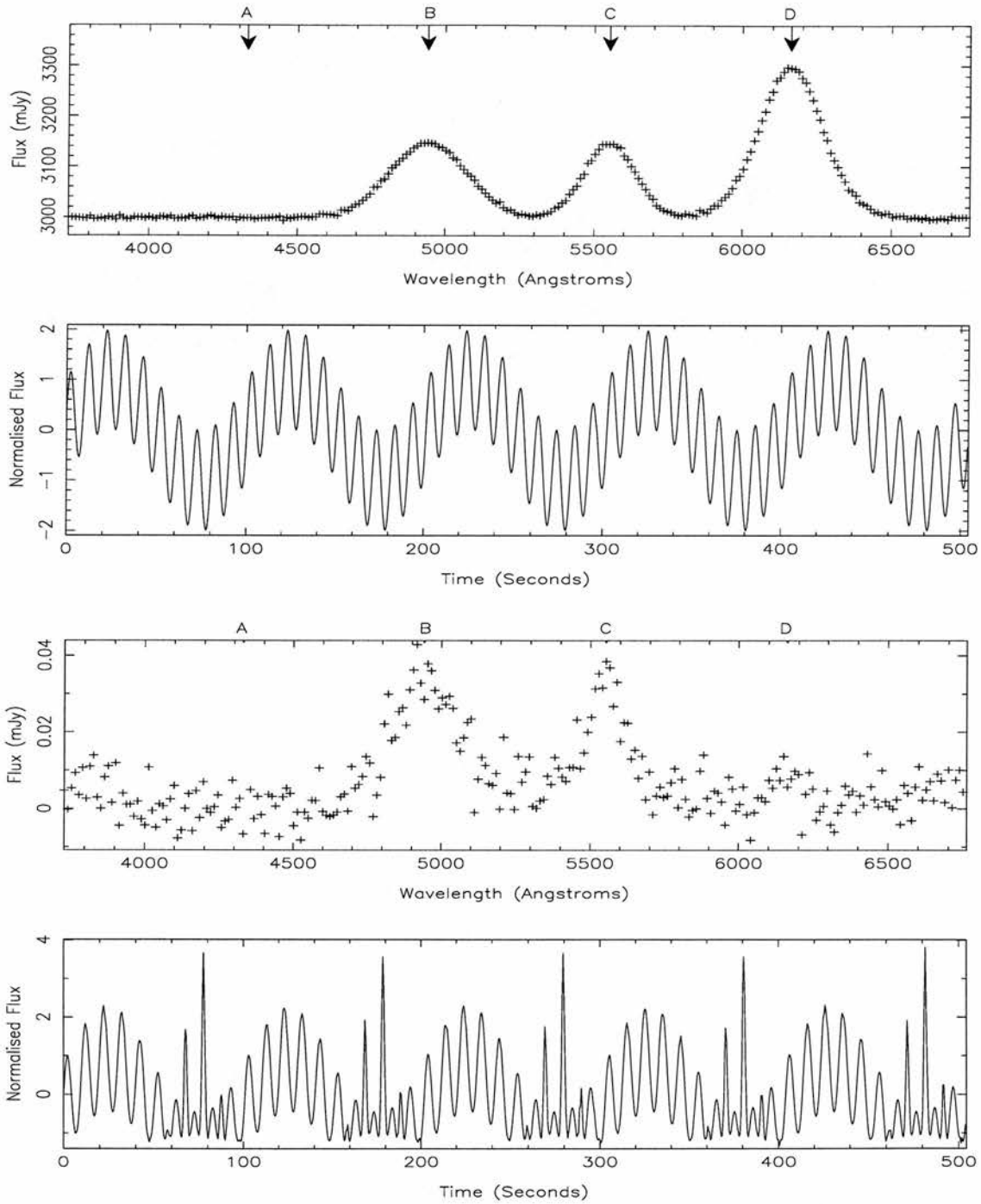

Figure 7.3: Upper two panels, the spectrum and its associated lightcurve for our synthetic spectral time series, showing the line profiles of the second, third and fourth lines and the variability of these components. Lower panels, the average spectrum and lightcurve of the residuals from our synthetic spectral time series.

These expressions can be solved iteratively, evaluating the badness of fit for each iteration until a suitable convergence criterion is reached. A suitable convergence criterion is that the change in the value of the 'reduced χ^2' (the χ^2 per degree of freedom) is less than some critical value. Once the fitting has converged, the residuals are found by subtracting the model from the input data. These residuals are separated into an average spectrum and lightcurve as shown in Figure 7.1.

The results from this decomposition applied to our synthetic spectral time series are shown in Figures 7.2-7.3. Figure 7.2 shown the best-fit constant spectrum which is identical to the average spectrum obtained by the previous method, shown in the upper panel of Figure 7.1. The upper panels of Figure 7.3 show the spectrum and lightcurve of the variable component as defined in Equation 7.5. In this plot the variability is seen in profile B, C and D, whilst profile A is now clearly constant. The lightcurve of this variability is still complicated, showing both periodicities present. The lower two panels of Figure 7.3 shows the residuals of the fit. These residuals are much weaker than the signal detected in the variability spectrum and represent the additional noise due to Poisson statistics.

7.1.3 Orthogonal variable components

If two variable components are present in the lightcurve, the data can be modeled with a further spectrum-lightcurve pair. This model is useful in X-ray binaries to separate the fast and slow components of variability created by different mechanisms. In this case the model spectral time-series is represented by,

$$M(\lambda, t) = S_0(\lambda) + S_1(\lambda)\,\overline{L_1(t)} + S_2(\lambda)\,\overline{L_2(t)}. \tag{7.6}$$

The components of this model are found in the same way as before, by subtracting the components of the model from the real data and fitting a spectrum-lightcurve pair to the residuals. The components are given by,

$$S_0(\lambda) = \frac{\sum_{j=1}^{K} \frac{D(\lambda,t_j) - S_1(\lambda)L_1(t_j) - S_2(\lambda)L_2(t_j)}{\sigma^2(\lambda,t_j)}}{\sum_{j=1}^{K} \frac{1}{\sigma^2(\lambda,t_j)}}$$

$$S_1(\lambda) = \frac{\sum_{j=1}^{K} \frac{(D(\lambda,t_j) - S_0(\lambda) - S_2(\lambda)L_2(t_j))L_1(t_j)}{\sigma^2(\lambda,t_j)}}{\sum_{j=1}^{K} \frac{L_1(t_j)L_1(t_j)}{\sigma^2(\lambda,t_j)}}$$

$$
\begin{aligned}
L_1(t) &= \frac{\sum_{i=1}^{N} \frac{(D(\lambda_i,t)-S_0(\lambda_i)-S_2(\lambda_i)L_2(t))S_1(\lambda_i)}{\sigma^2(\lambda_i,t)}}{\sum_{i=1}^{N} \frac{S_1(\lambda_i)S_1(\lambda_i)}{\sigma^2(\lambda_i,t)}} \\
S_2(\lambda) &= \frac{\sum_{j=1}^{K} \frac{(D(\lambda,t_j)-S_0(\lambda)-S_1(\lambda)L_1(t_j))L_2(t_j)}{\sigma^2(\lambda,t_j)}}{\sum_{j=1}^{K} \frac{L_2(t_j)L_2(t_j)}{\sigma^2(\lambda,t_j)}} \\
L_2(t) &= \frac{\sum_{i=1}^{N} \frac{(D(\lambda_i,t)-S_0(\lambda_i)-S_1(\lambda_i)L_1(t))S_2(\lambda_i)}{\sigma^2(\lambda_i,t)}}{\sum_{i=1}^{N} \frac{S_2(\lambda_i)S_2(\lambda_i)}{\sigma^2(\lambda_i,t)}}.
\end{aligned}
\tag{7.7}
$$

In order to solve these equations we solve first for the first spectrum-lightcurve pair, S_1, L_1, using the input constant spectrum, S_0, as in the previous section. Once this has reached a suitable convergence criterion, these are used as inputs to solve for the second spectrum-lightcurve pair, which are again solved iteratively until a convergence criterion is reached. This will in turn affect the best-fit first spectrum-lightcurve pair, so it is necessary to repeat the first loop. This can then be iterated until a global criterion is reached. In our case we require the changes to both spectrum-lightcurve pair to be less than a suitable threshold.

The results from this method applied to our synthetic spectral time series are shown in Figures 7.4-7.5. Figure 7.4 shows that the constant spectrum is again well defined and equal to that from the first method. The upper two panels of Figure 7.5 show the spectrum-lightcurve pair of the first variable component, whilst the lower two panels show the second spectrum-lightcurve pair. These plots show that the component, C, is detected in the second spectrum-lightcurve pair, but that the lightcurve contains a beat frequency between the two fundamental frequencies of the variable components.

One further step to determine the different components of the variability is to separate the components using a suitable high-pass filter on the variability lightcurve, thus ensuring the lightcurve represents the slowly varying components. If applied to the first spectrum-lightcurve pair this forces the second spectrum-lightcurve pair to represent any fast variability orthogonal to this. If the filter is applied to the second spectrum-lightcurve pair this limits the range of possible frequencies present in the lightcurve. If applied to the second spectrum-lightcurve pair this allows any white noise component to be removed.

The filter applied was a Savitzky-Golay filter, see Press et al. (1992), which was chosen over a simple running mean filter since it retains higher moments of the data.

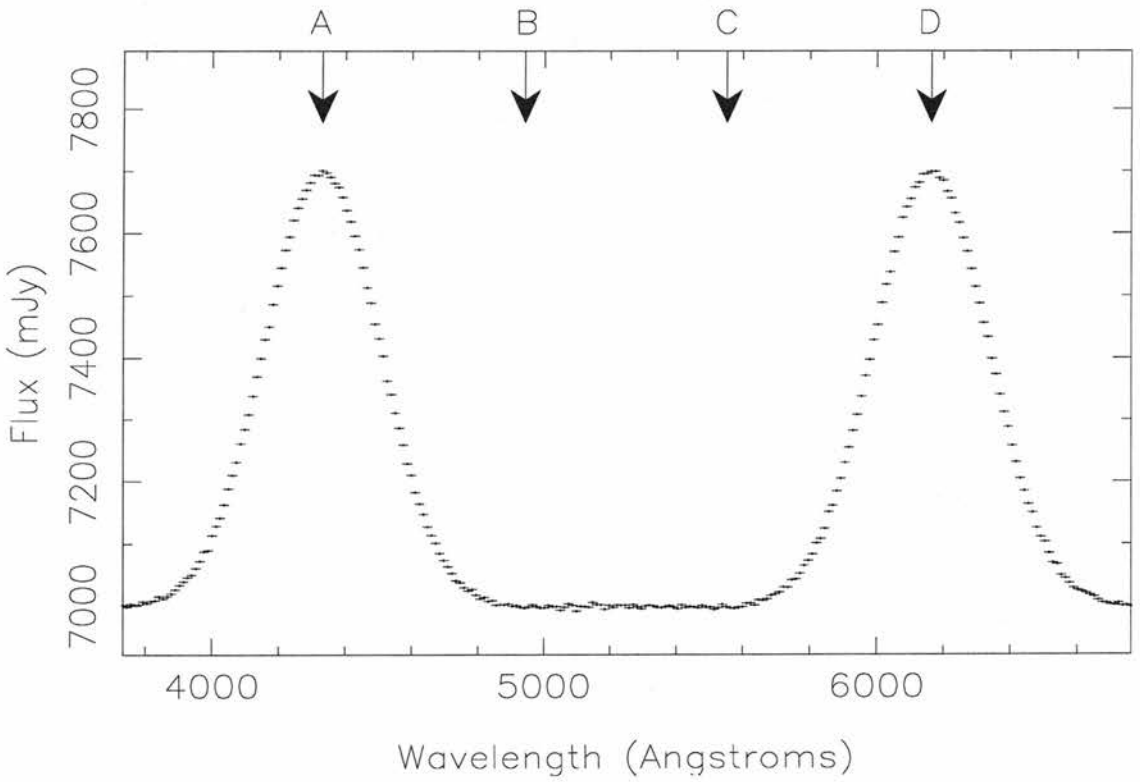

Figure 7.4: The constant spectrum for our synthetic spectral time series, based on a fit with one variability component.

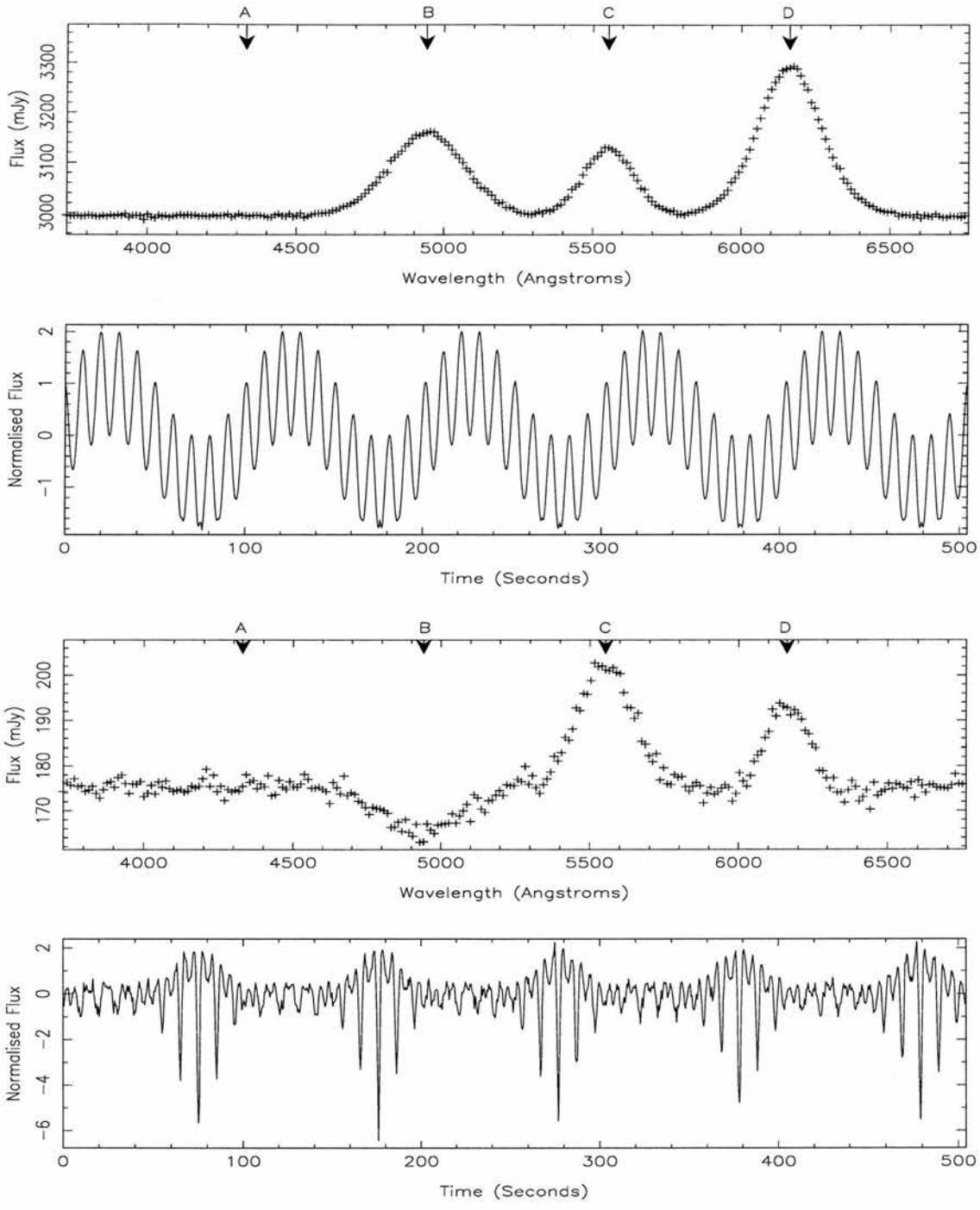

Figure 7.5: Upper panels, the spectrum and its associated lightcurve for our synthetic spectral time series, showing the line profiles of the second, third and fourth lines and the variability of these components. Lower panels, the average spectrum and lightcurve of the residuals from our synthetic spectral time series.

Since the filter is applied to the lightcurve on each iteration this data is important. The Savitzky-Golay filter conserves the required frequencies present in the lightcurve well. The filter effectively fits a polynomial to the data, the inputs are the widths, the order and the number of data points present in the lightcurve. It assumes that the data points are equally spaced in time, which is a reasonable assumption in the case of our data. One further filtering method employed is to coarsely detrend the data with a low-order polynomial fit to the first variability lightcurve. This will remove any factors, such as the orbital motion of the binary, from affecting the first variability spectrum.

When applied to our synthetic spectral time series, the individual components were separated very well. This is shown in Figures 7.6-7.7. In Figure 7.6 the constant spectrum is shown as before. The top panels in Figure 7.7 show the spectrum-lightcurve pair for the first component of the variability. This component has been filtered using a filter width of 40, to remove the fast variability. This fast variability is fitted using the second spectrum-lightcurve pair and the results are shown in the lower two panels of Figure 7.7. The spectra of the two variable components are clear and well separated. The reason for the slight deviations at the beginning and end of the second lightcurve is the filter.

This method including filtering the data set was found to be very useful when trying to find the spectrum of the quasi-periodic oscillation in Hercules X-1, see chapter 9.

These methods were implemented as a subroutine, called VARSPEC, in the MOLLY spectral data analysis package, which allowed the number of variable components to be set as well as the width of the filters applied and any detrending involved.

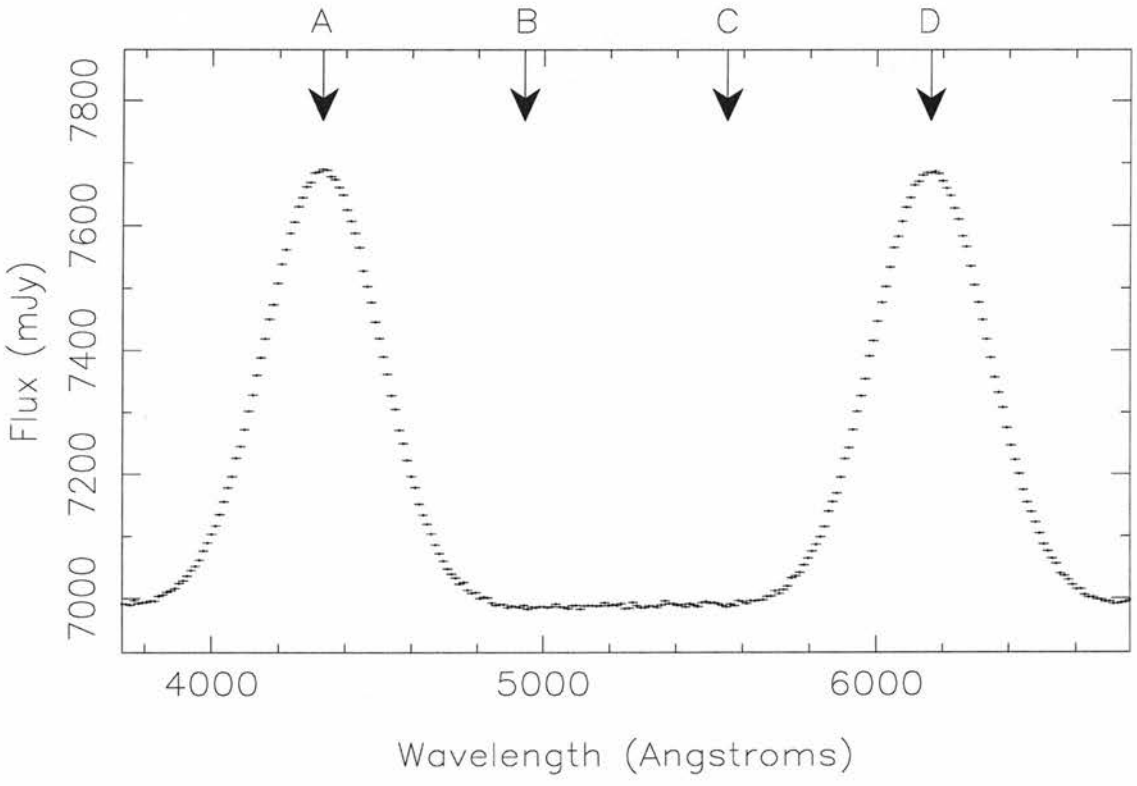

Figure 7.6: The constant spectrum for our synthetic spectral time series, based on a fit with one variability component.

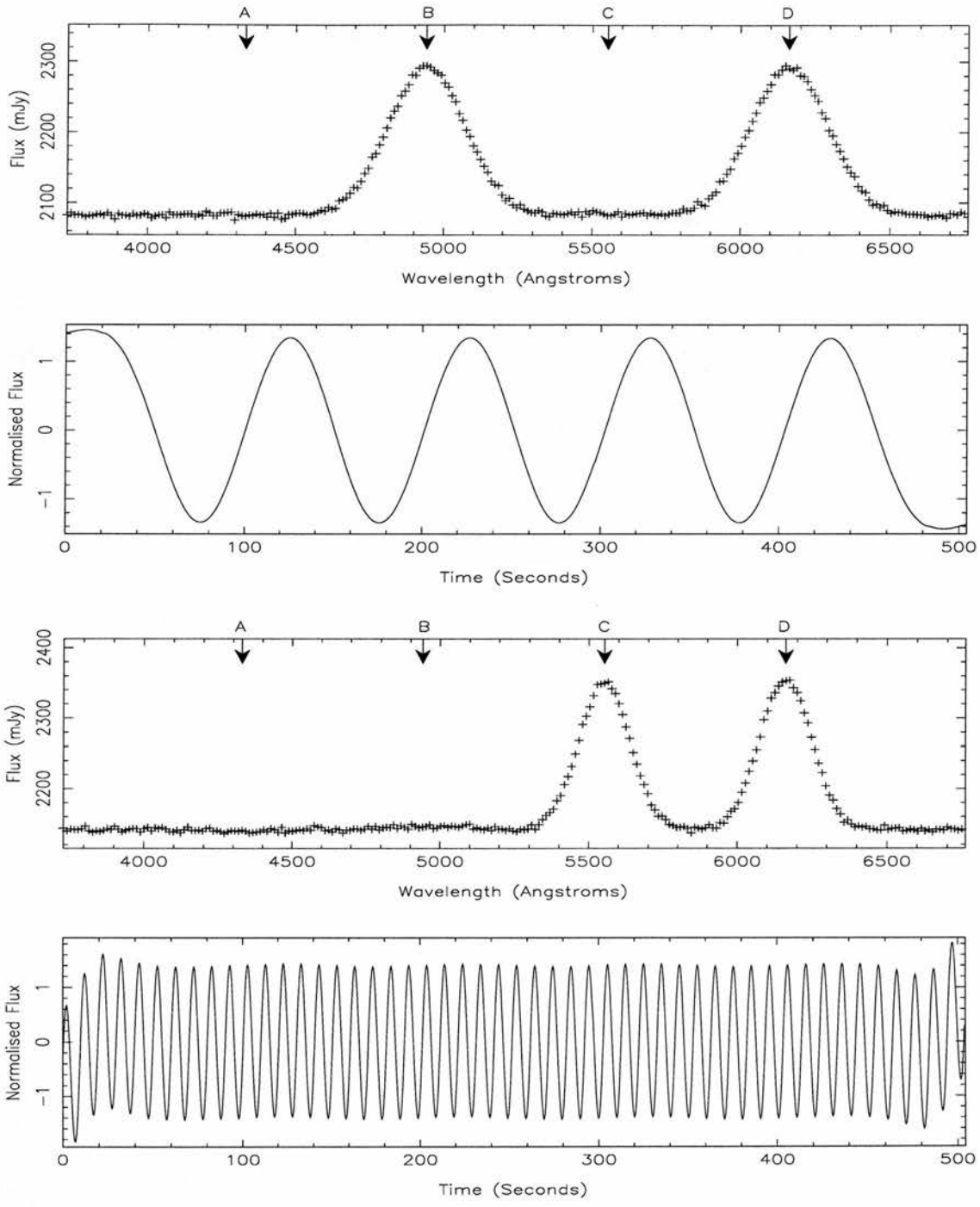

Figure 7.7: The spectrum and its associated lightcurve for our synthetic spectral time series, showing the line profiles of the second, third and fourth lines and the variability of these components. The average spectrum and lightcurve of the residuals from our synthetic spectral time series.

7.2 Power spectra

7.2.1 Fourier transform

Any lightcurve, $x(t)$, can be described as a sum of an infinite number of sine waves with different frequencies, ω, and suitable weights. Thus the lightcurve can be written as the summation of these sine waves over the range of frequencies,

$$x\,(t) = \frac{1}{N}\sum_{j}(A_j\,\cos\omega_j t + B_j \sin\omega_j t). \tag{7.8}$$

The coefficients A_j and B_j, known as the Fourier coefficients, represent the correlation coefficient between the input lightcurve and a synthetic lightcurve, based on Equation 7.8. These can therefore be written as,

$$\begin{aligned} A_j &= \sum_{k} x_k \cos\omega_j t_k \\ B_j &= \sum_{k} x_k \sin\omega_j t_k, \end{aligned} \tag{7.9}$$

where $x_k = x\,(t_k)$. The Fourier coefficients can also be described using complex number notation, ie.

$$\begin{aligned} a_j &= \sum_{k} x_k \exp\left(i\omega_j t_k\right) \\ x_k &= \frac{1}{N}\sum_{j} a_j \exp\left(-i\omega_j t_k\right), \end{aligned} \tag{7.10}$$

where a_j is now a complex number representing the Fourier coefficients for the frequency ω_j,

$$a_j = A_j + iB_j. \tag{7.11}$$

The Fourier amplitude is given by the modulus, $|a_j|$, and the Fourier phase by the argument, $arg(a_j)$.

7.2.2 Discrete Fourier transform

In the previous section no limits, such as sampling and duration, were placed on the lightcurve. We will now consider a more realistic case where the lightcurve is defined as a series of N data points. The lightcurve, $x_k\,(k = 0, ..., N-1)$ can then be described as a

sum of N sine waves, using the discrete Fourier transform coefficients, a_j ($j = -N/2, ..., N/2-1$). If the lightcurve is evenly sampled the the lightcurve-transform pair becomes

$$\begin{aligned} a_j &= \sum_{k=0}^{N-1} x_k \exp(2\pi ijk/N) \\ x_k &= \frac{1}{N} \sum_{j=-N/2}^{N/2-1} a_j \exp(-2\pi ijk/N), \end{aligned} \tag{7.12}$$

where $t_k = kT/N$ and T is the length of the time-series. In this case the Fourier frequencies are evenly spaced. There are several methods for calculating the Fourier coefficients, including the fast Fourier transform (FFT). The FFT is most successful on evenly sampled data and $N >> 1$.

Due to the existence of gaps in our optical data set, the method I have chosen to employ is simple sine wave fitting, see section 7.2.3. This method allows us to use not only the data points but also the individual variances on the data points to optimally weight the contribution of each data point. This method also allows us to calculate an individual variance for each Fourier coefficient, as well as the phase of the variability.

7.2.3 Not-quite-so-fast Fourier transform

This method uses optimal scaling of a sine wave to fit the input lightcurve to determine the best fit Fourier coefficients. The amplitude and its variance are calculated iteratively using the expressions,

$$\begin{aligned} A_j^{new} &= A_j^{old} + \frac{\sum_{k=0}^{N-1} \frac{(x_k - M_k)\cos\omega_j t_k}{\sigma_k^2}}{\sum_{k=0}^{N-1} \frac{\cos^2\omega_j t_k}{\sigma_k^2}} \\ B_j^{new} &= B_j^{old} + \frac{\sum_{k=0}^{N-1} \frac{(x_k - M_k)\sin\omega_j t_k}{\sigma_k^2}}{\sum_{k=0}^{N-1} \frac{\sin^2\omega_j t_k}{\sigma_k^2}} \end{aligned} \tag{7.13}$$

$$\begin{aligned} \sigma^2(A_j) &= \frac{1}{\sum_{k=0}^{N-1} \frac{\cos^2\omega_j t_k}{\sigma_k^2}} \\ \sigma^2(B_j) &= \frac{1}{\sum_{k=0}^{N-1} \frac{\sin^2\omega_j t_k}{\sigma_k^2}}, \end{aligned} \tag{7.14}$$

where the model, M_k is given by

$$M_k = \sum_{j=0}^{N-1} (A_j^{old}\cos\omega_j t_k + B_j^{old}\sin\omega_j t_k). \tag{7.15}$$

7.2.4 Leahy power spectrum

If the noise in a lightcurve is dominated by photon statistics, as is the case with data from the PCA onboard *RXTE*, then the power spectrum for the lightcurve can be normalized following the method described by Leahy et al. (1983),

$$P_j = \frac{2}{a_0}|a_j|^2, \tag{7.16}$$

where $j = 0, ..., N/2$ and $a_0 = N_{ph}$, the total number of photons in the lightcurve. This results in a power spectrum that is represented by a χ^2 statistic with 2 degrees of freedom.

7.2.5 Flux power spectrum

If the noise in a lightcurve is not only determined by the number of photons, but is calibrated in some other units then we can use a flux calibrated power spectrum. This is the case when using optical data where the noise model has contributions from not only photon statistics but also from the read-out noise. In this case the simple sine-wave fitting to flux calibrated lightcurves produces power spectra with units of mJy^2/Hz.

CHAPTER 8

Timing analysis of X-ray and optical variability in Cygnus X-2

Cygnus X-2 is one of the best studied Low Mass X-ray Binaries (LMXBs) due to its X-ray variability and observable optical counterpart. Cygnus X-2 is a close binary comprising a 1.78 $M_{\odot}$ neutron star in a 9.84 day binary orbit with a 0.6 $M_{\odot}$ companion star (Orosz & Kuulkers 1999). Since its discovery in 1965 (Bowyer et al. 1965) there have been a host of observations in the optical (eg. van Paradijs et al. (1990)), ultraviolet (eg. Vrtilek et al. (1990)) and X-ray (eg. (Kuulkers, van der Klis & Vaughan 1996)) wavebands. The optical counterpart of Cygnus X-2, V1341 Cygni, has been shown to have a spectral type A9III and to contribute about 50% of the total visual flux (Casares, Charles & Kuulkers 1998). The reprocessing of X-rays in Cygnus X-2 is shown in the contribution to the UV continuum and emission line flux, predominantly from the X-ray heated accretion disk.

Cygnus X-2 belongs to the sub-class of LMXBs know as Z-sources, where the X-ray spectra trace a Z shape pattern in the colour-colour diagram, CD (see Hasinger & van der Klis (1989)). The source is seen to move smoothly along the branches of the Z-curve, from the Horizontal Branch (HB), through the Normal Branch (NB) and onto the Flaring Branch (FB) as the mass accretion rate increases (Hasinger & van der Klis 1989). The position of the Z in the CD and the shapes of the HIDs also vary smoothly on a timescale of weeks (Kuulkers, van der Klis & Vaughan 1996). During this time Cygnus X-2 varies between three levels; a high, medium and low level. While the low level is rare, the system appears to move slowly between the medium and high intenisty levels. This can be seen in the *RXTE* ASM lightcurve, a section of which is shown in Figure 8.1. The source can be seen to move slowly between the medium level, with a count rate of $\sim$ 30 and the high state where the count rate $\sim$ 50. However large deviations from these levels can be seen,

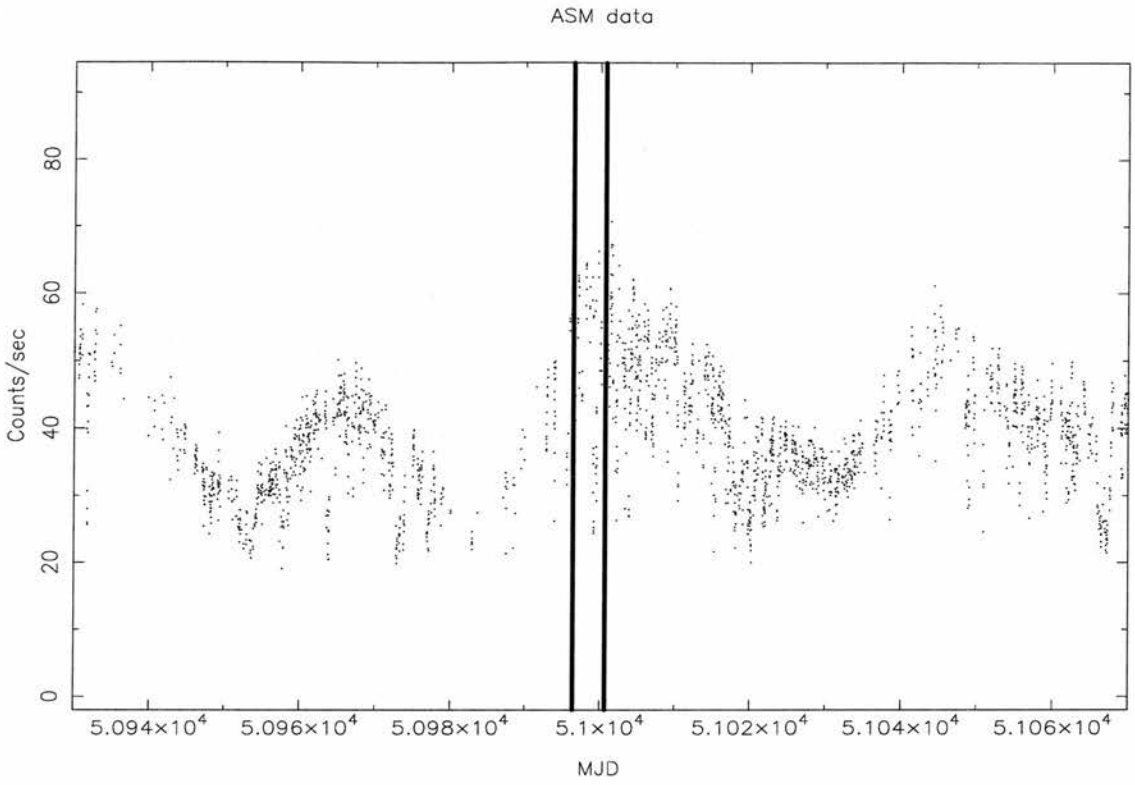

Figure 8.1: The RXTE All Sky Monitor lightcurve for Cygnus X-2. The vertical lines show the beginning and end of the Keck and RXTE observations used in our analysis.

which are caused by motion along the Z-curve.

The CD and HIDs for the different states are very different. In the High state the hard colour intensity diagram shows virtually horizontal Normal and Flaring Branches, whilst in the medium level the branches are more curved and the Flaring Branch intensity varies smoothly with the X-ray intensity. The Flaring Branch is also truncated during the High level, which is thought to be due to obscuration by material in the binary. This is most noticable during the Flaring Branch as it coincides with the highest mass accretion rate. In this chapter I will discuss how we have used the X-ray and optical variability along the Z-curve to investigate the accretion flow on timescales of seconds to hours.

The characteristics of the QPOs found at various places on the Z-curve also tell us something about the different branches. On the Horizontal Branch, QPOs are found (called HBOs) with a frequency of 12Hz at the end of the Horizontal Branch. These increase in frequency as the source moves along the Horizontal Branch, reaching 55 Hz at

the hard vertex (S_z=1) and then remaining constant until arond halfway along the Normal Branch (S_z= 1.5), where they cease. In contrast the Flaring Branch oscillation (FBO), which has yet to be observed in Cygnus X-2, is first observed in other Z-sources around halfway along the Normal Branch and increases in both frequency and power towards the Flaring Branch. The HBO and FBO are thought to be due to different phenomena as they are observed to coexist in some sources.

Cygnus X-2 is one of the LMXBs that exhibit Type I X-ray bursts, confirming the existence of a neutron star, as seen in GX17+2 (Kahn & Grindlay (1984),Kuulkers et al. (1997)). These bursts typically have rise times of 1-10 seconds and are thought to be due to thermonuclear burning of accreting material on the surface of the neutron star (Smale 1998). There is also tentative evidence for a third periodicity in Cygnus X-2 with a period of 78 days, although the interpretation of this is complicated by the changes in X-ray flux as Cygnus X-2 moves around the CD. Wijnands, Kuulkers & Smale (1996) associate this periodicity with that of a precessing accretion disk, as seen in Hercules X-1 (Giacconi et al. 1973).

8.1 Data

The data were taken between the nights of UT 01/07/98 and UT 06/07/98 as part of our campaign to search for correlated optical and X-ray variability in X-ray binaries. In this chapter I will concentrate on selected X-ray and optical data from the full dataset. This is due to the size of the full dataset and the existence of an intermittent problem with the calibration of the optical data during the first four nights. Hence, I will concentrate on the optical data from the last night of our observations, although I will show a small subset of the optical observations from the first night of observations that do not suffer from the calibration problem. When dealing with the X-ray spectral variability in section 8.2 I will use the whole X-ray dataset.

File	K4005	K4007	K4009	K4011
Number of Spectra	20230	53950	51940	23840
Bin Factor	7	7	7	7
Start Time	76110	79405	85286	92016
Elapsed Time	14600	3890	3746	1710

Table 8.1: Summary of the Keck II optical observations. The start time is the number of seconds since HJD 2451000. The Bin factor of 7 gives an integration time of 0.504 seconds for the resulting lightcurves.

8.1.1 Optical data

The optical data were taken using the Low Resolution Imaging Spectragraph (LRIS) on the 10-m Keck II telescope on Mauna Kea, Hawaii (see chapter 6 for more details on the telescope set-up, etc). We used a novel data system, the Gomerizer (see chapter 6 for details), to obtain more than 165,000 2048-pixel spectra of Cygnus X-2. Each spectrum has a mean integration time of 72.1 msecs. There is 11 ksec of *RXTE* data simultaneous with the optical observations, split into 5 *RXTE* orbits, separated by gaps when Cygnus X 2 was occulted by the earth.

8.1.2 X-ray data

The X-ray data were taken with the PCA onboard the *RXTE* satellite. It contains 114 ksec of data taken over 5 nights between 1-6 July 1998. The data were analysed using the FTOOLS software. The B_2MS_16_0_35_Q mode data, containing 16 energy channels in the range 1.71 - 13.1 keV, were used with a time resolution of 16 seconds to create colour-colour and hardness-intensity diagrams, and with a time resolution of 4 seconds for studying the fast simultaneous variability. These were extracted in 4 energy ranges, using the channels 0-8, 9-13, 14-21 and 22-35. This corresponds to 1.71 - 3.17 keV, 3.17 - 5.37 keV, 5.37 - 8.31 keV and 8.31 - 13.1 keV. The minimum count rate of 4000 counts/sec shows that background subtraction is not necessary. At these levels the background accounts for ~ 2

8.2 The X-ray spectral variations in Cygnus X-2

The broadband X-ray spectral variations of Z-sources are clearly shown in an X-ray colour-colour diagram. The colour-colour diagram from our *RXTE* observation is shown in Figure 8.2. The soft colour is defined as the logarithm of the ratio of the intensities in the ranges 1.71 - 3.17 keV and 3.17 - 5.37 keV. The hard colour is the logarithm of ratio of the intensities in the ranges 5.37 - 8.31 keV and 8.31 - 13.1 keV.

Cygnus X-2 can clearly be seen to trace out all three branches of the Z-curve, beginning on the Horizontal Branch during the first two nights, then moving onto the Normal Branch during the third night and finally onto the lower Normal Branch and the Flaring Branch during the fourth and fifth nights. As motion along the 'Z' is thought to be due to changes in the mass accretion rate, we infer that $\dot{M}$ increases from night to night.

The hardness intensity diagrams (HIDs), which plot the colour changes as a function of intensity show that the hard colour varies smoothly with intensity whilst on a given branch, as expected from previous observations of the source. The transition between the NB and the FB, referred to as the soft vertex, is clearly seen, but the HB to NB transition region, referred to as the hard vertex, is not covered in any of our observations.

The soft colour HID also shows a linear trend on the horizontal and normal branches. This is interpreted as changes in the X-ray production mechanism as a function of the increasing mass accretion rate. The soft colour hardness intensity diagram deviates from the expected linear relationship whilst on the flaring branch. This can be seen as deviations from the expected Z-curve, which is plotted over the data in Figure 8.2. These deviations are clearly seen in the lightcurve of the data, as strong dips, where the X-ray intensity drops by almost 40% from the expected level, see Figure 8.5.

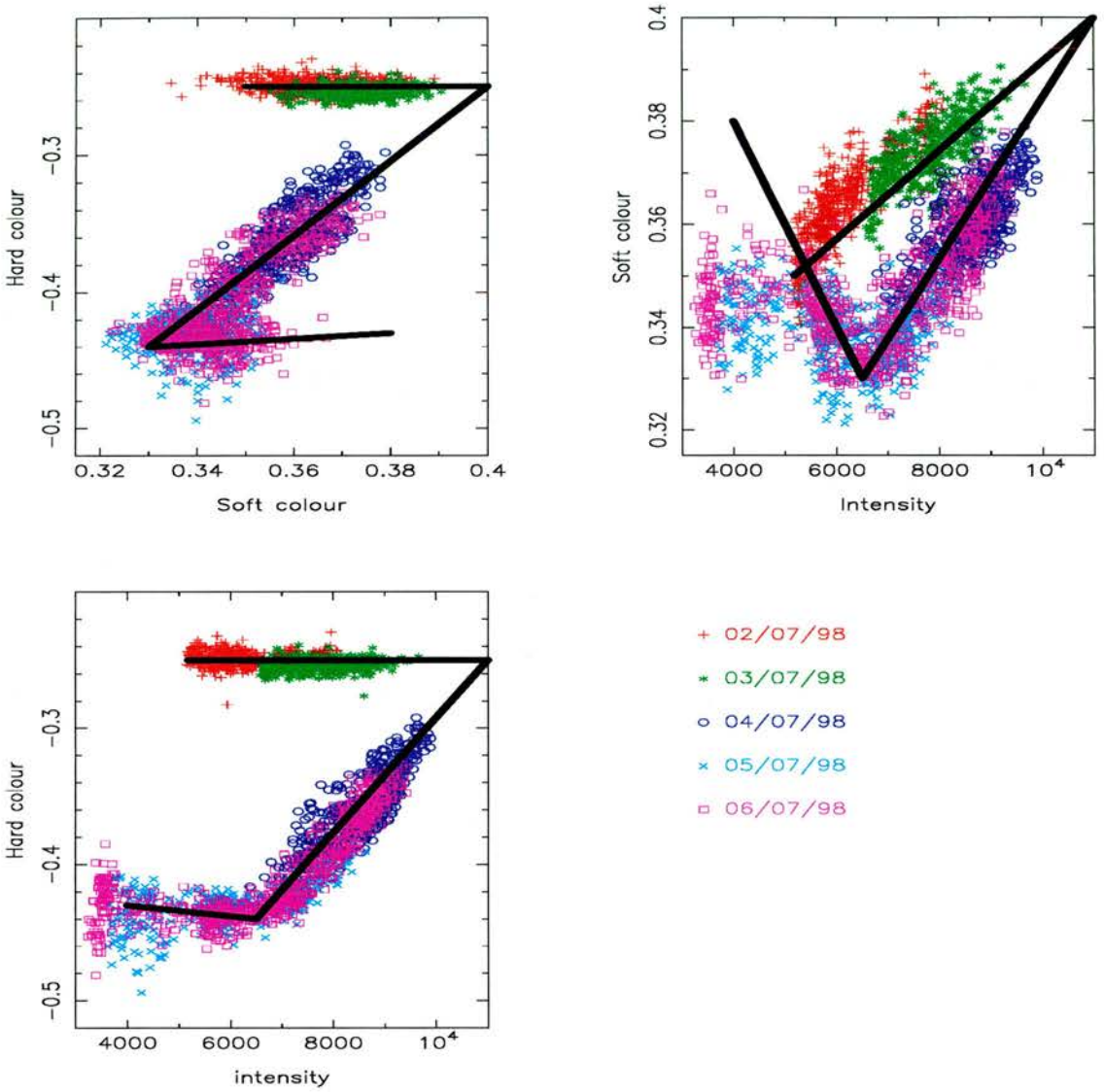

Figure 8.2: Top left, Colour-Colour diagram for Cygnus X-2, based on the *RXTE* PCA data between UT 01/07/98 - 06/07/98. The data is taken from the B_2ms_16_0_35_Q mode, with a time resolution of 16 seconds. The soft colour is logarithm of the ratio of the intensities in the ranges 1.71 - 3.17 keV and 3.17 - 5.37 keV. The hard colour is the logarithm of the ratio of the intensities in the ranges 5.37 - 8.31 keV and 8.31 - 13.1 keV. The coloured symbols represent different nights of data, shown in the key. Bottom left, the hardness intensity diagram for the hard colour and the total intensity. Top right, the hardness intensity diagram for the soft colour and the total intensity. The black line is the fit to the 'Z' curve, used to calculate the rank number S_z.

8.3 The correlations between the X-ray and optical data

Figure 8.5 shows that the optical flux is only weakly correlated, if at all with the colour variations. This relationship is shown in Figure 8.3. The soft vertex is clearly seen at an optical flux of $\sim$ 5.3 mJy. Whilst the soft colour varies smoothly with optical flux, the hard colour shows similar behaviour until the optical flux reaches 5.9 mJy, and then the hard colour begins to drop again.

The overall X-ray intensity versus optical flux for the lower NB and FB data, shown in Figure 8.3, shows surprising behaviour. The overall anti-correlation is clearly visible, but the X-ray flux appears to be bounded by two limits. Whilst the upper limit varies smoothly with optical intensity, the lower limit changes from one slope to another as Cygnus X-2 moves through the soft vertex. There is also evidence for a lower limit to the X-ray intensity, possible due to a scattered component, which varies with S_z (or equivalently the optical flux). Deviations outside this envelope occur, as the X-ray intensity appears to be reddened by excess material. During these dips the optical flux shows no similar behaviour. Interestingly during the dips the X-ray flux drops to the observed lower intensity bound, possible meaning the direct line of sight to the neutron star is obscured and the remaining flux is due solely to a scattered component.

Similar reddening is observed at the end of the horizontal branch, where the soft colour changes with no drop in intensity. Intriguingly this intensity level is different to that observed during the FB dips. This is shown in Figure 8.3. Indeed we do see that the correlated X-ray and optical behaviour is similar to that on the flaring branch, the X-rays drop to a minimum level while the optical continues to go down. Both the X-ray and optical variability is much reduced on the Normal branch and this is shown by the narrower range of the envelope in the Figure 8.3.

If we assume that the optical flux is directly proportional to S_z, (Hirano et al. 1995) we can recreate the optical flux versus intensity diagram without the optical data. From our observations we know that at S_z=1.5 the opt=4.3 and at S_z=2 opt = 5.3. Using this we can trace the mean X-ray flux versus S_z from the soft HID. This can then be plotted against S_z. The turn over in the HB in the soft HID tells us that the lower bound on the

variability crosses the 'scattered light limit' when the X-ray intensity is ~ 5000 and $S_z \sim 0.1$.

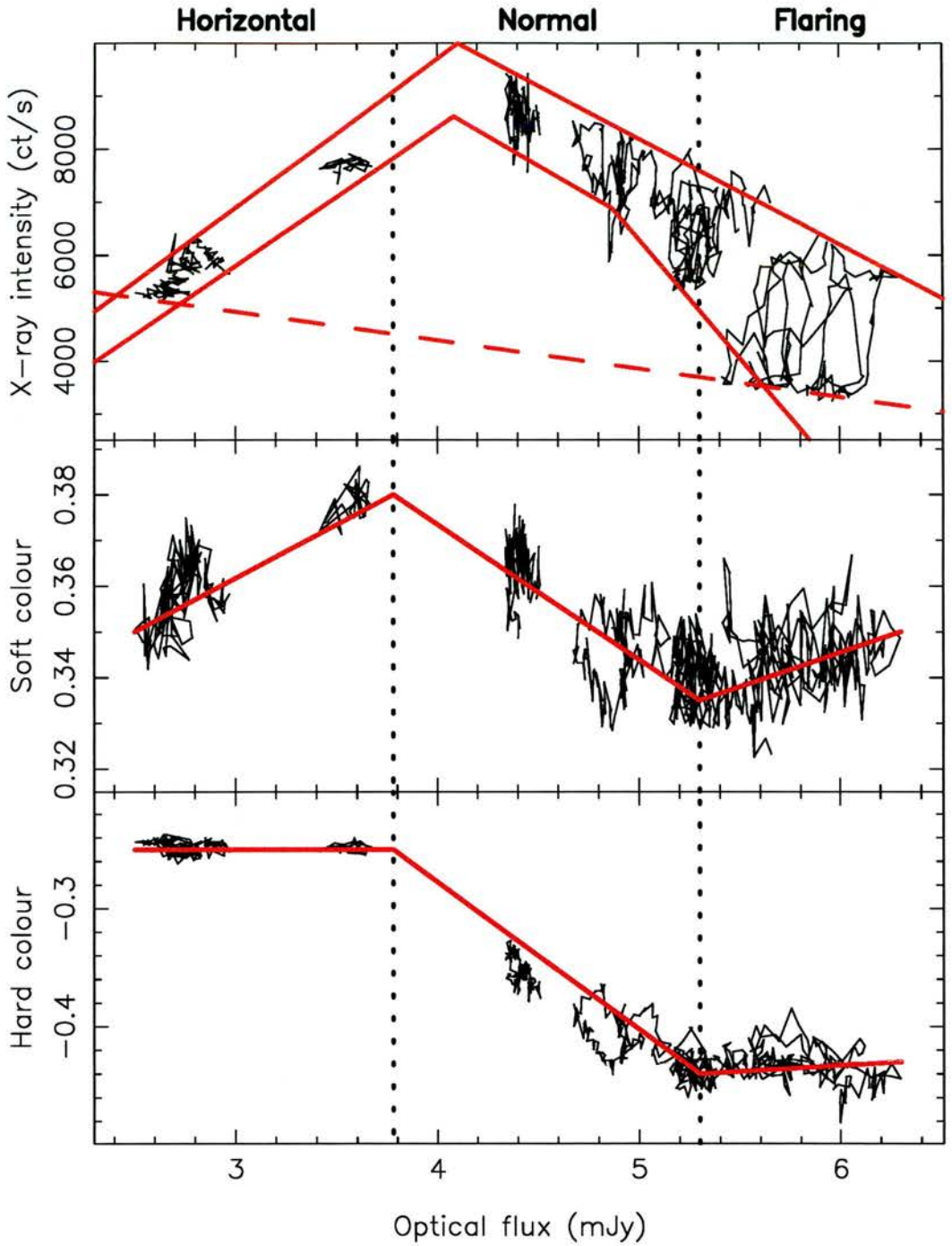

Figure 8.3: Top panel, a plot of the X-ray versus optical flux. Middle and bottom panels, X-ray soft and hard colours, respectively, versus optical flux, taken from the simultaneous observations of Cygnus X-2 on the first and fifth nights. The time resolution is 16 seconds. The thick line represents a fit to the data taken from the best-fit model to the Z-curve. The dashed vertical lines show the inferred positions of the soft and hard vertices.

8.4 The simultaneous X-ray and optical variability in Cygnus X-2

In this section I will describe how we have used the simultaneous X-ray and optical observations to try to determine a model for the Z-curve that fits the data. I will begin by describing the overall features seen in the lightcurves, then I will concentrate on individual data 'windows', which represent orbits of the *RXTE* satellite. In the final section, I will describe the correlated variability before summing up what we have learned about the system from the simultaneous observations.

8.4.1 General features of night 5, UT 05-06/07/98

In Figure 8.4, the colour-colour and hardness-intensity diagrams are shown for the 5 RXTE visits on UT 06/07/98. At the beginning of the night Cygnus X-2 is on the Flaring Branch and during the night moved off the Flaring and onto the Normal Branch, finishing approximately half way between the soft and hard vertices ($S_z \sim$ 1.5). The hard HID is characteristic of the high state HID described by Kuulkers, van der Klis & Vaughan (1996), exhibiting an almost horizontal FB in the Hard colour HID. Significant deviations from the assumed linear relationships in the HIDs are clearly seen. These appear to be caused by absorption, which causes the X-ray flux to drop to a low level floor in the X-ray flux.

The overall X-ray intensity is surprisingly anti-correlated with the optical flux, as shown in Figure 8.5. The behaviour appears to be well correlated with S_z. If the optical light was dominated by reprocessing one would expect to see a strong positive correlation between the optical and X-ray intensities. We can infer that not all the observed X-ray flux is reprocessed into optical emission. We suspect, this is due to a difference between the observed X-ray flux and that seen by the reprocessing regions.

Window 1, UT 21:08 - 21:27

The simultaneous observations for the First *RXTE* window on night 5 of the observations are shown in Figure 8.6. During this window Cygnus X-2 remained on the FB, showing

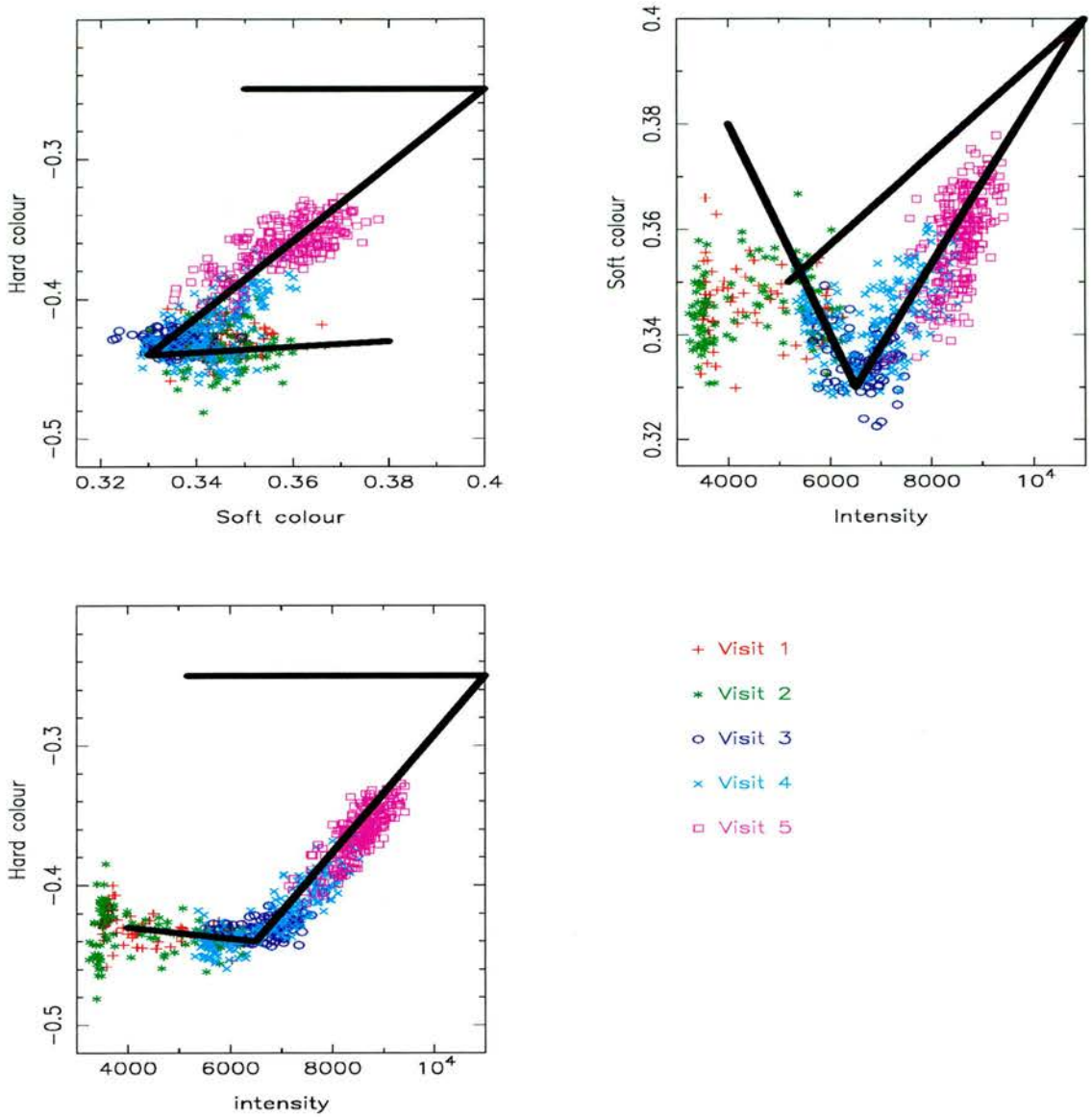

Figure 8.4: Top left, Colour-Colour diagram for Cygnus X-2, based on the *RXTE* PCA data on UT 06/07/98. The data is taken from the B_2MS_16_0_35_Q mode, with a time resolution of 16 seconds. The soft colour is logarithm of the ration of the intensities in the ranges 1.71 - 3.17 keV and 3.17 - 5.37 keV. The hard colour is the logarithm of the intensities in the ranges 5.37 - 8.31 keV and 8.31 - 13.1 keV. The coloured symbols represent different visits, shown in the key. Bottom left, The hardness intensity diagrams for the hard colour and the total intensity. Top right, The hardness intensity diagrams for the soft colour and the total intensity. The black line is the fit to the 'Z' curve found in the previous section

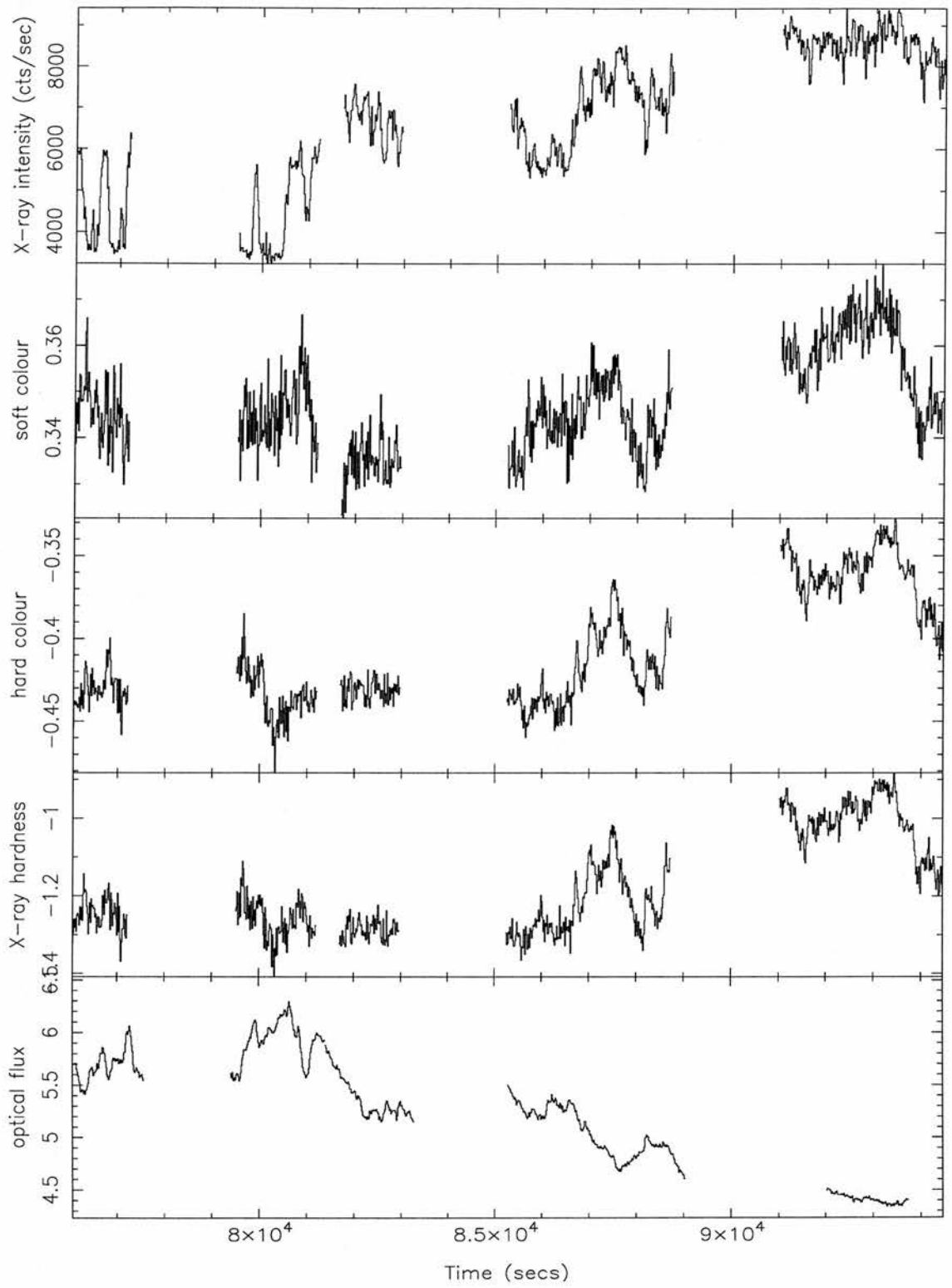

Figure 8.5: Top panel, the total X-ray intensity during the 5 RXTE visits from night 5, upper middle, the soft colour variations, middle, the Hard colour variations. Lower middle, the overall hardness. Bottom panel, the optical continuum flux in the range 5000 - 5800 $\AA$.

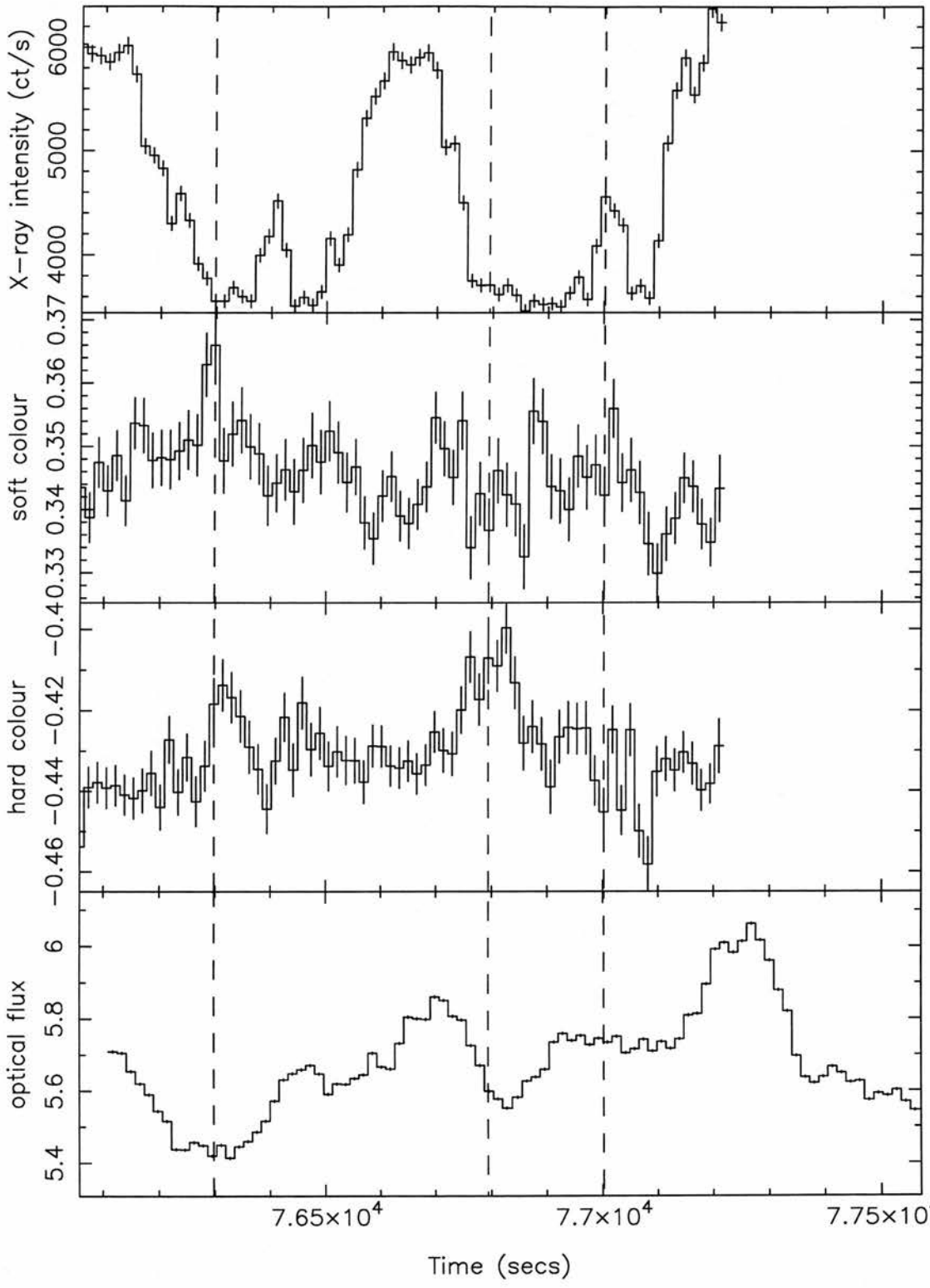

Figure 8.6: Simultaneous X-ray and optical lightcurves for the 1st RXTE visit on night 5.

large X-ray flares, with $\sim$ 50% changes in X-ray flux, with a rise time of around 100 seconds. The pattern of the X-rays appears to repeat on a timescale of $\sim$ 600 seconds. The soft X-ray colour rises slowly at the beginning of the observation (t > 76300 seconds), before steadily decreasing to the end of the observation. The Hard X-ray colour rises during the observation, before declining slightly towards the end (t > 77000 seconds). Superimposed on the slow hard colour variability are two peaks (t $\sim$ 76300 and 76700 seconds). The long-term soft and hard X-ray colours variations are anti-correlated, which is indicative of the FB.

The optical flux shows the same 600 second periodicity as the X-ray flux, but delayed in time relative to the X-rays, with a mean time delay of approximately 60 seconds. Superimposed on this is a slow rise in the mean optical level, which is indicative of a decrease in the mass accretion rate as Cygnus X-2moves towards the normal branch.

Window 2, UT 22:05 - 22:33

The simultaneous observations for the second *RXTE* window on night 5 of the observations are shown in Figure 8.7. Window 2 begins with both the X-ray intensity and the optical flux at their lower levels for this observation, indicating we are still on the Flaring Branch. The X-rays are at $\sim$ 3500 counts/sec and the optical flux at 5.5 mJy. Cygnus X-2shows similar behaviour to that seen during the previous window, until t $\sim$ 80400 seconds, when the X-ray hardness reaches a minimum, signifying that Cygnus X-2has moved through the soft vertex, onto the normal branch.

At this point the soft colour begins to increase to a peak around t = 80900 seconds. The hard colour also begins to increase and continues to increase until the end of the observation. The soft colour begins to decrease again after t = 80900 seconds, which coincides with a dip in the X-ray intensity. This dip is well correlated with a dip in the optical flux around t = 81000 and a peak in the soft colour. At this point the hardness begins to decrease again, marking a change in direction along the Normal Branch back towards the Flaring Branch. However this motion appears to be short lived as the hardness once again decreases and Cygnus X-2 moves back towards the Normal Branch.

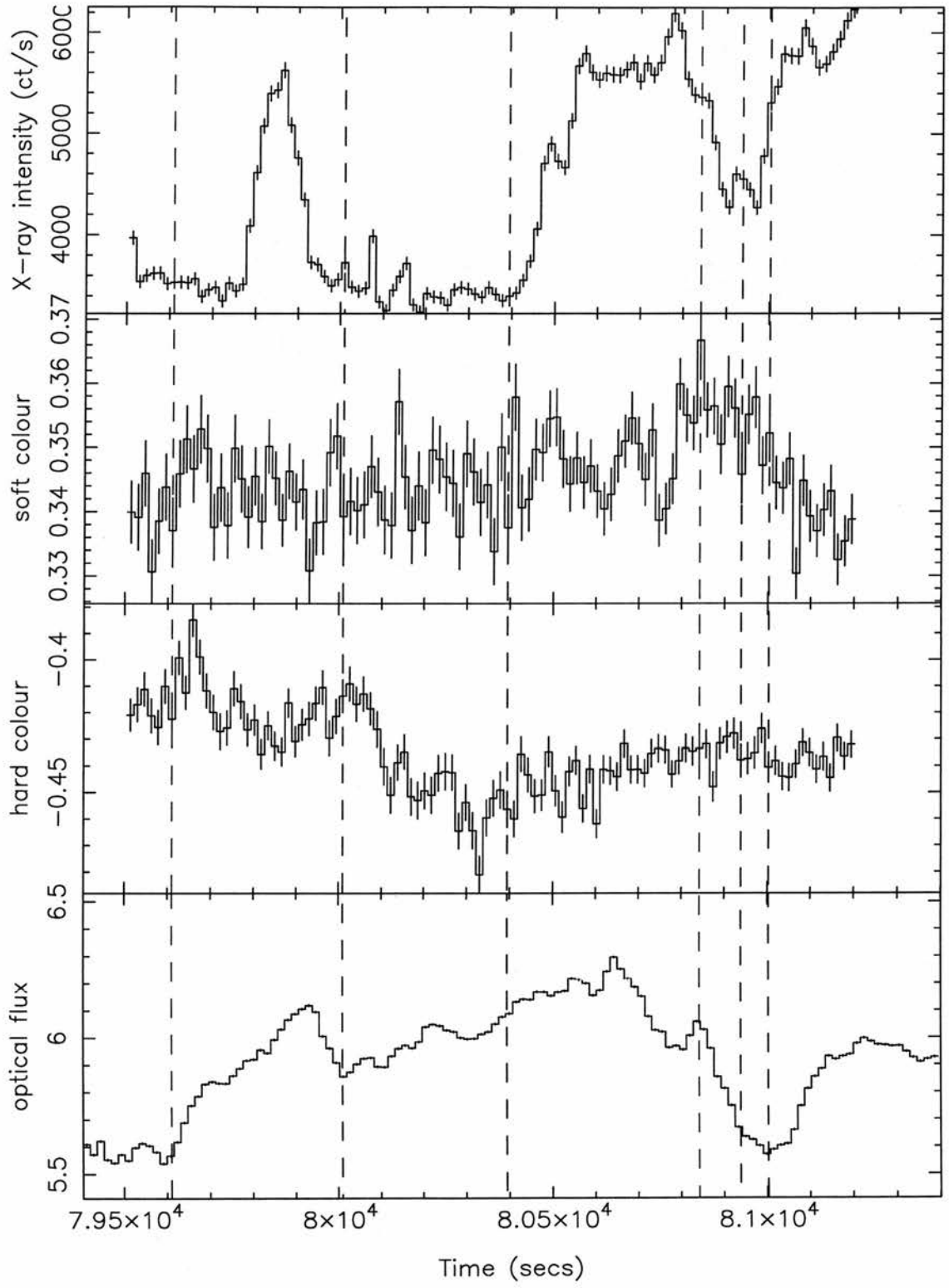

Figure 8.7: Simultaneous X-ray and optical lightcurves for the 2nd RXTE visit on night 5.

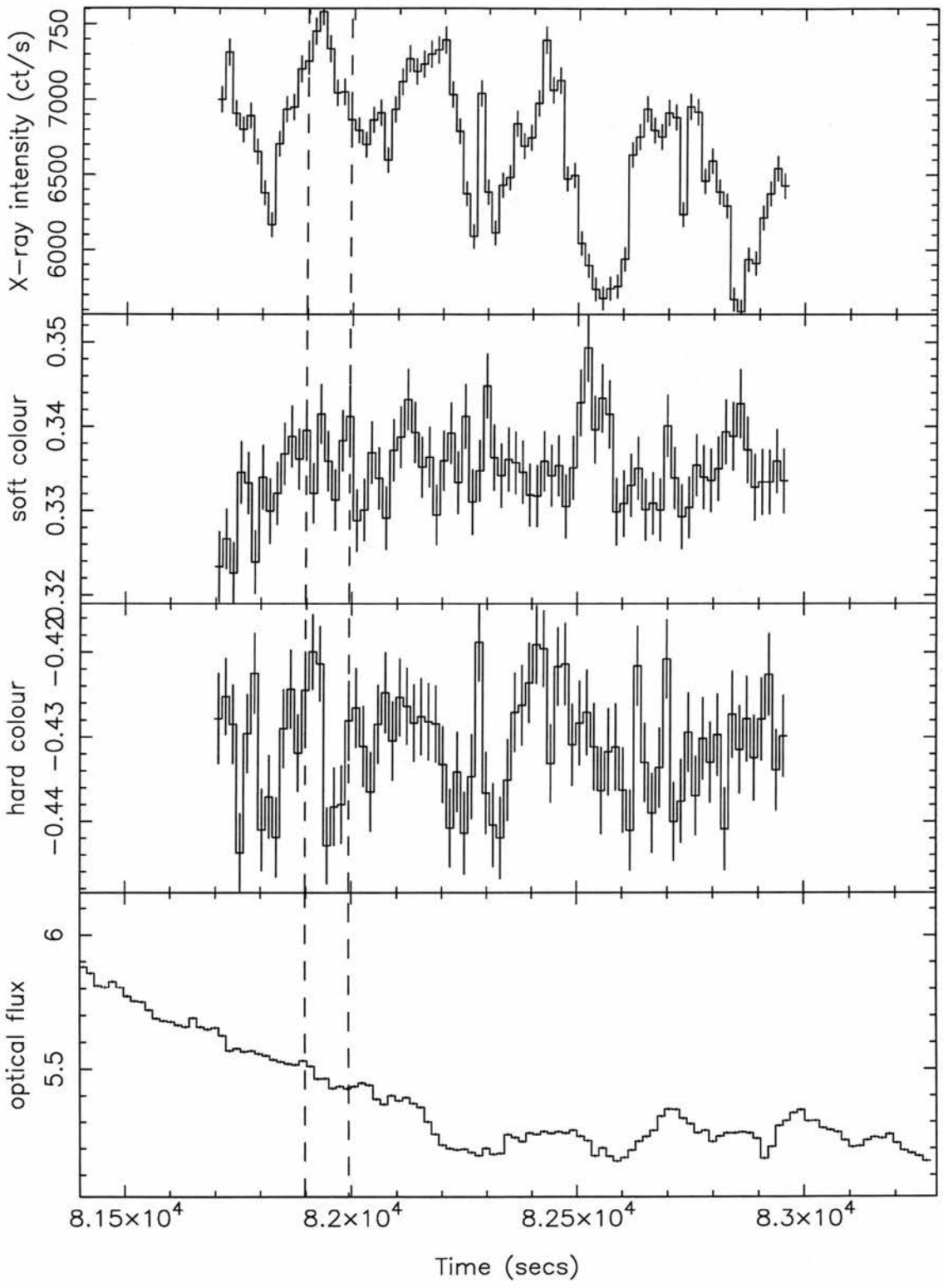

Figure 8.8: Simultaneous X-ray and optical lightcurves for the 3rd RXTE visit on night 5.

Window 3, UT 22:42 - 23:03

The simultaneous observations for the third *RXTE* window on night 5 of the observations are shown in Figure 8.8. During window 3 the optical observations show that Cygnus X-2 has moved off the Flaring Branch onto the Normal Branch. This coincides with a large, steady fall in the optical flux down to a level of $\sim$ 5.2 mJy at t = 82000 seconds. During this time we also see an overall decrease in the X-ray intensity. The soft X-ray colour increases at the beginning of the observation, until t $\sim$ 81000, where it levels off at around 0.35, which coincides with a change in the overall hardness. The mean soft and hard X-ray colours remain roughly constant, until the end of the X-ray window, suggesting that Cygnus X-2 remains roughly stationary on the z-curve. Superimposed on this mean level are a series of soft X-ray peaks and hard X-ray troughs. This causes a modulation of the X-ray intensity, with a timescale of around 300 seconds. These X-ray colour dependent variations are also seen in the optical lightcurve, although it is unclear of what time delay, if any, is present between the X-ray and optical variability.

Window 4, UT 23:42 - 00:38

The simultaneous observations for the fourth *RXTE* window on night 5 of the observations are shown in Figure 8.9. The fourth window begins with Cygnus X-2 moving from the Flaring Branch onto the Normal Branch. The soft colour increases from the beginning of the observation until it peaks at t $\sim$ 87600 seconds, whereas the hard colour remains constant until t = 86500, when it begins to rise, marking movement onto the Flaring Branch. The hard colour then increases with the soft colour until it also peaks at t = 87600. Super-imposed on this slow hard colour increase are 3 hard X-ray colour peaks, separated by around 300 seconds. The total X-ray intensity is well correlated with the colour variations, including the peaks observed in the hard colour lightcurve. The optical intensity variations are however anti-correlated with the overall X-ray intensity, reaching a minimum near t = 87600, when the X-ray flux is at its maximum. The X-ray intensity and colours begin to reduce again, showing more correlated variability with the optical lightcurve. The window ends with the X-rays increasing in intensity and hardness, whilst the optical reduces, indicating that Cygnus X-2 is now firmly on the Normal Branch.

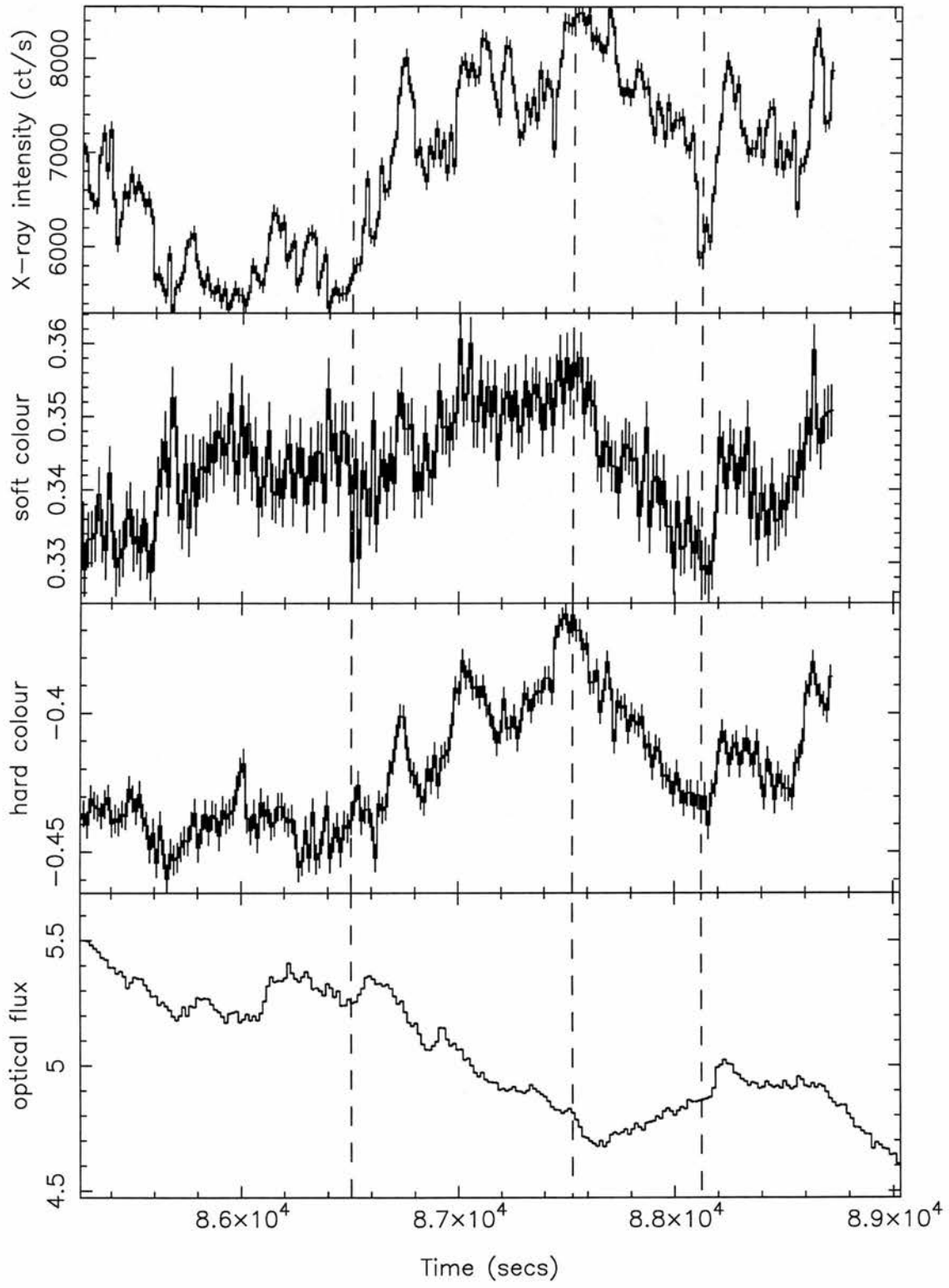

Figure 8.9: Simultaneous X-ray and optical lightcurves for the 4th RXTE visit on night 5.

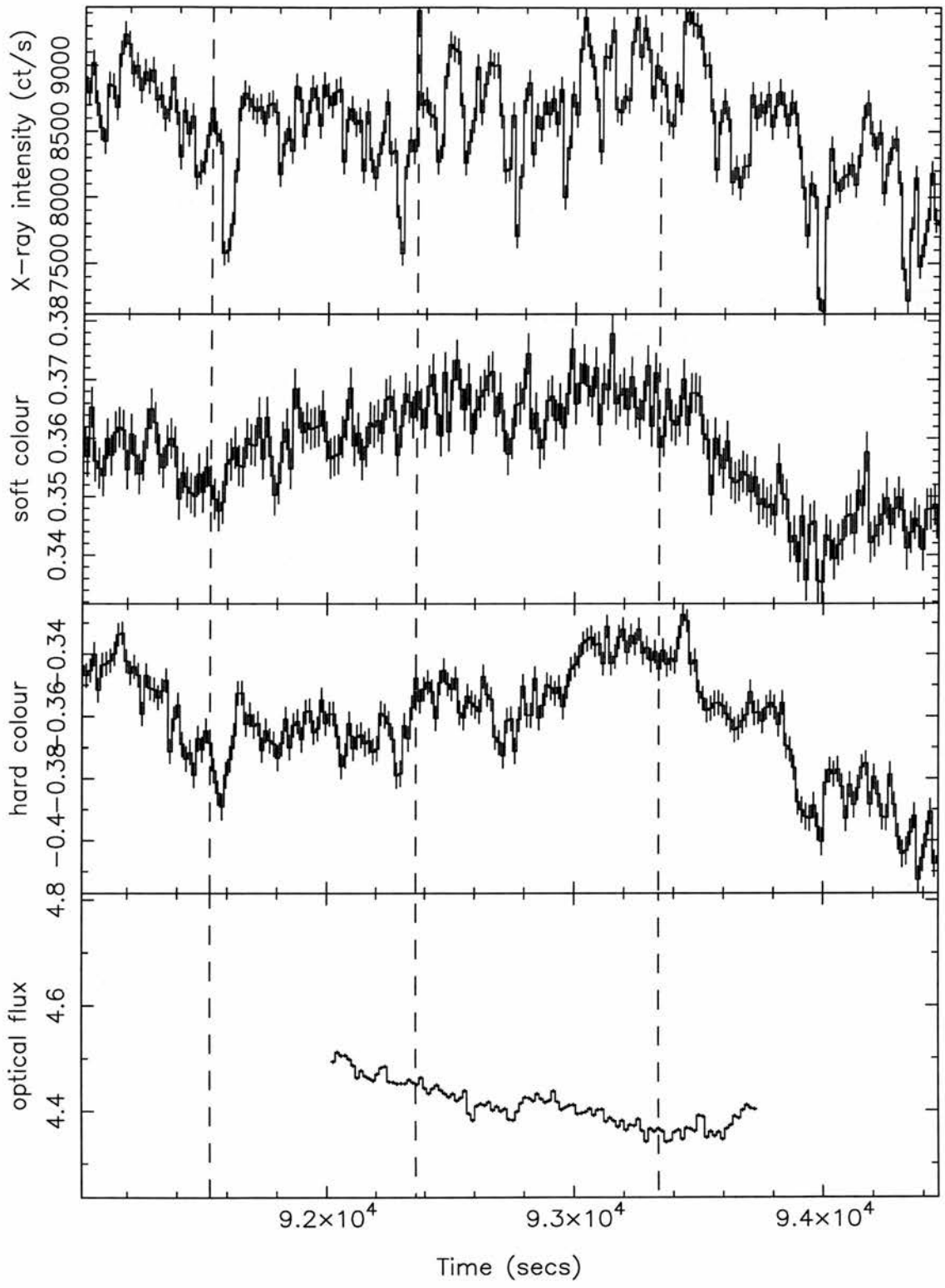

Figure 8.10: Simultaneous X-ray and optical lightcurves for the 5th RXTE visit on night 5.

Window 5, UT 01:17 - 02:14

The simultaneous observations for the fifth *RXTE* window on night 5 of the observations are shown in Figure 8.10. The fifth window begins the hardness decreasing, showing that Cygnus X-2 is moving along the Normal Branch towards the Flaring Branch. After the hardness reaches a minimum around t = 91500, it begins to increase slowly as the soft colour increases, this positive correlation being indicative of the Normal Branch. The optical coverage begins during this hardening of the X-rays, showing an overall decrease in flux. An X-ray burst occurs shortly after the beginning of the simultaneous coverage around t = 92400. However there is no evidence for any reprocessed optical burst. The maximum hardness is reached around t = 93300, where it begins to decrease. This is correlated with an increase in the optical flux at the end of the optical coverage. The X-rays continue to soften and reduce in intensity until the end of the observation.

8.4.2 General features of night 1, UT 01-02/07/98

Window 1, UT 22:48 - 23:02

The simultaneous observations for the first *RXTE* window on night 1 of the observations are shown in Figure 8.13. This short window shows an overall decrease in the X-ray flux. The optical flux remains roughly constant during the observation, although it is difficult to determine if the X-ray and optical variations are correlated, predominantly due to the short duration of the simultaneous coverage.

Window 2, UT 01:15 - 02:15

The simultaneous observations for the second *RXTE* window on night 1 of the observations are shown in Figure 8.14. This window begins with an increase in the X-ray flux correlated with a decrease in the hard and soft X-ray colours as Cygnus X-2 moves along the Horizontal Branch towards the Hard Vertex. The Soft Colour begins to increase around t = 91500, correlated with an increase in the Hardness of the source. During this time the optical flux is decreasing, which is surprising as we expect a positive correlation between

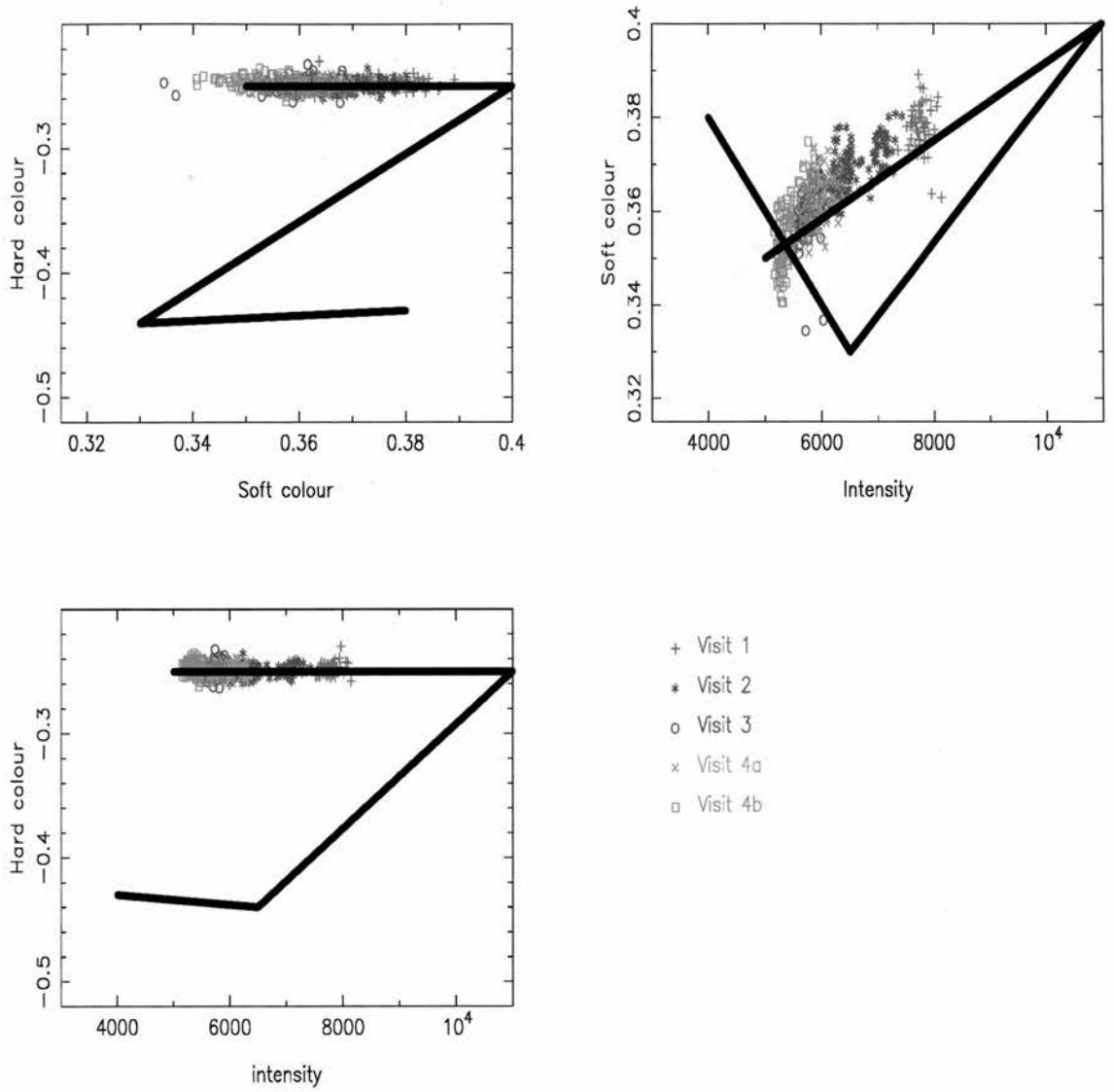

Figure 8.11: Top left, Colour-Colour diagram for Cygnus X-2, based on the *RXTE* PCA data on UT 01/07/98. The data is taken from the B_2MS_16_0_35_Q mode, with a time resolution of 16 seconds. The soft colour is logarithm of the ratio of the intensities in the ranges 1.71 - 3.17 keV and 3.17 - 5.37 keV. The hard colour is the logarithm of ratio of the intensities in the ranges 5.37 - 8.31 keV and 8.31 - 13.1 keV. The coloured symbols represent different visits, shown in the key. Bottom left, The hardness intensity diagrams for the hard colour and the total intensity. Top right, The hardness intensity diagrams for the soft colour and the total intensity. The black line is the fit to the 'Z' curve found in the previous section

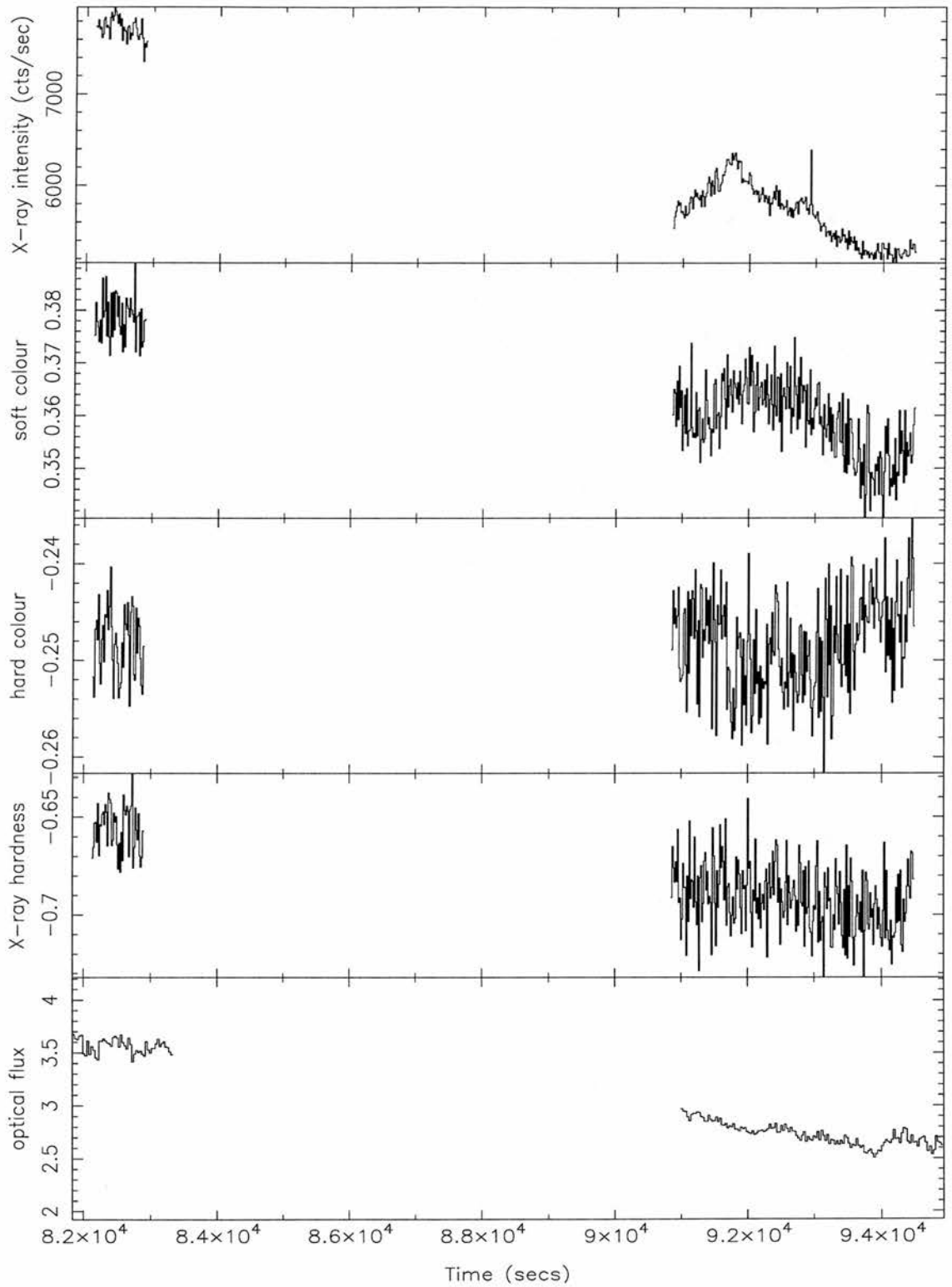

Figure 8.12: Top panel, the total X-ray intensity during the 2 RXTE visits from night 1, upper middle, the soft colour variations, middle, the Hard colour variations. Lower middle, the overall hardness. Bottom panel, the optical continuum flux in the range 5000 - 5800 $\mathring{A}$.

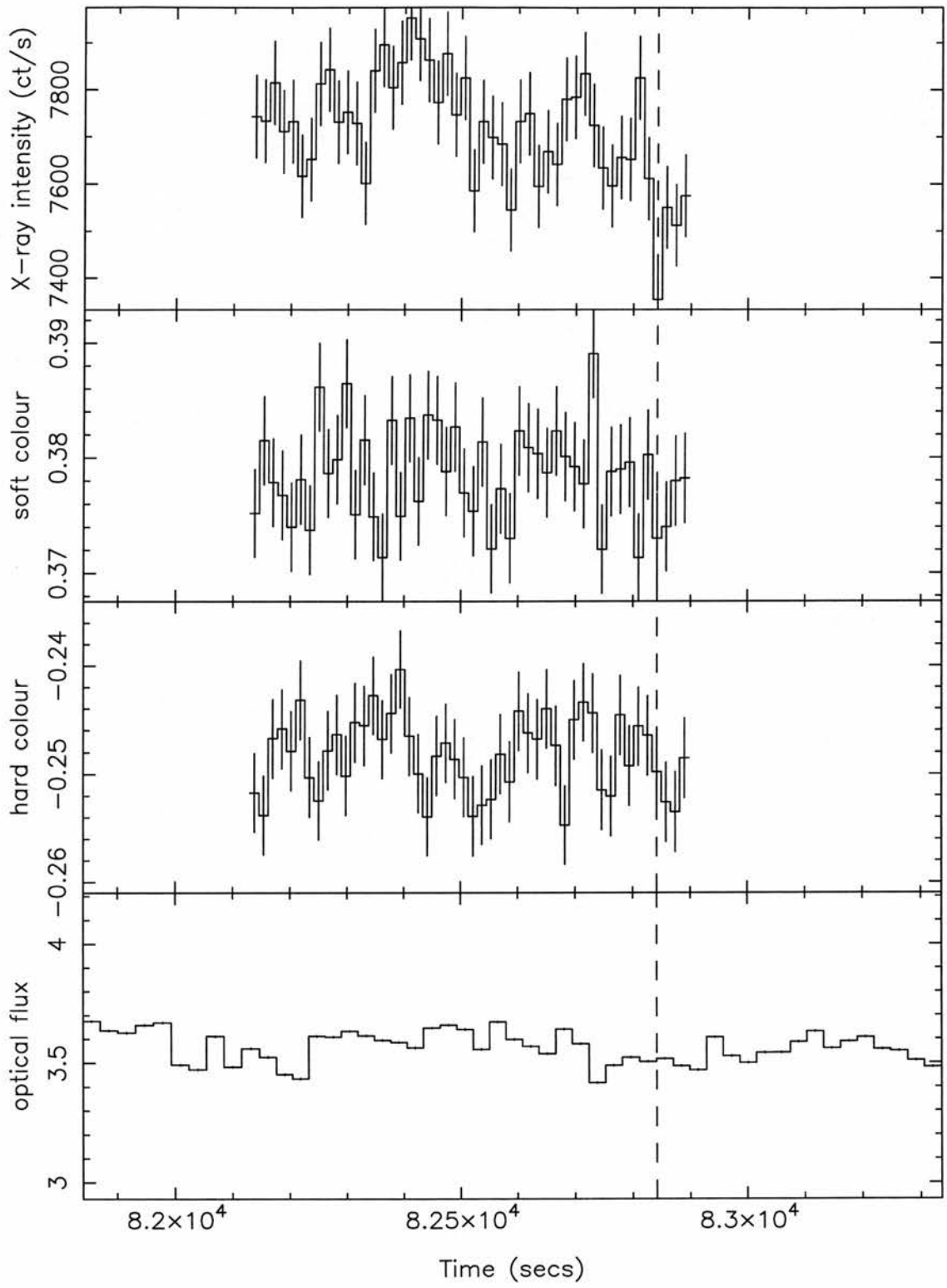

Figure 8.13: Simultaneous X-ray and optical lightcurves for the 1st RXTE visit on night 1.

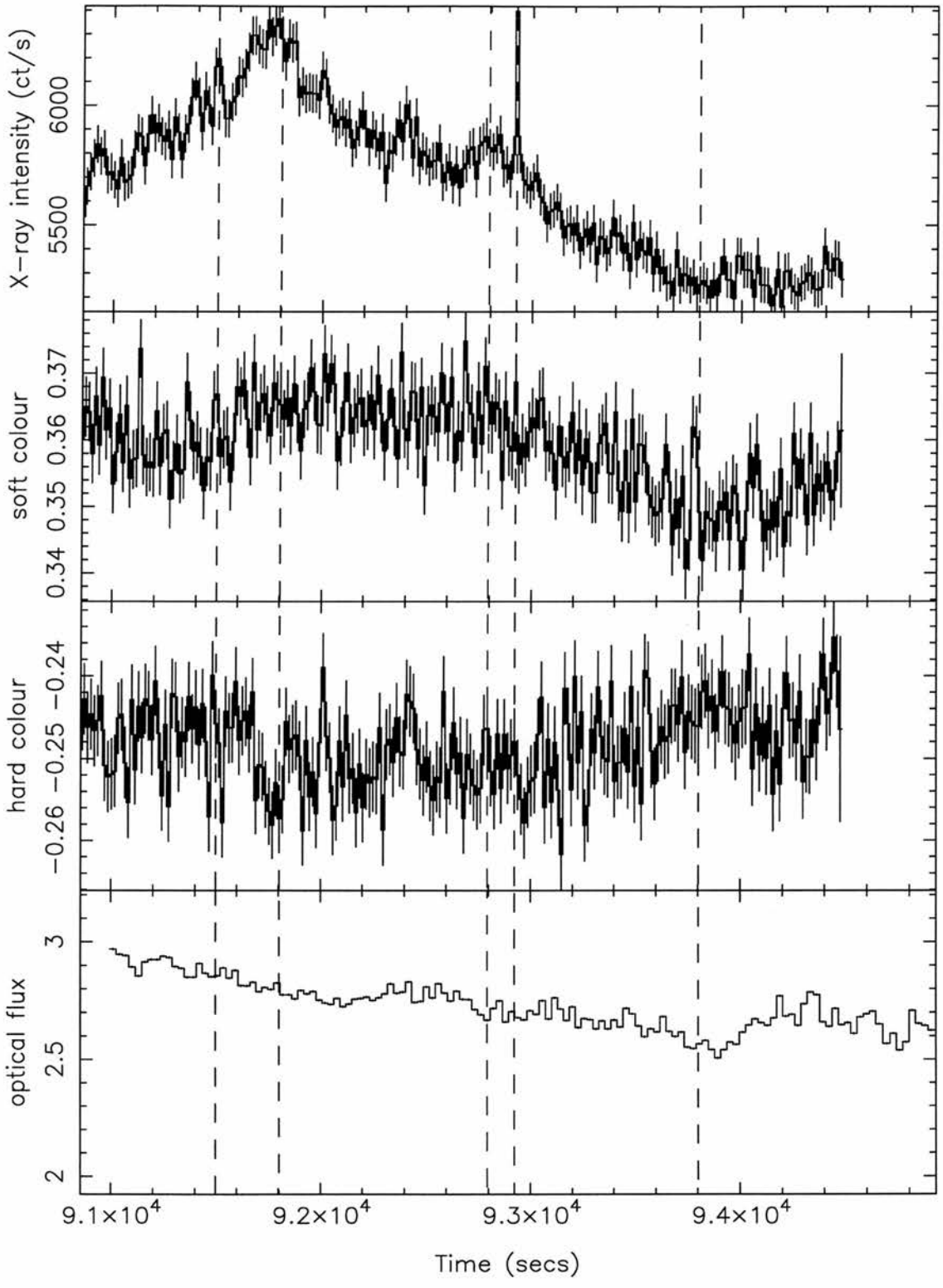

Figure 8.14: Simultaneous X-ray and optical lightcurves for the 2nd RXTE visit on night 1.

the X-ray and optical fluxes on the Horizontal Branch. The X-ray intensity reaches a maximum around t = 91800, where the hard colour is at a minimum. The X-ray intensity then begins to fall, along with the optical flux, until another small rise around t = 92800, which is followed by an X-ray burst. Again there is no optical counterpart for this optical burst, although there is a small rise in the optical flux at this time. The X-rays then fall to a minimum level and the optical also reaches a minimum at this point. Correlated with this is an overall softening of the source, as the soft colour reaches a minimum and the hard colour reaches a maximum at t = 93800. At this point, the source is at the end of the Horizontal Branch, where the mass accretion rate is at its lowest value.

8.5 The spectrum of the optical variability in Cygnus X-2

In order to characterize the optical variability in Cygnus X-2, I have determined the optical variability spectrum during each of the *RXTE* orbits, to investigate the variability of the spectrum as a function of the rank number, S_z, and hence the mass accretion rate (see chapter 1). This is done using variability spectrum-lightcurve pairs based on the method described in chapter 7.1. The model, $M(\lambda, t)$, can be written as,

$$M(\lambda, t) = S_0(\lambda) + S_1(\lambda)\,\overline{L_1(t)}, \tag{8.1}$$

where S_0 is the average spectrum, S_1 and L_1, are the spectrum and lightcurve of the variable component. The resulting average spectra and the variability spectrum-lightcurve pairs can be seen in Figures 8.15 - 8.19.

8.5.1 Continuum spectral fits

I have used blackbody spectra to describe the observed continuum fluxes. The spectrum observed from a blackbody is given by,

$$\begin{aligned} F_\nu(\lambda) &= \int B_\nu(\lambda, T)\, d\Omega \\ &= \frac{\pi R^2}{D^2} \frac{2hc}{\lambda^3 \left[\exp\left(\frac{hc}{k\lambda T}\right) - 1\right]}, \end{aligned} \tag{8.2}$$

for a region with a radius, R, and a temperature, T, at a distance D. If D is known, the Blackbody fit will tell us the temperature and size of the emitting region. This model is most appropriate for a region that has a roughly constant temperature for the duration of the observations.

These models are fitted to the continuum regions of the spectra that are least contaminated with spectral lines. The best fit values, together with their 1-parameter 1-sigma confidence regions are shown in Table 8.2. The data together with the best fit and the spectral regions used are shown in Figures 8.20 - 8.24.

The continuum regions of the mean spectra for the different windows are best-fit with an average temperature of around 15000 K and size of approximately 66×10^{22} cm^2, although the large value of χ^2 shows that the fit is not very good. This is also seen in

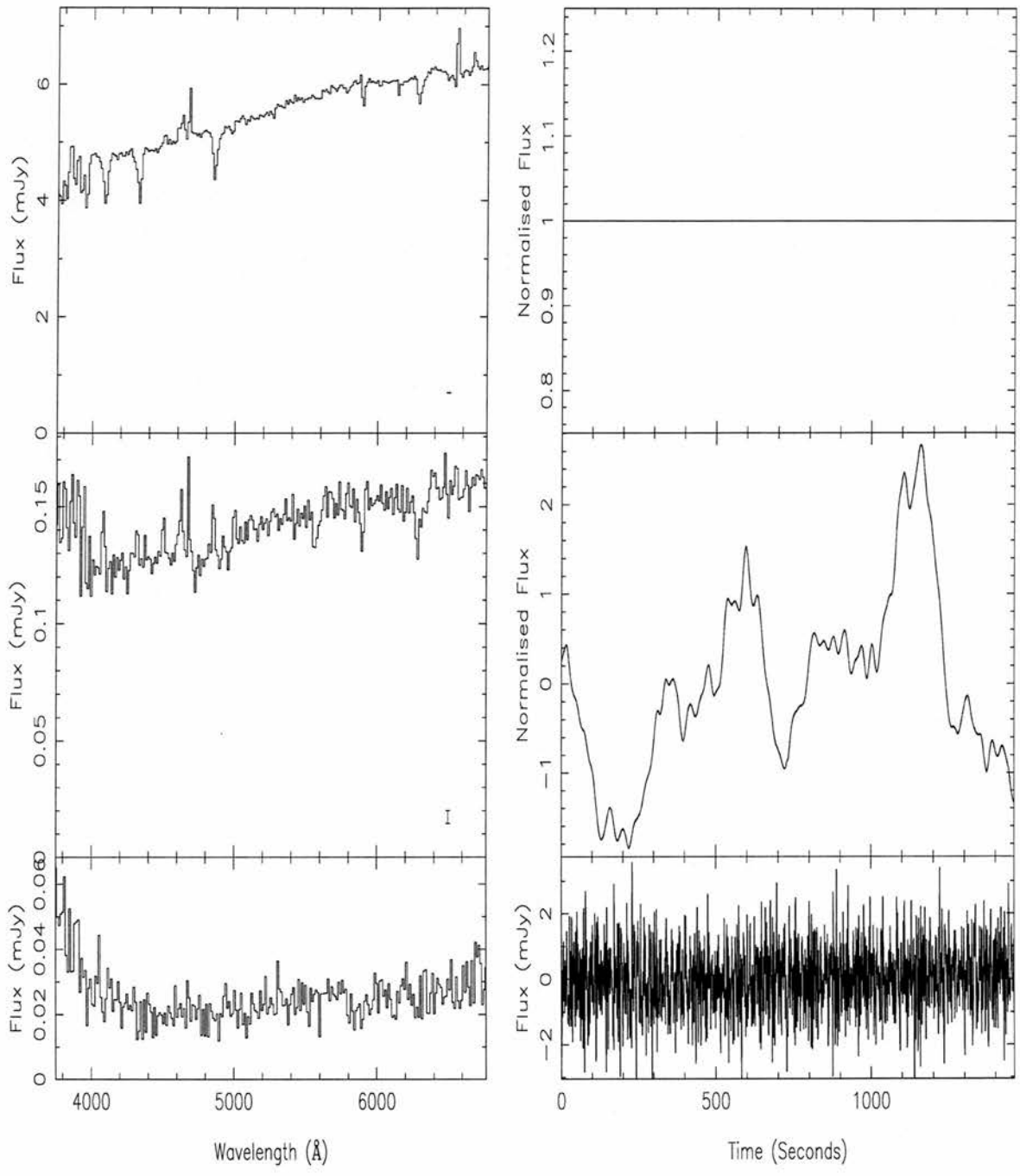

Figure 8.15: The average (top left) and variability (middle left) spectra for the optical data simultaneous with the first RXTE visit, together with their associated lightcurves (right). The residual spectrum and lightcurve of the fit are shown (bottom left and right respectively). Average error bars are shown.

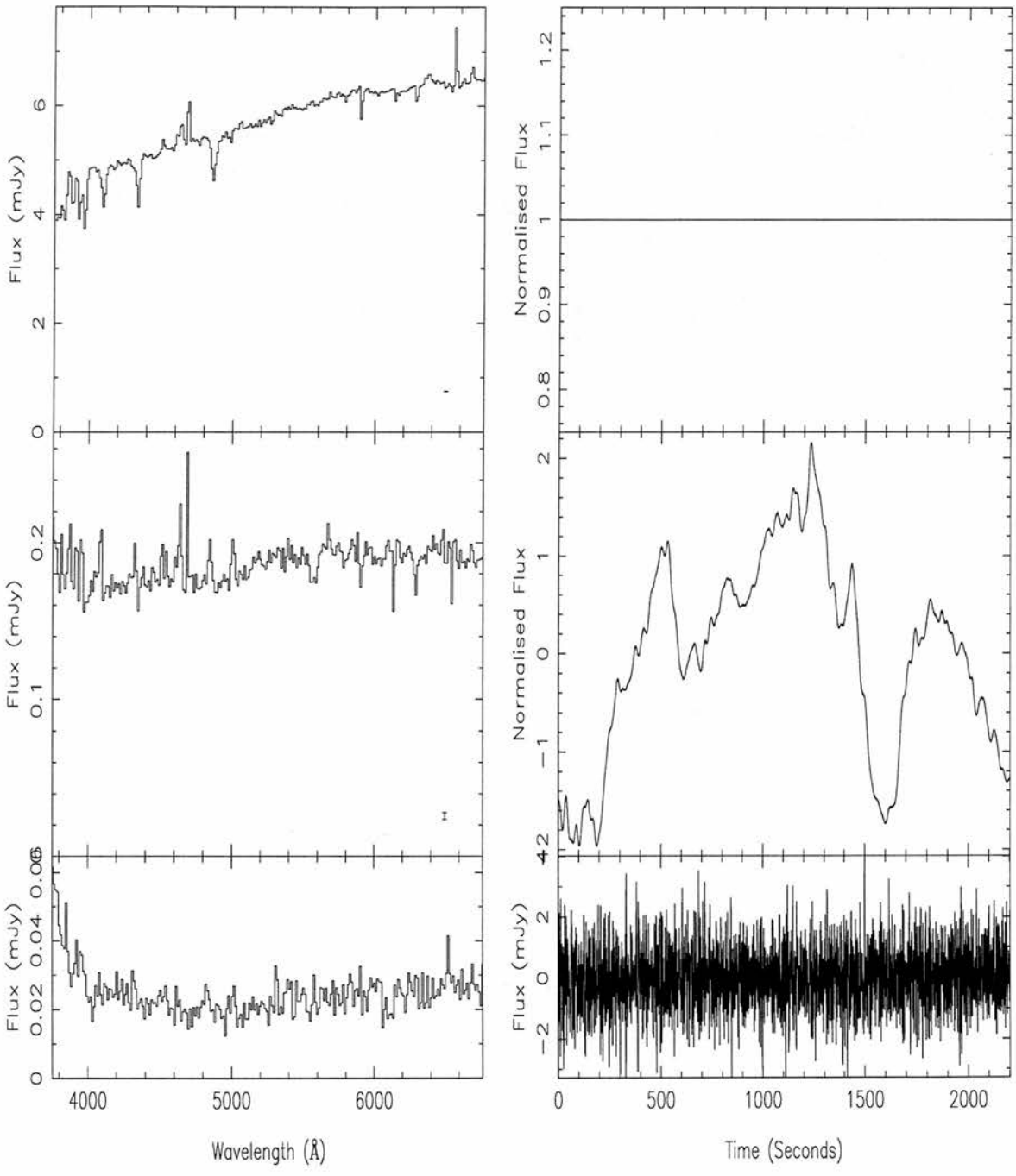

Figure 8.16: The average (top left) and variability (middle left) spectra for the optical data simultaneous with the second RXTE visit, together with their associated lightcurves (right). The residual spectrum and lightcurve of the fit are shown (bottom left and right respectively). Average error bars are shown.

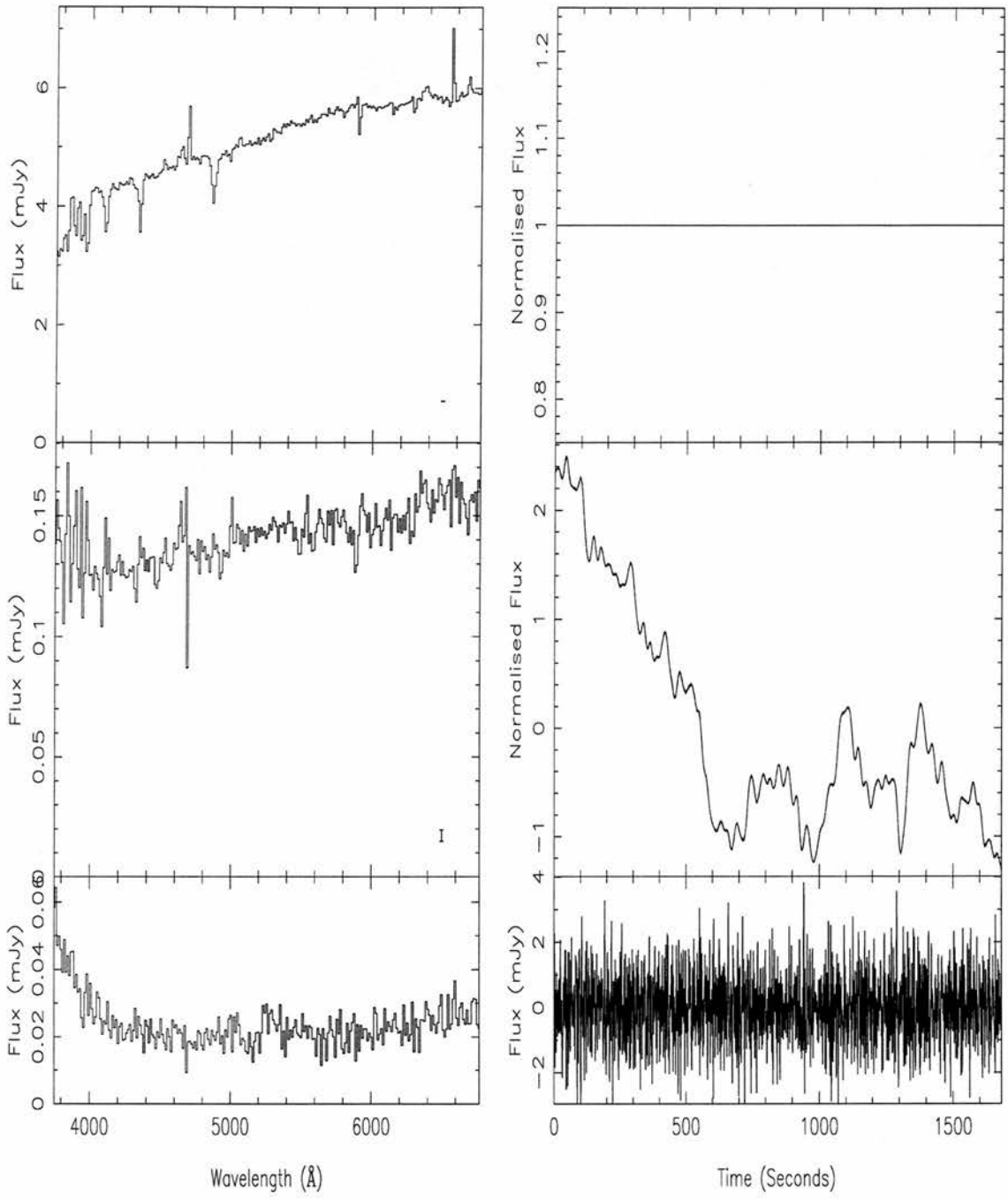

Figure 8.17: The average (top left) and variability (middle left) spectra for the optical data simultaneous with the third RXTE visit, together with their associated lightcurves (right). The residual spectrum and lightcurve of the fit are shown (bottom left and right respectively). Average error bars are shown.

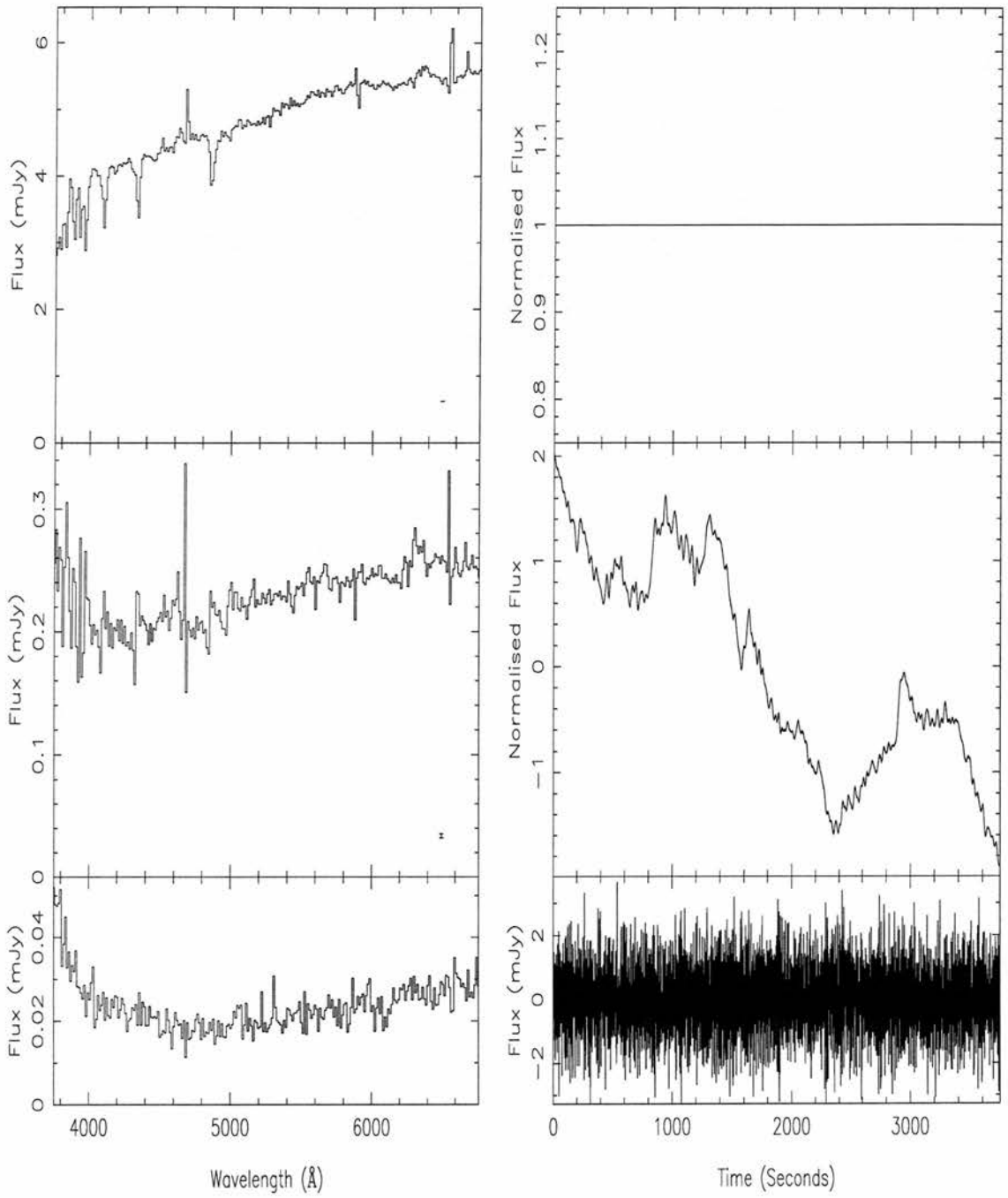

Figure 8.18: The average (top left) and variability (middle left) spectra for the optical data simultaneous with the fourth RXTE visit, together with their associated lightcurves (right). The residual spectrum and lightcurve of the fit are shown (bottom left and right respectively). Average error bars are shown.

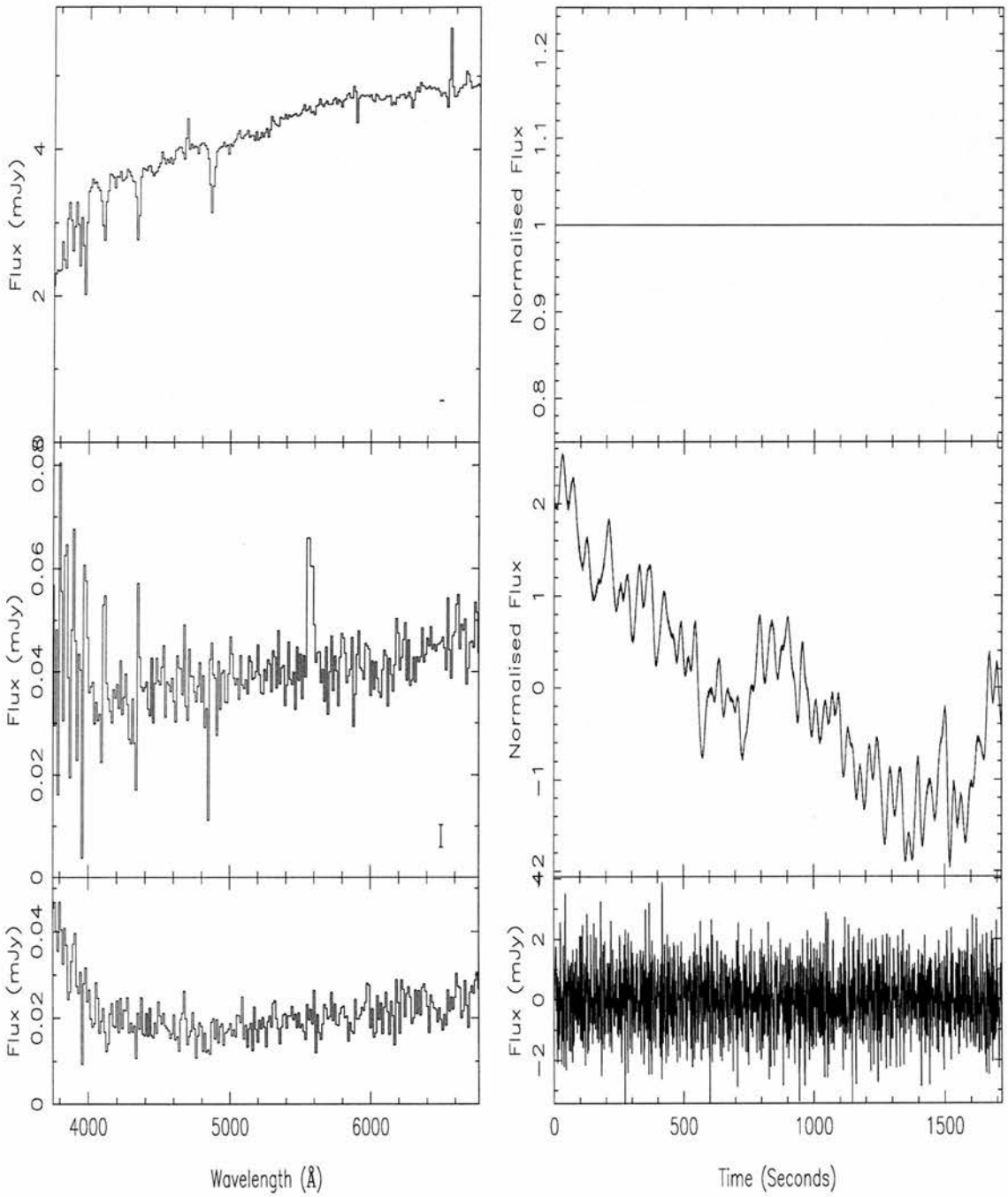

Figure 8.19: The average (top left) and variability (middle left) spectra for the optical data simultaneous with the fifth RXTE visit, together with their associated lightcurves (right). The residual spectrum and lightcurve of the fit are shown (bottom left and right respectively). Average error bars are shown.

	Visit	Temperature (K)	Area (10^{22} cm^2)	$\chi^2/NDOF$
average	1	$15370\ ^{+150}_{-160}$	$67.3\ ^{+1.5}_{-1.4}$	11200/94
	2	$15280\ ^{+140}_{-130}$	$70.6\ ^{+1.5}_{-1.2}$	14434/94
	3	$14560\ ^{+150}_{-150}$	$70.6\ ^{+1.5}_{-1.2}$	10066/94
	4	$14920\ ^{+150}_{-140}$	$63.6\ ^{+1.1}_{-1.1}$	25521/94
	5	$14740\ ^{+150}_{-150}$	$57.0\ ^{+1.4}_{-1.0}$	11406/94
variability	1	$15050\ ^{+400}_{-350}$	$1.79\ ^{+0.10}_{-0.09}$	47.07/87
	2	$20150\ ^{+700}_{-600}$	$1.32\ ^{+0.08}_{-0.07}$	106.9/87
	3	$18250\ ^{+650}_{-550}$	$1.20\ ^{+0.08}_{-0.07}$	66.63/87
	4	$15770\ ^{+400}_{-350}$	$2.60\ ^{+0.14}_{-0.13}$	335.8/87
	5	$17050\ ^{+1500}_{-1250}$	$0.38\ ^{+0.06}_{-0.06}$	41.02/87

Table 8.2: Summary of best fit parameters to the spectral fitting of the spectra from the variability model, together with their 1-parameter 1-sigma confidence regions. A distance of 7.2kpc and E(B-V)=0.4 were assumed throughout (Orosz & Kuulkers 1999).

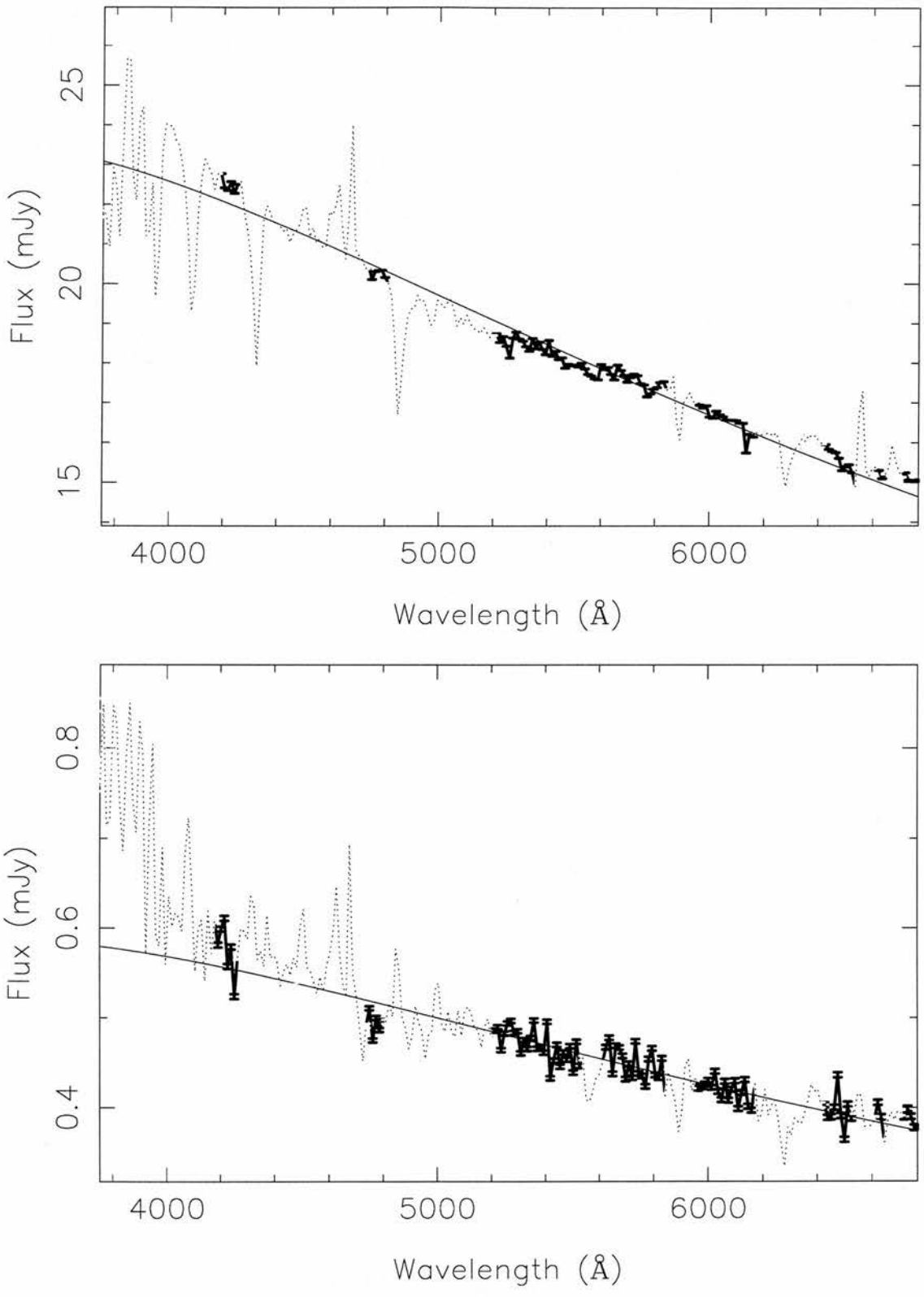

Figure 8.20: Top panel, a plot of the de-reddened average spectrum and its best-fit blackbody for Visit 1. The dotted line shows the data points not used in the fitting routine, the solid points are the data used and the solid line is the best fit blackbody. Lower panel, The same plot for the variable component.

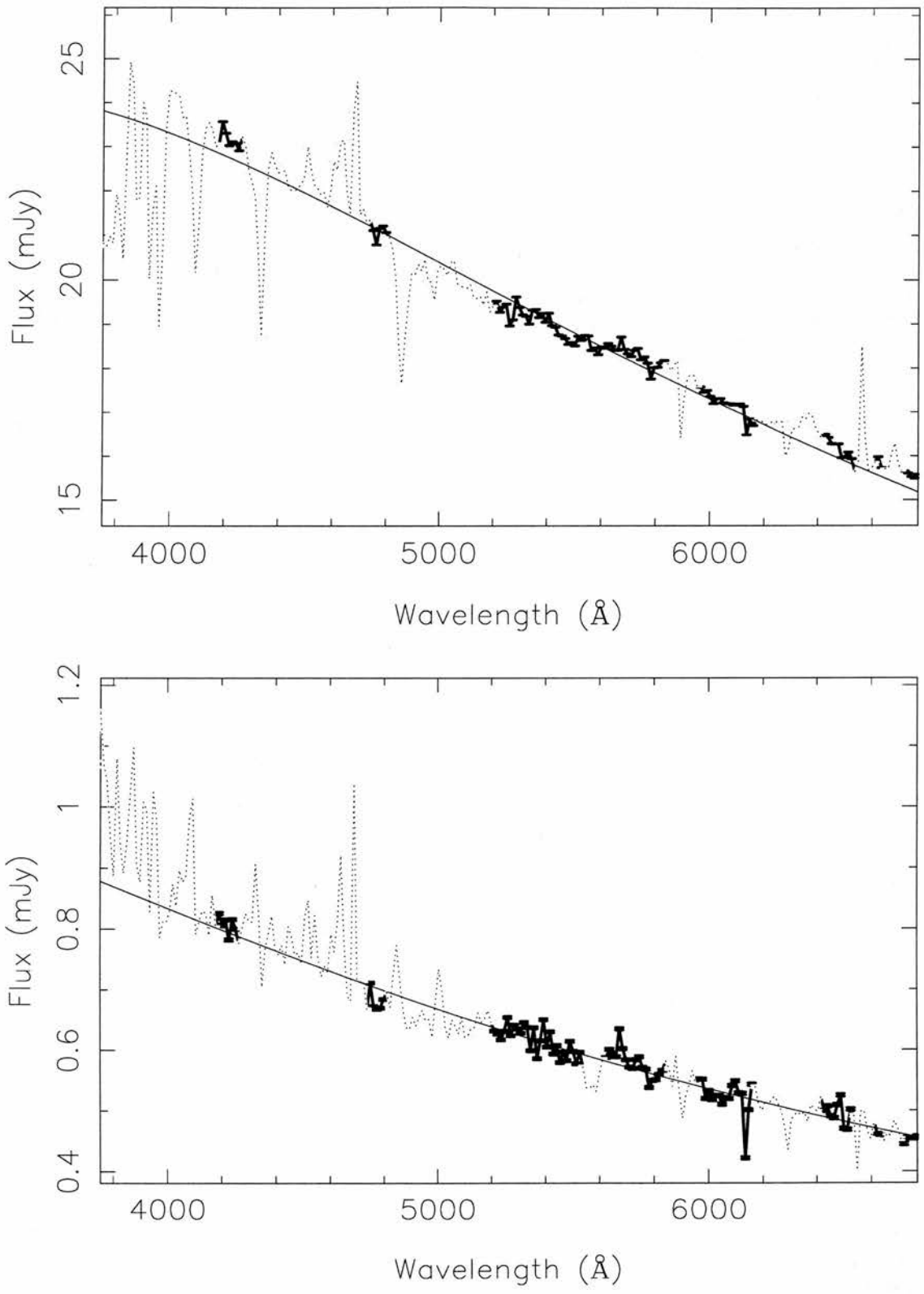

Figure 8.21: Top panel, a plot of the de-reddened average spectrum and its best-fit blackbody for Visit 2. The dotted line shows the data points not used in the fitting routine, the solid points are the data used and the solid line is the best fit blackbody. Lower panel, The same plot for the variable component.

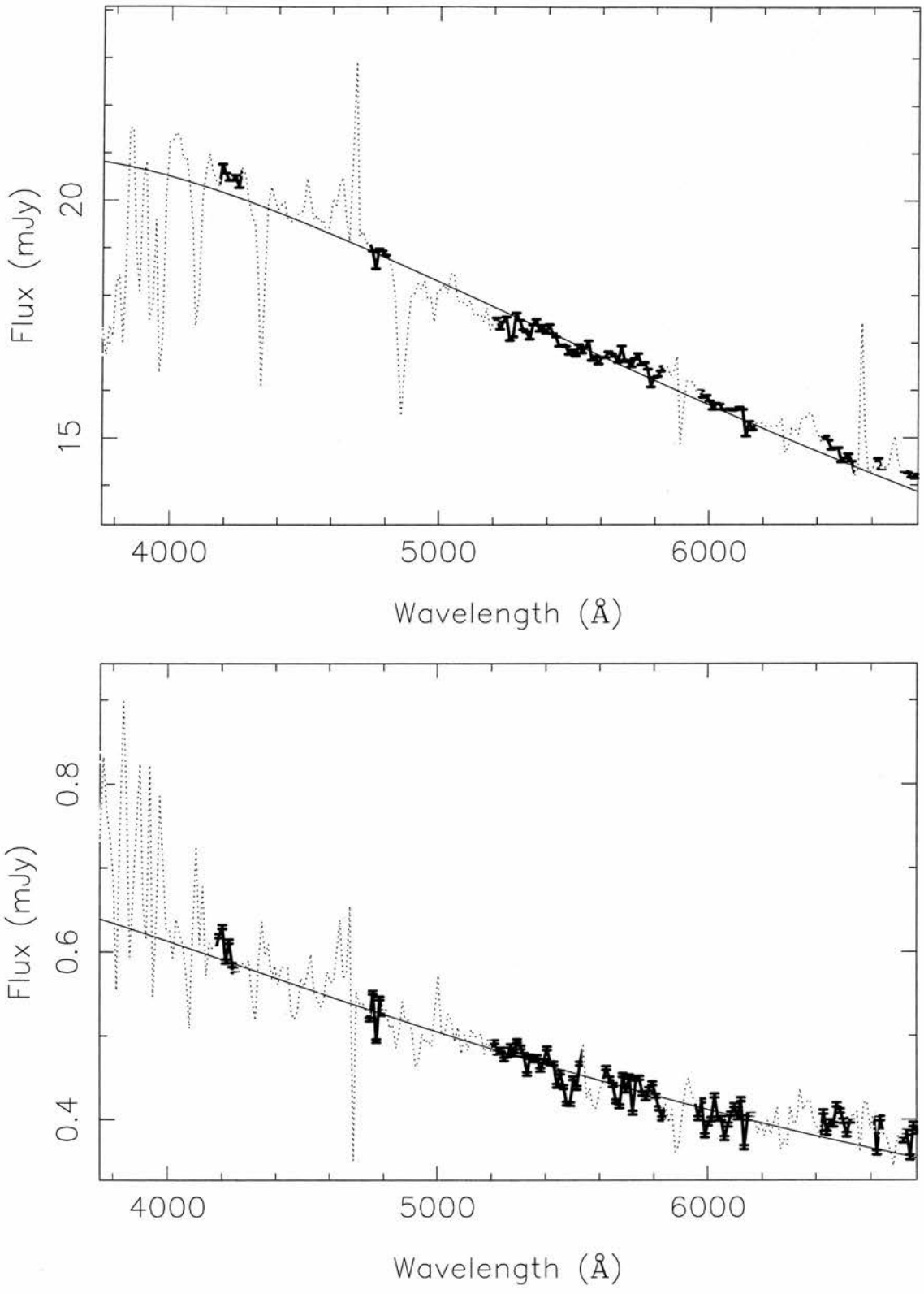

Figure 8.22: Top panel, a plot of the de-reddened average spectrum and its best-fit blackbody for Visit 3. The dotted line shows the data points not used in the fitting routine, the solid points are the data used and the solid line is the best fit blackbody. Lower panel, The same plot for the variable component.

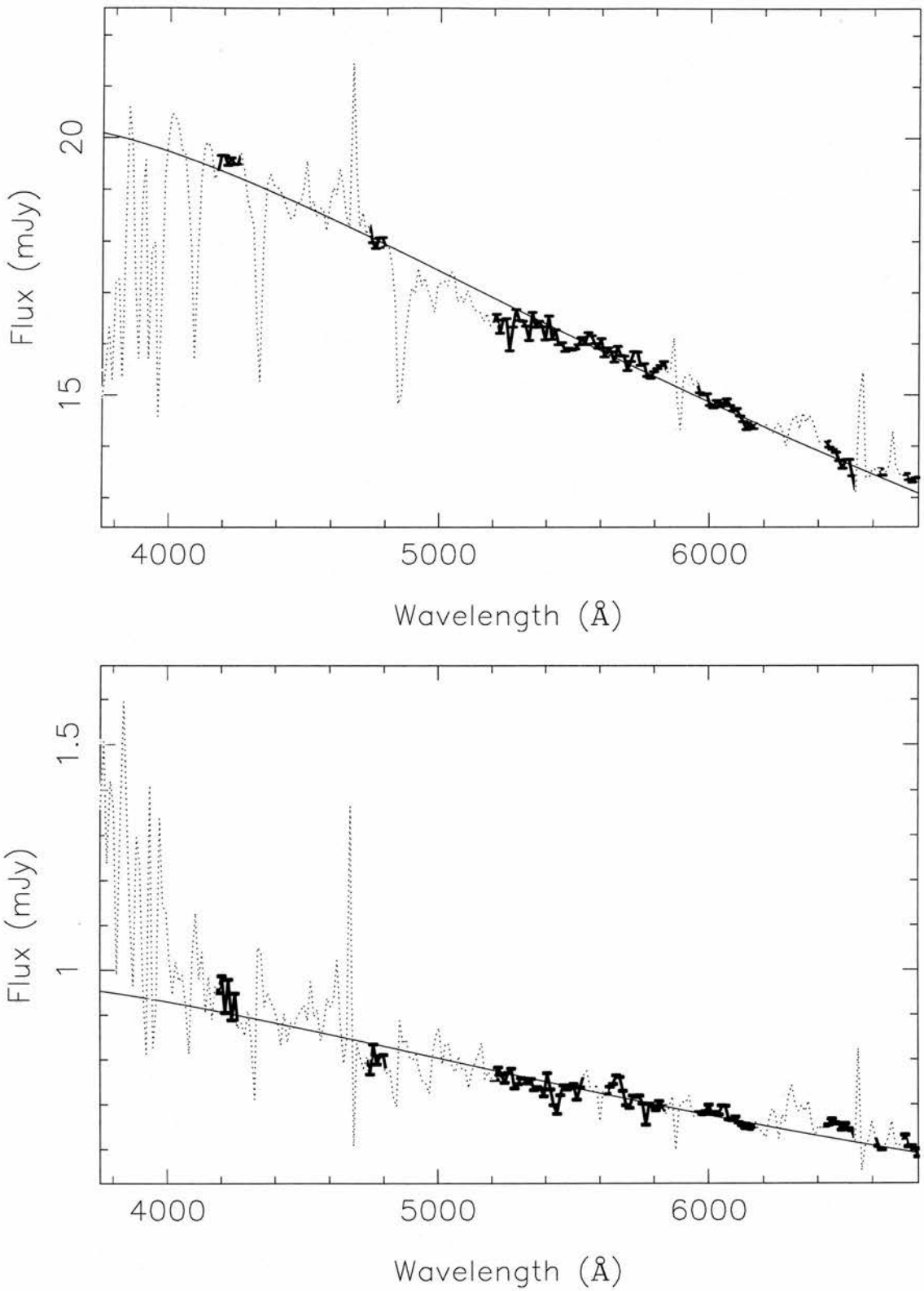

Figure 8.23: Top panel, a plot of the de-reddened average spectrum and its best-fit blackbody for Visit 4. The dotted line shows the data points not used in the fitting routine, the solid points are the data used and the solid line is the best fit blackbody. Lower panel, The same plot for the variable component.

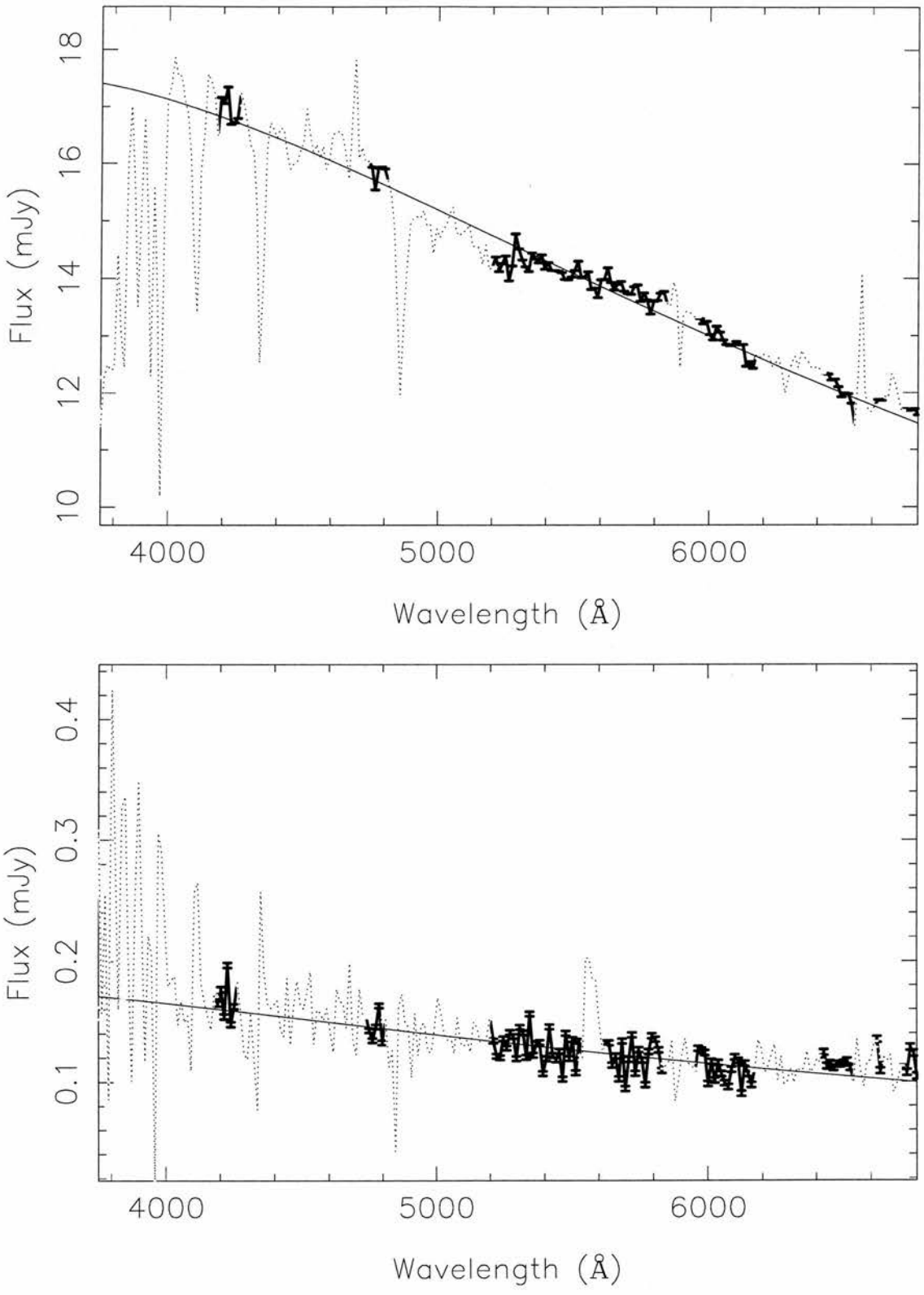

Figure 8.24: Top panel, a plot of the de-reddened average spectrum and its best-fit blackbody for Visit 5 . The dotted line shows the data points not used in the fitting routine, the solid points are the data used and the solid line is the best fit blackbody. Lower panel, The same plot for the variable component.

the figures. The reason for this poor fit is that the mean spectrum is that of a stellar spectrum and not a simple blackbody. However, the use of a blackbody is not entirely unjustified as the continuum regions should be similar to a blackbody, with the characteristic temperature of the photosphere. In the case of X-ray binaries this temperature will be modified due to the existence of strong X-ray irradiation by the central compact object (Basko, Sunyaev & Titarchuk 1974).

The best fit to the continnum regions of the variability spectra have a higher mean temperature, T $\sim$ 15000 - 20000 K, and a smaller average size, $\sim 1.5 \times 10^{22}$ cm^2 than their associated average spectra. The blackbody continuum spectra are a better fit than those used for the average spectra, as expected if the variability is caused by the irradiation, where the irradiated regions are heated and emit photons as they cool down to their steady-state temperatures.

8.5.2 The spectral lines

The average optical spectra for the observations, an example of which is shown in Figure 8.25, have a clear stellar spectrum, with the characteristic Balmer absorption lines clearly observed. They also show stong emission lines, most notably He II (λ4686) and the Bowen blend, ($\sim \lambda$4640), as well as weak He I (λ6678) and a strong Hα emission core, resulting in a weak emission line. The He II and Bowen blends are characteristic of hot, irradiated regions. He II (λ 4686) has a binding energy of 54 eV and can hence only be formed in the hottest regions. The strong Hα emission core is most probably formed in the accretion disk surrounding the central compact object.

We have extracted from our spectra line flux lightcurves for Hα, Hβ, Hγ, He II and the Bowen blend. This has been done by subtracting the continuum flux, using a low order spline fit to the continuum from spectra with a time resolution of 16 seconds. The lightcurves are created by summing in the wavelength range around the line in the resulting continuum-subtracted spectra. A continuum lightcurve, with the same time reolution, was created from the wavelength range $\lambda 5000 - 5800$.

In order to determine if the lines are due to reprocessing we have plotted the line

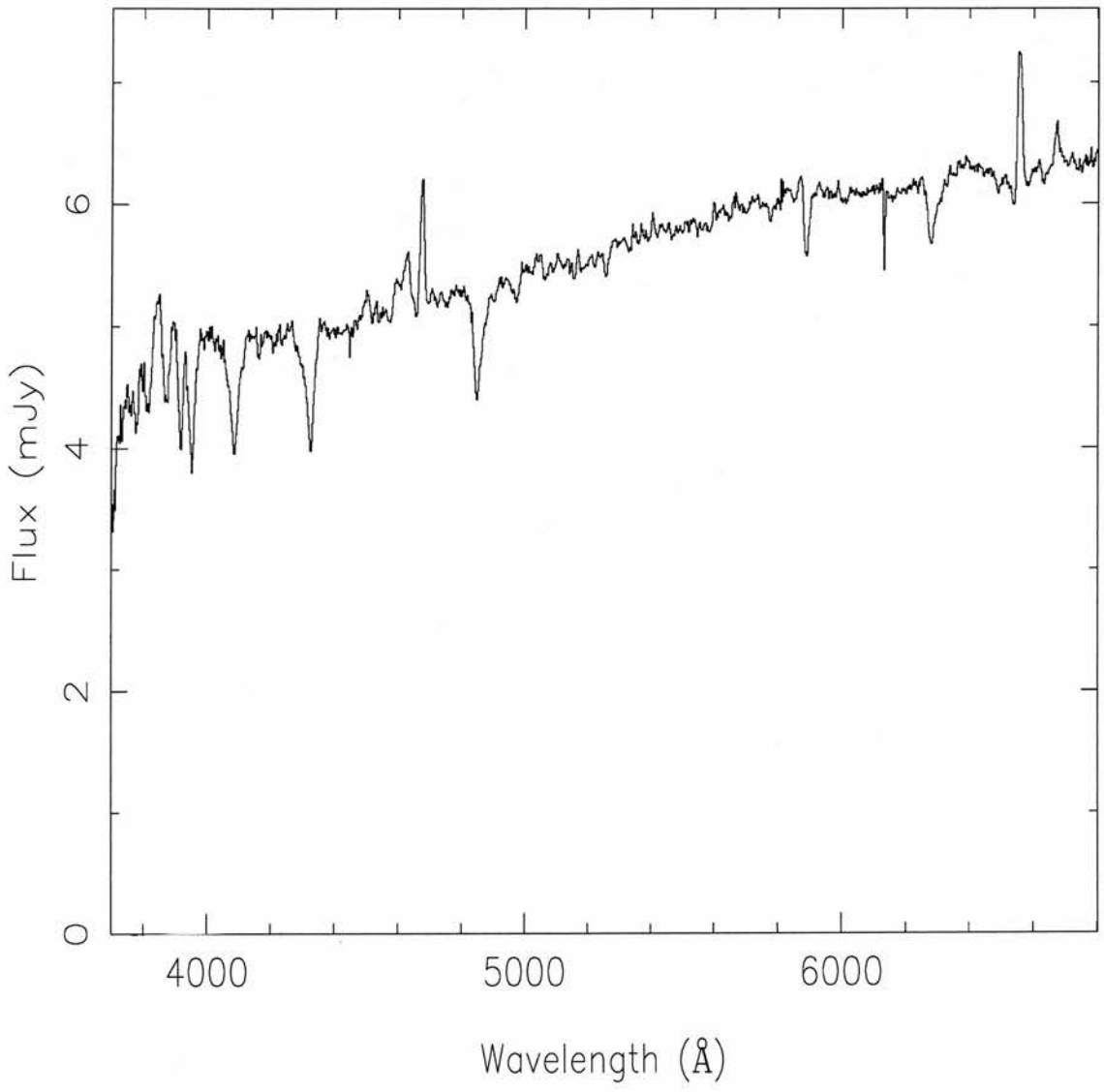

Figure 8.25: The average optical spectrum from Keck II, simultaneous with the first RXTE visit.

flux as a function of the continuum. The results of this analysis are shown in Figure 8.26. In this plot best-fit solutions using a linear fit, with 3-σ clipped outliers, are shown. The vertical dashed line denotes the extrapolation of the Bowen blend to zero flux, interpreted, in a linear reprocessing model, as the zero irradiation case. At this point we can see the intrinsic colours of the companion star and we note that the H α line flux is consistent with zero, which is greater than expected if it were from the companion star alone. We interpret this as excess emission from material in the accretion disk surrounding the compact object.

Unlike the other lines, He II does not show a linear relationship, despite the fact that it is associated with reprocessing. Instead it shows a roughly linear trend, but with large deviations superimposed. The reason for this is unclear. One possible interpretation is that the He II line is reacting on a different timescale to the optical continuum, causing hysterisis.

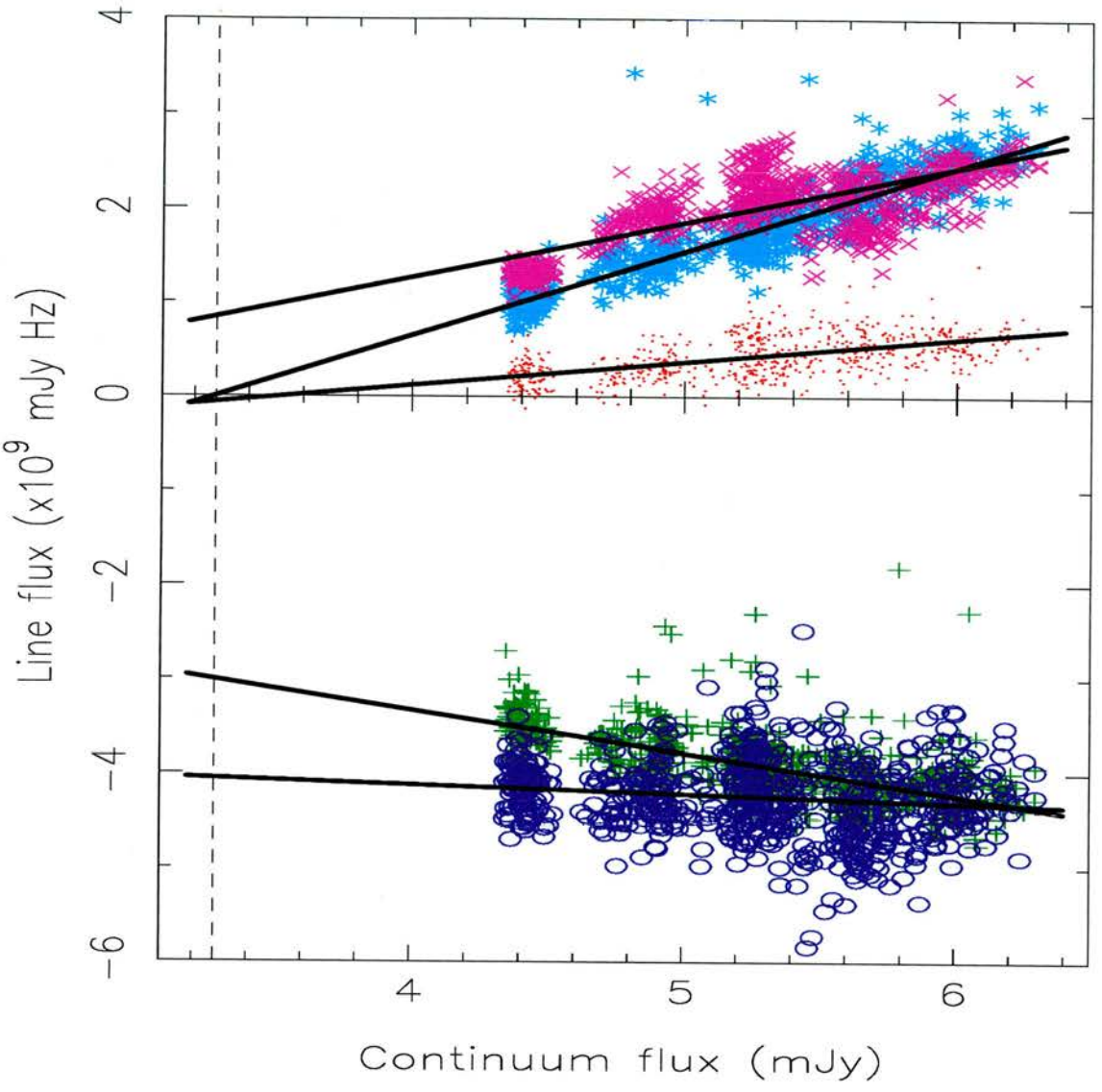

Figure 8.26: The relationship between the line and continuum (5000-5800 Å) fluxes of the optical spectra of Cygnus X-2 from the 5th night of our observation. The lines shown are H α (red dots), H β (green pluses), H γ (blue circles), Bowen blend (cyan stars) and He II (purple crosses). The thick lines are the best-fit lines to the individual lines. The vertical dashed line denotes the unirradiated limit, when the Bowen line flux is zero.

8.6 Discussion

I have used the unique dataset from Keck II and *RXTE* to investigate the simultaneous X-ray and optical variability in Cygnus X-2. I have found that on long timescales, $\sim$ hours, the X-ray and optical variability show a positive-correlation on the Normal Branch, changing to an anti-correlation on the Flaring Branch. However, on short timescales, $\sim$ seconds - minutes, the optical lightcurves show correlated, time-delayed features of the X-ray lightcurves. This is as expected in a linear reprocessing model. The short timescale correlated variability is seen to have a mean delay of around 60 seconds, which is too long for the delay to be due to reprocessing from the inner face of the companion star at the binary phase of the observations. This is however the time delay expected from reprocessing from the outer regions of the accretion disk.

The lightcurves show examples of both correlated (X-ray and optical) and non-correlated (X-ray only) dips. The correlated dips show large changes in the X-ray colour, as the spectrum gets harder during the dip. These dips are associated with obscuration of the central source by material in the inner regions of the accretion disk. The non-correlated dips however show little, if any, colour changes, indicating that the material is optically thick to X-rays. These are associated with material obscuring the line of sight from the splash of the accretion stream as it hits the outer regions of the accretion disk. This naturally leads to an explanation for the lack of correlated optical variability. The reprocessing region does not see the same changes in the X-ray flux and hence there is no reprocessed dip. This is to be expected if the material is along our line of sight and the reprocessing is taking place in the outer regions of the accretion disk, as the largest projected area for reprocessing will be on the far side of the disk.

The simultanseous X-ray and optical fluxes show a complicated correlation. Initially, whilst on the Horizontal Branch they are correlated with a fairly tight correlation. Then, when Cygnus X-2 is on the Normal Branch, the X-ray and optical flux changes become anti-correlated, whilst still exhibiting a strong correlation. Then, around S_z=1.5, the correlated variability changes again: the correlation becomes weaker with large changes in both the X-ray and optical variability.

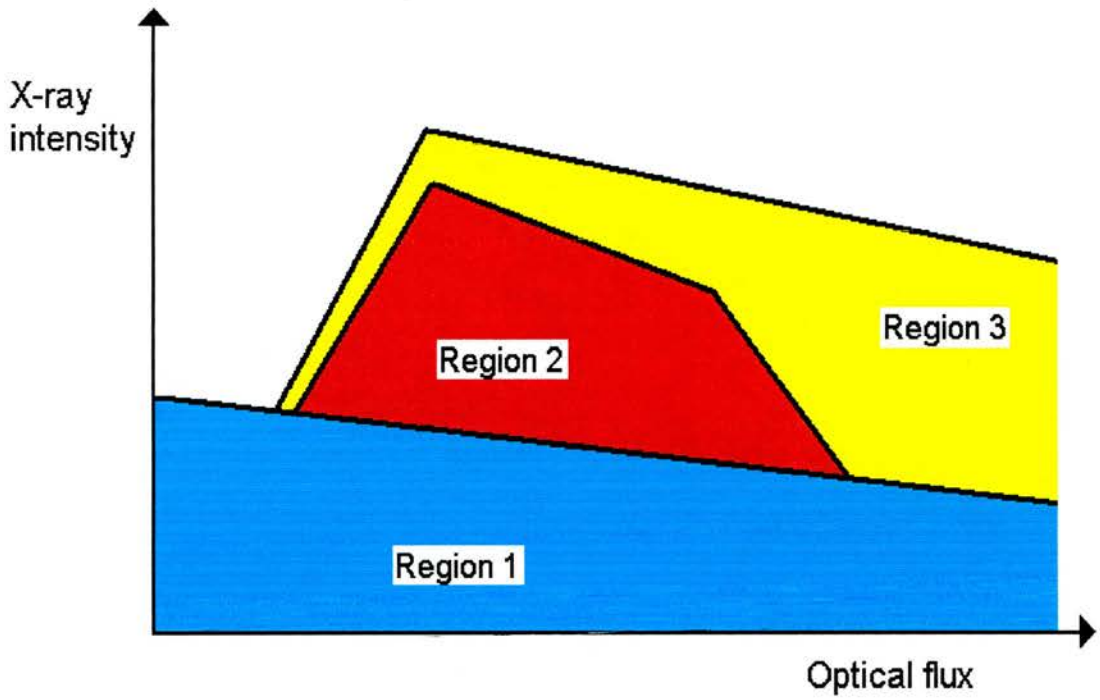

Figure 8.27: Schematic plot showing the correlated X-ray and optical behaviour. The plot is divided into three regions based on the descriptions in the text. Region 1 (blue) is the background component, region 2 (red) is the constant component and region 3 (yellow) is the variable component.

The X-ray flux appears to have three components, which I shall discuss individually and attempt to associate with physical processes occuring in the binary. The three components are associated with the components identified in Section 8.3 from Figure 8.3. This figure is shown schematically in Figure 8.27 to help identify the components. The first component coloured in blue represents a background level in the X-ray flux. The total X-ray flux does not enter into this region at any time in our observations, although it does lie on the upper bound of this level at several times, which is why I have called it the background level. The second component is the region coloured in red, which describes the average, slowly varying component of the flux. I have called this component the constant component, which isn't strictly accurate, but helps to distinguish the components easily, in a model independent manner. This component varies slowly with optical flux (or more precisely $\dot{M}$) and appears to represent the component seen in the X-ray colour-colour and hardness-intensity diagrams. The third component, coloured in yellow, represents the rapidly variable component of the X-ray flux. During our observations Cygnus X-2 is seen to vary between the upper and lower limits of this region. The only excursions it makes outside of this region are during colour independent dips and the two X-ray bursts observed.

If the X-ray flux represents changes in the accretion flow caused by the increasing mass accretion rate, we can attempt to link these three regions with regions of the accretion flow. It is clear that there are different phases in the behaviour of Cygnus X-2, represented by the different Branches of the colour-colour diagram. This would appear to represent the complex inter-dependency of more than one component of the X-ray emission. In order to attempt to decompose these components, I shall discuss each component independently and then try to bring them all together at the end. For ease, I have named the three components the variable, constant and background components.

[NB. In the following discussion I shall use the term 'mass transfer rate' to describe the total amount of material that has passed through the inner Lagrangian point and the term 'mass accretion rate' to describe the amount of material being accreted onto the neutron star. These are equal if the mass loss rate from the system is zero.]

1. The variable component (yellow region):

   At low mass transfer rates, the variable component is small, increasing, possibly linearly, with mass transfer rate. The X-ray flux appears to change randomly in this region, but remains in the region, except during X-ray bursts and non-correlated dips, which I therefore do not associate with this region. As the mass transfer rate increases the ram pressure of the material in the inner accretion flow will increase. This will cause a 'pinching' of the magnetosphere, as material is allowed to fall further into the potential well of the neutron star before being threaded onto the magnetic field lines. During this time the accretion flow will emit thermal X-rays, due to the increasing temperature of the flow. It is for this reason that I associate the variable component with the soft component from the inner regions of the accretion disk.

   Interestingly, the short timescale correlated variability, also appears to be linked with this component. Evidence for this is in the correlated flares at the beginning of the observations and the lack of correlations on the Horizontal Branch. I will discuss this later, when I disuss the contributions from all three components. The correlated dips are also associated with this region. The spectra harden during the dips, which can be described by an attenuation of the soft component by material in the inner regions of the accretion flow.

2. The constant component (red region):

   If I associate the variable component with that from the inner regions of the accretion disk and assume that the constant and variable components come from physically different regions, then this naturally leads to considering the constant component as coming from the polar regions of the neutron star. Accretion onto the neutron star from this region should reduce as the mass transfer rate increases, as more material is accreted via the method described in the variable component, leaving less material available to accrete onto the polar regions. In this model one would expect the constant component to *decrease* with increasing mass transfer rate, however as one can see from the diagram, this is only true for the highest mass transfer rates, when Cygnus X-2 is on the lower Normal and Flaring branches. The rest of the time the constant component *increases* with mass transfer rate. This would seem to defeat

this model. However, as I stated earlier, one must draw the distinction between mass transfer and mass accretion rates. In Z-sources, it has been observed that the radio emission, which is linked to the mass outflow from the system, possibly in the form of a jet (Fender & Hendry 2000), is greatest at the lowest mass transfer rates (Penninx et al. 1988). This means that the material available for accretion onto the poles of the neutron star is small at the lowest *and* highest mass transfer rates, as observed.

The optical flux does not appear to be well correlated with this constant component, as it increases linearly throughout the observations and doesn't show any effects of the increasing and then decreasing X-ray intensity.

3. The background component (blue region):

   I have called the third component the background component, but it is not clear what physical mechanism is responsible for it. As I have said earlier the background component appears to describe the lowest possible X-ray intensity. The intensity is seen to fall to this level, but never below, during X-ray dips. The occurence of such dips to the background level increases as the mass transfer rate increases, which is possibly associated with changes in the inner accretion flow, as discussed earlier in the section on the variable component.

   The observed background level changes between the observations of the Horizontal and Flaring Branches. However it is not possible to determine from these limited observations, if this change is due to the change in mass transfer rate, binary phase, the super-periodicity, or some other slowly varying undiscovered cause. Some possible mechanisms for producing such and effect are that it comes from the outflow, that changes with mass transfer rate, from reflection from the inner face of the donor star, that modulates with binary phase (although this is unlikely due to the lack of evidence for reprocessing on the companion star) or that it is from whatever mechanism is driving the super-periodicity.

The identification of these three distinct components, based on not only their X-ray but also optical characteristics, allows us to explain some of the other observed phenomena. One of the most interesting, and puzzling in the reprocessing model, features of

the lightcurves is the observation of X-ray flares that do not show any correlated optical variability. These features can now be easily explained using the different components. Material accreting at the polar regions of the neutron star will build up until sufficient is available to cause a nuclear reaction, that is observed as an X-ray burst. However, we have shown that only the soft component appears to be available for reprocessing, so we do not expect to see any reprocessed optical burst.

Another prediction of this model that agrees with observations is the features of the HBOs observed in Cygnus X-2. If this QPO is associated with the region where material is threaded onto the magnetic field lines, then the frequency will increase as the mass transfer rate increases, due to the increase in ram pressure of the material of the disk. The amplitude will however decrease as less material will be threaded onto the field lines and also the range of frequencies, the FWHM of the QPO, will increase as the range of threading radii increases with the increasing mass transfer rate. These predictions are in excellent agreement with observations of the behaviour of HBOs in Z-sources (Jonker et al. 2000).

In this chapter I have shown that there is a complicated correlation between the different components of the X-ray variability in Cygnus X-2. However, using the simultaneous X-ray and optical observations presented here, we have been able to identify separate components of the variability and associate them with physically different regions of the binary. By isolating the different components of the variability and including radio observations, we may be able to investigate further the X-ray emission mechanisms and the effects of the irradiation in Cygnus X-2 and other LMXBs.

CHAPTER 9

Timing analysis of X-ray and optical variability in Hercules X-1

Hercules X-1/HZ Herculis belongs to the sub-class of LMXBs known as X-ray Pulsars. Hercules X-1 is a $1.4M_{\odot}$ neutron star with a 1.24 second pulse period. It is in a 1.7 day binary orbit with its $\sim 2M_{\odot}$ companion star, HZ Herculis, whose spectral type varies from late A to early B over the orbital cycle, presumably from heating of the innerface by strong irradiation from Hercules X-1 (Reynolds et al. 1997). Due to the high inclination of the system, $i = 85°$, it is an eclipsing system.

The variability of Hercules X-1 has been very well studied at all wavelengths. In the X-rays the spin of the neutron star is observed, modulated by the orbital eclipses and a third 35-day cycle. This 35-day X-ray periodicity was first discovered by Tananbaum et al. (1972) using the *UHURU* satellite as an X-ray on-state followed by an extended off-state. Jones & Forman (1976) later reported a weaker short-on state during the off-state. Figure 9.1 shows the form of the 35-day cycle, it shows the average of nearly 19 000 observations covering 966 days between MJD 50133-51099 by the All Sky Monitor (ASM) onboard *RXTE*. The data have been folded on the 35-day period and binned to a suitable resolution, using the method described by Scott & Leahy (1999). In this plot the definition of phase 0 is chosen to be at turn-on of the main-on state and the cycle is repeated to show more than one complete cycle. As can be seen from the figure, the phase folded lightcurve consists of a main-on state, lasting about 10 days, and a short-on state lasting 5 days, separated by periods where the X-ray flux drops to almost zero. The X-ray pulsations are clearly seen during the on-states but appear with a much lower amplitude during the off states, as expected if the cycle is caused by the obscuration of the central regions of the accretion disk. The evolution of the pulse profile between and during these on-states has

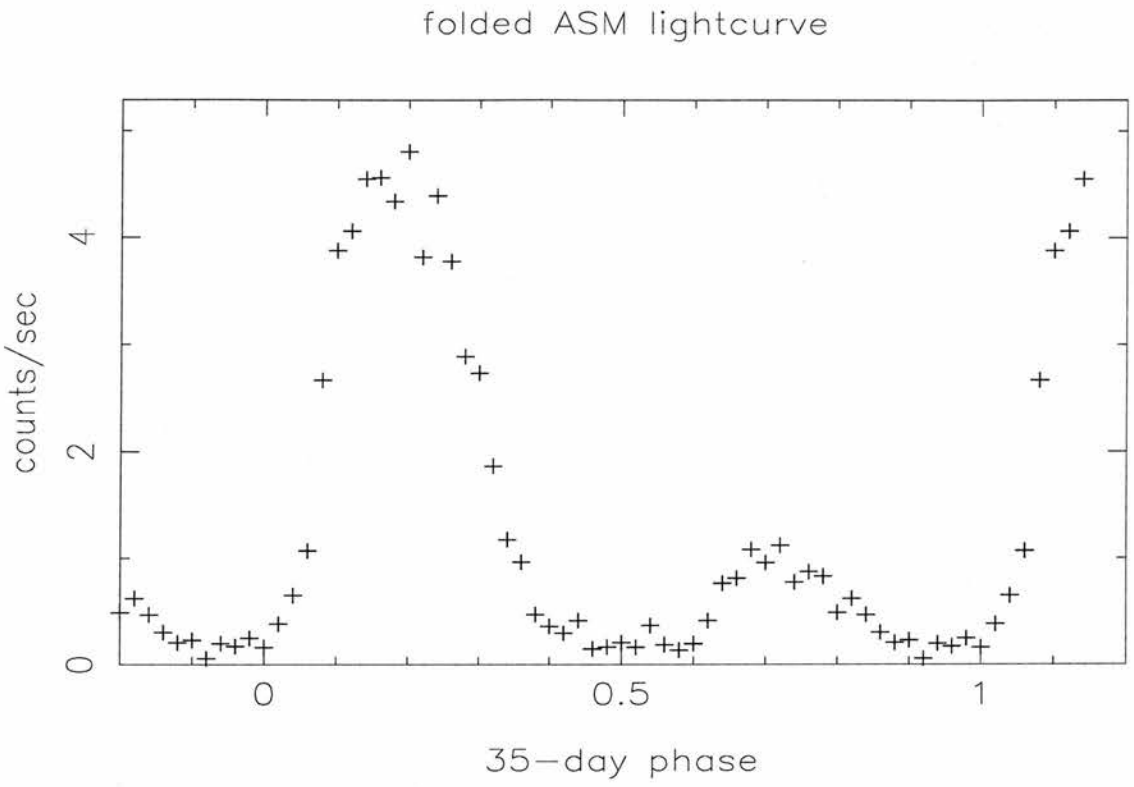

Figure 9.1: *RXTE* ASM lightcurve showing the orbital and 35-day modulations in the X-ray lightcurve.

been well studied but the origins and evolution of its complex structure remain poorly defined. Deeter et al. (1998) used *Ginga* and *UHURU* data to define the behaviour of several distinct features in the folded pulse profile. They have been able to place several constraints on the mechanism and position of the formation of the pulse profile. They find that the changes in the distinct features are indeed repeatable over several 35-day cycles and that the mechanism responsible for the 35-day period is likely to be the cause of the changes in the pulse profile.

While the existence and form of the 35-day cycle is well documented, the mechanism responsible is less well understood. It is thought to be caused by a warped, precessing accretion disk that occults the neutron star at certain disk phases. The warp in the disk may be formed by an X-ray driven coronal wind (Schandl & Meyer 1994). In this model the X-rays from the central compact object irradiate the inner regions of the accretion disk and produce a hot corona, when the sound velocity of the gas exceeds the escape velocity of the potential well the material leaves the binary as a coronal wind, exerting a

repulsive force on the disk. Schandl & Meyer (1994) showed that, with suitable boundary conditions, they could create a suitable warp to explain the general features of the 35-day cycle. This model can also explain the observed anomalous and pre-eclipse dips as an interaction of the accretion stream with the warped disk, causing disk thickness increases that temporarily obscure the line of sight to the X-ray source, causing a dip in the X-ray flux (Schandl 1996). The most likely and well studied model for the disk precession is the interaction of the tidal force of the companion star with the tilted disk, which forces the disk to precess at a rate determined by the orbital period (Katz (1973), Larwood (1998)).

At optical wavelengths, much of the light is due to X-ray heating of the inner face of the companion star. This effect is seen to modulate on the binary phase and with the 35-day super-period, implying the companion star is irradiated even during the observed X-ray off states. Evidence for reprocessing of X-rays on the companion star of Hercules X-1 comes from the observed optical pulsations (Middleditch & Nelson 1976).

While it would appear that with this wealth of observational data we should have a clear understanding of the multi-wavelength variability in Hercules X-1, in reality the system continues to do surprising things. In 1999, shortly before a series of observations to study the simultaneous X-ray/UV/optical variability in the source, the X-rays appeared to switch off and the system went into an anomalous low state (Parmar et al. 1999).

We have observed another new phenomenon in this object. We have found a low frequency optical Quasi-Periodic Oscillation (QPO) with a frequency of 35 mHz. This QPO has also been observed in the UV (Boroson et al. 2000) with a frequency of 45 mHz. While these observations are not simultaneous with the optical data presented here, the similarity of the frequencies implies a similar production mechanism.

In this chapter I will describe the optical characteristics of the QPO and attempt to determine the position of the region in the binary producing the variability.

9.1 Discovery of a low frequency optical QPO

9.2 Data

The optical data were taken using the Low Resolution Imaging Spectrograph (LRIS) on the 10-m Keck II telescope on Mauna Kea, Hawaii between UT 07:40 and UT 08:50 on 6/7/98. We used a novel data system, the GOMERIZER (see chapter 6 for details), to obtain more than 58,000 2048 pixel spectra of Hercules X-1. The lightcurve showing the total dataset is shown in figure 9.2, while a subset of the data, that clearly shows the QPO is shown in Figure 9.3. Each spectrum has a mean integration time of 72 msecs and a signal-to-noise of $\sim 10\text{pixel}^{-1}$ in the wavelength range $\lambda\lambda 3600-8000\mathring{A}$, with a resolution of 2.45 $\mathring{A}/pixel$. The data were wavelength and flux calibrated using the methods described in Chapter 6.

9.3 Results

To characterize the variability of the source, I used two methods described in Chapter 7. I have firstly created power spectra of the source to determine the temporal characteristics of the variability, then I have used this information to determine the spectral characteristics by means of a variability spectrum.

9.3.1 The power spectrum

I created power spectra for the data-set by simple sine-curve fitting to the lightcurve. This method was preferred to fast Fourier transforms (FFTs) due to the presence of irregular gaps in the data. The resulting power spectrum is shown in Figure 9.4. The power spectrum can be decomposed into three distinct components; (1) white noise power at all frequencies, P_{wn}, (2) a low frequency power-law describing the intrinsic flickering of the source, P_{pl}, and (3) a hump-like QPO feature, P_{qpo}, described as a Gaussian. These features can be described numerically as,

$$P(\omega) = P_{wn}(\omega) + P_{pl}(\omega) + P_{qpo}(\omega)$$

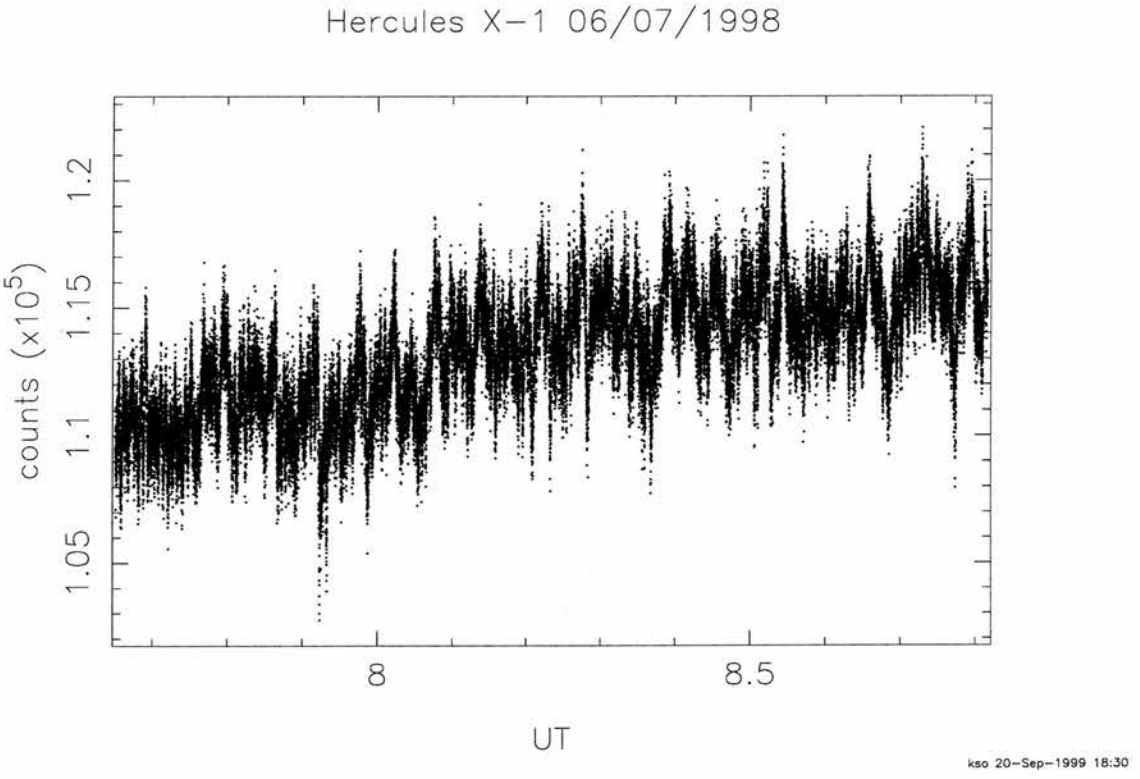

Figure 9.2: Lightcurve showing the total number of counts in the range 3700 - 7000 $\AA$ for all the data.

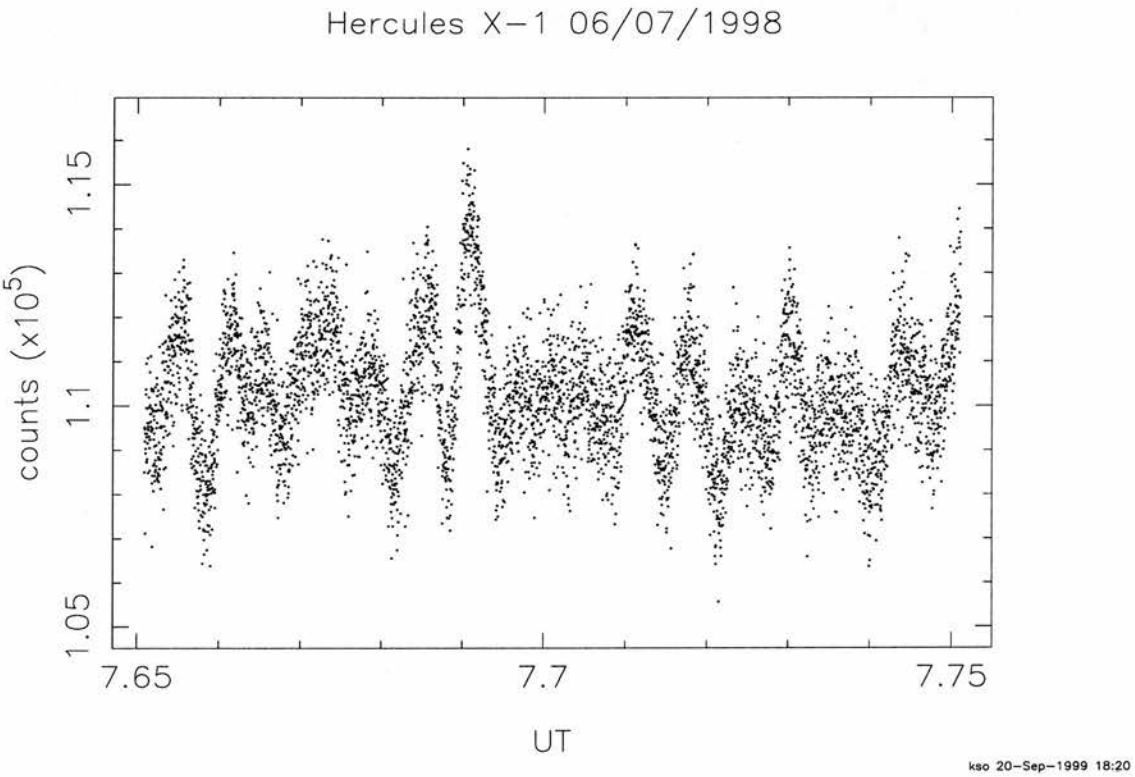

Figure 9.3: Lightcurve showing the total number of counts in the range 3700 - 7000 $\mathring{A}$ for a segment of the data, showing the presence of the QPO.

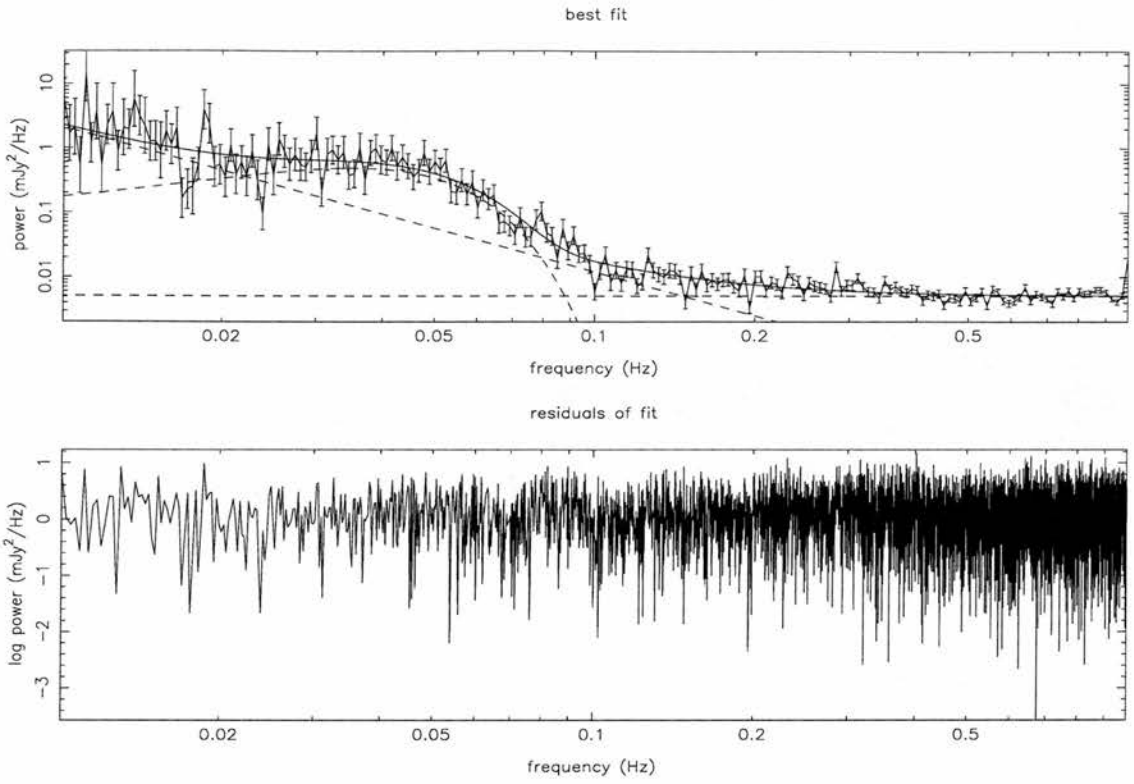

Figure 9.4: Top, the binned power spectrum for the total dataset, showing the best fit model (solid line), with a $\chi^2 = 1.581$ for 4687 degrees of freedom. The individual components (dashed lines) are also shown based on their best fit parameters. Bottom, the residuals of the fit, showing the full resolution of the power spectrum.

$$\begin{aligned} &= A_{wn} \\ &+ A_{pl}\left(\frac{\omega}{\omega_p}\right)^{-\alpha} \\ &+ A_{qpo}\exp\left[-\frac{1}{2}\left(\frac{\omega-\omega_0}{\Delta\omega}\right)^2\right], \end{aligned} \tag{9.1}$$

where A_{wn} is the power of the white noise level, A_{pl} is the power of the power law slope at ω_p, where ω_p is fixed to be 0.1 Hz, α is the power law index, A_{qpo} is the peak power of the Gaussian QPO feature at ω_0, the central frequency of the QPO and $\Delta\omega$ is the width of the QPO. From this we can find the coherence, Q, and power, P_{qpo} of the QPO. The coherence of the oscillation is given by

$$Q = \frac{\omega_0}{\Delta\omega}. \tag{9.2}$$

The total power contained in the QPO, P_{qpo}, is found by integrating the expression for

the fit to the QPO,

$$\begin{aligned} P_{qpo} &= \int_0^\infty A_{qpo} \exp\left[-\frac{1}{2}\left(\frac{\omega-\omega_0}{\Delta\omega}\right)^2\right] d\omega \\ &= \sqrt{2\pi}\, A_{qpo}\, \Delta\omega. \end{aligned} \tag{9.3}$$

The fractional peak to peak amplitude is given by,

$$amp = \frac{2 * \sqrt{P_{qpo}}}{(Average flux)}, \tag{9.4}$$

where the average flux is found from the input lightcurve. The fractional error in the power is given by,

$$\frac{\delta(P_{qpo})}{P_{qpo}} = \sqrt{\left(\frac{\delta(A)}{A}\right)^2 + \left(\frac{\delta(\Delta\omega)}{\Delta\omega}\right)^2}. \tag{9.5}$$

This gives a fractional error in the peak to peak amplitude of

$$\begin{aligned} \frac{\delta(amp)}{amp} &= \frac{1}{(Average flux)} \frac{\delta(P_{qpo})}{P_{qpo}} \\ &= \frac{1}{(Average flux)} \sqrt{\left(\frac{\delta(A)}{A}\right)^2 + \left(\frac{\delta(\Delta\omega)}{\Delta\omega}\right)^2}. \end{aligned} \tag{9.6}$$

The best fit values of the free parameters are shown in Table 9.1. These are found using an amoeba code to search through the parameter space (see Press et al. (1992) for a discussion of amoeba codes). The best fit has a reduced χ^2 of 1.581 for 4687 degrees of freedom. I have determined the 1-parameter 1-sigma confidence regions for each parameter by fixing a parameter and then optimizing the fit until the reduced χ^2 is equal to χ^2_{aim}. χ^2_{aim} is determined using the value of χ^2_{min}, where,

$$\chi^2_{aim} = \chi^2_{min} + \frac{\chi^2_{min}}{N-P}, \tag{9.7}$$

where $N-P$ is the number of degrees of freedom in the fit. The confidence regions are also shown in Table 9.1. The average flux in the lightcurve was 18.53, this means that the peak-to-peak amplitude of the QPO is 5.0%, this is shown together with its 1-sigma confidence region based on Equation 9.6 in Table 9.1.

9.3.2 A reprocessed X-ray QPO ?

In order to determine if the optical QPO is a reprocessed version of an X-ray QPO I have calculated power spectra of the X-ray data simultaneous with our optical data. I

Parameter	unit	value	upper bound	lower bound
A_{wn}	$10^{-3}\,mJy^2\,Hz^{-1}$	5.09	0.14	0.15
α		2.25	0.13	0.18
A_{pl}	$10^{-2}\,mJy^2\,Hz^{-1}$	12.0	1.4	1.4
A_{qpo}	$10^{-2}\,mJy^2\,Hz^{-1}$	49.30	10.4	7.1
ω_0	mHz	35.2	4.3	8.1
$\Delta\omega$	mHz	17.4	3.7	2.6
P_{qpo}	$10^{-2}\,mJy^2$	21.5	6.4	4.5
QPO peak-to-peak amplitude	percent	5.00	0.24	0.17

Table 9.1: Best fit values for the model described in Equation 9.1, used to fit to the power spectrum of total dataset. The best fit reduced χ^2 was 1.581 for 4687 degrees of freedom.

have chopped the total X-ray lightcurve into 200-s segments and created individual Leahy normalized power spectra for each lightcurve. I have then combined the separate power spectra to create a total power spectrum for the observations. This method is more successful at determining the power in the QPO as the QPO spans a broad range of frequencies and is only coherent over short timescales.

The average power spectrum shows no evidence for the QPO at 0.035 Hz, implying the optical QPO is not simply a reprocessed version of an X-ray QPO.

9.3.3 Discussion

This represents the first detection of a low frequency optical QPO from Hercules X-1. Using a suitable model for the power spectrum, consisting of components from the white noise, the power-law and the QPO, I have determined the characteristics of the QPO. This has been done using a χ^2 analysis and an amoeba code to search through the parameter space. The best fit to the power spectrum of the QPO has a central frequency of 35 mHz and a peak-to-peak amplitude of 5 %. The coherence of the oscillation is however very low ($\sim$ 2), implying that the variability is probably from a lot of short-lived distinct events. I have shown that there is no evidence in the simultaneous X-ray lightcurve for an X-ray counterpart to the QPO, implying that the QPO is not simply reprocessed somewhere in the binary. This is in contrast to previous observations of optical pulsations on the spin period, that are thought to be reprocessed X-ray pulsations, probably originating on the inner face of the companion star.

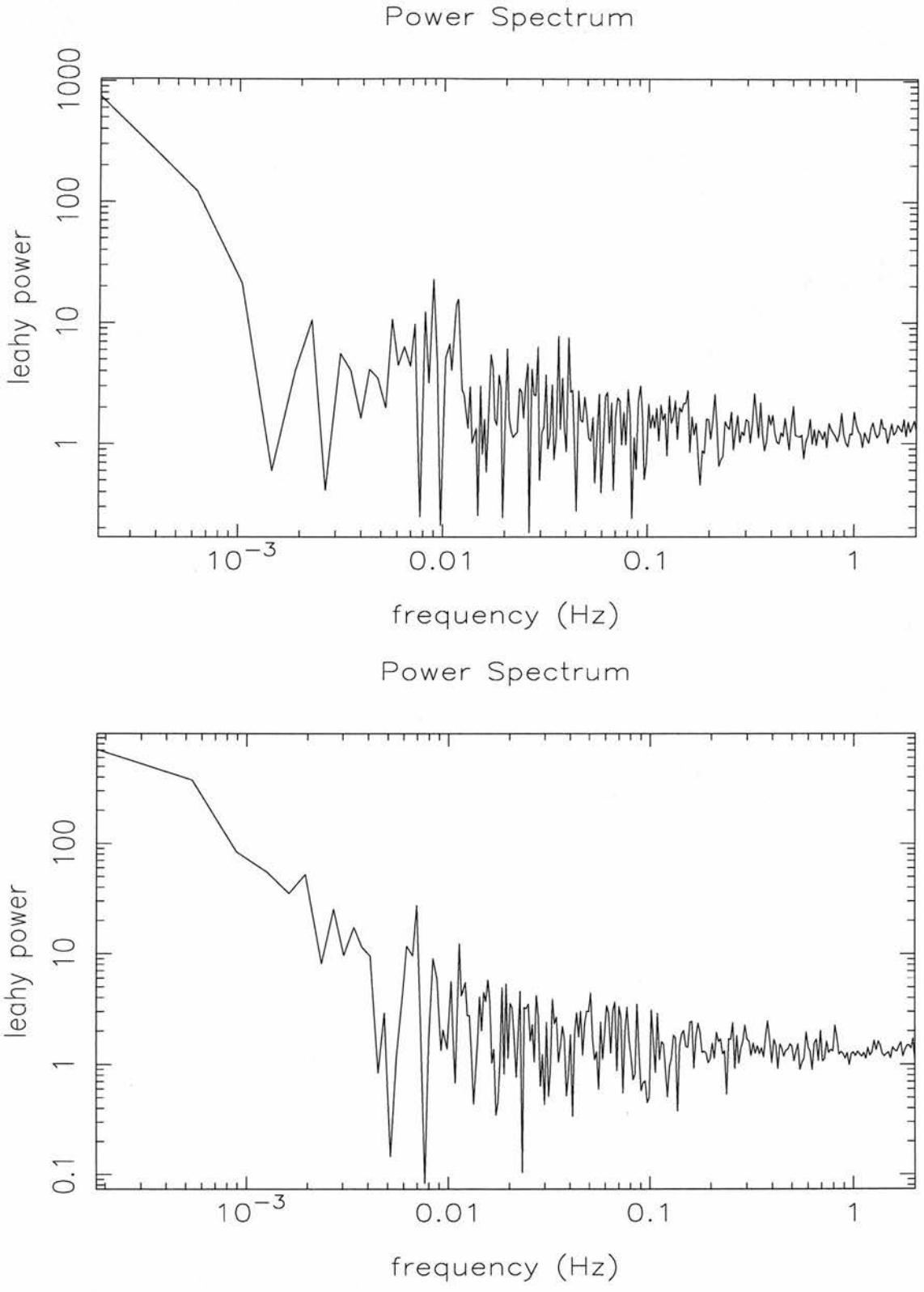

Figure 9.5: Top panel, the total X-ray power spectrum for orbit 1, binned to a minimum resolution of 0.01 Hz. Lower panel, the same plot but for the data from Orbit 2. These power spectra show no evidence for excess power in the region of the QPO.

9.4 The spectrum of the variability

Having determined the existence of the QPO and its pulse fraction, the next stage is to find the spectrum of the QPO in order to try and find the possible regions of the binary that could be responsible for its production. In order to do this we have created variability spectrum-lightcurve pairs based on the method described in Chapter 7.1. The model, $M(\lambda, t)$, can be written as,

$$M(\lambda, t) = S_0(\lambda) + S_1(\lambda)\,\overline{L_1(t)} + S_2(\lambda)\,\overline{L_2(t)}, \tag{9.8}$$

where S_0 is the average spectrum, S_1 and L_1, are the spectrum and lightcurve of the first variable component and S_2 and L_2 are the spectrum and lightcurve of the second variable component.

The input lightcurve is shown in Figure 9.2 and the results of the fitting routine in Figures 9.6 and 9.7. In order to separate the variability components we have filtered the lightcurves with Savitzky-Golay filters of different widths. The first spectrum-lightcurve pair had a filter of width 80-s, to remove any variability on shorter timescales, leaving only the slower variability. In addition to this the lightcurve was detrended with a linear fit to remove the overall trend in the data, caused by the orbital motion of the binary (This is known as the slow component). The second spectrum-lightcurve pair was also filtered using a Savitzky-Golay filter, with a filter width of 10-s. The purpose of this filter was to remove most of the white noise component from the lightcurve. Thus the second spectrum-lightcurve pair represents the variability with frequencies between the two filter widths, the frequencies around the QPO (This is known as the QPO component).

In the first variability lightcurve the fluctuations seen with frequencies around 0.01 Hz are resolved. The spectrum of this variability is bluer than the average spectrum and accounts for about 1% of the total flux, as can be seen in Figure 9.8. The second variability lightcurve shows the variability of the 35 mHz QPO and how it is not coherent over more than a few cycles. The spectrum of this variable component accounts for about 0.5% of the total flux and is also bluer than the average spectrum. It shows similar spectral features to those of the first variability spectrum. Both variability spectra show that the Balmer lines vary on average more than the continuum,whereas the He II line at 4685 Å

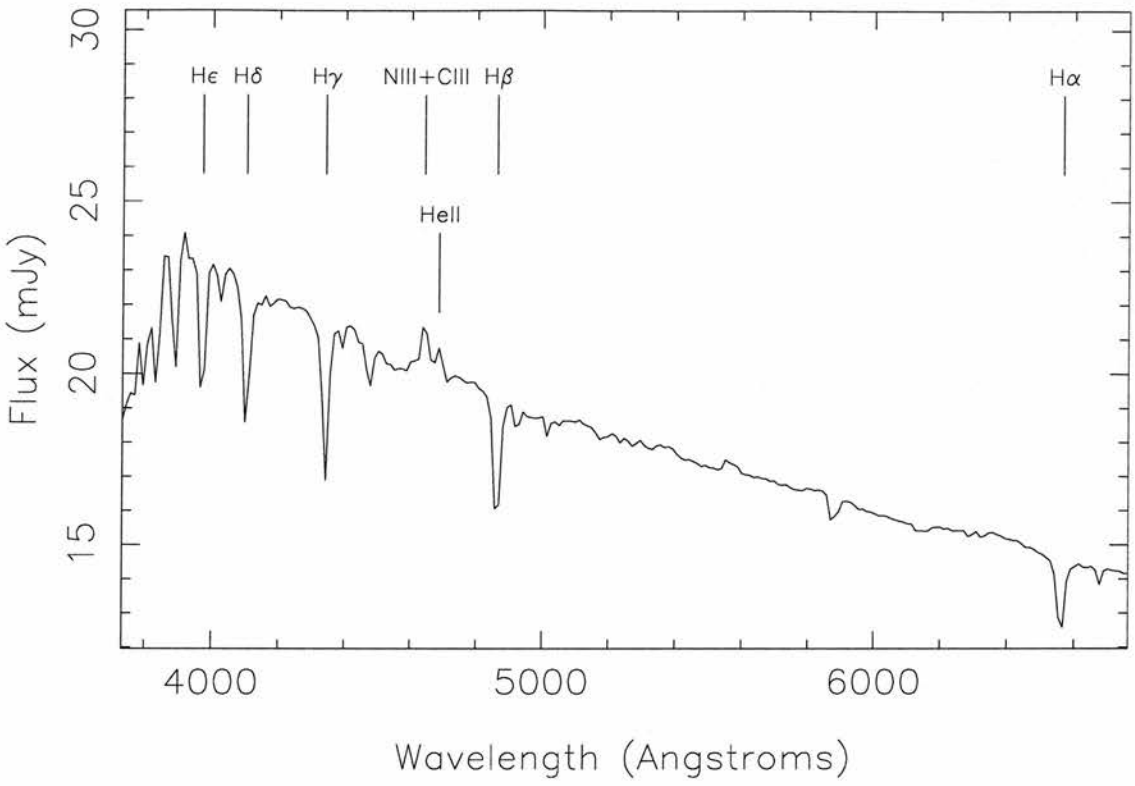

Figure 9.6: The constant spectrum of Hercules X-1.

varies less than the continuum. The NIII + CIII blend at 4641 Å also appears to show a strong variable component. This line is especially interesting as it is a blend of two formed by Bowen Fluorescence and it thought to be caused by irradiation of the binary by the central X-ray source.

These results agree well with the previous power spectra. The average flux in the second variability spectrum, shown in the third panel in Figure 9.7, is in good agreement with the flux in the QPO and the variability lightcurve shows variability on the same timescales as the QPO period. This strongly suggests that the second variability spectrum represents the spectrum of the QPO.

In the next section I will describe fits to the component spectra to constrain the size and temperature of the emitting regions.

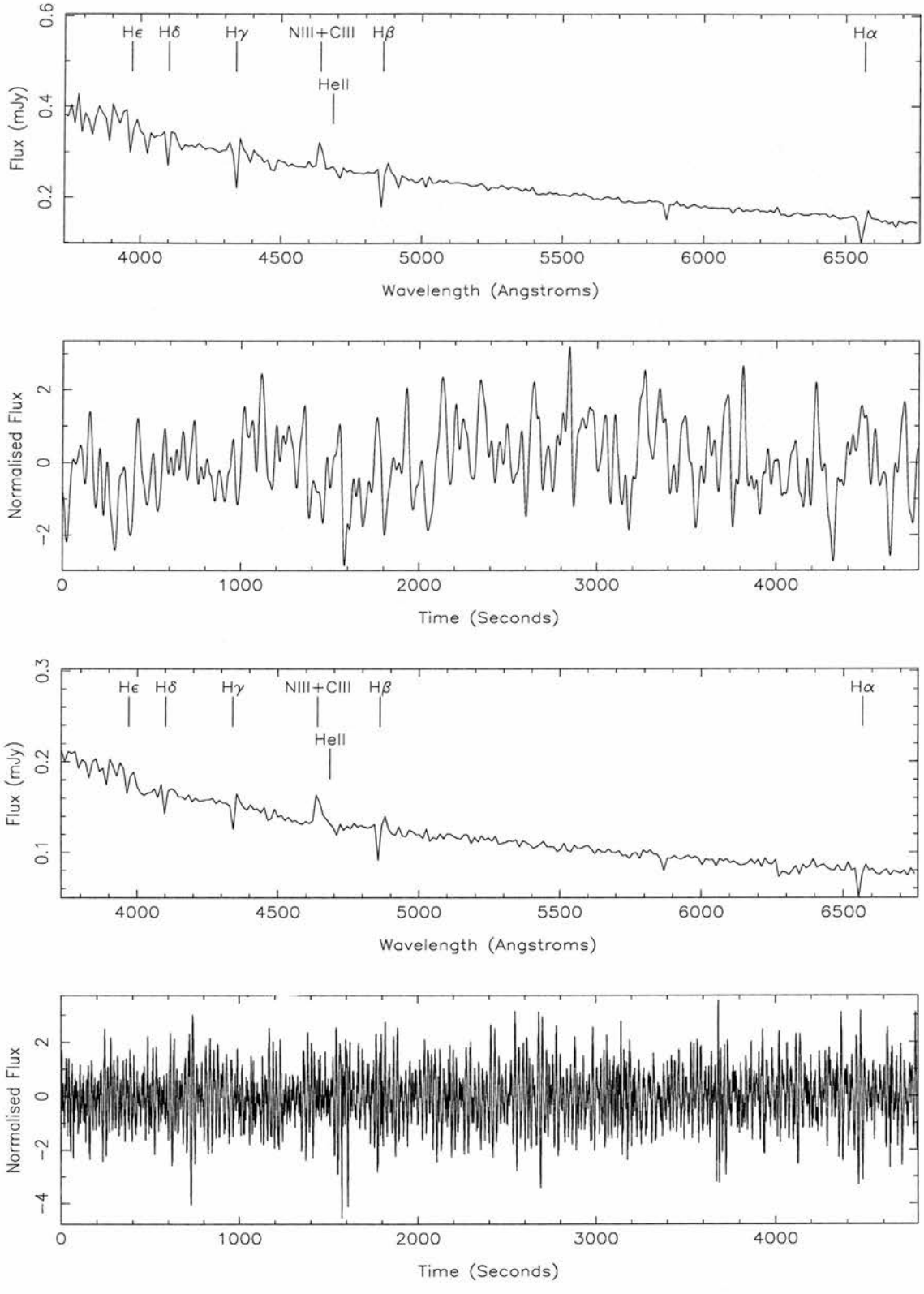

Figure 9.7: The first and second variability spectra and their associated lightcurves. The first variability lightcurve is detrended and filtered with a half-width 40 seconds. The second variability lightcurve is filtered with a half-width of 5 seconds.

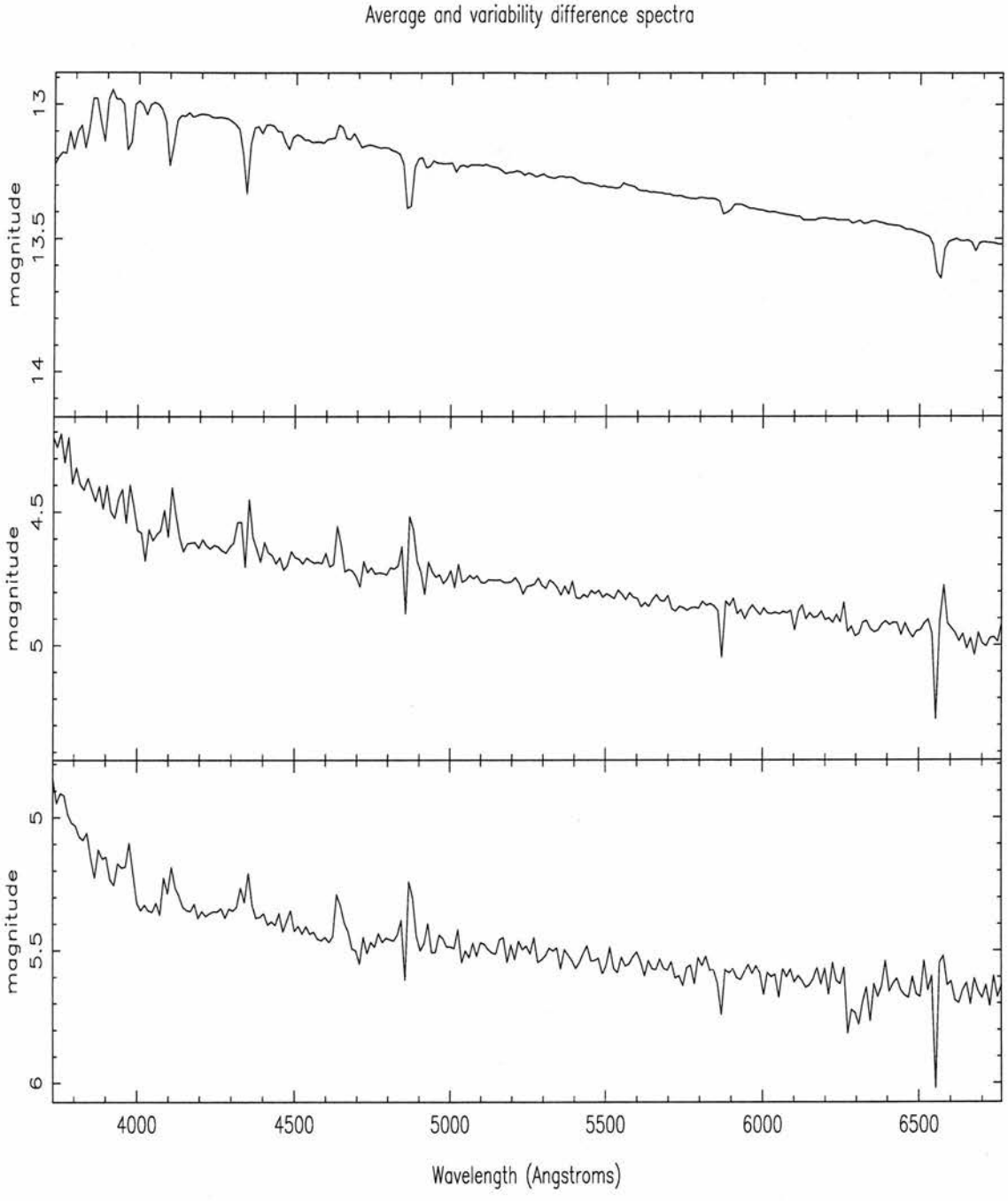

Figure 9.8: Top panel, the average spectrum in magnitudes of Hercules X-1. Middle and bottom panels, the difference between the first and second variability spectra, respectively, and the average spectrum.

9.5 Spectral fits to variability spectra

The next stage of the analysis is to fit model spectra to the data to fit physical parameters to the observed average and variability spectra from the previous analysis. To do this I have used two models to see which best represents the data. Both models use blackbody spectra to describe the observed continuum fluxes. The spectrum observed from a blackbody is given by,

$$\begin{aligned} F_\nu(\lambda) &= \int B_\nu(\lambda, T)\, d\Omega \\ &= \frac{\pi R^2}{D^2} \frac{2hc}{\lambda^3 \left[\exp\left(\frac{hc}{k\lambda T}\right) - 1\right]}, \end{aligned} \tag{9.9}$$

for a region with a radius, R, and a temperature, T, at a distance D.

1. A single blackbody:

   This will tell us the temperature and size of the emitting region. The model spectrum is defined at a wavelength, λ, as,

   $$F_\nu(\lambda) = \frac{\pi R^2}{D^2} B_\nu(\lambda, T_{mean}) \tag{9.10}$$

   for a region with a radius, R, a temperature, T_{mean}, at a distance D. This model is most useful for a region that has a roughly constant temperature for the duration of the observations.

2. The derivative of a blackbody:

   The second model is fitting the derivative of a blackbody to the data. This involves fitting the difference of two blackbodies with different temperatures, T_{mean} and T_{max}, where $T_{max} > T_{mean}$. The model spectrum is defined at a wavelength λ as,

   $$F_\nu(\lambda) = \frac{\pi R^2}{D^2} \left[B_\nu(\lambda, T_{max}) - B_\nu(\lambda, T_{mean})\right] \tag{9.11}$$

   for a region with a radius,R, at a distance D. This model is most useful for describing a region whose temperature varies during the observations. These variations are limited to coming from the same region, ie a single region where the temperature varies between T_{mean} and T_{max}.

	unit	average spectrum	slow variability	fast variability
model 1:				
Temp	K	$16500\ ^{+100}_{-100}$	$37000\ ^{+1000}_{-1000}$	$33600\ ^{+1500}_{-1400}$
Radius	10^{10} cm	$29.36\ ^{+0.19}_{-0.20}$	$1.64\ ^{+0.04}_{-0.03}$	$1.26\ ^{+0.03}_{-0.04}$
$\chi^2/100$		9016	3.919	2.966
model 2:				
T_2	K	$600\ ^{+1900}_{-\text{inf}}$	$7600\ ^{+9900}_{-3800}$	$600\ ^{+4400}_{-\text{inf}}$
T_1	K	$16500\ ^{+100}_{-100}$	$31400\ ^{+5700}_{-14600}$	$33600\ ^{+1500}_{-1700}$
Radius	10^{10} cm	$29.4\ ^{+0.2}_{-0.2}$	$1.89\ ^{+\text{inf}}_{-0.24}$	$1.26\ ^{+0.04}_{-0.04}$
$\chi^2/99$		9107	3.904	2.996

Table 9.2: Summary of best fit parameters to the spectral fitting of the spectra from the variability model, together with their 1-parameter 1-sigma confidence regions. A distance of 5kpc was assumed throughout.

These models are fitted to regions of the spectra that are least contaminated with lines. The best fit values, together with their 1-parameter 1-sigma confidence regions are shown in Table 9.2. The data together with the best fit and the regions used are shown in Figures 9.9 - 9.11.

9.5.1 Discussion

In this section I have characterized the observed optical variability in Hercules X-1. I have found that the average spectrum is different from the spectra of the variability, by decomposing the spectral time-series into distinct components, based on information from the previous section on the power spectrum of the variability. I find that the temperature observed for the average spectrum is consistent with an irradiated region covering a large fraction of the inner face of the donor star. However the temperature and size of the region responsible for the variability associated with the QPO are more likely found in the accretion disk.

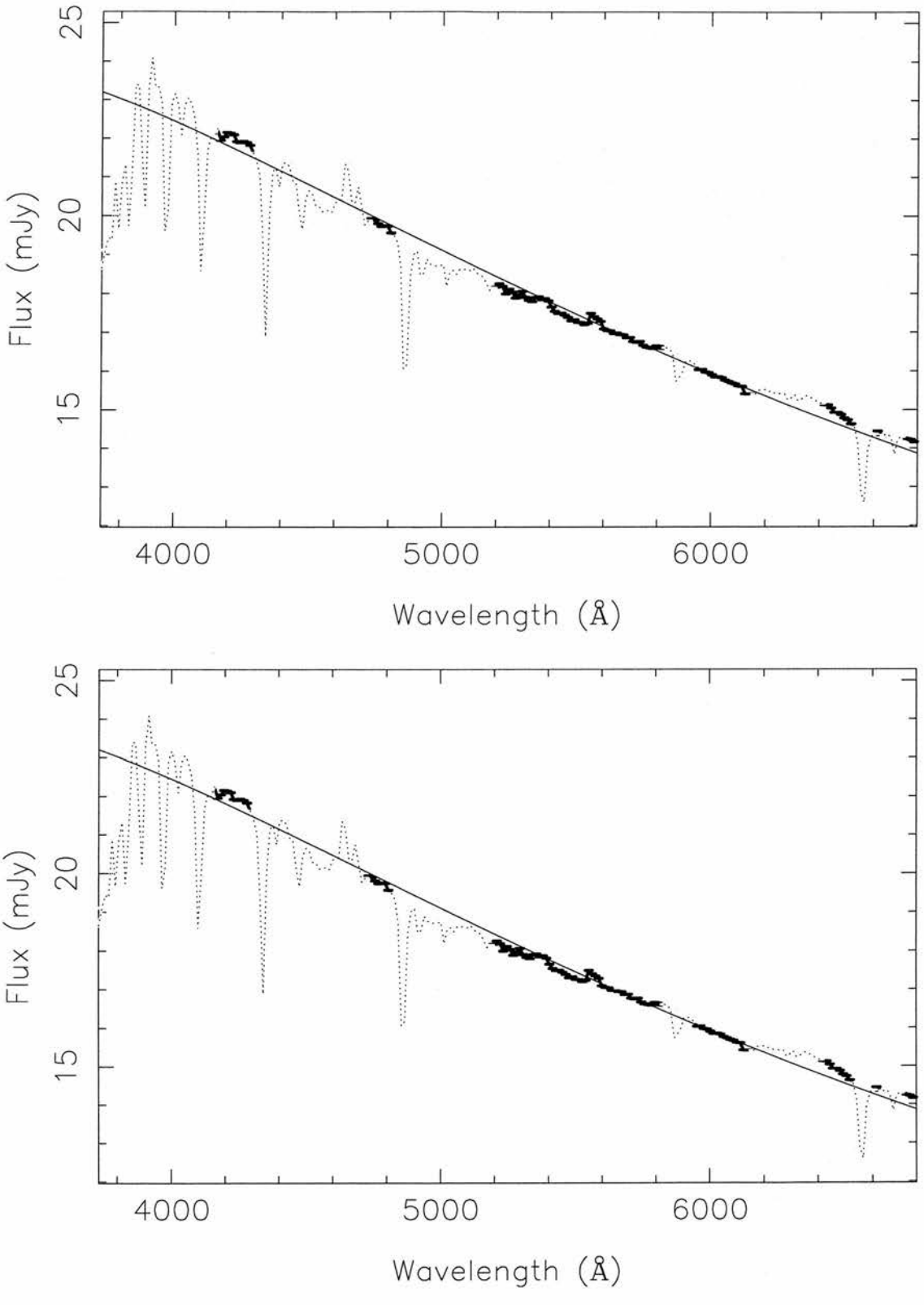

Figure 9.9: Top panel, a plot of the average spectrum and its best-fit blackbody. The dotted line shows the data points not used in the fitting routine, the solid points are the data used and the solid line is the best fit blackbody. Lower panel, The same plot as above with the blackbody derivative model.

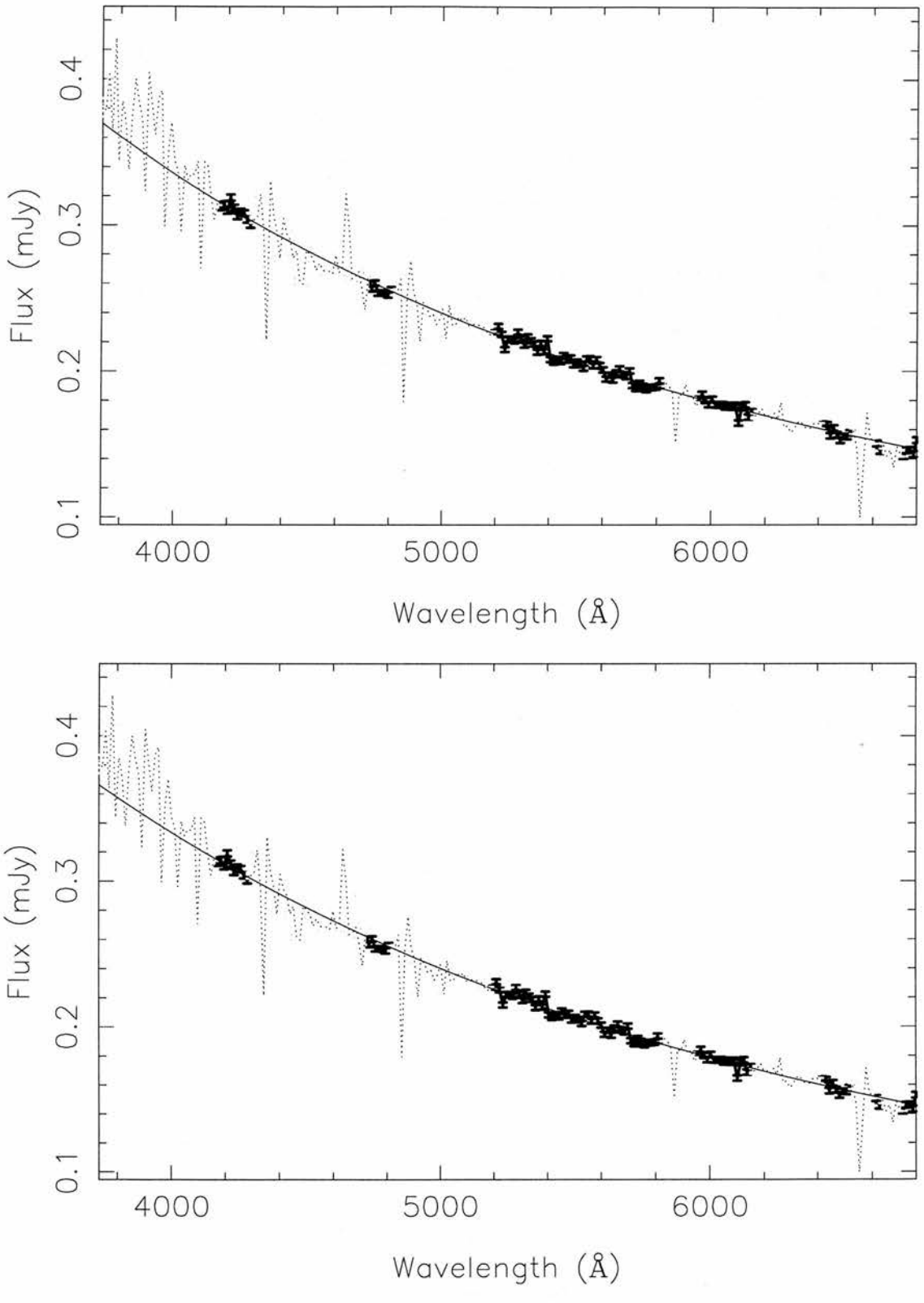

Figure 9.10: Top panel, a plot of the slow variability spectrum and its best-fit blackbody. The dotted line shows the data points not used in the fitting routine, the solid points are the data used and the solid line is the best fit blackbody. Lower panel, The same plot as above with the blackbody derivative model.

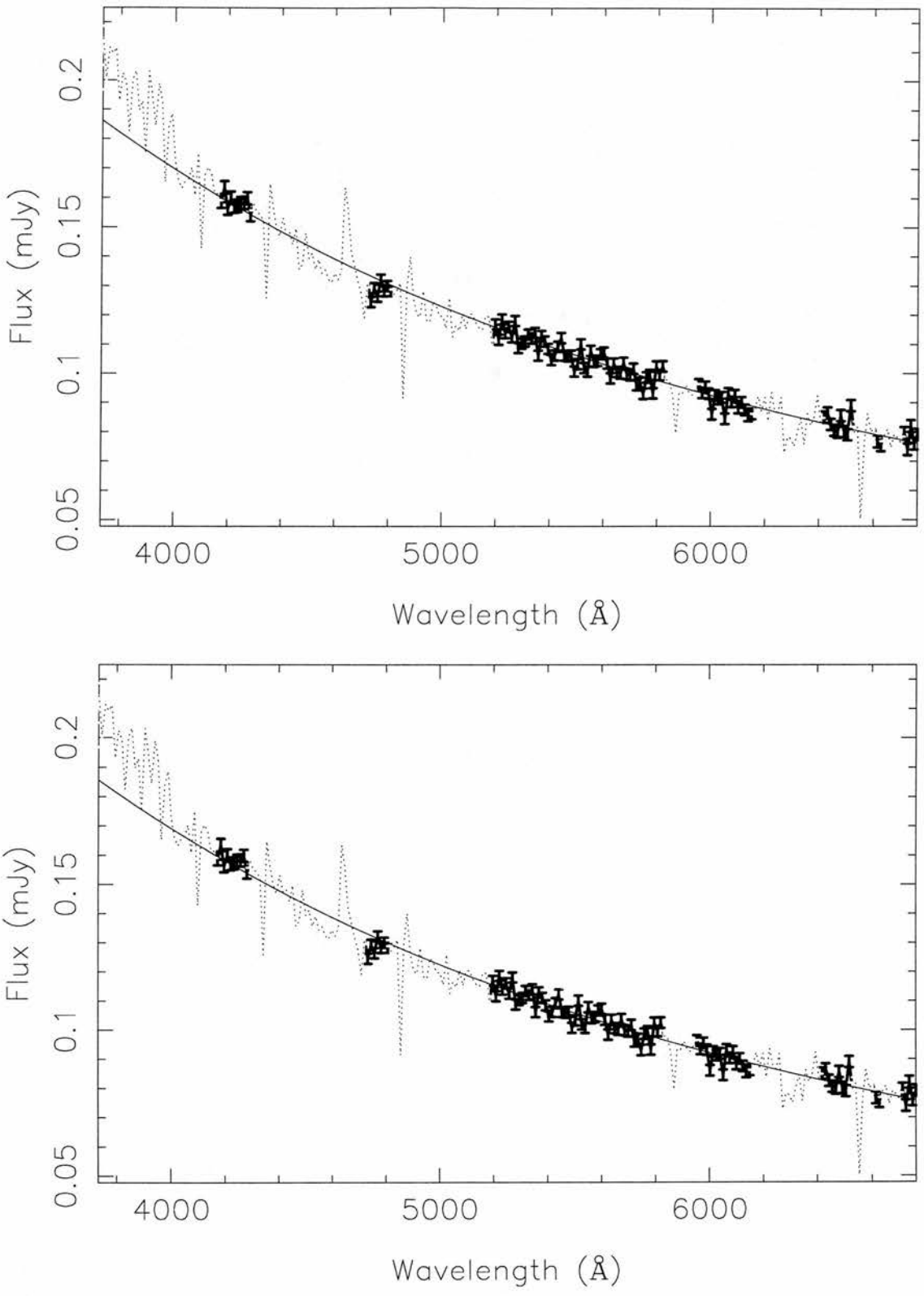

Figure 9.11: Top panel, a plot of the QPO spectrum and its best-fit blackbody. The dotted line shows the data points not used in the fitting routine, the solid points are the data used and the solid line is the best fit blackbody. Lower panel, The same plot as above with the blackbody derivative model.

		orbit 1	orbit2
MJD	start	51000.266061	51000.332743
	end	51000.293567	51000.364678
binary phase	start	0.31	0.35
	end	0.33	0.37
35-day phase	start	0.5229	0.5248
	end	0.5236	0.5257

Table 9.3: Summary of Observations. The orbital phases have been determined using the ephemeris of Scott & Leahy (1999). The 35-day phases have been determined using the BATSE ephemeris of the beginning of the main-on.

9.6 Observations of X-ray spin pulsations during the X-ray low state

9.6.1 Observations

The observations took place on UT 06/07/98, using the PCA onboard *RXTE*. Lightcurves were created from the STANDARD-1 mode data-set, with a time resolution of 0.125 seconds and no spectral information. The energy range of the PCA is 2-60 keV. The lightcurves were corrected to the solar-system barycentre, using the subroutine FXBARY in the FTOOLS software suite. They were also corrected for the motion of the neutron star in its binary orbit around its $2.2M_{\odot}$ companion HZ Herculis.

9.6.2 Power spectra

The power spectra were obtained by fitting sine and cosine waveforms to the data, the amplitudes of which were added in quadrature to obtain the power at a given frequency. The advantage of this simple fitting over modern Fast-Fourier Transforms (FFTs) is the ability to assign inverse variance weights to the model, creating an optimal fit for each waveform. This also allows us to calculate the variance of the amplitudes for each given frequency. The resultant power spectra are normalized, using the method described by Leahy et al. (1983). The results of this analysis are shown in the upper panel of Figure 9.12

and Figure 9.13 for orbits 1 and 2 respectively. The pulse period at 0.808 Hz is clearly seen in both power spectra, although it is clearly more defined in the power spectrum for orbit 2.

We can also determine the significance of the peaks in the power spectra. The probability that a peak in the power spectrum will have a power, P, which has an expectation value, $< P >$, is given by

$$PROB\,(R \leq x) = 1 - exp(-x), \tag{9.12}$$

where $R = P/ < P >$. If there are M independent frequencies in the power spectrum, the probability of finding one with a power, P, is

$$PROB\,(R \leq x) = (1 - exp(-x))^M\,. \tag{9.13}$$

The results of this analysis are shown in the lower panel of Figures 9.12 and 9.13. The probability associated with the detection of the spin frequency is 93.2% for orbit 1 and 99.9% for orbit 2. There is a tentative observation of the first harmonic in the power spectrum of Orbit 2, but it is not detected to any significant level. There are several other features shown in this probability distribution, however only the spin frequency is detected with any significance in both power spectra.

9.6.3 Pulse profiles

The next stage of the analysis is to fold the lightcurve onto the spin frequency obtained from the power spectra. The results of this phase folding for orbits 1 and 2 are shown in top and bottom panels of Figure 9.15 respectively. The pulse profile for orbit 1 shows some evidence a sinusoidal modulation that peaks around phase 0.1, with a second, less pronounced, peak around phase 0.7. In orbit 2, there is also some evidence for two peaks, at 0.7 and 0.2. This would be the case if the we are observing two pole emission, although the signal to noise of the data is not good enough to determine any individual features in the pulse profile to any degree of accuracy.

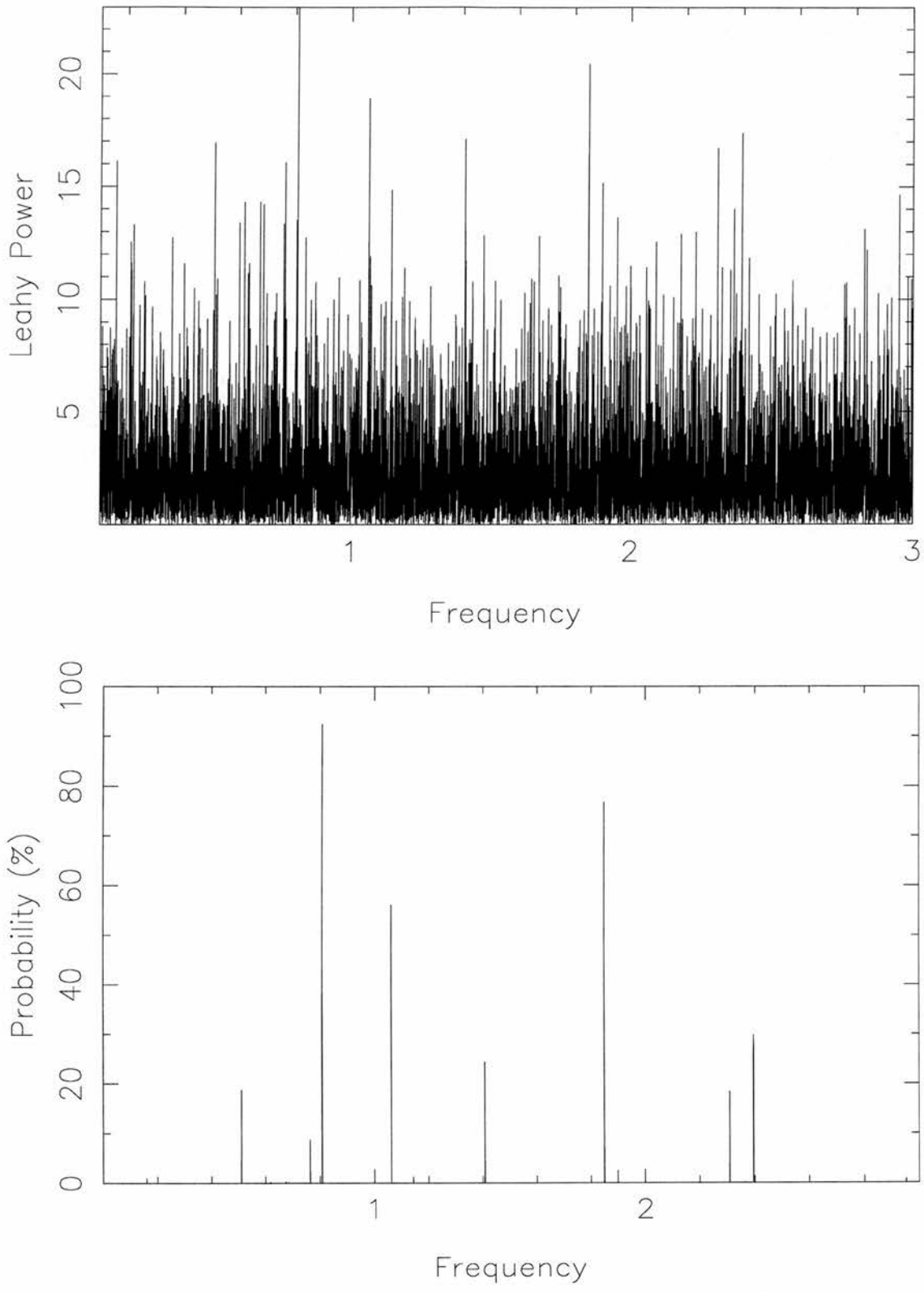

Figure 9.12: Top panel, the X-ray power spectrum for orbit 1, showing the expected spin frequency of 0.808Hz. Lower panel, the probability distribution for the significance of the peaks in the power spectrum in the upper panel, the spin frequency has a significance of 93.2%.

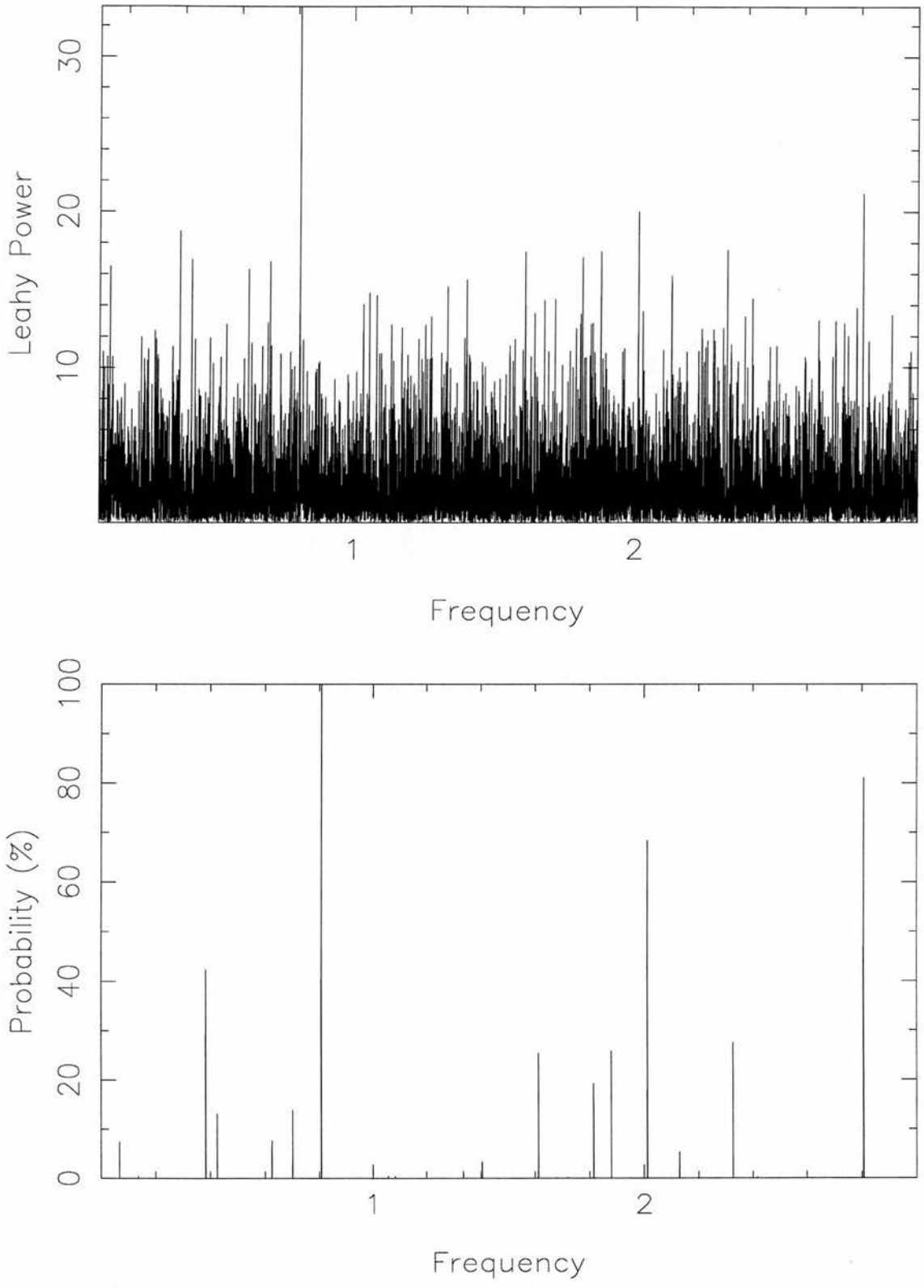

Figure 9.13: Top panel, the X-ray power spectrum for orbit 2, showing the expected spin frequency of 0.808Hz. Lower panel, the probability distribution for the significance of the peaks in the power spectrum in the upper panel, the spin frequency has a significance of 99.9%, the first harmonic of the spin frequency is also visible with a significance of 30%.

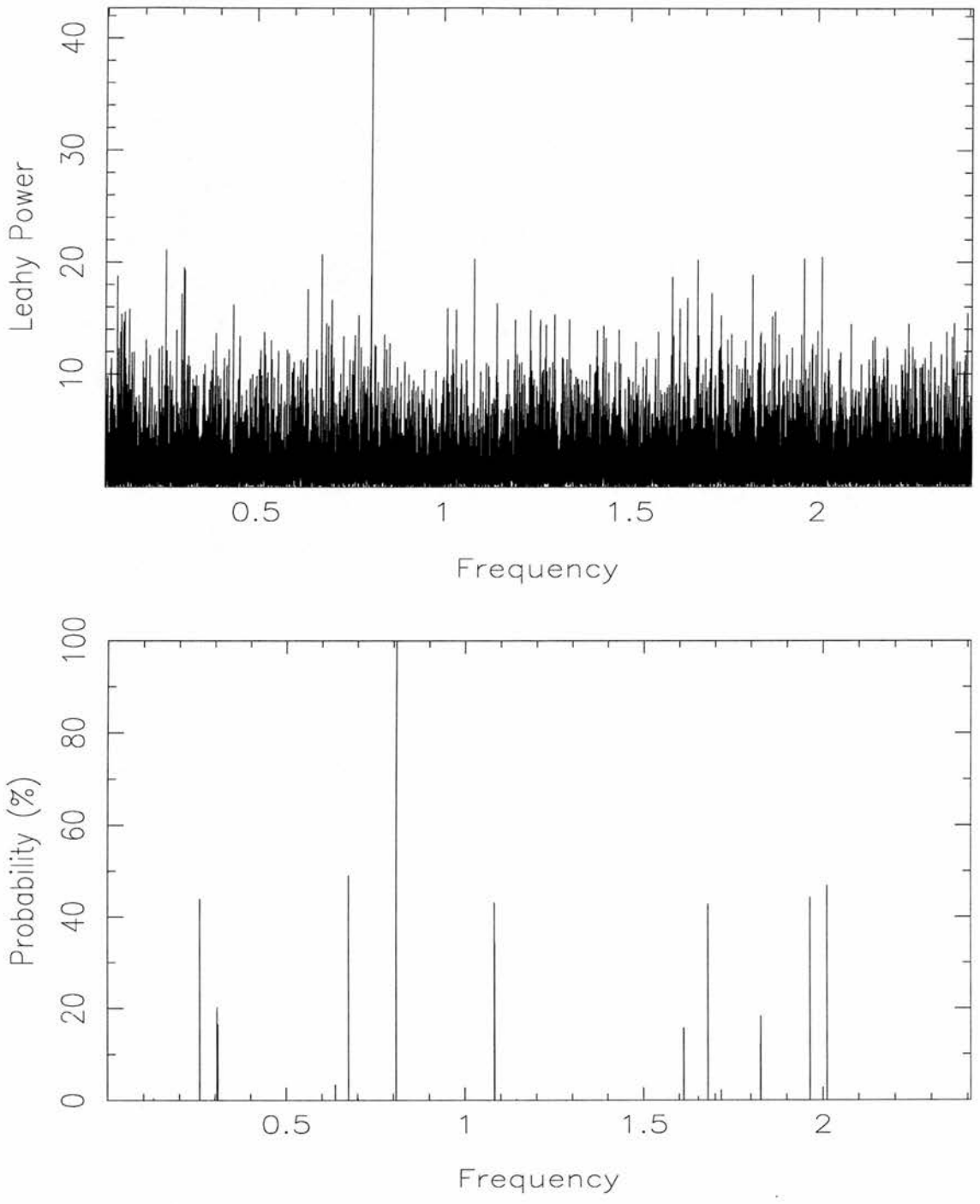

Figure 9.14: Top panel, the X-ray power spectrum for the combined orbits, showing the expected spin frequency of 0.80789(12) Hz. Lower panel, the probability distribution for the significance of the peaks in the power spectrum in the upper panel, the spin frequency has a significance of 99.999%, the first harmonic of the spin frequency is also visible with a significance of 20%.

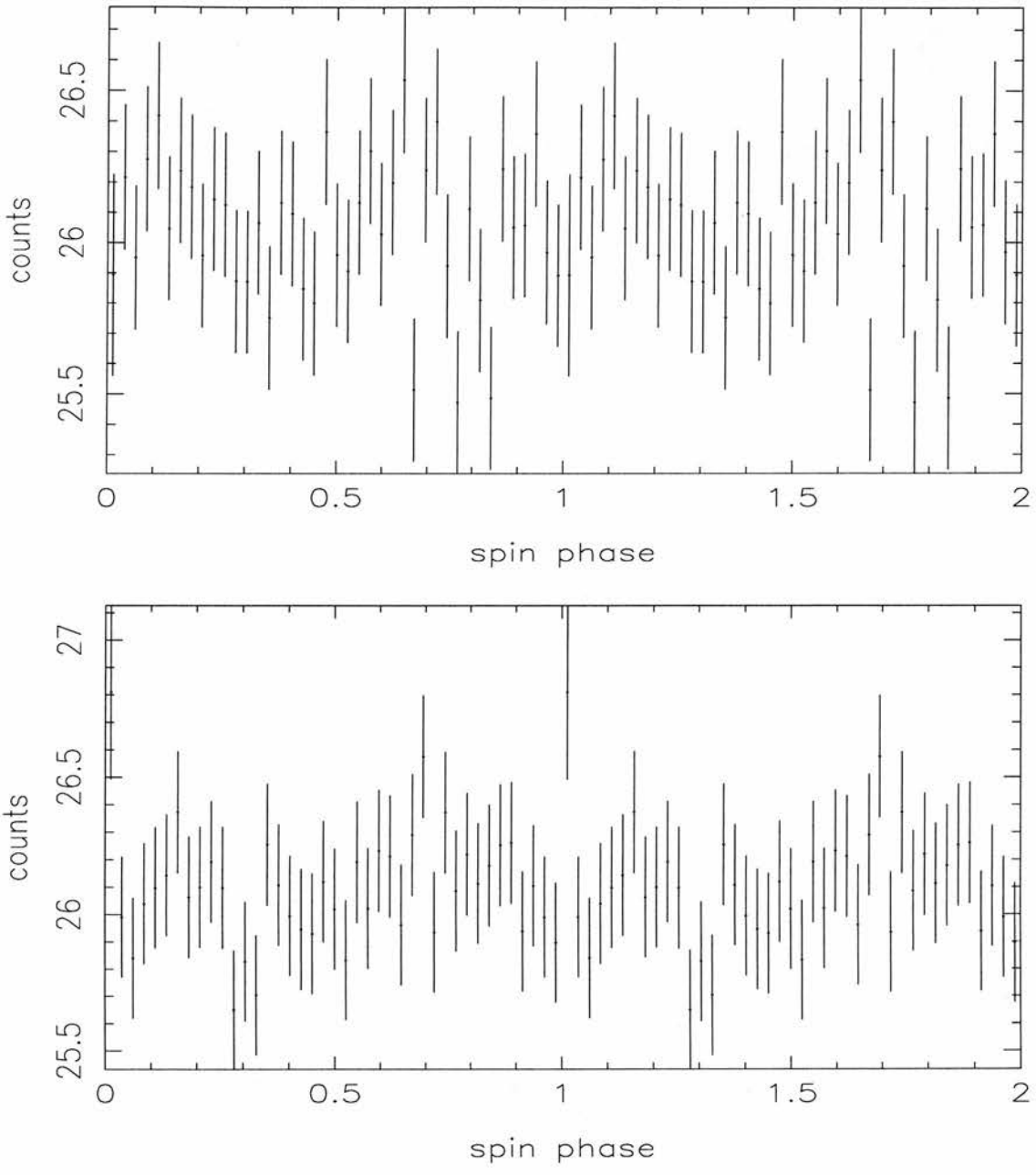

Figure 9.15: The spin profiles created by folding the lightcurve from orbit 1 (top) and orbit 2(bottom) on the best-fit period of 1.2378 seconds.

9.6.4 Discussion

In this section I have determined the characteristics of the spin pulsations of the neutron star in Hercules X-1 from X-ray observations with *RXTE*. These represent the first detection of the spin pulsations during the X-ray off-state, where the X-ray flux is only a small fraction of that during the main-on state, due to absorption of the X-rays by material in the inner regions of the accretion disk. The reduced flux level does not allow us to determine the shape of the pulse profile to any degree of accuracy, but the significance of the peak is found to be at the 99.999% level, with a possible detection of the first harmonic of the spin detected at the 30% level.

9.7 X-ray spectral fits

I have used the FTOOLS software package SAEXTRCT to extract a spectrum for each of the orbits. This is background subtracted using spectra extracted in the same way as the source spectra from background models supplied by heasarc, generated using the FTOOLS command RUNPCABACKEST. The response of the detector and its energy calibration we performed using the FTOOLS command PCARSP. I have created spectral fits to these spectra using models for X-ray spectra in the software package XSPEC. Throughout the fitting I have ignored channels 1-3, due to inaccuracies in the background model at low energies and channels 65-256, due to poor counting statistics.

The model used has five components that are chosen to be physical and fit the observed features in the spectrum. The model chosen has a power law continuum, $P(E)$ with a high energy cut-off, $H(E)$, and an emission line at the iron K-edge energy, $G(E)$. These are absorbed at the source with a partially covering absorber, $C(E)$, and then further absorbed by interstellar material, $A(E)$. This has been used by previous authors to look at the spectrum of Hercules X-1 during the on-state and during the recent (and ongoing) Anomalous Low-State (see for example Oosterbroek et al. (2000), Coburn et al. (1999) and Still et al. (2000)). The total model can be written as,

$$F(E) = A(E)C(E)\left[H(E)P(E) + G(E)\right] \tag{9.14}$$

This is written in XSPEC as PHABS*PCFABS*(HIGH*POWER + GAUSS). The individual components can be written numerically as

1. Power law:

$$P\left(E\right) = A_{pl}\left(\frac{E}{1keV}\right)^{-\Gamma}, \tag{9.15}$$

   where A_{pl} is a normalization coefficient, which represents the number of photons/keV/cm^2/s at 1 keV and Γ is the photon index.

2. High energy cut-off:

$$\begin{aligned} H\left(E > E_{cut}\right) &= \exp\left[\frac{E_{cut} - E}{E_{fold}}\right] \\ H\left(E < E_{cut}\right) &= 1, \end{aligned} \tag{9.16}$$

where E_{cut} is the energy above which the power law is cut off and E_{fold} is the e-folding energy above this cut off energy.

3. Gaussian line profile:

$$G(E) = \frac{A_{line}}{\sqrt{(2\pi\,\sigma_{line}^2)}} \exp\left[-\frac{1}{2}\left(\frac{E - E_{line}}{\sigma_{line}}\right)^2\right] \tag{9.17}$$

where A_{line} is the total number of photons/cm^2/s in the line, E_{line} is the energy of the peak of the line in keV and $\sigma(E)$ is the width of the line in keV.

4. Partial covering fraction photo-electric absorption:

$$C(E) = f \exp\left(-\sigma(E) N_C\right) + (1 - f) \tag{9.18}$$

where f is the covering fraction and N_C is the hydrogen column density in atoms/cm^2 of the covering material and $\sigma(E)$ is the photo-electric cross-section (Balucinska-Church & McCammon 1992).

5. Interstellar photo-electric absorption:

$$A(E) = \exp\left(-\sigma(E) N_A\right) \tag{9.19}$$

where N_A is the hydrogen column density in atoms/cm^2 of interstellar material along the line of sight.

The best fit model for orbits 1 and 2 are shown folded onto the data in Figure 9.16.

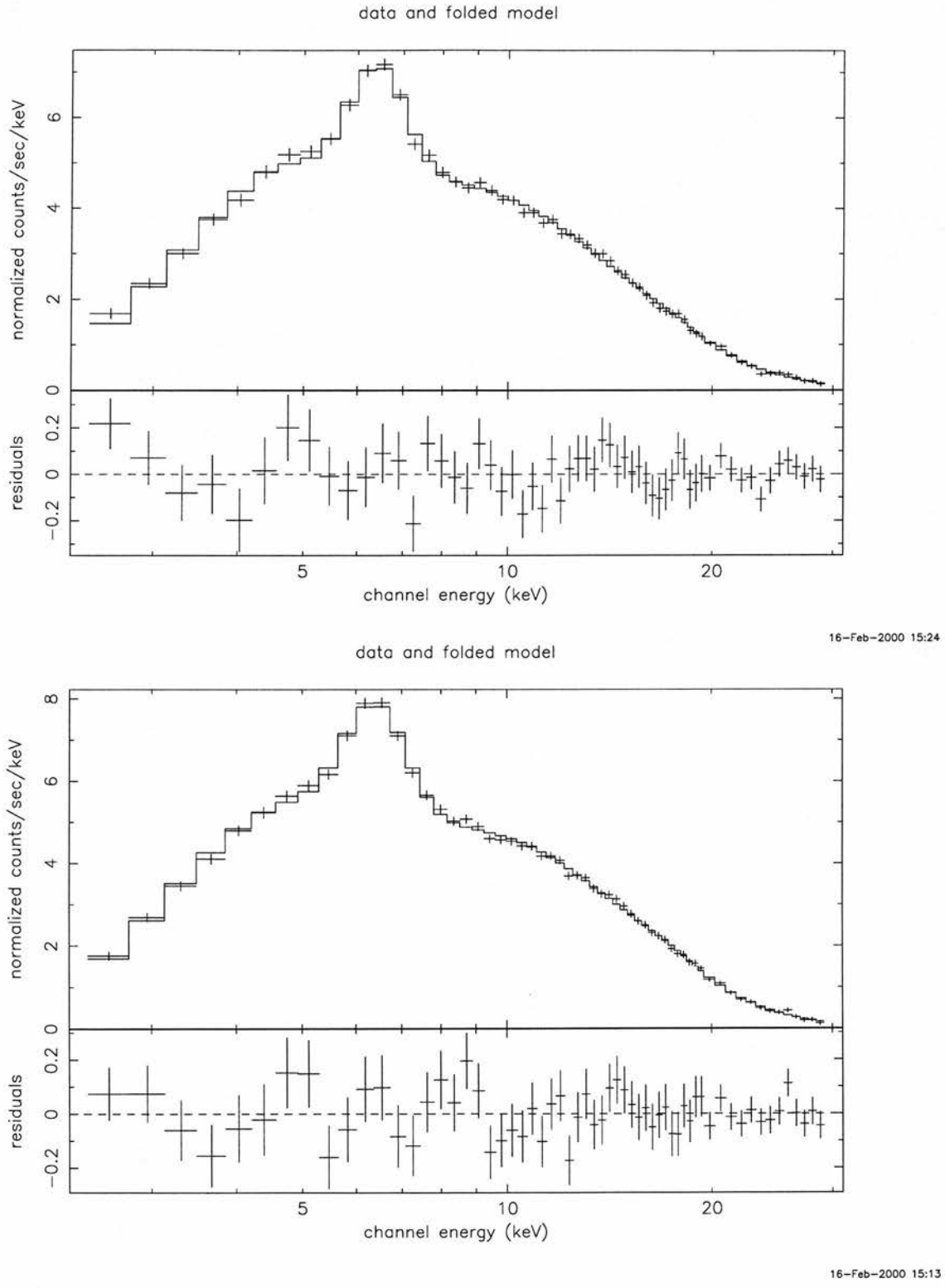

Figure 9.16: The data and folded model for the model fit to the spectrum obtained from orbit 2.

parameter	model	unit	orbit 1	orbit 2
N_C	pcfabs	10^{22} cm^2	22 ± 12	77 ± 35
f	pcfabs		0.24 ± 0.15	0.18 ± 0.10
E_{cut}	highecut	keV	17.64 ± 0.58	17.54 ± 0.39
E_{fold}	highecut	keV	11.0 ± 1.5	9.8 ± 0.9
Γ	powerlaw		0.76 ± 0.13	0.68 ± 0.08
A_{pl}	powerlaw	10^{-3} ph cm^{-2} s^{-1} keV^{-1}	4.4 ± 2.1	4.3 ± 1.4
E_{line}	gaussian	keV	6.36 ± 0.03	6.32 ± 0.05
σ_{line}	gaussian	keV	0.38 ± .06	0.50 ± 0.05
A_{line}	gaussian	10^{-4} ph cm^{-2} s^{-1}	8.6 ± 1.3	12.5 ± .2
$\chi^2/52$			0.928	0.897

Table 9.4: The best fit parameters for the model of the X-ray spectrum of Hercules X-1. The interstellar column density is fixed to $1.22 \times 10^{20} cm^{-2}$ during both fits.

9.8 Discussion

I have studied the X-ray and optical variability in the binary pulsar Hercules X-1. Whilst we have not detected the optical pulsations seen previously, we have detected a new phenomenon, a mHz QPO. I have characterized the temporal frequency distribution of this QPO as having a Gaussian shape. This has been fitted along with the white noise level and a power law at low frequencies. The best fit to this model has a reduced χ^2 of 1.58 for 4687 degrees of freedom and a peak frequency of 35.2 mHz. The power of the QPO is found by integrating the power under the Gaussian and the peak-to-peak amplitude is 5%, whilst the coherence of the oscillation is low, as expected from a QPO, with a value of 2.

In order to further determine the characteristics of the QPO, I have extracted the spectrum of the variability from the temporal frequency range of the QPO. I have also determined the average spectrum and the spectrum of any slower variability, that has characteristic frequencies from the red noise, power law region of the power spectrum. These are shown in Figures 9.6 and 9.7. The variability spectra are bluer and fainter than the average spectrum, indicating they are from a small high temperature region. The average spectrum is predominately that of the companion star, HZ Herculis, see below. It shows strong absorption in the Balmer lines, as well as some helium I absorption lines, although there is some evidence of the irradiation of the companion in the form of a weak helium II (λ4686) emission line and Bowen fluorescence lines (λ4634,λ4641,λ4642), which can be used as a diagnostic of the physical conditions in the binary (Schachter, Fillipenko & Kahn 1989). Unfortunately we can not determine the Bowen yield due to the low spectral resolution of the lines and the lack of any 'pump-frequency' lines in our wavelength range. The variability spectra both show a bluer continuum than the average spectrum with Balmer and helium I absorption lines, however in these spectra the wings of the lines show more variability than the cores of the lines. The Bowen lines also show more variability than the average spectrum, as expected if the variability is coming from a region that has been heated by the irradiation of the X-ray source.

The next stage of the analysis is to try to fit the observed spectra. In order to do

this I have assumed the shape of the continuum spectrum is fitted by a single temperature blackbody spectrum or that of the difference between two blackbodies, representing a region that is varying between one temperature and another. The results of this fitting are shown in Table 9.2, along with their 1-parameter 1-sigma confidence regions. Whilst it would appear from the extremely high χ^2 values that the fits are not representative of the data, the fits shown in Figures 9.9 - 9.11 do appear to fit the data reasonably well, implying that the spectrum shows consistent deviations from that of a blackbody. This is to be expected as I have made no attempt to include any of the absorption lines from the companion star. A more sophisticated irradiated model atmosphere fit to this data would be needed to fit to all the observed features. Whilst this model atmosphere fitting would undoubtedly lead to a better representation of the data it is outside the scope of this thesis and is relegated to the 'Future work' section. The fitting of blackbodies to the observed spectra is sufficient to distinguish between different scenarios for the formation of the QPO.

The best fit model to the average spectrum is a single temperature blackbody, with a mean temperature of 16500 K. The size of the emitting region is $6.8^{22} cm^2$. Whilst this temperature is inconsistent with the temperature of the companion star in the absence of irradiation, which has been observed during eclipse of the accretion disk to have a temperature of $\sim$ 7000 K, it is most likely to be due to the strongly irradiated inner face of the companion star. The size of emitting region would cover approximately 20% of the inner-face of the companion star, assuming a distance of 5 kpc and an effective Roche lobe radius of 3.5×10^{11} cm (Eggleton 1983). This is entirely consistent with a companion star irradiated by an X-ray source at the centre of an accretion disk, that partially shields the companion star from irradiation.

The best fit model to the variability spectra of the slowly varying component also enables us to place constraints on the size and possible locations of the emitting region. The slowly varying component is best fit with the derivative of a blackbody model, although it is only slightly better than the single temperature blackbody. In this model the source has a mean temperature of 7600 K and a variability temperature of $\sim$ 31000 K, from a region of $2.8 \times 10^{20} cm^2$, although in this case a model with a mean temperature equal to that of

the temperature of the average spectrum is only ruled out at the 1-sigma level. This means that a model where the mean temperature is between the temperature of the irradiated and unirradiated regions is within our 1-sigma confidence region. For this reason I believe the best candidate for this component is the same region on the companion star as the average spectrum, but with a smaller area, possibly the most highly irradiated regions close to the inner Lagrangian point.

The best fit model to the spectrum of the QPO is that of a single temperature blackbody with a mean temperature of $\sim$ 33600 K, with an area of $1.25 \times 10^{20} cm^2$. The data is also consistent with the model of a derivative of a blackbody as used to describe the slowly varying component, although the reduced χ^2 is slightly higher for this model. For this reason I associate the QPO with a physically distinct region from the slowly varying component. This region is a small, high temperature, probably in the accretion disk surrounding the compact object. Therefore if the frequency of the QPO is the Kepler frequency of material orbiting around the neutron star, the Kepler radius of the material orbiting with a frequency of 35 mHz around a 1.4 $M_\odot$ neutron star would be $3.3 \times 10^9 cm$. This would appear to be too small to contain the region responsible for the observed spectrum. However if we take the *range* of frequencies included in the QPO, we find that the Kepler radii covered are 9.4×10^8 - $5 \times 10^{10} cm$, which is large enough to encompass the observed region. Assuming these are the bounds of the region responsible for the spectrum of the QPO, the observed area covers $\sim$ 1.6% of this region. If we assume that this area defines a sector of the inner disk, it corresponds to a range of disk azimuths of $\sim 5\,^\circ$.

Characterizing the spectrum as coming from a limited range of azimuths in the disk leads to possible production mechanisms for the QPO frequencies. There are two obvious mechanisms whereby this anisotropy could cause the observed QPO. The first is the material in the preferred region of the disk is orbiting the neutron star and we are seeing the irradiated inner-face of the region, as it passes across the backside of the disk. The observation of the weak signal in the X-ray power spectrum of a beat with X-ray spin frequency supports this model. The beat frequency would be due to either the reflected fraction of the incident X-ray photons, modulated at the spin frequency of the QPO, or enhanced absorption of the X-ray flux as the inhomogeneity passes across the line of sight

to the X-ray source. The second explanation is that the azimuths are fixed in the plane of the binary and that inhomogeneities in the material traveling through these regions gives rise to enhanced emission. This material would orbit the neutron star and emit when it passes through the preferred azimuths. This model predicts that the observation of the observed X-ray beat frequency comes from the enhanced absorption of the X-rays as material passes across our line of sight to the compact object.

Schandl (1996) modeled the warp in the accretion disk to explain the occurrence of the anomalous and pre-eclipse dips, using a coronal wind model. In this model it is the variation with synodic period of the penetration depth of the stream into the inner regions of the accretion that accounts for an increase in material along the line of sight to the binary that accounts for the observed dips. The Keck II observations were taken at the synodic orbital phase of 0.894. At this phase the accretion stream can penetrate down to the inner regions of the accretion disk. According to Schandl's calculations at this synodic period the stream will penetrate the disk at a radius of $\sim 5.1 \times 10^{10} cm$. This is in excellent agreement with the lowest Kepler frequency of the observed QPO. This model predicts that the thickness of the disk will increase as the stream interacts with the disk. This thickening will last for the dynamical timescale, which is of order the Kepler period, naturally explaining the low coherency of our QPO.

The observations of the spin frequency in the X-ray lightcurves of Hercules X-1 imply that we are viewing the compact object directly. The peak to peak amplitude of the oscillation is found to be 2.2% . Observing the pulsed X-ray emission is unusual at this point in the 35-day periodicity, as normally the pulsations are only observed during the main- and short-on states. The best fit model to the X-ray spectrum of Hercules X-1 at this point in the 35-day cycle shows a partially covered power law source, that is cut off at high frequencies. This is consistent with observations of Hercules X-1 during the anomalous low state, which is thought to be caused by an increase in obscuring material. The observation of a beat frequency with the optical QPO in the X-ray power spectrum, could also be evidence for material crossing our line of sight. The lack of excess power at the frequency of the QPO implies that the material responsible for the QPO does not emit X-rays itself, again consistent with our model.

CHAPTER 10

Summary and observations

In this thesis I have investigated some of the features of the X ray and optical variability in X-ray binaries. I have concentrated on the correlated features of such lightcurves in order to characterize some of the effects that the strong X-ray irradiation, by the central compact object, has on the regions it irradiates. These reprocessing sites emit, at optical/UV wavelengths, echoes of the X-ray irradiating flux.

In Chapters 4 & 5, I have used these echoes to constrain the positions of the reprocessing sites in the binary, by creating time-delay transfer functions, that describe the offset of the regions from the central irradiating source. In Scorpius X-1 we find that the X-rays are reprocessed in the accretion disk and the donor star, which leads to a range of time delays that spans the maximum range of possible time delays. However, in GRO J1655-40 we find that the range of time delays is much smaller compared to the maximum allowed. We suggest this is evidence for a thick accretion disk that is the primary reprocessing region, casting a shadow over the inner face of the donor star, causing it to intercept a small percentage of the X-ray flux. This source was observed shortly after outburst and it will need further observations of similar sources at similar time in their outburst cycle to determine if this swelling of the outer disk is a common phenomenon in SXTs.

We have designed and used a novel data acquisition system, that allows us to perform very fast spectroscopy, covering a wide wavelength range. This was attached to the Low Resolution Imaging Spectrograph on Keck II 10-metre telescope, during 5 nights of unused engineering time. This allows us to study a new and relatively un-explored regime.

The observations yielded a unique data-set, with which to study rapid phenomena in a variety of sources, which I have described in Chapter 6.

In this thesis I have concentrated on two series of observations that were simultaneous with the X-ray satellite *RXTE*. This has lead to a series of discoveries that have allowed us to gain a deeper understanding of the role of X-ray irradiation in the source Cygnus X-2, which are described in detail in Chapter 8. I have described how the optical variability appears to trace the mass accretion rate onto the neutron star in the centre of the accretion disk and how we can use this to examine the X-ray variability. With this new insight gained from the simultaneous X-ray and optical variability, I have proposed a model for the X-ray emission based on three components whose importance change as the mass accretion rate changes. Whilst these observations alone can help to distinguish between different models of the structure of the inner accretion disk, further observations of a similar object, Scorpius X-1, are contained in the data-set. These observations are not presented here, but hopefully, when analyzed will help us to discover whether the observations discussed here can be applied to a wider range of sources.

There are also several observable consequences of the model discussed in this thesis, the most important of which is the need for simultaneous X-ray/optical/radio observations to test the importance of the outflow of material in these systems. Such an outflow is proposed as the cause of the change of the relationship between the X-ray and optical intensities observed, when Cygnus X-2 is at the vertex between the Horizontal and Normal Branches of the colour-colour diagram. This would alter the view that the position of the source in the colour-colour diagram is directly proportional to the mass accretion rate, as you would have to consider the mass outflow rate in the model.

I have also reported the first detection of an optical Quasi-Periodic Oscillation (QPO) in the binary X-ray pulsar Hercules X-1, in Chapter 9. I have performed fits to the spectrum of the QPO, created using information on the range of frequencies involved from the power spectrum of the lightcurves. The QPO is found to originate in a hot, relatively small region of the binary. This region is possibly the inner accretion disk, which would also explain the range of frequencies as Kepler frequencies of the orbiting material. This QPO is an example of a number of mHz QPOs that are being detected in

X-ray binaries recently. However the spectral information contained in our data-set offers possibly a unique opportunity to study such a phenomenon.

REFERENCES

Anders E., Grevesse N., 1989, Geochimica et Cosmochimica Acta, 53, 197

Balucinska-Church M., McCammon D., 1992, ApJ, 400, 699

Basko M. M., Sunyaev R. A., Titarchuk L. G., 1974, A&A, 31, 249

Boroson B., O'Brien K., Horne K., Kallman T., Still M., Boyd P., Quaintrell H., Vrtilek S., 2000, ApJ, submitted

Bowyer S., Byam E., Chubb T., Friedmann H., 1965, Science, 17, 894

Casares J., Charles P., Kuulkers E., 1998, ApJ, 493, L39

Chester T. J., 1979, ApJ, 227, 569

Coburn W. et al., 1999, ApJ, submitted

de Jong J. A., van Paradijs J., Augusteijn T., 1996, A&A, 314, 484

Deeter J. E., Scott D. M., Boynton P. E., Miyamoto S., Kitamoto S., Takahama S., Nagase F., 1998, ApJ, 502, 802

Edelson R. A., Krolik J. H., 1988, ApJ, 333, 646

Eggleton P. P., 1983, ApJ, 268, 368+

Fender R. P., Hendry M. A., 2000, MNRAS, submitted

Fender R. P., 1999, astro-ph/9907050

Gaskell C. M., Peterson B. M., 1987, ApJS, 65, 1

Giacconi R., Gursky H., paolini F., Rossi B., 1962, Phys. Rev. Letters, 9, 439

Giacconi R., Gurksy H., Kellogg E., Levinson R., Schreier E., Tananbaum H., 1973, ApJ, 184, 227

Hameury J.-M., Ritter H., 1997, A&AS, 123, 273

Harmon B. A. et al., 1995, Nat, 374, 703+

Hasinger G., van der Klis M., 1989, A&A, 225, 79

Hasinger G., van der Klis M., Ebisawa K., Dotani T., Mitsuda K., 1990, A&A, 235, 131

Hirano A., Kitamoto S., Yamada T. T., Mineshige S., Fukue J., 1995, ApJ, 446, 350+

Hummer D. G., Seaton M. J., 1963, MNRAS, 125, 437

Hynes R. I. et al., 1998, MNRAS, 300, 64

Hynes R. I., O'Brien K., Horne K., Chen W., Haswell C., 1998b, MNRAS, 299, L37

Jones C., Forman W., 1976, ApJ, 209, L131

Jonker P. G., Wijnands R., van der Klis M., Psaltis D., Kuulkers E., Lamb F. K., 1998, ApJ, 499, L191

Jonker P. G. et al., 2000, ApJ, submitted

Kahn S. M., Grindlay J. E., 1984, ApJ, 281, 826

Kallman T., Raymond J., Vrtilek S., 1991, ApJ, 370, 717

Katz J. L., 1973, Nature Phys. Sci., 246, 87

Ko Y.-K., Kallman T., 1991, ApJ, 374, 721

Kuulkers E., van der Klis M., 1996, A&A, 314, 567

Kuulkers E., van der Klis M., 1998, A&A, 332, 845

Kuulkers E., van der Klis M., Oosterbroek T., Van Paradijs J., Lewin W. H. G., 1997, MNRAS, 287, 495

Kuulkers E., van der Klis M., Vaughan B., 1996, A&A, 311, 197

Larwood J., 1998, MNRAS, 299, L32

Leahy D. A., Darbro W., Elsner R., Weisskopf M., Sutherland P., Kahn S., Grindlay J., 1983, ApJ, 266, 160

Matsuoka M. et al., 1984, ApJ, 283, 774

Méndez M., van der Klis M., Ford E. C., Wijnands R., van Paradijs J., 1999, ApJ, 511, L49

Middleditch J., Nelson J., 1976, ApJ, 208, 567

Oke J. B. et al., 1995, PASP, 107, 375

Oke J. B., 1990, AJ, 99, 1621

Oosterbroek T., Parmar A. N., Dal Fiume D., Orlandini M., Santangelo A., Del Sordo S., Segreto A., 2000, A&A, 353, 575

Orosz J. A., Bailyn C. D., 1997, ApJ, 477, 876

Orosz J. A., Kuulkers E., 1999, MNRAS, 305, 132

Parmar A. N., Oosterbroek T., dal Fiume D., Orlandini M., Santangelo A., Segreto A., del Sordo S., 1999, A&A, 350, L5

Pedersen H. et al., 1982, ApJ, 263, 325

Penninx W., Lewin W. H. G., Zijlstra A. A., Mitsuda K., van Paradijs J., 1988, Nature, 336, 146

Penninx W., Lewin W. H. G., Tan J., Mitsuda K., van der Klis M., van Paradijs J., 1991, MNRAS, 249, 113

Petro L. D., Bradt H. V., Kelley R. L., Horne K., Gomer R., 1981, ApJ, 251, L7

ponman T. J., cooke B. A., Stella L., 1988, MNRAS, 231, 999

Press W. H., Teukolsky S. A., Vetterling W. T., Flannery B. P., 1992, Numerical Recipes in Fortran. Cambridge University Press

Remillard R., Bradt H., Cui W., Levine A., Morgan E., Shirey B., Smith D., 1996, IAU Circ, 6393, 1+

Reynolds A. P., Quaintrell H., Still M. D., Roche P., Chakrabarty D., Levine S. E., 1997, MNRAS, 288, 43

Rutten R., Dhillon V., 1994, A&A, 288, 773

Schachter J., Fillipenko A., Kahn S., 1989, ApJ, 340, 1049

Schandl S., Meyer F., 1994, A&A, 289, 149

Schandl S., 1996, A&A, 307, 95+

Scott D. M., Leahy D. A., 1999, ApJ, 510, 974

Smale A. P., 1998, ApJ, 498, L141

Still M., O'Brien K., Horne K., Boroson B., Titarchuk L. G., Vrtilek S. D., Quaintrell H., Fiedler H., 2000, ApJ, submitted

Tananbaum H., Gurksy H., Kellogg E., Levinson R., Schreier E., Giacconi R., 1972, ApJ, 174, L143

Tuchman Y., Mineshige S., Wheeler J., 1990, ApJ, 359, 164

van der Klis M., Swank J. H., Zhang W., Jahoda K., Morgan E. H., Lewin W. H. G., Vaughan B., van Paradijs J., 1996, ApJ, 469, L1

van der Klis M., 1989, in Ogelman H., van den Heuvel E., eds, Timing Neutron Stars. Kluwer, p. 27

van der Klis M., 1997, in Maoz D., Sternberg A., Leibowitz E. M., eds, Astronomical Time Series. Dordrecht: Kluwer, p. 121+

van Paradijs J. et al., 1990, A&A, 235, 156

Vrtilek S., Raymond J., Garcia M., Verbunt F., Hasinger G., Kurster M., 1990, A&A, 235, 162

Vrtilek S., Penninx J., Raymond J., Verbunt F., Hertz P., Wood K., Lewin W., Mitsuda K., 1991, ApJ, 376, 278

White R. J., Peterson B. M., 1994, PASP, 106, 879

White N. E., Nagase F., Parmar A. N., 1995, in Lewin, van Paradijs, van den Heuvel, eds, X-ray Binaries. Cambridge University Press, p. 1

Wijnands R. A. D., Kuulkers E., Smale A. P., 1996, ApJ, 473, L45

Wijnands R. et al., 1997, ApJ, 490, L157

Wijnands R. et al., 1998, ApJ, 493, L87

Wijnands R., Mendez M., van der Klis M., Psaltis D., Kuulkers E., Lamb F. K., 1998, ApJ, 504, L35

Zhang W., Strohmayer T. E., Swank J. H., 1998, ApJ, 500, L167

Tananbaum H., Gurksy H., Kellogg E., Levinson R., Schreier E., Giacconi R., 1972, ApJ, 174, L143

Tuchman Y., Mineshige S., Wheeler J., 1990, ApJ, 359, 164

van der Klis M., Swank J. H., Zhang W., Jahoda K., Morgan E. H., Lewin W. H. G., Vaughan B., van Paradijs J., 1996, ApJ, 469, L1

van der Klis M., 1989, in Ogelman H., van den Heuvel E., eds, Timing Neutron Stars. Kluwer, p. 27

van der Klis M., 1997, in Maoz D., Sternberg A., Leibowitz E. M., eds, Astronomical Time Series. Dordrecht: Kluwer, p. 121+

van Paradijs J. et al., 1990, A&A, 235, 156

Vrtilek S., Raymond J., Garcia M., Verbunt F., Hasinger G., Kurster M., 1990, A&A, 235, 162

Vrtilek S., Penninx J., Raymond J., Verbunt F., Hertz P., Wood K., Lewin W., Mitsuda K., 1991, ApJ, 376, 278

White R. J., Peterson B. M., 1994, PASP, 106, 879

White N. E., Nagase F., Parmar A. N., 1995, in Lewin, van Paradijs, van den Heuvel, eds, X-ray Binaries. Cambridge University Press, p. 1

Wijnands R. A. D., Kuulkers E., Smale A. P., 1996, ApJ, 473, L45

Wijnands R. et al., 1997, ApJ, 490, L157

Wijnands R. et al., 1998, ApJ, 493, L87

Wijnands R., Mendez M., van der Klis M., Psaltis D., Kuulkers E., Lamb F. K., 1998, ApJ, 504, L35

Zhang W., Strohmayer T. E., Swank J. H., 1998, ApJ, 500, L167